THE GENERATION MECHANISMS OF ACOUSTIC EMISSION IN METAL CUTTING

António João de Melo Martins de Araújo

A SUBMISSION PRESENTED IN PARTIAL FULFILMENT OF THE REQUIREMENTS OF
THE UNIVERSITY OF GLAMORGAN/PRIFYSGOL MORGANNWG
FOR THE DEGREE OF DOCTOR OF PHILOSOPHY

December 2006

to my aunt Maria José,
she taught me the most important things

Abstract

The objective of the present thesis is the investigation of the generation mechanism of the ultrasonic vibrations, commonly called acoustic emissions (AE), detected during the course of metal cutting, since, although quite a lot of research effort has been put into the use of AE to monitor metal cutting condition, the mechanism by which AE is generated is still not fully understood.

If chip generation is continuous, without built-up edge, and a sharp tool is used, continuous-type AE is normally assumed. Most published models relate the energy of AE to the total cutting power, but this can be shown to be rather incorrect. Consequently, as continuous-type AE is mostly generated due to plastic deformation, and as dislocation motion is the main mechanism of plastic deformation of metals, a relationship between AE and dislocation motion is developed for the typical plastic deformation regimes encountered in metal cutting (due to the high temperatures, flow stress decreases with temperature in the so-called diffusion controlled regime, and due to the high strain rates, opposing viscous damping becomes the dominant mechanism governing dislocation movement). Although viscous damping governs the mechanics of deformation in metal cutting, it is proposed that AE is generated due to the interaction between dislocations and obstacles, since as a dislocation approaches an obstacle, strain energy is stored, which is rapidly released as soon as the dislocation surmounts the obstacle, resulting in the emission of an AE event. The detected AE is a result of many consequential likewise events. Consequently, a qualitative original model of AE generation is developed, in which the energetic level of AE is predicted to increase with strain and strain rate, but decrease with temperature, and the frequency content of AE is predicted to increase with strain rate, decrease with temperature, and remain unchanged with strain.

In order to access the validity of the above-mentioned model, two sets of metal cutting experiments were accomplished for four different work materials, in which the cutting conditions were varied over a wide range, and the workpiece temperature was artificially modified. Both energy and frequency information were computed from the experimental data using the most appropriate data processing technics, i.e. AE mode and mean frequency, respectively. In addition, a semi-empirical metal cutting theory was utilized to predict basic metal cutting parameters. As the experimental results are in close agreement with the predictions provided by the qualitative model, it is concluded that the main source of AE in metal cutting comes from the interaction of moving dislocations with obstacles, whose dynamics is, however, dictated by viscous damping.

Acknowledgments

First of all, I would like to deeply thank my director of studies Prof. Steven Wilcox for his scientific advice and orientation, exhaustive corrections, and endless patience. I also would like to express my gratitude to my supervisor Prof. Robert Reuben for helping setting up initial goals and his technical guidance. I am also very grateful to Clive Monks for his aid with the experimental work on the CNC centre and the manufacturing of some mechanical parts, and to Gareth Betteney for his help on the electronic circuitry.

Secondly, I would like to thank the innumerable friends that I have socialized with during the last interminable years that I have lived in Wales, London, and Portugal.

Finally, the most special thanks to my closest family: my aunts Maria José, Felisbina, and Maria, my two sisters (Zefa and Quela), and my mother (Madalena).

Contents

List of Figures

List of Tables

List of Symbols

α	tool rake angle
α_L	angle of longitudinal wave travelling in medium A with normal to its boundary
α_T	angle of transverse wave travelling in medium A with normal to its boundary
β	proportion of heat conducted into the work
β_L	angle of longitudinal wave travelling in medium B with normal to its boundary
β_T	angle of transverse wave travelling in medium B with normal to its boundary
δ	ratio of secondary plastic zone thickness to chip thickness
Δs_1	thickness of primary parallel-sided shear zone
Δs_2	thickness of secondary deformation zone
ΔT_{AB}	temperature rise in the primary shear plane
ΔT_C	mean temperature rise in the chip
ΔT_{max}	maximum temperature rise in the chip
ΔT_{SZ}	temperature rise in the primary shear zone
ε	uniaxial strain
$\dot{\varepsilon}$	uniaxial strain rate
$\dot{\varepsilon}_0$	constant in velocity-modified temperature equation
ε_{AB}	primary uniaxial strain
$\dot{\varepsilon}_{AB}$	primary uniaxial strain rate
$\dot{\varepsilon}_{ij}$	tensor notation for strain rate
$\dot{\varepsilon}_{int}$	secondary uniaxial strain rate

η	correction factor because not all primary plastic work occurs on the shear plane
γ	shear strain; plane strain
$\dot{\gamma}$	shear strain rate; plane strain rate
γ_{AB}	primary shear strain
$\dot{\gamma}_{AB}$	primary shear strain rate
γ_{EF}	total shear strain occurring on the primary shear zone
$\dot{\gamma}_{int}$	secondary shear strain rate
κ	conductivity
λ	tool-chip interface friction angle
μ	coefficient of friction
ν	constant in velocity-modified temperature equation
ω	angle representing the size of built-up edge
ϕ	primary shear angle
ψ	correction factor because interface temperature is an average value
ρ	density
ρ_B	density of dislocation obstacles
ρ_D	density of dislocations
ρ_{MD}	density of mobile dislocations
σ	uniaxial stress; normal stress
σ_1	constant of proportionality in empirical stress-strain equation
σ_{AB}	primary normal stress
σ_{ij}	tensor notation for applied stress
σ_{int}	secondary normal stress
σ_{max}	maximum normal stress
σ_{mean}	standard deviation of mean frequency
σ_N	normal stress at the cutting edge

σ'_{N}	normal stress at the cutting edge
τ	shear stress
τ^*	thermal activated stress required for material to flow
τ^*_0	value of τ^* at 0 K
τ_{A}	athermal stress required for material to flow
τ_{AB}	primary shear stress
τ_{B}	shear stress required to overcome dislocation obstacles
τ_{D}	shear stress required to overcome damping forces
τ_{int}	secondary shear stress
θ	angle between primary shear plane and resultant cutting force
a	wave attenuation coefficient
A	constant; common heat transfer area between elements (finite-difference); area of contact between element and surrounding air (finite-difference)
A_{AB}	primary shear plane area
A_{int}	tool-chip interface area
b	Burgers vector
b_{edge}	Burgers vector of pure edge dislocation
b_{screw}	Burgers vector of pure screw dislocation
B	constant; intercept; damping coefficient
c	specific heat
c_{AL}	velocity of longitudinal wave in medium A
c_{AT}	velocity of transverse wave in medium A
c_{BL}	velocity of longitudinal wave in medium B
c_{BT}	velocity of transverse wave in medium B
c_{L}	velocity of longitudinal wave
c_{T}	velocity of transverse wave

C	primary strain rate empirical constant
C_1	heat flow coefficient (finite-difference)
C_2	heat flow coefficient (finite-difference)
C_3	heat flow coefficient (finite-difference)
C_4	heat flow coefficient (finite-difference)
C_5	heat flow coefficient (finite-difference)
C_6	heat flow coefficient (finite-difference)
C_{S}	side cutting angle
d	distance; distance between elements (finite-difference)
d_{B}	distance between dislocation obstacles
e	convergence error criterium (finite-difference)
f	frequency
f_i	frequency at index i
f_{max}	frequency of maximum spectrum value
f_{mean}	mean frequency
F	force acting on a dislocation
F_{AB}	force tangential to the primary shear plane
F_{B}	force due to a dislocation obstacle
$F_{\mathrm{B}}^{\mathrm{max}}$	maximum force due to a dislocation obstacle
F_{D}	damping force
F_{int}	force tangential to the tool-chip interface; sliding friction force on tool-chip interface
F_{X}	tangential force
F'_{X}	corrected tangential force for orthogonality
F_{Y}	feed force
F'_{Y}	corrected feed force for orthogonality
F_{Z}	radial force

F'_{Z}	corrected radial force for orthogonality
h	heat convection coefficient (finite-difference)
i	element index in x direction (finite-difference)
I	amplitude
I_0	initial amplitude
I_i	acoustic emission amplitude at index i
$I_{\max}$	maximum amplitude
I_{mode}	acoustic emission mode
I_{power}	acoustic emission power
I_{RMS}	acoustic emission root mean square
I_{S}	remotely sensed acoustic emission amplitude
j	element index in y direction (finite-difference)
k	shear flow stress; plane stress; shear strength; element index in z direction (finite-difference)
k_{AB}	primary shear flow stress
k_{int}	secondary shear flow stress
K	constant of proportionality
K_1	factor for signal attenuation
K_2	factor for signal attenuation
K_3	factor for signal attenuation
l	distance
l_1	sticking zone length
l_2	sliding zone length
l_{AB}	primary shear plane length
l_{C}	length of a piece of chip
l_{D}	dislocation length

l_{int}	tool-chip interface length
m	constant; slope; index; coefficient of chip contact length; number of block subdivisions in x direction, resulting in $m+1$ elements (finite-difference)
n	index; empirical stress-strain equation index; number of samples; parabolic constant; slope of line in logarithmic scale; number of block subdivisions in y direction, resulting in $n+1$ elements (finite-difference)
n_1	index
n_2	index
N	total number of counts; iteration number (finite-difference)
$\dot{N}$	count rate
N_{AB}	force normal to the primary shear plane
N_{int}	force normal to the tool-chip interface
o	number of block subdivisions in z direction, resulting in $o+1$ elements (finite-difference)
$\dot{Q}_1$	heat flow into the element in positive x direction (finite-difference)
$\dot{Q}_2$	heat flow into the element in negative x direction (finite-difference)
$\dot{Q}_3$	heat flow into the element in positive y direction (finite-difference)
$\dot{Q}_4$	heat flow into the element in negative y direction (finite-difference)
$\dot{Q}_5$	heat flow into the element in positive z direction (finite-difference)
$\dot{Q}_6$	heat flow into the element in negative z direction (finite-difference)
$\dot{Q}_{\text{cond}}$	heat conduction between neighbouring elements (finite-difference)
$\dot{Q}_{\text{conv}}$	heat convection between peripheral element and surrounding air (finite-difference)
r	ratio of uncut to cut chip thickness; acoustic impedance
r^2	coefficient of multiple regression
r_{A}	acoustic impedance of material A
r_{B}	acoustic impedance of material B
R	resultant cutting force

R_1	resultant force on the chip along the primary shear plane
R_2	resultant force on the chip along the tool-chip interface
R_T	non-dimensional thermal number
S_i	signal power at frequency at index i
t	time
t_1	feed rate; uncut chip thickness
t_1'	corrected feed rate for orthogonality
t_2	chip thickness
T	temperature; temperature of element (finite-difference)
T'	temperature of neighbouring element (finite-difference)
T_∞	temperature of surrounding air (finite-difference)
T_1	temperature of thermocouple 1
T_2	temperature of thermocouple 2
T_AB	primary shear plane temperature
T_C	mean chip temperature
T_int	tool-chip interface temperature
T_mode	velocity-modified temperature
T_M	melting temperature
T_W	workpiece temperature
T_WS	workpiece surface temperature
u	specific cutting power
u_A	surface specific power
u_C	frictional specific power
u_M	momentum specific power
u_S	shear specific power
$\dot{U}$	total cutting power; work of deformation

$\dot{U}_{\mathrm{AB}}$	primary shear energy consumption
$\dot{U}_{\mathrm{B}}$	power transmitted by a dislocation to an obstacle
$\dot{U}_{\mathrm{D}}$	damping power
v	volume
v_{int}	secondary deformation volume
V	cutting speed
V_{B}	length of flank wear land
V_{C}	chip velocity
V_{D}	dislocation speed
V_{N}	velocity normal to primary shear plane
V_{S}	shear velocity (tangential to primary shear plane)
w	width of cut
w'	corrected width of cut for orthogonality
W_{C}	weight of a piece of chip
x	distance
x_0	initial distance
x^1	position where an obstacle starts opposing dislocation movement
x^2	position where an obstacle ends opposing dislocation movement
x_{D}	distance moved by a dislocation
x^{max}	position of maximum force due to a dislocation obstacle
y	distance

Chapter 1

Introduction

1.1 Metal Cutting Basics

Metal cutting or machining may be defined as a process by which a thin layer of metal, the chip or swarf, is removed by a wedge-shaped tool from a large body. Operations that do not involve chip formation can also be called metal cutting, but these will not be considered here. In the process of cutting, the metal removed is deformed plastically, and a large amount of energy is necessary to form the chip and to move it across the tool face. Hence, very high stresses are imposed and much heat is generated. The importance of metal cutting may be appreciated by the observation that nearly every device in our society has one or more machined surface or holes. The three most widely used cutting operations are: turning, milling, and drilling. However, since the present thesis deals uniquely with the process of turning, from this point on, only this process will receive

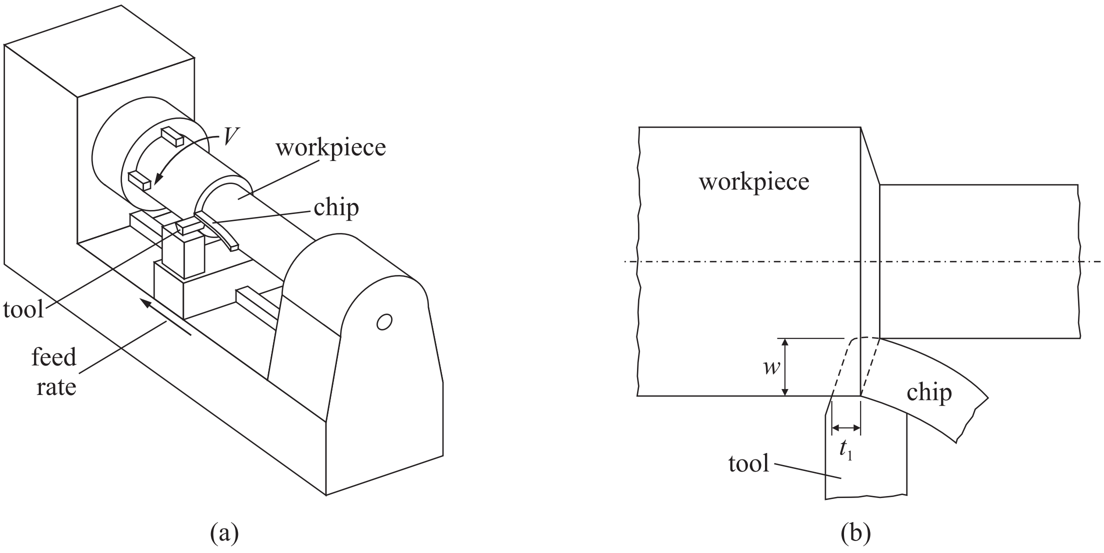

Figure 1.1: Turning operation. (a) Engine lathe. (b) Top view detail of the cutting zone.

relevant attention; also, when one refers exclusively to metal cutting in the context of a specific cutting operation, one is referring to turning.

Turning, the simplest of all cutting operations, is a process in which the work material is held in the chuck of a lathe and rotated. The tool is held rigidly in a tool post and moved along the axis of the workpiece, cutting away a layer of metal to form a cylinder or another profile (Figure 1.1). The variables that can be adjusted by the operator are: the cutting speed (V), the feed rate (t_1), and the width of cut (w). The cutting speed is the rate at which the rotating uncut surface of the work passes the tool; the feed rate is the distance moved by the tool along the axial axis of the workpiece during one revolution; the width of cut is the thickness of metal removed from the workpiece in the radial direction.

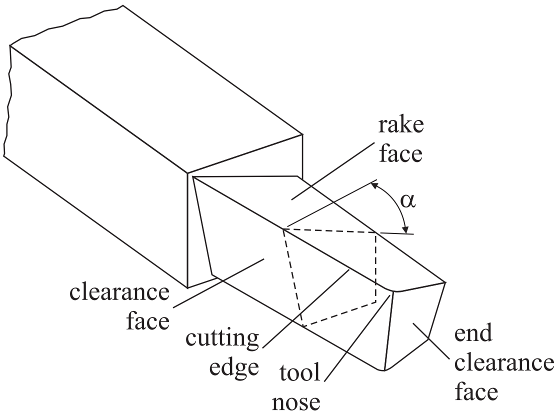

Figure 1.2: Turning tool.

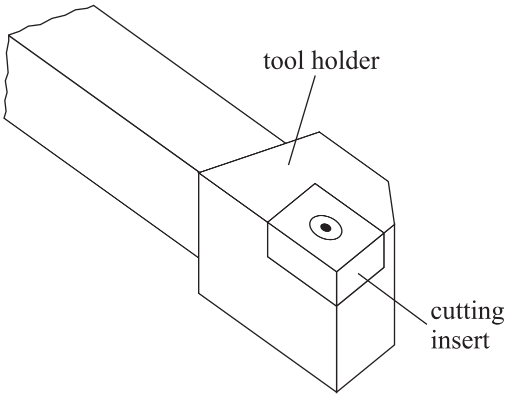

Figure 1.3: Turning tool holder and insert.

Figure 1.2 shows the main features of a cutting tool used in turning operations. The surface of the tool over which the chip flows is called the rake face; the cutting edge is formed by the intersection of the rake face with the clearance face of the tool; the clearance angle must be adequate so as to avoid contact between the tool and the newly cut metal surface; the rake angle (α)

is measured on a plane perpendicular to the cutting edge; the tool terminates in the end clearance face; the nose of the tool is the intersection of all these three faces. The major classes of tool materials include (in order of increasing hot hardness but in order of decreasing toughness) [1]: carbon steels, high-speed steels, cast alloys, tungsten carbides, cermets, titanium carbides, ceramic, polycrystalline diamond and cubic baron nitrits, and single crystal diamond. With the introduction of carbide materials, it became uneconomic to make the whole tool of one material. Consequently, small tool inserts started to be produced in order to be clamped on a tool holder (Figure 1.3). Indexable inserts are presently manufactured in a variety of shapes, having a number of cutting edges, so that when a cutting edge is worn out, the insert is unclamped and rotated to an unused cutting edge. When all edges are worn out, the insert is discarded rather than reconditioned.

Cutting can be simplified to a process called orthogonal cutting. In this process, the tool has a single and straight cutting edge, which is set normal to the cutting speed, removing a layer of work material of uniform thickness t_1 and width w (Figure 1.4). In turning, these conditions are secured by cutting only with the straight edge of the tool, which must be set normal to the cutting speed and feed rate directions, and by employing a workpiece in a tubular form whose wall thickness corresponds to the width of cut. In this method, the cutting speed is not exactly constant along the cutting edge, being slightly greater at the outside of the tube. However, if the tube diameter is reasonably large, this difference between speeds can be neglected. If turning is performed with a solid workpiece, the process is called semi-orthogonal, for the conditions at the nose of the tool are different from those at the outer surface of the bar. To avoid a great discrepancy from orthogonal conditions, the tool nose must be small relatively to the width of cut, so that most of the cutting edge engaged in cutting is straight. Orthogonal cutting may be simplified to a two-dimensional system as shown in Figure 1.5. The uncut chip thickness t_1 corresponds to the feed rate associated with turning operations, so that uncut chip thickness and feed rate can be treated indistinctively. The chip flows over the tool rake face with thickness t_2 and speed V_C.

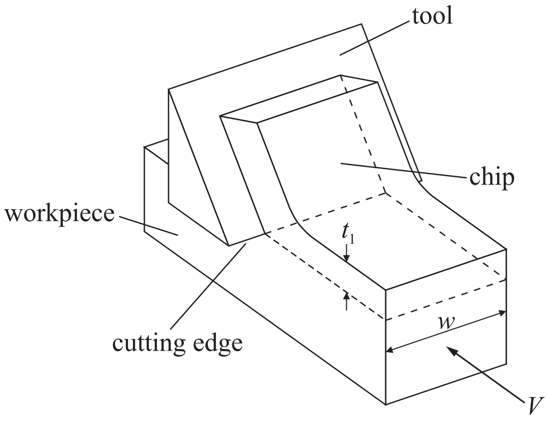

Figure 1.4: Orthogonal machining process.

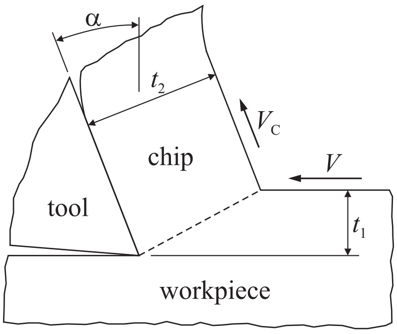

Figure 1.5: Two-dimensional representation of a cutting process.

1.2 Metal Cutting Monitoring

The objective of any machining process is the production of a part of a specific shape with adequate dimensional accuracy and surface condition from an appropriate workpiece. However, some cutting process abnormalities, such as tool wear, tool breakage, machine vibration (chatter), and improper chip formation may affect the quality of the finished machined part. Moreover, effective control of the condition of the tool may reduce tooling costs and down time. Subsequently, cutting processes must be monitored, which has been traditionally done by human operators. The introduction of automated machining systems have greatly increased productivity and decreased human involvement. However, for the successful implementation of fully unmanned machining systems, monitoring has to be performed with sensors and associated decision-making systems, which are able to interpret the incoming sensor information and decide on the appropriate corrective action.

The signals employed in the monitoring of a cutting process can be classified into two categories: direct and indirect. In direct signal monitoring, the actual variable of interest is directly measured, and, despite its high accuracy, it is rarely utilized because of the high cost and difficulty of installation of the sensors. In contrast, indirect signal monitoring utilizes sensors that are relatively economical and small, and they can be used for on-line monitoring if a relationship between the sensor signal and the variable of interest can be established. The most common indirect signals include: cutting forces, cutting power, vibration, sound, temperature, surface roughness, and acoustic emission (AE).

An advantage of AE from the other indirect sensing techniques is that AE is considered to be directly related to the micro-mechanical activities of the cutting process. Also, since AE is normally a high frequency signal, unwanted lower frequency noise signals from the machining process can be filtered off from the signal of interest. As a result, AE has been used in various monitoring applications. Reuben [2] gives a brief overview, not only on the use of AE in metal cutting monitoring, but also on other industrial applications to which AE monitoring has been successfully implemented. The use of AE to monitor the state of a cutting process has been investigated by several authors, and some promising results have been obtained. There are two main areas of interest in metal cutting monitoring:

Tool condition The use of AE has been employed in the detection of both progressive tool wear [3–9] and also sudden tool failure due to cracking, chipping, and fracture [10–13].

Chip management Another application of AE is the detection of the different types of chip formation during metal cutting and also the detection of undesirable congestion or entangling of chips [14–16].

However, despite much effort has been directed towards developing on-line condition monitoring systems that make use of features extracted from the AE signal, few of them have shown to be reliable enough as to be implemented in industry [17].

1.3 Thesis Objectives and Structure

In order to improve the accuracy of the AE monitoring techniques, the mechanisms by which AE is generated must be understood. As shown by two quite recent review papers [8, 9] and from the introduction of a very recent publication [17], most studies on the generation mechanisms of AE due to metal cutting have been accomplished during the 1980s and beginning of the 1990s. Since then, most research effort has been put on the study of a number of, more or less, sophisticated techniques that make use of the AE signal for monitoring metal cutting operations [8, 9]. From the studies on the origin of AE during metal cutting, some models have emerged; however, none of these models has given a completely satisfactory solution for the problem, and although much insight has been gained on the field, the exact mechanisms of AE from metal cutting are still not fully understood.

As a consequence, it is the general objective of the present thesis to investigate the generation mechanisms of AE during metal cutting, so that the generation mechanisms of AE are understood, and a relationship between AE and metal cutting is achieved. A comprehensive review on the most significant theories and techniques achieved in the fields of metal cutting, AE, and the relationship between the two is undertaken. Most suitable signal processing techniques are employed in the analysis of the data from a comprehensive set of metal cutting experiments, where different work materials and a wide range of cutting conditions are utilized. In addition, a semi-empirical metal cutting theory is employed as a metal cutting model, so that a relationship between plastic deformation and AE can be investigated. The main techniques utilized in the processing and analysis of the experimental data and also the most relevant theories utilized in the modelling of AE due to plastic deformation accompanying metal cutting are summarized next:

- A semi-empirical model developed by Oxley and co-workers [18] is used, so that important parameters that define the physics of metal cutting, such as the geometry of the process, stresses, strains, strain rates, and temperatures can be estimated. With these parameters, a relationship between plastic deformation and AE is analysed and discussed.

- A signal processing technique, named AE mode, which removes the influence of erroneous and undesirable outlying values from the AE data [7], is utilized to compute the energetic component of the AE signals.

- In order to compute a measure of the frequency content of AE, a technique, called mean frequency, which divides the AE spectrum into two parts of equal energy, presented by Rangwala and Dornfeld [19], is used.

- In addition to AE, force and temperature signals are measured during the experimental procedure. Since Oxley's model also predicts cutting forces and temperatures, these two quantities are used to evaluate the accuracy of the model. However, since the temperatures are measured remotely from the cutting zone, the finite-difference technique [20] is employed, so that the cutting temperatures can be estimated from the remote measurements.

- As dislocation motion is considered to be the main mechanism responsible for plastic deformation in metals [21, 22], it is suggested, as a result, that some mechanism involved in the motion of dislocations should generate the detected AE waves. Since most theories that relate AE to plastic deformation apply only for processes that occur at much lower strain rates than those encountered in metal cutting [23,24], a theory presented by Kumar *et al.* [25,26], which takes into account plastic deformation at high strain rates and temperatures, is utilized, resulting in the development of a novel qualitative model, which is observed to be in agreement with both experimental results and Oxley's model predictions.

The development of the proposed work is going to be described throughout the following chapters of this thesis, and this will be done according to the following structure:

Literature review (Chapter 2) The relevant knowledge necessary for the understanding of the two main fields investigated throughout this thesis, i.e. metal cutting and AE, is introduced. In the first part, metal cutting definitions and basic process mechanics are explained, followed by the most significant metal cutting models; two types of models are analysed: models with constant material properties and with variable material properties. Other areas, such as cutting temperatures and tool wear, are also briefly reviewed. The second part deals with the process of AE generation. To begin with, the concept of AE is defined; then, the processes by which AE is generated are examined, focusing specially on the process of dislocation movement accompanying plastic deformation; other stages of the AE process, such as propagation, detection, signal conditioning, and signal processing are also examined. Afterwards, metal cutting is evaluated as a source of AE, and different models of AE generation during the course of metal cutting are reviewed.

Experimental methodology (Chapter 3) In order to study the causes of the detected AE during metal cutting, a series of cutting experiments was carried out. The methodology adopted in the experiments, including the turning machine, the tooling system, the work materials (two carbon steels, a stainless steel, and an aluminium alloy), the sensors, and the testing conditions, is described here. The following signals were acquired: AE, cutting forces, vibration, and temperature. Two different types of cutting tests were accomplished: the first type utilized a wide range of cutting conditions, and the second type utilized preheated workpieces before cutting.

Experimental results (Chapter 4) Experimental results are shown for the two experiments described previously. Quite simple data processing was done with the acquired raw data, for, at this stage, the objective was to provide a general overview on the variation of the AE level with the basic cutting parameters V, t_1, and w. Cutting forces and temperature data are also presented.

Analysis and discussion (Chapter 5) To begin with, a preliminary discussion on the experimental results previously presented is undertaken; published results are also reviewed in order to be compared with the present ones. An empirical model relating the AE level to V and t_1 is presented next, so that the variation of AE with V and t_1 can be easily visualized. A type of model, which has been widely used by many authors, that relates the power of AE with the power of cutting is discussed subsequently; it is concluded that these models are partly incorrect. Afterwards, a semi-empirical theory (Oxley's model) that simulates the cutting process is analysed; simulated force and temperature results are compared with the current experimental results, and reasonable agreement is found between experimental and simulated results. However, since the temperature sensors were placed some distance away from the cutting zone, the finite difference technique was utilized in order to compute the temperature at the cutting zone by employing the sensors data. In order to explain why the rate of increase of the AE level decreases with w, a very simple model that simulates AE generation and propagation is developed; it is concluded that increasing w changes the phase delay of the AE waves arriving at a sensor placed on a remote location (AE events further apart result in higher phase difference of remote AE waves), whose effect is believed to be responsible for the lowering of the detected AE. Moreover, an analysis of the basic parameters involved in plastic deformation shows that the power of AE increases with primary strain and secondary strain rate, but it decreases with cutting temperature; besides, the frequency content of AE increases with strain rate and decreases with temperature. Finally, since dislocation motion is the basic process governing plastic deformation in metals, a qualitative model that predicts that AE is generated when dislocations surmount obstacles at the typical high strain rates and temperatures encountered in metal cutting is proposed; fairly good agreement is obtained by comparing model predictions with the current experimental results.

Conclusions and recommendations (Chapter 6) Finally, the conclusions encountered during the previous analysis are summarized in this chapter. Additionally, recommendations of further work that should be undertaken are also provided.

Chapter 2

Literature Review

This chapter is divided into two major parts. The first part provides an overview of metal cutting physics, a description of the main zones of deformation, and a review of the major cutting models. The second part is dedicated to the acoustic emission (AE) signal and, in particular, to its generation during metal cutting.

2.1 Metal Cutting Physics

There are three zones of interest in the cutting process (Figure 2.1). The first area, called the primary zone, is the boundary between the deformed and undeformed material. Once the material has been deformed through the primary zone to form the chip, a secondary zone of deformation is observed at the interface between the tool rake face and the chip as it flows over the tool. The tertiary zone corresponds to the contact between the tool clearance face and the newly machined surface of the workpiece.

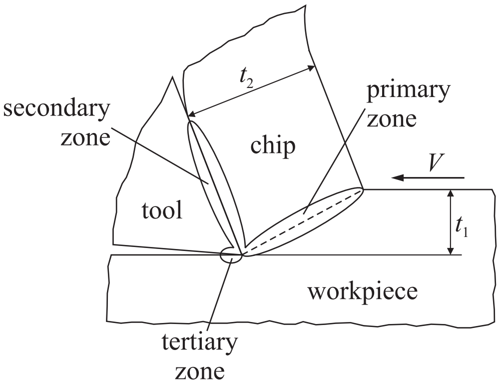

Figure 2.1: Zones of interest in cutting.

In Figure 2.1, the chip is represented as a continuous band of uniform thickness t_2 and width w. However, this is a simplification, for there are three major types of chip formation [1, 27]:

Continuous Chips are smooth continuous ribbons with reasonably constant thickness produced during machining at high speeds of ductile materials (Figure 2.2a).

Continuous with built-up edge At speeds where the temperature at the tool-chip interface is relatively low, a stagnant mass of chip material may adhere to the tool rake face. This detached material acts as the cutting edge, increasing the effective rake angle, and is called built-up edge (BUE) (Figure 2.2b).

Discontinuous This type of chip is formed during the machining of relatively brittle materials at low cutting speeds where individual segments are formed by alternate deformation and fracture of the metal (Figure 2.2c).

Segmented As shown in Figure Figure 2.2d, this type of chip is only partially fractured, and the back of the chip is very wavy. Two formation mechanisms have been proposed for the generation of segmented chips [1]: adiabatic shear, and fracture and rewelding.

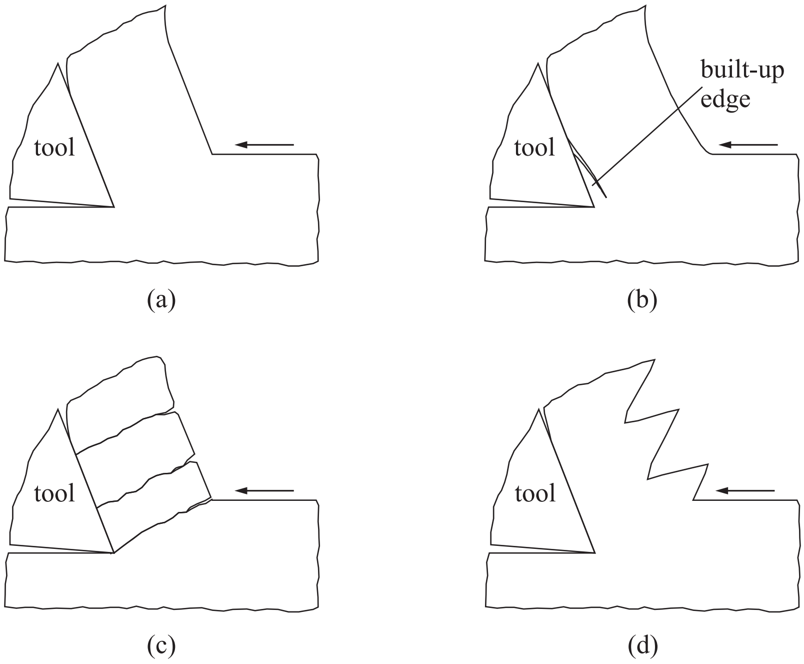

Figure 2.2: Types of chip formation. (a) Continuous. (b) Continuous with BUE. (c) Discontinuous. (d) Segmented.

For the purpose of studying chip formation, it is useful to start with the simplest possible conditions, and, hence, some restrictions have to be made. Throughout the next sections, the following conditions apply unless specifically stated:

- Cutting is orthogonal and can, therefore, be represented in two dimensions.

- The chip does not spread to either side (plane strain). This condition is practically encountered if the width w is large compared with the uncut chip thickness t_1.[1]
- The tool is perfectly sharp. With this condition, the tertiary zone is neglected, since there is no contact along the clearance face.
- The generation of chips is assumed continuous and without BUE.
- Relative vibration between the tool and workpiece, referred as chatter, are disregarded.
- There is no externally applied coolant or lubricant.

2.1.1 Zones of Deformation

Primary Zone

Experimental observation of photomicrographs[2] of partially formed chip sections have shown that chip formation occurs in a narrow zone of intense shear that extends from the tool edge to the work surface [1,27,28]. This zone can be approximated to a plane [29], called the shear plane and represented by plane AB in Figure 2.3a, across which the work velocity V is instantaneously changed to the chip velocity V_C. This requires a discontinuity in the tangential component of velocity across AB equal to V_S (shear velocity), as shown by the velocity diagram in Figure 2.3b. This velocity discontinuity only applies to ideal rigid-plastic materials of constant flow stress.

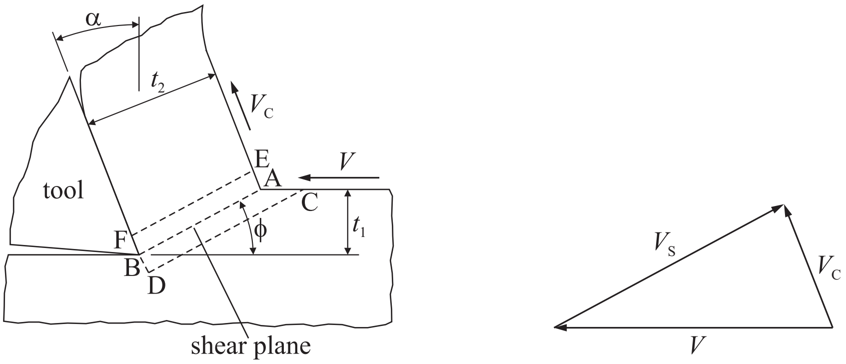

(a) (b)

Figure 2.3: Primary zone of deformation. (a) Shear plane and parallel-sided shear zone models. (b) Velocity diagram.

A very important angle is the one formed between the shear plane and the direction of V, called the shear angle (ϕ). Although the shear angle can be measured directly from pho-

---

[1] For example, Shaw [1] states that $w/t_1 \geq 5$, whereas Oxley [18] states that $w/t_1 \geq 10$, so that plane strain conditions can be assumed.

[2] Photomicrographs are photographs that are taken through a microscope of pre-prepared surface sections of partially formed chips from a cutting process that has been abruptly stopped.

tomicographs, ϕ is normally determined with the following relationship:

$$\tan\phi = \frac{r\cos\alpha}{1 - r\sin\alpha} \tag{2.1}$$

where r is the ratio of uncut to cut chip thickness t_1/t_2. Although the chip thickness t_2 can be obtained by direct measurement, this is not very precise due to the roughness on the back surface of the chip. In practical tests, the mean chip thickness can be obtained by taking the weight (W_C) of a piece of chip of length l_C. The mean chip thickness is then

$$t_2 = \frac{W_C}{\rho w l_C} \tag{2.2}$$

where ρ is the density of the work material. Moreover, the shear strain occurring in crossing the tangential velocity discontinuity V_S is given by

$$\gamma_{AB} = \frac{V_S}{V_N} = \frac{\cos\alpha}{\sin\phi\cos(\phi - \alpha)} \tag{2.3}$$

where V_N is the velocity normal to AB.

The instantaneous change in velocity across AB, assumed in the shear plane model, leads to an infinite value of the shear strain rate ($\dot{\gamma}_{AB}$). Consequently, a parallel-sided shear zone model has emerged [28, 30, 31], which is still in accordance with the observation that chips are formed in a narrow zone. The parallel-sided shear zone is represented by zone CDEF in Figure 2.3a. The change in speed from V to V_C occurs now along smooth stream lines from CD to EF. Stevenson and Oxley [32] concluded that the tangential velocity discontinuity V_S was still a good representation of the overall change in velocity in the primary zone. The mean value of the shear strain rate can then be obtained from

$$\dot{\gamma}_{AB} = \frac{V_S}{\Delta s_1} \tag{2.4}$$

where Δs_1 is the thickness of the parallel-sided shear zone. By analysing experimental results of the shear zone size from Kececiouglu [28], Stevenson and Oxley [32] realized that Δs_1 should be dependent only on scale and not on velocity. Moreover, using printed grids to measure the plastic flow in chip formation, Stevenson and Oxley showed that the strain rate distribution was approximately symmetrical about AB with the maximum value occurring at AB. Consequently, the following empirical equation was derived:

$$\dot{\gamma}_{AB} = C\frac{V_S}{t_1} \tag{2.5}$$

The material based constant C was found to be 2.59 for a 0.13% carbon steel. However, as pointed out by Oxley [18], Equation 2.5 should be changed to a more accurate equation:

$$\dot{\gamma}_{\mathrm{AB}} = C\frac{V_{\mathrm{S}}}{l_{\mathrm{AB}}} \tag{2.6}$$

where l_{AB} is the length of AB. Hastings *et al.* [33] found C to be approximately 5.9 for a 0.16% carbon steel. Furthermore, the total shear strain occurring in the shear zone (along EF) is given by

$$\gamma_{\mathrm{EF}} = \frac{\cos\alpha}{\sin\phi\cos(\phi-\alpha)} \tag{2.7}$$

Secondary Zone

The importance of the secondary zone of deformation must be realized by the fact that the primary chip formation process depends upon the secondary process as much as the secondary deformation process depends upon the primary process [34]. Due to the existence of this correlation, the primary and secondary processes can not be examined isolated from each other.

The earliest cutting process analysis treated the tool-chip interface as a classical sliding friction situation [29]. In this analysis, the force required to slide the chip along the tool rake face (F_{int}) is proportional to the force normal to the interface (N_{int}):

$$F_{\mathrm{int}} = \mu N_{\mathrm{int}} \tag{2.8}$$

where μ is the coefficient of friction, which is only dependent on forces F_{int} and N_{int} and is independent on the size of the apparent tool-chip contact area.

However, experimental observations of chip photomicrographs and worn tools have led to the conclusion that, over most of the area of the tool-chip interface, sliding is impossible under most cutting conditions [35]. Zorev [34] also showed that friction on the tool face is so great that, at least over a part of the contact area closest to the cutting edge, the contact layer of the chip is retarded or seized by the tool, and the process of friction between the two surfaces is replaced by plastic shear of the chip. Therefore, the tool-chip interface was divided into two distinct regions (Figure 2.4). The first region (nearest to the cutting edge), called the seizure or sticking zone, mainly involves shearing of the chip; the second region (nearest to the point at which the chip leaves the tool), called the friction zone, is governed by the classical laws of sliding friction. Shaw [1] pointed out that there should be a zone of transition between the sticking and the friction zones. Stevenson and Oxley [32] assumed that the tool-chip interface can be represented by a rectangular plastic zone with no sliding. Assuming that the velocity at the tool chip increases from zero at the tool face to the rigid chip velocity V_{C} in a distance Δs_2, the shear strain rate at the interface can be calculated as follows:

$$\dot{\gamma}_{\mathrm{int}} = \frac{V_{\mathrm{C}}}{\Delta s_2} \tag{2.9}$$

Stevenson and Oxley [32] found Δs_2 to be approximately $\frac{1}{8}$ of t_2.

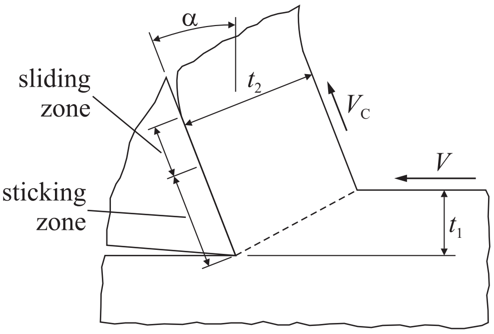

Figure 2.4: Secondary zone of deformation.

Tertiary Zone

It was stated previously that the effects of the tertiary zone are normally neglected if a sharp tool is used. However, in practice, and especially when the clearance face shows some degradation, there is always some contact of the work material with this face [35]. This contact can be reduced by increasing the clearance angle, but this results in weakening of the tool edge. Evidence from photomicrographs [35] and experiments with a controlled clearance face contact area [36] demonstrate that seizure also occurs on the clearance surface, particularly in the region closest to the cutting edge.

2.1.2 Mechanics of Cutting

Forces

Knowledge of the forces acting on the tool is an important aspect for the design and optimization of machines and cutting tools, and also for the scientific investigation of the cutting process.

The classic way of analysing the cutting forces in orthogonal cutting [29] is by isolating the chip as a free body and placing it in static equilibrium. This is achieved if the resultant force R_1 on the chip along the shear plane is equal, opposite, and co-linear to the resultant force R_2 on the chip along the tool-chip interface (Figure 2.5). The forces R_1 and R_2 can be resolved into three sets of components:

- Along the cutting speed and feed rate directions, tangential force (F_X) and feed force (F_Y), respectively.
- Along and normal to the shear plane AB, F_{AB} and N_{AB}, respectively.
- Along and normal to the tool-chip interface, F_{int} and N_{int}, respectively.

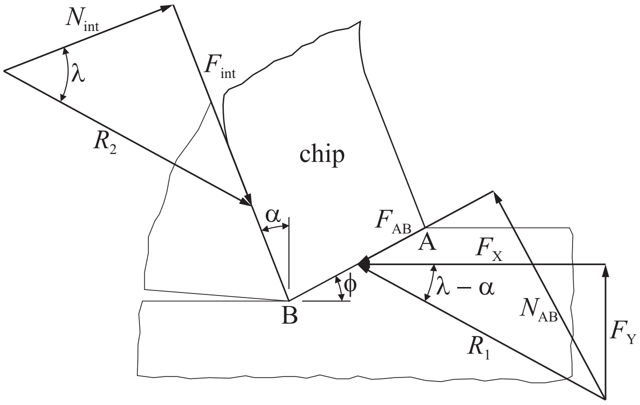

Figure 2.5: Cutting forces.

Normally, it is important to obtain the shear (F_{AB} and N_{AB}) and frictional (F_{int} and N_{int}) components of the forces in terms of F_X and F_Y. The following relationships apply:

$$F_{AB} = F_X \cos\phi - F_Y \sin\phi \tag{2.10}$$

$$N_{AB} = F_X \sin\phi + F_Y \cos\phi \tag{2.11}$$

$$F_{int} = F_X \sin\alpha + F_Y \cos\alpha \tag{2.12}$$

$$N_{int} = F_X \cos\alpha - F_Y \sin\alpha \tag{2.13}$$

The mean angle of friction (λ) is an important angle that describes the frictional conditions at the tool-chip interface, which can be determined by the following ratio:

$$\tan\lambda = \frac{F_{int}}{N_{int}} \tag{2.14}$$

For a semi-orthogonal turning operation, the resultant cutting force acting on the tool can be measured in three directions (Figure 2.6): the first component, the tangential force (F_X), acting along the vertical direction of the cutting speed, is normally the largest of the three force components; the second component, the force component acting on the horizontal direction of the feed rate, is referred to as the feed force (F_Y); the third component, the radial force (F_Z), acting in a direction normal to F_X and F_Y simultaneously, tends to push the tool away from the workpiece; this is the smallest of the three force components in semi-orthogonal cutting, being usually ignored, thus, reducing the force analysis to two dimensions, as presented in Figure 2.5.

Measurement of the cutting forces can be achieved with dynamometers. Some deformation is associated with the operation of every dynamometer, and the deflection produced is then measured and converted into force units, e.g. piezoelectric transducers and strain gauges. Shaw [1] gives a general overview of metal cutting dynamometry.

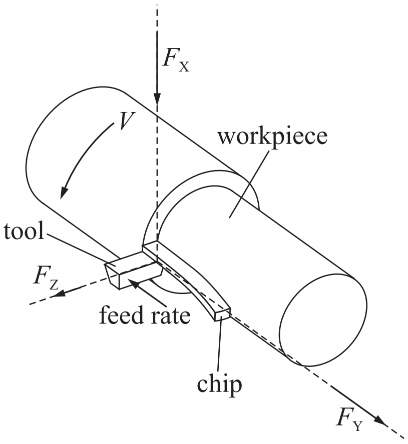

(a)

Figure 2.6: Cutting force components in semi-orthogonal turning.

Stresses

High shear and normal stresses occur both on the primary zone of deformation and on the rake face of the cutting tool. Moreover, the stresses acting on the chip from both primary and secondary deformation zones are related to each other by the conditions of static equilibrium of the chip.

In the primary zone, one can model the shear and normal stresses acting on the shear plane AB as mean quantities. Therefore, uniform shear shear stress (τ_{AB}) and uniform normal stress (σ_{AB}) distributions are assumed to act over the entire area of primary zone (A_{AB}):

$$\tau_{AB} = \frac{F_{AB}}{A_{AB}} \tag{2.15}$$

$$\sigma_{AB} = \frac{N_{AB}}{A_{AB}} \tag{2.16}$$

where

$$A_{AB} = \frac{t_1 w}{\sin\phi} \tag{2.17}$$

Fenton and Oxley [37] stated that the shear stresses along AB could be assumed as constant, but that the normal stresses along AB could only be assumed constant for a material of uniform flow stress. For non-uniform flow stress conditions, Fenton and Oxley modelled the normal stress distribution to change linearly along AB, so that $N_{AB} = (\sigma_A + \sigma_B)/2$, where σ_A and σ_B are the normal stresses at points A and B.

The nature of the tool-chip interface and the distribution of the shear (τ_{int}) and normal (σ_{int}) stresses are critical in understanding the cutting process. Very high stresses act on the secondary zone, combined with high temperatures and large strains in the chip adjacent to the tool face. The classical analysis of stresses on the tool face assumes that sliding friction is present and that the stresses are uniformly distributed. Hence, the mean values of τ_{int} and σ_{int} can be estimated as follows:

$$\tau_{\text{int}} = \frac{F_{\text{int}}}{A_{\text{int}}} \tag{2.18}$$

$$\sigma_{\text{int}} = \frac{N_{\text{int}}}{A_{\text{int}}} \tag{2.19}$$

where A_{int}, the tool-chip interface area, is given by

$$A_{\text{int}} = wl_{\text{int}} \tag{2.20}$$

where l_{int} is the length of the tool-chip contact zone.

However, experimental results suggest that the stresses are not uniformly distributed along the rake face [34,35,38,39]. Zorev [34] presented a stress distribution model in which the normal stress is assumed to take a maximum value (σ_{max}) at the tip of the tool and then to decrease, as a power function, down to the point at which the chip leaves the tool, where σ_{int} is zero (Figure 2.7). The normal stress is, thus, defined by

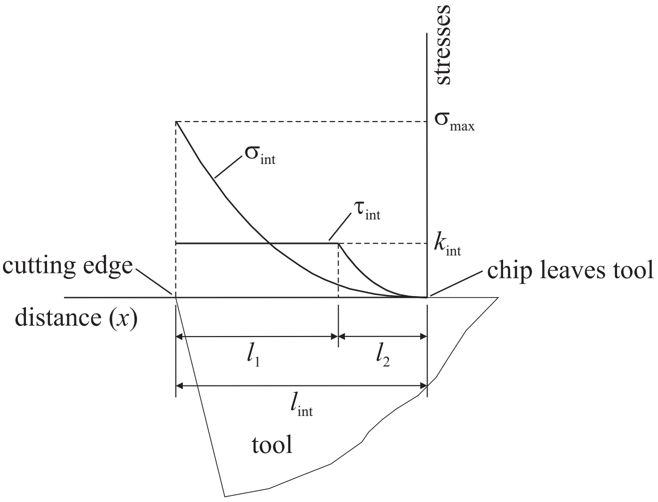

Figure 2.7: Distribution of stresses on the tool rake face [34].

$$\sigma_{\text{int}} = \sigma_{\text{max}} \left(\frac{x}{l_{\text{int}}} \right)^n \tag{2.21}$$

where x is the distance to the left from which the chip leaves the tool, and n is the exponent. In the sliding zone (length l_2), the shear and normal stresses are related:

$$\tau_{\text{int}} = \mu\sigma_{\text{int}} = \mu\sigma_{\text{max}} \left(\frac{x}{l_{\text{int}}} \right)^n \tag{2.22}$$

where μ is the coefficient of friction, as defined in Equation 2.8. However, as τ_{int} reaches the value of the shear flow stress (k_{int})[3] of the interface chip material, instead of sliding against the rake surface, it takes less energy for the material adjacent to the interface to shear internally. This can be described as sticking friction. Therefore, in the sticking zone (length l_1), τ_{int} assumes a constant value k_{int}, as it can be observed in Figure 2.7. The frictional force components N_{int} and F_{int} can be obtained by integrating the stresses of the area of contact, resulting in

$$N_{\text{int}} = \frac{\sigma_{\text{max}} w l_{\text{int}}}{1+n} \tag{2.23}$$

$$F_{\text{int}} = k_{\text{int}} w \left(l_1 + \frac{l_2}{1+n} \right) \tag{2.24}$$

Other stress distributions have been proposed. For example, Xiaoping [38], and Buryta and Sowerby [39] presented stress distributions where σ_{int} increases with increasing x, but at locations near the cutting edge, σ_{int} stops rising and assumes a constant value. Fenton and Oxley [37] assumed that the normal stress distribution is triangular with the maximum value at the cutting edge. Moreover, Fenton and Oxley neglected the sliding zone at the tool-chip interface and assumed that the material at the interface is in a state of plastic shear with an uniform shear stress distribution k_{int}.

Energy Considerations

In machining operations, the total energy per unit time (power) can be calculated as follows:

$$\dot{U} = F_X V \tag{2.25}$$

However, this energy can be normalized by dividing it by the volume of material being removed (v). This is called specific power (u), and since $v = t_1 w V$, u can be calculated as follows:

$$u = \frac{F_X}{t_1 w} \tag{2.26}$$

The specific power can be partitioned into four components [1]:

- Primary shear specific power (u_S).
- Secondary frictional specific power (u_C) on the tool-chip interface.
- Surface specific power (u_A) due to the formation of new surface areas in cutting.
- Momentum or kinetic specific power (u_M) due to the change in momentum of the chip.

Normally, u_A and u_M are negligible relative to the other two components so that

$$u = u_S + u_C \tag{2.27}$$

---

[3] The shear flow stress (k) is the state of pure shear that will induce yielding or the onset of plastic deformation [40].

However, u_{M} takes on increasing importance with very high speed machining. Furthermore, the primary and secondary components of the total specific power can be calculated as follows:

$$u_{\mathrm{S}} = \frac{F_{\mathrm{AB}}V_{\mathrm{S}}}{t_1 w V} \tag{2.28}$$

$$u_{\mathrm{C}} = \frac{F_{\mathrm{int}}V_{\mathrm{C}}}{t_1 w V} \tag{2.29}$$

The specific power tends to remain approximately constant for a given work material operating under different cutting conditions. However, u has been observed to decrease with t_1 (size effect), according to the following approximate relationship [1]:

$$u \propto \frac{1}{t_1^{0.2}} \tag{2.30}$$

2.1.3 Heat Generation and Cutting Temperatures

Practically all the work performed in machining is converted into heat [35], resulting in a temperature rise of the chip, tool, and work material. Three zones of heat generation can be distinguished: the primary deformation zone, the secondary tool-chip interface, and the tertiary zone; the latter source is normally neglected if a sharp tool is used. The importance of knowing the temperature distribution in metal cutting is very important, since temperature affects the mechanical properties of the work material, chip, and, therefore, the mechanics of cutting. Moreover, the rate of tool wear is also affected by the temperature at the tool.

There are different methods for the measurement of cutting temperatures [35,41,42]; the main methods are:

Tool-work thermocouple method This method employs the thermocouple[4] effect formed by the contact of the two dissimilar metals at the tool-chip interface. Although this method is easy to implement, there is no certainty as to which interfacial temperature is actually being measured. However, it is normally assumed that the method measures the average temperature at the tool-chip interface. Stephenson [43] presented the theory and some implementation issues for the tool-work thermocouple method.

Inserted thermocouples Small diameter thermocouples are inserted in different places in the interior of the tool, so that the temperature field within the tool can be obtained and the temperatures at the surfaces can be found by extrapolation. This technique is, however, tiresome because different tools are normally prepared for each individual thermocouple location. Chow and Wright [44] developed a technique in which the interfacial maximum, minimum, and tool edge temperatures are predicted from the signal of a thermocouple located at the bottom of a turning tool insert.

---

[4] A thermocouple is formed when two dissimilar metals touch each other. When the temperature of this junction is different to the temperature of other parts of the metals, a voltage that is dependent on this temperature difference is generated.

Radiation methods These methods are based on the measurement of the infrared radiation of the temperature from accessible surfaces of the tool, work, and chip. Chao *et al.* [45] used a special technique to measure the temperature distribution at the tool clearance face. Jaspers *et al.* [46] developed a method to compute the tool-chip interface temperature from the temperature distribution at the top free side of the chip, obtained with an infra-red camera. Radiation methods are complex and are best suited for laboratory studies.

Tool hardness The temperature distribution in the tool may be obtained by observing the changes in hardness of steel tools after machining. This method may provide more information about the temperatures near the cutting edge, but it is arduous, difficult, and only applies to steel tools.

There have been several attempts to predict cutting temperatures analytically. Silva and Wallbank [42] presented a review of the analytical methods used to estimate cutting temperatures. Stephenson [47] compared calculations from four cutting temperature models with experimental data from infrared and tool-work thermocouple measurements. Shear plane temperatures were obtained from the infrared data and tool-chip interface temperatures from the tool-work thermocouple data. It was concluded that although most cutting temperature models are qualitatively accurate, they tend to overestimate cutting temperatures. Moreover, no model was accurate when predicting tool-chip temperatures during a discontinuous chip formation process.

2.1.4 Metal Cutting Modelling

Most metal cutting models deal with the prediction of the shear angle ϕ because, for a given rake angle α, undeformed chip thickness t_1, and width of cut w, the geometry of the cutting process (Figure 2.3a) is not completely defined unless ϕ is known. Therefore, no estimation of cutting forces, stresses, and temperatures can be made without first evaluating ϕ. Two types of models are described next: the first type considers that deformation is performed at constant flow stress, i.e. the effects of strain, strain rate, and temperature on material properties are neglected; in contrast, the second type of model described makes use of experimental flow stress data to develop an approximate machining theory in which account is taken of the effect of strain, strain rate, and temperature.

Constant Material Properties

One of the first attempts to quantitatively model metal cutting was achieved by Ernst and Merchant [29] who considered primary deformation to take place on a single plane (AB in Figure 2.3a). Furthermore, the chip was assumed to slide over the rake face, following the classical laws of friction, being the coefficient of friction ($\mu = \tan\lambda$) expressed as in Equation 2.8. The shear stress on plane AB (τ_{AB}) was assumed to be uniform, as defined in Equation 2.15, which can also be expressed as follows:

$$\tau_{AB} = \frac{R\cos(\phi - \lambda - \alpha)\sin\alpha}{t_1 w} \tag{2.31}$$

where R is the resultant cutting force (R_1 or R_2 in Figure 2.5). Ernst and Merchant reasoned that ϕ should be such that τ_{AB} would be a maximum, and a relationship for ϕ was obtained by differentiating Equation 2.31 with respect to ϕ and equating the resulting expression to zero. Differentiation was performed by considering both R and λ independent of ϕ. As a result, the following relation for ϕ was derived:

$$\phi = \frac{\pi}{4} - \frac{1}{2}(\lambda - \alpha) \tag{2.32}$$

where ϕ is expressed in radians.

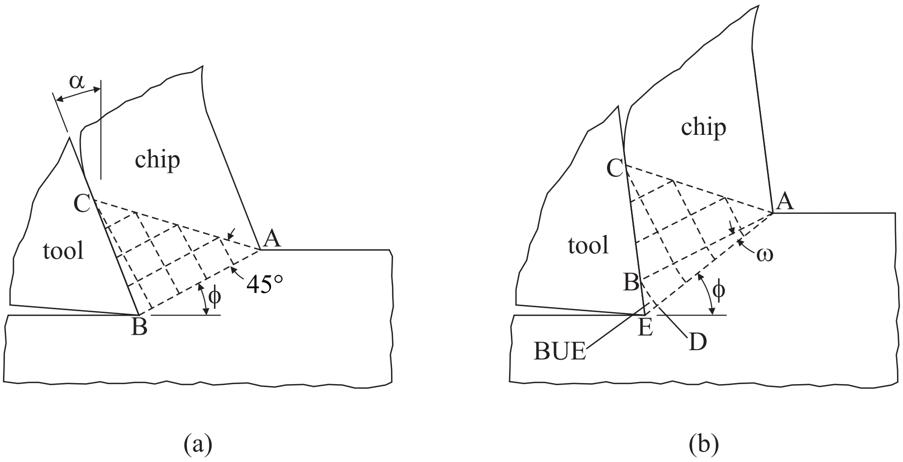

Figure 2.8: Slip line field solution for machining [48]. (a) Without BUE. (b) With BUE.

Lee and Shaffer [48] proposed a constant stress slip line [5] field, represented as triangle ABC in Figure 2.8a, for continuous chip formation processes without BUE. As in the previous model [29], the shear plane AB was assumed to be a direction of maximum shear stress. It should also be noted that in the previous model, AB also represents a slip line, since it is a direction of maximum shear stress. It was further assumed that BC represents the full tool-chip contact length, so that AC is a free surface (angle between AB and CA is 45°). From analysis of the Mohr's circle diagram of

---

[5] In plane strain deformation, slip lines consist of two families of orthogonal curves (I and II), whose directions coincide with the direction of maximum shear stress (k) acting on the plane of flow. Therefore, the two principal stresses (σ_1 and σ_3) acting on this plane make 45° with both slip lines. The normal to the plane of flow is a principal direction with principal stress $\sigma_2 = \frac{1}{2}(\sigma_1 + \sigma_3)$. Furthermore, $k = \frac{1}{2}|\sigma_1 - \sigma_3|$ and $p = -\sigma_2$, where p is the compressive stress that acts normal to the slip line. In classical slip line field theory, materials have constant shear flow stress k, and the following stress equilibrium equations apply: $p + 2k\psi =$ constant along a I line, and $p - 2k\psi =$ constant along a II line, where ψ is the angular rotation of the I lines from a fixed reference axis. Slip lines meet free surfaces and frictionless interfaces at 45°. In sticking friction interfaces, one type of slip line meets the interface tangentially and the other type at 90°. Reference [40] may be consulted for further information.

the field ABC represented in Figure 2.8a, the following shear angle expression was derived:

$$\phi = \frac{\pi}{4} - (\lambda - \alpha) \tag{2.33}$$

where ϕ is expressed in radians.

Lee and Shaffer [48] presented a second slip line field solution for machining operations with continuous chip formation and BUE. Figure 2.8b shows that the slip line field consists of a uniform stress region ABC and a region of varying stress ABD representing the BUE. The size of the BUE is defined by the angle ω. Analysis of the Mohr's circle diagrams of both fields ABC and ABD resulted in the following equation:

$$\phi = \frac{\pi}{4} + \omega - (\lambda - \alpha) \tag{2.34}$$

Angle ϕ is expressed in radians. Equation 2.34 differs from Equation 2.33 only by ω (size of BUE). When there is no BUE, ω is zero, and, consequently, Equation 2.34 results in Equation 2.33.

Kobayashi and Thomsen [49] presented experimental results for a range of work materials by plotting the shear angle ϕ against $\lambda - \alpha$. It was observed that, generally, for a given material, an increase in $\lambda - \alpha$ results in a decrease of ϕ. However, for a given value of $\lambda - \alpha$, different values of ϕ were observed for different materials. Moreover, Equations 2.32, 2.33 and 2.34 represent straight lines of type

$$\phi = B - m(\lambda - \alpha) \tag{2.35}$$

Therefore, since m and B are known constants in Equations 2.32, 2.33, and 2.34, an unique solution for ϕ is obtained for a given value of $\lambda - \alpha$ (Equation 2.34 may actually give different ϕ values if ω is allowed to vary), which is clearly unsuitable to represent the actual variation of ϕ with $\lambda - \alpha$. Better agreement with experimental results is achieved if Equation 2.35 is utilized, but the values of B and m have to be provided. The problem lies in the simplifications assumed for each analytical model, which may be a considerable cause of errors, such as: in the first model [29], tool-chip sliding friction is assumed, and differentiation is performed independently of R and λ; and the work material is assumed perfectly plastic in the slip line field models [48]. Shaw [1] reviewed the better known shear angle analysis and concluded that it is unlikely that a relatively simple model will possibly be established. Oxley [50] also stated that, at this stage, a purely analytical solution to the machining problem seems unachievable. Nevertheless, although oversimplified, analytical models have undoubtedly added to the understanding of the cutting process.

Variable Material Properties

The machining theory briefly presented next was derived by Oxley and his co-workers; it is described in detail in [18] and is briefly reviewed in Appendix A. Chip formation is assumed to be formed in the narrow plastic zone represented by the parallel sided shear zone CDEF in Figure 2.3a. In the centre of this zone, the shear plane AB is assumed to be a direction of maximum shear stress and maximum shear strain rate. The tool-chip interface is represented by a rectangular plastic zone with uniform shear stress distribution and triangular normal stress distribution [37]. In order to predict the shear angle ϕ, cutting forces, and temperatures for a given set of cutting conditions (V, t_1, and w) and tool rake angle α, an iterative process was developed. Basically, this process starts by selecting a range of ϕ values upon which, for each value of ϕ, the shear stress at the tool-chip interface (τ_{int}) is calculated from the stresses at the shear plane AB, and for the same range of ϕ values, the interfacial temperatures and strain rates are calculated and, subsequently, the shear flow stress of the chip at the interface (k_{int}). The solution is taken for the value of ϕ at which $\tau_{\text{int}} = k_{\text{int}}$.

The work material flow stress properties were obtained from high speed compression tests for a range of plain carbon steels and are represented by the two material constants σ_1 and n, which define the empirical stress-strain equation $\sigma = \sigma_1 \varepsilon^n$ for a given temperature and strain rate, where σ and ε are the uniaxial[6] flow stress and strain, respectively. Therefore, this model has only been applied to plain carbon steels, and in order to obtain σ_1 and n, the material temperature (T), the uniaxial strain rate ($\dot{\varepsilon}$), and the percentage of carbon in the steel are required quantities.

The method to determine τ_{int} for a given value ϕ starts by calculating the shear strain (γ_{AB}) and shear strain rate ($\dot{\gamma}_{\text{AB}}$) at AB (Figure 2.3a). Equation 2.6 is used to obtain $\dot{\gamma}_{\text{AB}}$. Since the temperature at AB (T_{AB}) is still unknown, at a first approach, T_{AB} is assumed to be equal to the initial workpiece temperature (T_{W}), and this value is used to determine the specific heat and thermal conductivity of the material. With the values of T_{AB} and $\dot{\gamma}_{\text{AB}}$, the work material flow stress properties σ_1 and n can be determined, and, thus, the shear flow stress at AB (k_{AB}). Subsequently, the shear force F_{AB} is computed by substituting τ_{AB} by k_{AB} in Equation 2.15. At this point, it is possible to recalculate T_{AB} by considering that all the work produced in the primary zone is converted into heat and that a known proportion of this heat is conducted into the work material. The calculations are then repeated with the new value of T_{AB}, and this procedure is repeated until T_{AB} converges to a specific value. Finally, the cutting forces at this converged temperature value are taken as the appropriate values for the assumed ϕ, and the shear stress τ_{int} is calculated from Equation 2.18.

In order to compute k_{int} for a given angle ϕ, an iterative procedure is again necessary to calculate the mean chip temperature (T_{C}). Initially, T_{C} is taken as the temperature in the primary shear zone, and this is then used to calculate the specific heat of the material. The temperature T_{C}

---

[6] The uniaxial stress (σ) is the stress necessary to initiate yielding in uniaxial tension or compression tests and is related to the shear flow stress k by the equation $\sigma = \sqrt{3}k$. Furthermore, $\varepsilon = \gamma/\sqrt{3}$ and $\dot{\varepsilon} = \dot{\gamma}/\sqrt{3}$, where ε and $\dot{\varepsilon}$ are the uniaxial strain and strain rates, and γ and $\dot{\gamma}$ are the maximum shear strain and shear strain rate in plane strain.

is then recalculated assuming that all the work done by the chip at the interface is converted into heat. This procedure is repeated until T_C converges to a specific value. Afterwards, an empirical relation is used to find the average temperature at the interface (T_{int}). The average shear strain rate ($\dot{\gamma}_{int}$) in the plastic zone adjacent to the interface is determined from an empirical equation. Finally, in order to calculate k_{int}, a stress-strain relation that neglects the influence of strain on flow stress is used, and, therefore, only the flow stress property σ_1 needs to be determined.

If τ_{int} and k_{int} are plotted against ϕ, the solution for ϕ is taken at the intercept of τ_{int} with k_{int}. However, when there is more than one intercept, Hastings *et al.* [33] reasoned that the solution should be taken for the intercept corresponding to the highest value of ϕ.

Hastings *et al.* [51] applied this theory for two plain carbon steels and for a range of cutting conditions. Excellent agreement was obtained between predicted and experimental cutting forces for machining without BUE (F_X and F_Y decreasing with increasing V and α). The specific power u was observed to decrease with t_1 (size effect). Furthermore, ϕ was predicted and experimentally found to increase with V. Hastings *et al.* proposed that the decrease in the cutting forces and the increase in ϕ with V are due to the decrease in k_{int} caused by the increase of the interfacial temperatures. The cutting forces were hardly affected by the difference in carbon content of the two work materials; however, the carbon content was observed to increase ϕ. The secondary shear zone thickness Δs_2 was predicted to decrease with increasing V, α, and carbon content, and with decreasing t_1; these trends were confirmed by photomicrographs of chip sections.

2.1.5 Tool Wear

Although the present work does not consider the wear of the cutting tool, a brief overview of the types of tool wear encountered is given here.

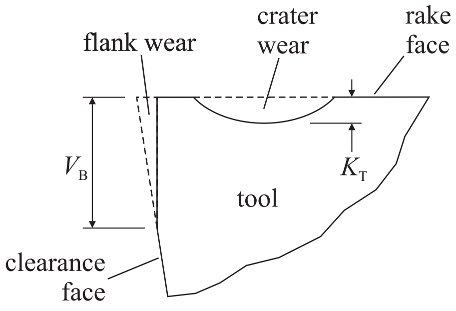

Figure 2.9: Flank and crater tool wear.

During metal cutting, the tool is subjected to high stresses and temperatures, the action of cutting gradually changes the shape of the tool edge, resulting in ineffective cutting or total tool failure. The main causes of tool deterioration are described next [1,35,52]:

Flank or clearance face wear As shown in Figure 2.9, this type of wear results in a loss of relief angle on the clearance face and is formed due to the frictional contact between the clearance face and the newly machined surface of the workpiece.

Crater wear At high cutting speeds, due to the high temperatures and stresses present at the rake face, a characteristic crater develops at a short distance from the cutting edge (Figure 2.9), caused by the sticking contact of the chip with the rake face.

Plastic deformation When the cutting edge reaches a sufficiently high temperature, plastic deformation starts due to the weakening of the mechanical strength of the tool material.

Fracture and chipping Tool fracture and chipping result due to excessive loading or thermal-mechanical shock at the cutting edge. Chipping causes a small damage of the tool edge, whereas fracture results in a significant loss of the cutting zone. Tool failure due to fracture must be avoidable due to its unpredictable nature.

2.2 Acoustic Emission

Acoustic emission may be defined as the transient elastic wave generated by the rapid release of energy within a material [53]. This elastic wave propagates in all directions, ultimately reaching the surface of the material, where it may be detected by a suitable sensor. The detected emissions normally undergo some signal conditioning process, so that they may be acquired and stored for future signal processing and analysis. This process is shown schematically in Figure 2.10 and is discussed in more detail in Section 2.2.1, where the basis of the known AE theory is described. Subsequently, Section 2.2.2 deals with the generation of AE during the course of metal cutting, along with the introduction of the most relevant published models.

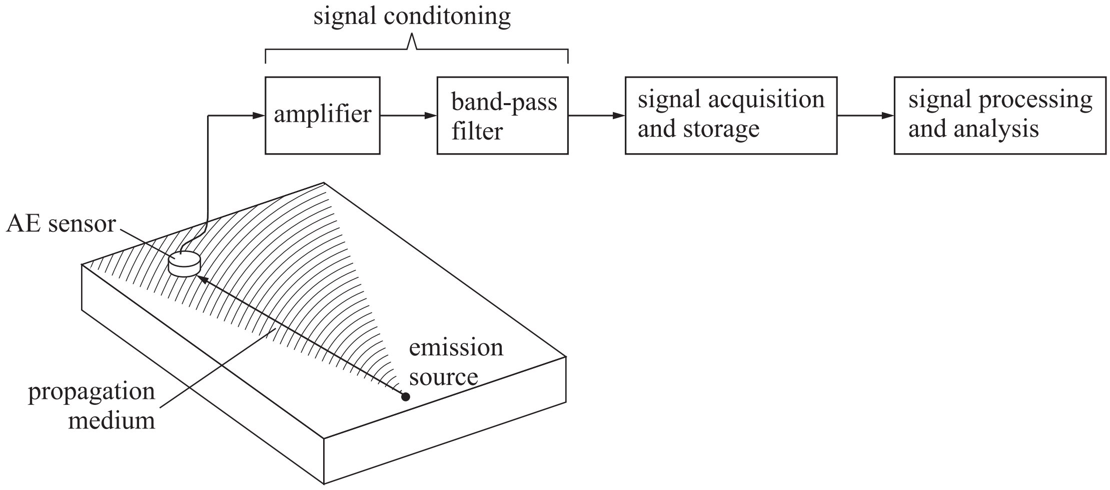

Figure 2.10: Diagram of the different stages of the AE process.

2.2.1 Acoustic Emission Theory

This section introduces some of the AE theory necessary for the understanding of the AE signals generated during the process of metal cutting. It goes over the different stages of the AE process, as introduced in Figure 2.10, i.e. generation, propagation, detection, signal conditioning, and signal processing.

Generation

Basically, AE is a high frequency and low amplitude elastic stress wave generated due to the rapid release of strain energy from localized sources within a material. Thus, if a material is loaded, stresses gradually build up, and, as the material deforms elastically, strain energy is stored. If the stresses at some location of the material reach its maximum strength, this strain energy is rapidly released, resulting in a rearrangement of the internal structure of the material. This localized release of strain energy is called an AE event, and since it is highly complex and non-uniform, the resulting AE wave will be non-stationary and stochastic in character. Consequently, Ivanov [54] proposed a stochastic pulse process to be a complete model of an AE event, so that AE is formed due to a series of discrete pulses, the characteristic and shape of which depend on the physical mechanisms of each individual event. In metals, the main sources of AE are normally associated with the dislocation movement accompanying plastic deformation and with the initiation and extension of cracks in a structure under stress.

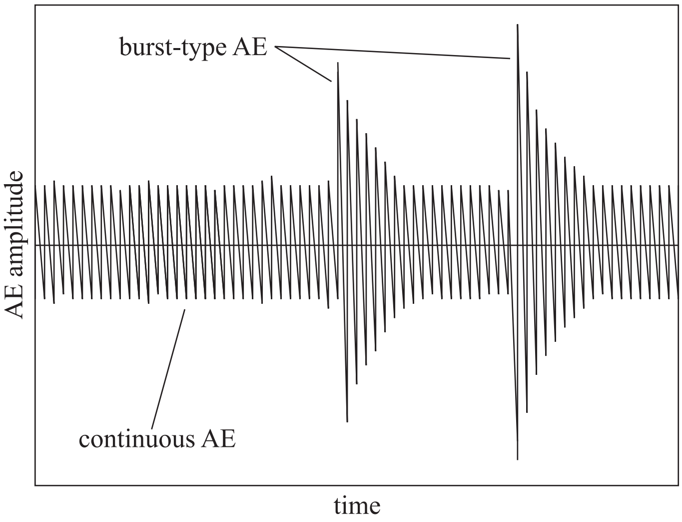

Figure 2.11: Continuous and burst-type AE.

The rate by which the AE events are generated will qualitatively define the appearance of the propagating AE wave. Thus, as shown in Figure 2.11, two types of AE waves are normally distinguished:

Bust-type AE Burst-type emissions are short duration pulses and are associated with the discrete release of high amplitude strain energy, such as the development of cracks. If AE events are sufficiently separated in time, the emission will appear as a train of individual busts, and each event can be readily detected.

Continuous AE If many events from different sources are generated at the same time, individual events can no longer be distinguished, and the emissions will appear to be continuous. The waveform of a continuous-type AE signal is similar to a Gaussian random noise, but the amplitude varies with acoustic emission activity. In metals, this form of emission is generally considered to be associated with the motion of dislocations.

However, as shown in Figure 2.11, higher amplitude bust-type AE may be observed in conjunction with continuous emissions, and it is possible that the two types of emissions are due to concurrent generating mechanisms. For example, in a process where plastic deformation and fracture subsist, continuous AE is normally attributed to plastic deformation, whereas the individual bursts are attributed to the fracture process.

Moving dislocations are the dominant mechanism of plastic deformation in metals.[7] A description of the basic mechanisms by which dislocations can cause AE was suggested by Gillis [55]. Basically, it is based on the fact that dislocations have periodic positions in the lattice, which provides a minimum energy configuration. As a dislocation moves from one minimum energy position to the next, the lattice elastic strain is increased until the middle position is reached. After this, the elastic strain is suddenly released to produce a vibrational wave in the lattice, which is believed to be the origin of the detected AE waves. Gillis also speculated that all dislocation lines move cooperatively, since each tends to move according to the stress field imposed by its moving neighbours, and this has important consequences because then the vibration waves produced by one dislocation tend to be in phase with the others.

Rouby *et al.* [56] proposed that continuous AE from plastic deformation is due to the effect of a large number of elementary sources, homogeneously distributed within the specimen, and randomly emitting during time. In order to explain the spectral characteristics of the emissions, Rouby *et al.* proposed that if each dislocation (with length l_{D}) moves at speed V_{D} between two obstacles separated by distance d_{B}, far way form the source, an AE signal may be detected, whose frequency spectrum will display a maximum value that appears at frequency

$$f_{\max} = \frac{V_{\mathrm{D}}}{2d_{\mathrm{B}}} \tag{2.36}$$

As plastic strain increases, more obstacles are generated, and thus d_{B} decreases, leading to an increase of $f_{\max}$.

More generally, in a review paper by Skal's'kyi *et al.* [23], it was concluded that the accelerated motion of dislocations and their sudden stop are the generation source of AE elastic waves. However, the exact mechanism by which AE is generated during plastic deformation is still quite

---

[7] A description of dislocation theory is out of the scope of this review. For information on dislocations, literature may be consulted [21, 22]. Also, there is a short introduction on dislocation theory in Appendix B.

unclear, as it was concluded in a recent review about the current understanding of the mechanisms of AE [24], since though the understanding of AE from materials during fracture has advanced greatly, that due to plastic deformation remains still quite elusive. Besides, these two publications [23, 24] showed that no model relating AE to plastic deformation at the typically high levels of strain rate normally encountered in metal cutting have evolved so far, and it is unreasonable to assume that the low strain rate AE source mechanisms are prevalent at high strain rates, since at high strain rates, the deformation mechanisms and the dynamics of dislocation motion are very different from the low strain rate case [57].

Propagation

As AE is generated, it propagates as ultrasonic waves, which can be longitudinal (vibration in direction of motion) or transverse (vibration perpendicular to direction of motion). Longitudinal and transverse waves travel at different speeds c_{L} and c_{T}, respectively, and, for many materials, $c_{\mathrm{L}} \approx 2c_{\mathrm{T}}$. As they travel through different media, the characteristics of the AE waves undergo considerable distortions. There are two main causes of distortion of acoustic waves [53, 58]: geometrical losses and attenuation. Since AE is generally supposed to be generated from a point source, AE is considered to propagate as spherical waves, whose amplitude (I) decreases inversely with distance (x) from the source:

$$I = I_0 \frac{x_0}{x} \tag{2.37}$$

where I_0 is the amplitude at distance x_0. These are called geometrical losses and are independent of frequency and material properties. Moreover, far from the generating source, AE can be assumed to propagate as plane waves, so that geometrical losses can be neglected. The amplitude of AE wave attenuates as it progresses thorough the medium due to three major causes: diffraction, scattering, and absorption. The following equation holds for wave amplitude attenuation:

$$I = I_0 e^{-a(x-x_0)} \tag{2.38}$$

where, I_0 is the amplitude at x_0, and a is the attenuation coefficient which can be expressed as

$$a = Af + Bf^4 \tag{2.39}$$

where f is the frequency, and A and B are constants which depend on material and type of wave (longitudinal or transverse).

Another important phenomenon is the reflection and transmission of waves resulting when an acoustic wave strikes the boundary with another medium. As shown in Figure 2.12, if a longitudinal wave travelling through a solid medium A meets the boundary with medium B at an angle α_{L} with the normal to the boundary, the following waves are reflected at the boundary: a longitudinal wave reflected at an angle $-\alpha_{\mathrm{L}}$ to the normal to the boundary and a transverse

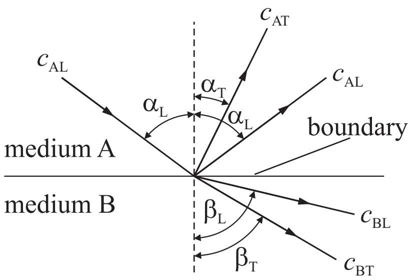

Figure 2.12: Reflection and transmission of waves at the boundary with another material.

wave reflected at an angle $-\alpha_T$ to the normal to the boundary. In addition, a longitudinal wave transmitted into medium B is refracted at the boundary with an angle $180^\circ + \beta_L$ to the normal to the boundary, and, if material B is a solid, a transverse wave will also be transmitted and refracted at the boundary with an angle $180^\circ + \beta_T$ to the normal to the boundary. The acoustic velocities for the various waves are related to one another in the following manner:

$$\frac{c_{AL}}{\sin\alpha_L} = \frac{c_{AT}}{\sin\alpha_T} = \frac{c_{BL}}{\sin\beta_L} = \frac{c_{BT}}{\sin\beta_T} \tag{2.40}$$

where c_{AL} and c_{AT} are the longitudinal and the transverse wave speeds in medium A, and c_{BL} and c_{BT} are the longitudinal and the transverse wave speeds in medium B.

When the incident transverse wave strikes the boundary at a right angle ($\alpha_L = 0^\circ$), a transverse wave is reflected back into medium A, and also another transverse wave is transmitted forward through medium B, both at 90° with the boundary. The relative amounts of reflected and transmitted energies are dependent on the dissimilarities of the two materials, and these dissimilarities are represented by the relative values of the characteristic acoustic impedances of both materials A and B (r_A and r_B, respectively). For a given material, the characteristic acoustic impedance is solely dependent on the physical characteristics of the material and can be found from

$$r = \rho c_L \tag{2.41}$$

where ρ is the material density. Therefore, if $r_A = r_B$, no energy is reflected, but the more r_A differs from r_B, the more energy is reflected back into medium B.

Detection

At the surface of the material, the amplitude of the AE vibrations is very small (usually a few nanometres), and, therefore, a high sensitivity transducer, which converts the mechanical surface vibrations into electrical signals, is required for reliable detection of AE. Most commercial AE transducers involve a piezoelectric ceramic element manufactured from lead zirconate titanate (PZT). Figure 2.13 shows a conventional PZT transducer. However, although other type of sensors have also been proposed, PZT sensors are the most reliable, sensitive, and robust and are, therefore, the most widely used [2].

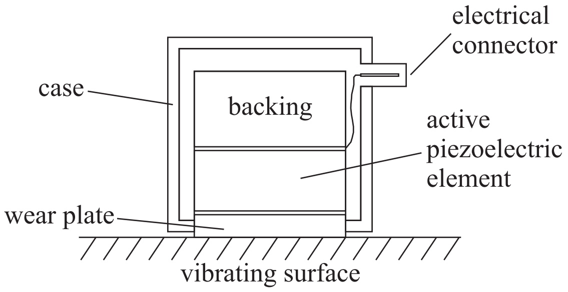

Figure 2.13: Piezoelectric transducer.

For efficient coupling of ultrasound between the transducer and a solid surface, a suitable coupling film (e.g. oil or grease) must be provided to avoid an air gap between the solid and the transducer, which would give rise to very small transmission of AE to the transducer. This is due to the fact that there is a very large difference between the characteristic acoustic impedances of, for instance, a solid like steel and air ($r_{\mathrm{steel}}/r_{\mathrm{air}} \approx 10^5$), and, as shown previously, nearly no acoustic energy would be transmitted to the transducer. Since r_{oil} is much closer to the value of r_{steel} ($r_{\mathrm{steel}}/r_{\mathrm{oil}} \approx 50$), much more acoustic energy is transmitted to the transducer.[8]

Signal Conditioning

Signal condition, which is dependent on each particular system requirement, is purely electronic and takes the electrical output signal from the AE sensor and provides an electrical signal for further data acquisition or other processing. The most common systems include a preamplifier, a band-pass filter, and an amplifier. A typical AE system operates in the ultrasonic frequency range (e.g. 100–1000 kHz). The lower frequency limit is imposed by the maximum frequency of unwanted background noises that may be colouring the signal of interest; the upper frequency limit is imposed by attenuation, which tends to limit the upper range of detection of AE signals; also, in order to prevent aliasing,[9] if the AE signal is going to be acquired, the maximum frequency of the signal must be less than at least half of the sampling rate of the acquisition system. Therefore, the low-pass frequency of the band-pass filter has to be sufficient to suppress low frequency noise signals, and its high-pass frequency has to be low enough in order to prevent aliasing.

Signal processing

Due to the stochastic character of the AE signals, the analysis and interpretation of AE is normally quite complex. Consequently, signal processing techniques are needed to process the raw AE

---

[8] The values of the characteristic acoustic impedances were taken from Blitz [58].

[9] The sample rate must be greater or equal to two times the highest frequency content in the input signal. When this rule is violated, undesired signals appear in the frequency band of interest. This is called aliasing.

signals. Next, the most important and common AE signal processing techniques are reviewed:[10]

Energy representation The most common way to represent the energy of a signal[11] is by calculating its root mean square (RMS). This is done by taking the square root of the mean of the square of the signal time series:

$$I_{\mathrm{RMS}} = \sqrt{\frac{1}{n}\sum_{i=1}^{n} I_i^2} \tag{2.42}$$

where I_i is the amplitude of the signal at sampling instant i, and n is the number of samples in the series. However, since the RMS computation does not avoid the influence of undesirable outlying values, such as randomly appearing burst-type signals that may be colouring a continuous emission, a new technique was developed [7], where the raw signal is first full-wave rectified and additionally low-pass filtered; then, the maximum value of the probability density function of the resulting time series is found, so that the most common amplitude, the mode, can be obtained. The mode of a time series I_i may be designated as I_{mode}. Furthermore, the power of AE (I_{power}) can be calculated either as I^2_{RMS} or I^2_{mode}.

Count techniques There are two major techniques: total number of counts (N) and count rate ($\dot{N}$). The total number of counts is the number of times a signal overcomes a given threshold. The number of counts per unit time is the count rate. The dependence of the count techniques on a threshold level can lead to problems, since if the signal amplitude changes, the count becomes meaningless if the threshold is also not changed.

Frequency analysis When a signal is sampled, it is represented as a series of amplitudes as a function of time (time domain). The signals can also be represented as a function of frequency (frequency domain), and normally the fast Fourier transform (FFT) algorithm is utilized to compute the transformation from the time to the frequency domain. The distribution of the power of the signal in the frequency domain is known as the power spectrum. However, the power spectrum is still a series of amplitudes containing half of the number of samples of the original time series, and, therefore, a simpler parameter is necessary to characterize a signal in the frequency domain, and such a parameter is the mean frequency (f_{mean}), which indicates the frequency value that divides the spectrum into two parts of equal energy [19]:

$$f_{\mathrm{mean}} = \frac{\sum_{i=1}^{n} S_i f_i}{\sum_{i=1}^{n} S_i} \tag{2.43}$$

---

[10] Literature may be consulted for more complex techniques; for example, Li [9] and Diniz *et al.* [59] reviewed some processing methods utilized to extract features from AE signals in view of metal cutting monitoring.

[11] When one refers to AE energy, one is actually referring to energy per unit time, i.e. power. Moreover, since signals are normally obtained in volts (V), the power of the signals are presented in square volts (V^2), which are also the power units commonly found in AE literature.

where f_i is the frequency at sample i, S_i is the signal power at frequency f_i, and n is the number of frequency samples.

2.2.2 Acoustic Emission from Metal Cutting

In metal cutting, there are two major processes normally associated with the generation of AE: plastic deformation and fracture. It has been proposed [9, 60, 61] that the sources that contribute to the generation of AE during metal cutting are the following (Figure 2.14):

- Plastic deformation in the primary and secondary zones.
- Tool-chip and tool-work sliding friction in the secondary and tertiary zones, respectively.
- Collision, entangling, and fracture of chips.
- Fracture of the cutting tool.

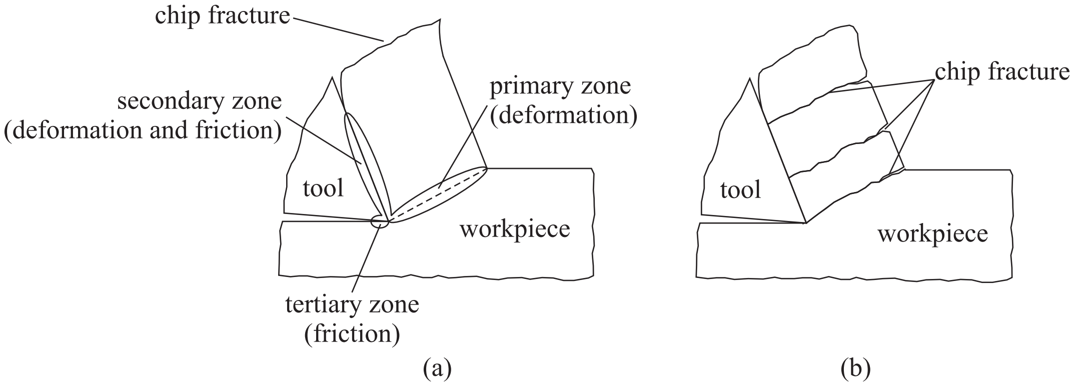

Figure 2.14: Sources of AE in metal cutting. (a) Continuous chip formation. (b) Discontinuous chip formation.

Plastic deformation and friction is known to produce continuous AE, whereas collision, entangling, and fracture of chips, and breakage of the cutting tool is known to produce burst-type emissions. Moreover, AE has been reported to be dependent on many parameters, such as work and tool materials, tool geometry, cutting speed, feed rate, width of cut, cutting fluids, etc.

Energy Analysis of Continuous Acoustic Emission

For continuous AE generation, it must be assumed that chip generation is continuous and without BUE. Furthermore, the tool is normally considered to be perfectly sharp, so that the tertiary zone source of AE can be neglected. In this section, the most relevant AE generation models from continuous chip operations are reviewed.

One of the first attempts to model continuous AE from metal cutting was achieved by Dornfeld and Kannatey-Asibu [62]; the energy rate (power) of the AE signals was stated to be proportional to the plastic work of deformation ($\dot{U}$). Generally, $\dot{U}$ can be defined as:

$$\dot{U} = \int_{v} \sigma_{ij}\dot{\varepsilon}_{ij}\mathrm{d}v \tag{2.44}$$

where σ_{ij} and $\dot{\varepsilon}_{ij}$ are the tensor notations for the applied stresses and strain rates,[12] respectively, acting on a volume v of the material participating into deformation. Moreover, I_{RMS} was used to represent the AE energy rate. An expression for $\dot{U}$ was obtained by considering only primary deformation, so that Equation 2.44 was simplified and equated to I^2_{RMS} as follows:

$$I^2_{\mathrm{RMS}} = Kk\dot{\gamma}_{\mathrm{AB}}v \tag{2.45}$$

where K is a constant of proportionality, k is the shear strength of the material (assumed to be constant), and $\dot{\gamma}_{\mathrm{AB}}$ is the mean shear strain rate at the primary zone. The volume v was derived from the slip line field for orthogonal cutting without BUE from Lee and Shaffer [48]. The strain rate $\dot{\gamma}_{\mathrm{AB}}$ was derived based upon experimental values of shear zone thickness from Kececioglu [28]. Moreover, it was observed that metal cutting was a good source of AE and that AE was sensitive to strain rate, as proposed in Equation 2.45. However, since the model only accounts for deformation in the primary deformation zone, and since other important sources of AE were neglected, Dornfeld and Kannatey-Asibu concluded that the level of AE predicted by the model would be underestimated.

Kannatey-Asibu and Dornfeld [60] developed a more sophisticated model by considering that AE was generated mainly due to plastic deformation in the primary and secondary zones and also sliding friction in the secondary zone. The influence of the tertiary zone was neglected, since cutting with a sharp tool was assumed. The work rate done in the primary and secondary zones was equated to I^2_{RMS}, and by assuming constant shear strength k, and simplified linear friction conditions at the tool-chip interface, the following relationship was obtained:

$$I^2_{\mathrm{RMS}} = K\left[kwV\left(\frac{\cos\alpha}{\sin\phi\cos(\phi-\alpha)}t_1 + \frac{1}{3}(l_{\mathrm{int}} + 2l_1)\frac{\sin\phi}{\cos(\phi-\alpha)}\right)\right] \tag{2.46}$$

where K is a constant of proportionality, and all the other variables are as previously defined. In order to evaluate the validity of Equation 2.46, orthogonal cutting tests were performed with tubular workpieces of an aluminium alloy and a mild steel. In a first set of tests, the feed rate was kept constant, and α, V, and the workpiece material were allowed to vary. The level of AE was observed to be strongly dependent on V, increasing with increasing V. The steel workpiece

---

[12] In a three-dimensional coordinate system (x, y, and z), a small body (dimensions dx, dy, and dx) is subjected to nine stress components σ_{ij} (i and j are iterated over x, y, and z). This collection of stresses is called the stress tensor. The same principle can be used for the strain and strain rate tensors. Reference [40] may be consulted for more information.

produced a higher level of AE than the aluminium alloy, as expected, since the shear strength of the steel is higher than that of the aluminium. The level of I_{RMS} was also observed to increase with α. Moreover, a plot of predicted against experimental values of I_{RMS}, indicated that Equation 2.46 was not universal since a dependency on α was present (the constant of proportionality K was rake angle dependent). Equation 2.46 was subsequently modified by replacing constant K by $K\sin\alpha$ to give a better relationship between predicted and experimental I_{RMS} values. Furthermore, a second set of tests was performed by employing tools with restricted contact lengths, so that variations of AE with tool-chip contact length could be estimated. In order to keep the AE generated from the primary shear zone constant with varying tool-chip contact length, the shear angle was kept constant by adjusting the feed rate accordingly. It was observed that I^2_{RMS} increased linearly with contact length for the lower lengths, and then it started to reduce in slope for the higher contact lengths. The reduction in slope at the higher contact lengths was attributed to the onset of sliding friction, suggesting that less AE activity is generated due to friction than bulk plastic deformation. The point at which the slope starts to change was used to estimate the boundary between sticking and sliding.

Schmenk [63] used the model developed by Kannatey-Asibu and Dornfeld [60] (Equation 2.46) to derive an expression for I^2_{RMS}/v (specific AE output). For a tool with 0° rake angle, and by assuming a shear angle of 30°, and that $l_1 = l_{\mathrm{int}}/2 = t_1$, the specific AE output was simplified to the following expression:

$$\frac{I^2_{\mathrm{RMS}}}{v} = u = K(2+0.67) \tag{2.47}$$

where $v = t_1 wV$. Within the brackets, the left hand term represents the contribution of the primary shear zone, while the right hand term represents the contribution of the tool-chip interface. As a result, Schmenk concluded that deformation in the primary zone was the dominant source of AE. Cutting tests with a ductile aluminium alloy, performed on a milling machine, showed that there was a significant decrease of specific AE output with uncut chip thickness, which was attributed to the size effect.

In order to quantify the relative contribution from the primary and secondary zones, Lan and Dornfeld [64] extracted two terms from Equation 2.46: $t_1\cos\alpha/[\sin\phi\cos(\phi-\alpha)]$, representing the primary zone contribution to AE, and $(l_{\mathrm{int}}+2l_1)\sin\phi/[3\cos(\phi-\alpha)]$, representing the secondary zone contribution to AE. Machining tests with a high speed steel, in which measurements of the shear angle ϕ and total tool-chip contact length l_{int} were included, revealed that both the primary and secondary shear zones contributed approximately by the same amount of energy to the total AE signal. These results oppose Schmenk's conclusions [63], i.e. the primary zone is the major AE contributor, which was attributed to the assumption that $l_{\mathrm{int}} = 2t_1$. Furthermore, Lan and Dornfeld developed a further model considering signal attenuation and tool flank contact:

$$I_{\mathrm{RMS}} = K\left(kwV\left[K_1\frac{\cos\alpha}{\sin\phi\cos(\phi-\alpha)}t_1 + K_2\frac{1}{3}(l_{\mathrm{int}}+2l_1)\frac{\sin\phi}{\cos(\phi-\alpha)} + K_3V_{\mathrm{B}}\right]\right)^m \tag{2.48}$$

where m is material dependent, V_B is the average length of the flank wear land, and K_1, K_2, and K_3 are factors for signal attenuation, corresponding to signal transmission losses between the primary shear zone, tool-chip interface zone, flank wear zone, and the transducer, respectively. The magnitude of K_1 was found to be between 0.2 and 0.25, while both K_2 and K_3 were assumed to be one. Moreover, machining tests performed with a low carbon steel showed that I_{RMS} was not very sensitive to the variations in feed rate and width of cut, contradicting Equation 2.48 predictions. In order to justify this contradiction, Lan and Dornfeld pointed out that the analytical derivation of Equation 2.48 was based upon orthogonal machining, whereas the experiments were conducted with oblique machining conditions. The size effect was also mentioned as a reason for the high values of AE energy encountered at low values of uncut chip thickness.

Messaritis and Borthwick [5] proposed the use of Oxley's semi-empirical theory [50] for the prediction of AE activity during metal cutting, since the shear plane model used to derive the AE energy models described above was, according to the authors, an over-simplistic representation of the cutting process. Preliminary machining tests on a low carbon work material showed that although I_{RMS} was slightly higher in semi-orthogonal cutting than in orthogonal cutting, semi-orthogonal conditions could still be used with reasonable accuracy in conjunction with Oxley's theory. Predictions of $\dot{\gamma}$ (strain rate), showed that $\dot{\gamma}$ was invariable with w, decreased with t_1 and increased with V. The same trends were observed with experimental results of I^2_{RMS} with w, t_1, and V. The relative insensitivity of I_{RMS} to varying widths of cut showed that the dependence of AE on volume was very small, and since k is dependent on $\dot{\gamma}$, Messaritis and Borthwick concluded that $\dot{\gamma}$ was the dominant parameter in AE generation, and, as a result, the following relationship was suggested:

$$I^2_{\mathrm{RMS}} = A + B\dot{\gamma} \tag{2.49}$$

where A and B are dimensional constants dependent on the wave propagation path and transducer installation.

Blum and Inasaki [7] observed that I_{RMS} contains the influence of randomly appearing bursts caused by unavoidable noise sources, such as chip breakage and impact. Consequently, a new AE energy parameter, which eliminates the interference of randomly appearing noises, named I_{mode} (mode of the previously full-wave rectified and low-pass filtered raw AE signals, as defined in Section 2.2.1), was proposed. Experimental machining tests were conducted with a medium carbon steel work material, and the primary ($\dot{U}_{\mathrm{AB}} = F_{\mathrm{AB}}V_{\mathrm{S}}$) and secondary ($\dot{U}_{\mathrm{int}} = F_{\mathrm{int}}V_{\mathrm{C}}$) energy consumptions were calculated. It was observed that $\dot{U}_{\mathrm{AB}}$, $\dot{U}_{\mathrm{int}}$, and I_{mode} increased with increasing V. Despite both energy consumptions increased with increasing t_1, I_{mode} showed an opposite falling tendency. Both I_{mode} and $\dot{U}_{\mathrm{AB}}$ decreased with increasing α, although $\dot{U}_{\mathrm{int}}$ increased with increasing α. As in previous results, I_{mode} exhibited insensitivity to varying w, demonstrating that AE generation is not significantly affected by the volume of deforming material. However, both energy consumptions showed a strong increase with rising w. Furthermore, the following relationship was suggested:

$$I_{\mathrm{mode}}^2 \propto \dot{\gamma}^m \tag{2.50}$$

where m is the strain rate sensitivity. Kececioglu's [28] shear zone thickness results were used to determine $\dot{\gamma}$. Experimental results of I_{mode} were plotted against calculated $\dot{\gamma}$ values and appeared to be in agreement with the relationship proposed in Equation 2.50.

Since, at the high strain rates encountered in metal cutting (higher than 1000 s^{-1}), the deformation mechanisms and the dynamics of the motion of dislocation are very different from the low strain rate deformation regimes, Rangwala and Dornfeld [57], based on Kumar *et al.* [25] and Kumar [26], proposed a new mechanism of AE generation during metal cutting. A linear relationship between flow stress and strain rate was considered, suggesting that the dynamics of dislocation motion was governed by damping mechanisms, i.e. $F = BV_{\mathrm{D}}$, where F is the unit force acting on the dislocation per unit length, V_{D} the velocity of the dislocation between obstacles, and B the damping coefficient. Moreover, if dislocation damping was responsible for AE generation, Rangwala and Dornfeld suggested that the power of the AE signal (I_{RMS}^2) should be proportional to the damping power ($\dot{U}_{\mathrm{D}}$):

$$I_{\mathrm{RMS}}^2 \propto \dot{U}_{\mathrm{D}} = \frac{B}{\rho_{\mathrm{MD}} b^2}\dot{\varepsilon}^2 v \tag{2.51}$$

where ρ_{MD} is the mobile dislocation density, b the Burgers vector of the crystal lattice[13] and v the volume involved in plastic deformation. In order to evaluate the viability of dislocation damping as a source mechanism of AE at high strain rates, orthogonal machining tests were performed with an aluminium alloy tubular workpiece. A first set of tests used a restricted contact length tool with variable cutting speeds and feed rates. A linear relationship between I_{RMS} and calculated shear velocity V_{S} was observed, implying that, at constant contact length, I_{RMS} was a linear function of the strain rate in the primary zone. This relationship is also observed in Equation 2.51, corroborating the assumption that dislocation damping may be one of the contributing mechanisms for AE generation in metal cutting. Assuming that AE is generated only by dislocation damping associated with plastic deformation in the primary and secondary shear zones, that the primary zone thickness is equal to the secondary zone thickness, and that there is no sliding zone at the tool-chip interface, Rangwala and Dornfeld derived the following relationship:

$$I_{\mathrm{RMS}}^2 = KV_{\mathrm{S}}^2\left(\frac{t_1}{\sin\phi} + l_{\mathrm{int}}\sin^2\phi\right) \tag{2.52}$$

A second set of tests employed tools with varied contact lengths for different cutting speeds and constant feed rate. With low contact length tools, the relationship between experimental values and Equation 2.52 predictions of I_{RMS} were reasonably linear. However, as the contact length

---

[13] For more information on dislocation theory, Appendix B and relevant literature on the subject [21, 22] may be consulted.

increased, a decay from linearity was observed. This was attributed to the onset of sliding friction for higher tool contact lengths, which was neglected in the development of Equation 2.52.

Saini and Park [65] have also developed a model that equates I_{RMS}^2 to the work rate done in the primary and secondary zones of deformation:

$$I_{\mathrm{RMS}}^2 = kwVt_1 \left[K_1 \frac{\cos\alpha}{\sin\phi\cos(\phi-\alpha)} + K_2 \frac{2m\sin(\phi+\lambda-\alpha)}{(n+2)\cos\lambda\cos(\phi-\alpha)} \right] \tag{2.53}$$

where λ is the friction angle (Equation 2.14), m is the coefficient of the chip contact length ($m = 2$ for carbon steel), and n (parabolic constant) was determined from

$$n = \frac{2kwl_{\mathrm{int}}}{F_{\mathrm{Y}}\sin\alpha + F_{\mathrm{X}}\cos\alpha} - 2 \tag{2.54}$$

where the cutting forces F_{X} and F_{Y} were determined from experimental measurements. The signal attenuation constants K_1 and K_2, for the primary and secondary deformation zones, respectively, were found by a computational statistical analysis technique, resulting in $K_1 = 0.00098$ and $K_2 = 0.00157$. Orthogonal turning tests, carried out with a carbon steel, showed that the with of cut had no influence on I_{RMS}. The variation of I_{RMS} with V and α showed that the predictions from Equation 2.54 and the experimental results were in agreement, where I_{RMS} increased with V and decreased with α. Saini and Park argued that one major advantage of this model was in the determination of l_1 and l_2, which were based on realistic assumptions of the frictional stresses in the sticking and sliding zones.

In conclusion, by assuming that the AE energy rate is proportional to the plastic work of deformation, it can be derived that the AE energy is virtually proportional to the applied stress, strain rate, and volume of material participating into deformation. All published experimental results led to the definite conclusion that the AE power was strongly dependent on strain rate [5,7,57,62], and since strain rate is directly dependent on cutting speed, a strong relationship was also observed between the cutting speed and the AE energy rate [3,5,7,60,62,65]. Moreover, the AE energy was observed to be essentially unaffected by the width of cut [3,5,7,64], although increasing AE energy with increasing width of cut has also been reported [66]. The independence of the AE power from the width of cut implies that the dependence of AE on volume is insignificant, since the volume of deforming material is proportional to the width of cut, and, in principle, the width of cut affects neither the shear strength nor the strain rate. Hence, since the flow stress is a function of strain rate, it was proposed [5,7] that the AE energy was essentially only strain rate dependent. Some experimental results showed that the AE energy decreased with feed rate [5,7,62], whereas other results [3,57,62,64,66] showed that the AE energy remained roughly constant with varying feed rate. However, in most cases, it was also observed that the variation of AE power with feed rate showed a similar trend to the variation of strain rate with feed rate [5,7,57], supporting the theory that the AE energy is a function of strain rate and not volume dependent. With the exception of the results presented by Kannatey-Asibu and Dornfeld [60], the AE energy was observed to decrease with increasing tool rake angle [7, 64, 65]. Experimental data on the variation of AE with different material properties is scarce and insufficiently systematized. Lan and Dornfeld [64] heat treated workpieces of a medium carbon steel to different hardness values and observed I_{RMS} to increase linearly with increasing hardness. In addition, materials with higher shear strength values were observed to generate higher levels of AE energy [60, 66].

Frequency Analysis of Continuous Acoustic Emission

This section reviews published material about the frequency characteristics of AE during metal cutting. Unfortunately, not much work has been done on this subject.

Grabec and Leskovar [67] studied the spectrum of AE in the 0–100 kHz range, generated during the machining of an aluminium alloy, and observed that in the low frequency range, below 15 kHz, the spectrum was practically discrete, which was attributed to the several modes of mechanical resonance of the whole cutting system. In the range above 15 kHz, the spectrum was observed to be continuous, which was attributed to the deformation and friction from the cutting process. It was also observed that both feed rate and width of cut did not influence the spectrum appreciably, so that the cutting speed was the dominant factor affecting the high frequency content of the spectrum.

Yaohui and Rongbao [68] utilized a method called maximum entropy spectrum to analyse the AE generated during the machining of aluminium. With this method, individual separate zones were identified in the spectrum, corresponding to different AE generation mechanisms, such as plastic deformation, friction and BUE. It was also observed that AE generated due to fracture and impact of chips to be a random noise signal with a wide frequency band.

Rangwala and Dornfeld [19] presented a study of the spectral characteristics of AE generated during the machining of an aluminium alloy. Two parameters of the signal power spectrum were used: the mean frequency (f_{mean}, as defined in Section 2.2.1) and the standard deviation of the mean frequency (σ_{mean}). The value of f_{mean} was observed to increase with V up to a certain value of V, after which f_{mean} started to decrease. Rangwala and Dornfeld explained this trend by noting that at low cutting speeds, as V increases, the strain rate also increases, and then AE is expected to shift towards higher frequencies; however, at high strain rates, the tool-chip interface temperature also increases, and, at some point, it is expected that the temperature effects offset the effects of strain rate, causing AE to shift towards lower frequencies. Moreover, The value of σ_{mean} was observed to increase with V, and this was attributed to the widening of the primary shear zone with increasing V, resulting in a larger variation of strain rates; consequently, the AE sources operate in a wider frequency region, causing a higher spread of the spectral power distribution. In addition, f_{mean} and σ_{mean} did not exhibit any clear trend with varying feed rate, and no definite explanation was provided by Rangwala and Dornfeld. Finally, f_{mean} was observed to increase with tool-chip contact length, indicating that AE due to chip sliding is concentrated in the higher frequencies. This is consistent with the fact that the temperatures in the sliding zone are not very high, causing AE to shift towards higher frequencies.

Burst-Type Acoustic Emission from Metal Cutting

The study of bust-type AE can be divided into two major fields:

Chip form The main types of chip formation are shown in Figure 2.2 as continuous, continuous with BUE, discontinuous, and segmented. Another possible application of AE is the detection of chip form during metal cutting. It has been suggested that the burst-type AE signals generated due to chip breakage can be used to distinguish between continuous and discontinuous chip formation, since continuous chips generate continuous type AE. In discontinuous chip formation processes, each AE burst has been observed to be related to the breaking of the chip [14–16]. Different chip forms were generated from the variation in the feed rate [14, 16], and the average chip breaking frequency (number of chips produced per unit time) was calculated and observed to be well correlated to the average rate of AE burst events. Uehara and Kanda [15] used four different materials to produce different chip forms (continuous with BUE, discontinuous, and segmented) and demonstrated that the different types of chip form produce different AE patterns. Furthermore, during operations with continuous chips, the congestion or entanglement of the chip around the tool and workpiece is undesirable. It was observed that during chip congestion or entanglement, there is a sudden increase of high amplitude AE signals [14, 16].

Tool fracture Another promising use of AE is the detection of tool failure. Burst-type AE signals are detected when cracking, chipping, and fracture of the cutting tool is observed [10, 11]. In order to facilitate tool failure, Lan and Dornfeld [11] used a hardened work material and pre-slotted inserts. A significant burst of acoustic emission was detected at the moment of tool fracture. It was observed that I_{RMS}^2 increased with increasing fracture area. Moreover, chipping was seen to generate a lower burst AE signal because of the smaller fracture area. It was also observed that it was difficult to distinguish between a burst AE signal related to chipping and noise signals due to chip breakage and impact. Diei and Dornfeld [12] proposed a quantitative model, relating the peak of I_{RMS} to both the fractured area and the resulting cutting force at tool fracture. Good agreement was obtained between experimental values and model predictions.

Tool Wear and Acoustic Emission

Acoustic emission has been proposed as a suitable method for detecting cutting tool wear. Li [9] presented an updated review of the AE-based methods for tool wear monitoring during turning. Generally, the level of AE generation has been observed to increase with flank wear [3–7]. Inasaki and Yonetsu [3] observed an approximate linear increase of the level of AE with flank wear, and the rate of increase was observed to be higher for higher cutting speeds. However, Messarits and Borthwick [5] observed that the rate of increase of I_{RMS} with flank wear decreased with increasing flank wear. Blum and Inasaki [7] observed that, when no significant crater was developed, although both energy consumptions in the primary and secondary zones increased only slightly with flank wear, I_{mode} exhibited a steep increase with flank wear. Reverse cutting tests (workpiece rotates backwards and only the flank surface of the tool touches the workpiece) revealed that the amount of AE generated due to sliding friction in the tertiary zone was small compared to the amount of AE generated during normal cutting. Therefore, as the flank surface of the tool wears, V_{B} increases and the rightmost term of Equation 2.48 [64] becomes significant. Moreover, Uehara and Kanda [15] observed that the power spectrum of the AE signals were strongly affected by tool wear.

Most studies have only considered the influence of flank wear on the AE parameters, but Naerheim and Lan [6] concluded that when crater wear occurred along with flank wear, one influence cancelled the other. The AE level tended to become constant as cutting time elapsed, since the increase in flank wear increased AE generation, whereas the increase in crater wear decreased AE generation, owing to the fact that the increase in crater wear increased the effective rake angle. Lan and Dornfeld [4] had already observed that the level of AE seemed to decrease with crater wear. Therefore, when flank and crater wear were present, the level of wear from the analysis of I_{RMS} was difficult to estimate due to the opposing effects of the two types of wear.

2.3 Summary of Literature

As stated at the beginning of this chapter, the review of the relevant literature was divided into two major areas: metal cutting and AE.

The most simplified metal cutting conditions were assumed: metal cutting is orthogonal, the chip does not spread to either side, the tool is perfectly sharp, the chips are continuous and without BUE, no chatter is present, and there is no externally applied coolant or lubricant. With these conditions, two important zones of deformation can be identified: primary zone and secondary zone. The chip is formed in the primary zone, which is a narrow zone of intense shear that extends from the tool edge to the work surface. This zone has been modelled as a plane [29], called the shear plane, and a very important angle can be defined between this plane and the direction of the cutting speed, the shear angle ϕ; a parallel-sided shear zone has also been used to model the primary zone of deformation [18]. The secondary zone of deformation is defined by the contact between the tool rake face and the chip as it flows over the tool. The earliest analysis treated the tool-chip interface as a sliding friction situation [29]; however, it has been found that the tool-chip interface is formed by a region of sliding friction (nearest to the point where the chip leaves the tool) and a region involving plastic shear of the chip (nearest to the cutting edge) [34]; the tool-chip interface has also been modelled as a zone of constant plastic shear with no sliding [18].

Metal cutting modelling deals mainly with the prediction of ϕ, since this angle defines the geometry of the cutting process. No estimation of forces, stresses, and temperatures can be made without first evaluating ϕ. Two types of models have emerged: the fist type considers that deformation is performed with constant material properties [29,48,49], and, in the second type, material properties are allowed to vary due to the effects of strain, strain rate, and temperature [18]. Modelling with constant material properties is an oversimplification, and, although contributing to the understanding of the cutting process, predictions of ϕ are quite inaccurate when compared with experimental results from different work materials. A semi-empirical model that allows material properties to vary, developed by Oxley and co-workers [18], has proven to give excellent predictions of ϕ, cutting forces, and temperatures when compared with experimental results; however, at present, this model can only provide predictions for carbon steel work materials.

Acoustic emission may be defined as the transient elastic wave generated by the rapid release of strain energy within a material, which propagates in all directions, ultimately reaching the surface of the material, where it can be detected by an appropriate sensor. In metals, the main sources of AE are normally associated with the dislocation movement accompanying plastic deformation and with the initiation and extension of cracks in a structure under stress; dislocation movement is normally associated with a continuous type of AE, whereas high amplitude and short duration pulses, called burst-type AE, are associated with cracking processes.

In metal cutting processes with continuous chip formation, without BUE, and with a perfectly sharp tool, AE generation is normally attributed to the plastic work of deformation occurring in the primary and secondary deformation zones, and, consequently, AE is expected to be of continuous type. A number of more or less sophisticated models that relate AE from metal cutting have emerged; basically, most of theses models are based on the same principle: the power of the AE signals is proportional to the plastic work of deformation [7,57,60,62,63,65]. Theses models seem to be in agreement with experimental data when only V is allowed to vary, and t_1 and w are kept constant. According to some of the above-mentioned models, the power of AE should increase with t_1 and w [60, 63, 65]; however, experimental results showed that AE is essentially unaffected by w [3, 5, 7, 64], although AE has also been reported to increase with w [66]; some experimental results showed that AE power decreases with t_1 [5, 7, 62], whereas other results showed that AE power remains relatively unaffected by t_1 [3, 57, 62, 64, 66]. A preliminary analysis of the published results shows that AE should be strain rate dependent and volume independent.

In conclusion, none of the AE models developed so far appear to give a satisfactory solution for the problem, since they only agree with the experimental results when only V is allowed to change, and all the other variables are maintained constant, and, consequently, a different approach to the problem is necessary. Therefore, as stated in Section 1.3, it is the objective of the present thesis to investigate the generation mechanisms of AE during metal cutting, and as dislocation motion is considered to be the main mechanism responsible for plastic deformation, a relationship between AE and the motion of dislocations accompanying plastic deformation at the typical strain rates and temperatures encountered in metal cutting is going to be examined. Since most published experiments were performed for quite limited cutting conditions and work materials, a series of cutting tests is going to be performed for a wide range of cutting conditions and work materials. For the prediction of important parameters that define the physics of metal cutting, the semi-empirical model developed by Oxley and co-workers [18] is going to be employed. A signal processing technique [7], named AE mode, which minimizes the influence of undesirable outlying values from the AE data, is going to be used to compute the power of AE. Finally, a technique [19], called mean frequency, is going to be employed to calculate the average frequency content of AE.

Chapter 3

Experimental Methodology

In order to study the generation of acoustic emission (AE) in metal cutting, a systematic set of experiments were performed on a CNC turning centre, and data from different sensors were collected. This chapter describes the methodology adopted for the experiments. In the first part, the experimental apparatus utilized is described, and, in the second part, the experimental procedure adopted is illustrated.

3.1 Apparatus

This section describes the turning machine, tool, and work materials selected for the experiments, and also the instrumentation system conceived for the acquisition of data.

3.1.1 Machine, Tool, and Materials

Figure 3.1: Image of the turning centre used for the experiments.

All turning tests were performed on a MT50 CNC Turning Centre from MHP Machines (Figure 3.1). The chuck of the machine can be rotated up to a maximum of 4000 rpm and can provide a constant power of 34 kW between 1000 and 3000 rpm. The maximum resolution of the main cutting parameters are: cutting speed, 1 m/min; feed rate, 0.001 mm/rev; width of cut, 0.001 mm.

Continuous chip formation and semi-orthogonal machining were the primary motivations for the choice of the tooling system. A tool holder, ISO code SCLCL 2020K12, was used in combination with an ungrooved and uncoated carbide insert, ISO code CCMW 120404, grade K10 (Figure 3.2). This combination resulted in the following tool geometry:[1] side cutting edge angle, $-5°$; end cutting edge angle, 5°; inclination angle, 0°; normal rake angle, 0°; clearance angle, 7°.

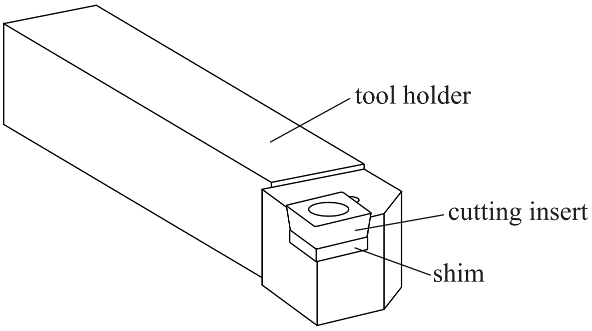

Figure 3.2: Tool holder and insert (front-top view).

Four different work materials were used: a low and a medium carbon steel, an austenitic stainless steel, and an aluminium alloy. These materials are described next in detail:

080A15 (BS 970) This low carbon steel was supplied in round bars of 90 mm diameter. The chemical composition (provided by the supplier) was 0.15% C, 0.17% Si, 0.78% Mn, 0.015% P, 0.027% Ni, 0.021% Cr, 0.003% Mo, 0.018% S, 0.049% Cu, 0.002% Sn, and 0.001% Al.

080M40 (BS 970) This medium carbon steel was supplied in round bars of 90 mm diameter. The chemical composition (provided by the supplier) was 0.44% C, 0.24% Si, 0.72% Mn, 0.024% P, and 0.009% S.

304S15 (BS 970) This austenitic stainless steel was supplied in round bars of 76.2 mm diameter. The chemical composition (provided by the supplier) was 0.023% C, 0.35% Si, 1.67% Mn, 0.023% P, 10.09% Ni, 18.13% Cr, 0.36% Mo, 0.029% S, 0.2% Cu, 0.066% N, and 0.14% Co.

6082-T6 (BS 1474) This medium strength aluminium alloy, in the T6 condition, was supplied in round bars of 88.9 mm. The chemical composition was not provided by the supplier, but

---

[1] The definition and nomenclature of a three-dimensional tool geometry can be found, for example, in reference [18].

the typical composition is 0.7–1.3% Si, 0.4–1% Mn, 0.1% max. Ni, 0.25% max. Cr, 0.1% max. Cu, 0.5% max. Fe, 0.6–1.2% Mg, 0.2% max. Zn, and 0.1% max. Ti.

3.1.2 Instrumentation

In conjunction with the measurement of AE, other signals were measured such as the cutting forces, vibrations, and temperatures. This section describes the sensors, analog signal conditioning, and signal acquisition. Figure 3.3 shows a diagram of the overall measurement system.

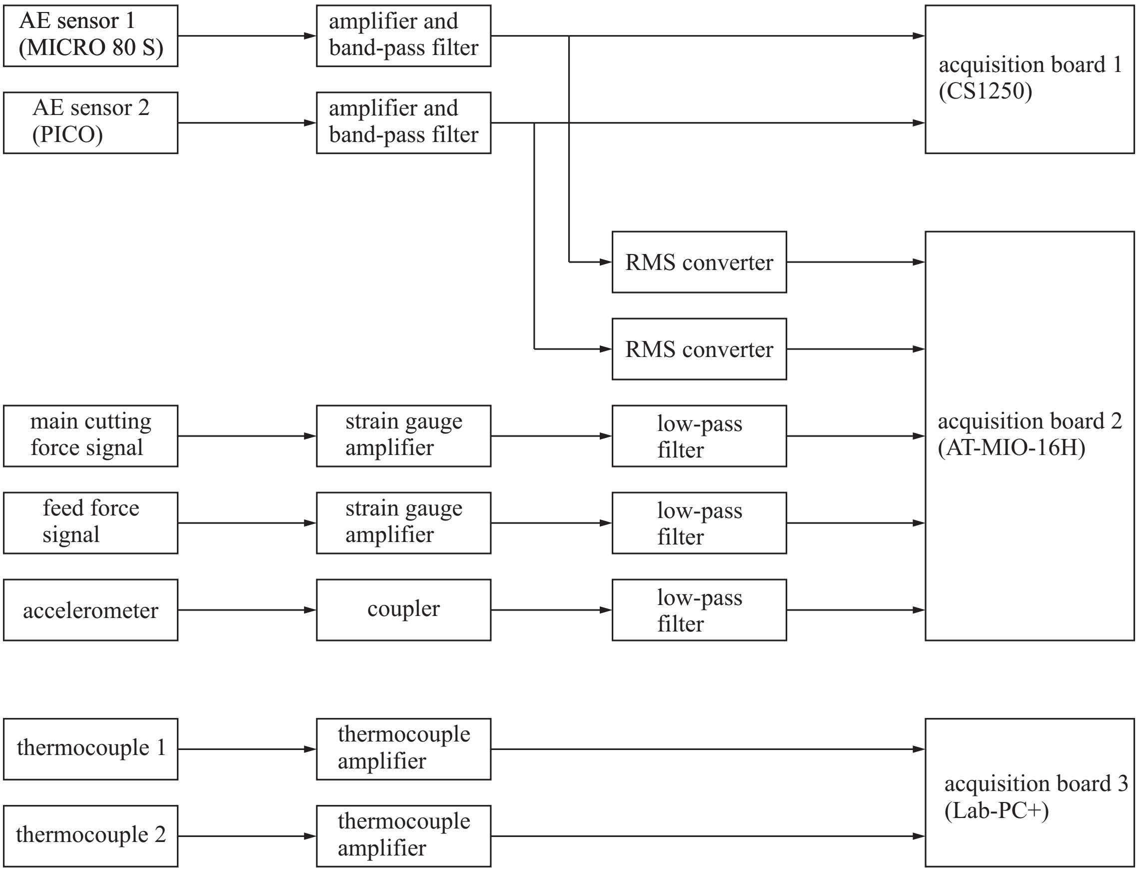

Figure 3.3: Instrumentation system.

Acoustic Emission Measurement

The main criterion for the selection of the AE transducers was based on the flatness of the sensors response in the 100–1000 kHz bandwidth. Two piezoelectric sensors were selected from Physical Acoustics Corporation:

MICRO 80S This sensor is 10 mm in diameter and 12 mm in height, and the operating frequency range is 175–1000 kHz. Figure 3.4a shows the frequency response of the sensor as obtained from its calibration certificate.

PICO This sensor is 5 mm in diameter and 4 mm in height, and the operating frequency range is 200–750 kHz. Figure 3.4b shows the frequency response of the sensor as obtained from its calibration certificate.

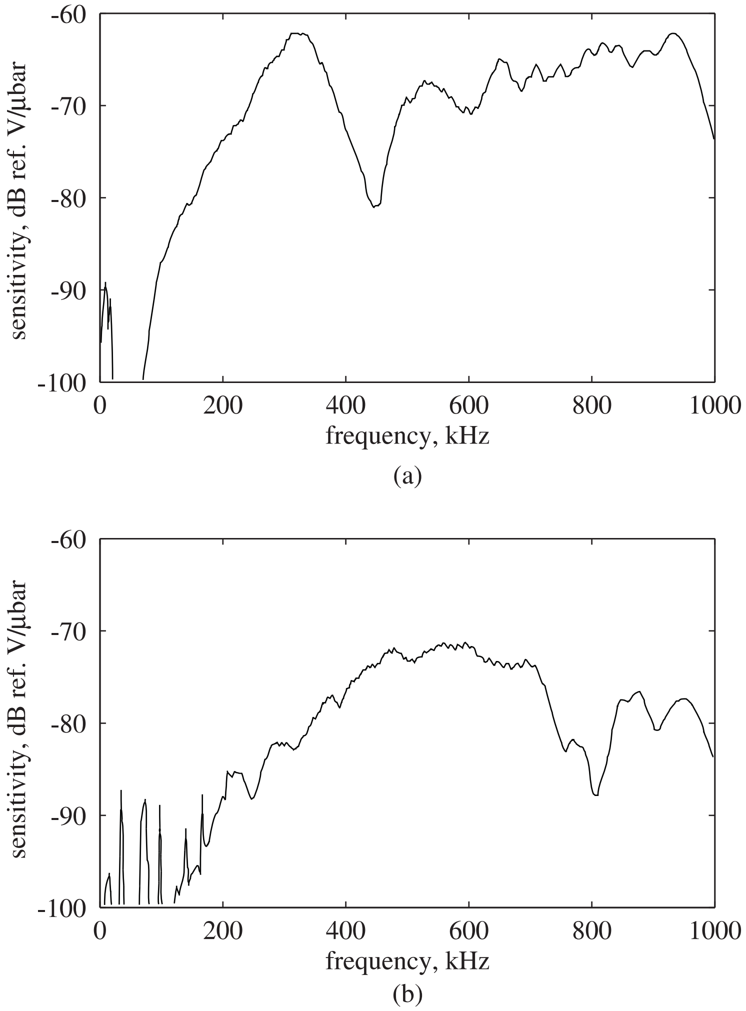

(a)

(b)

Figure 3.4: Frequency response calibration of AE transducers. (a) MICRO 80S. (b) PICO.

The two sensors were mounted at different locations (Figure 3.5) on the tool holder, and grease was used to couple the sensors to the surfaces of the tool holder. As shown in Figure 3.5, the PICO was mounted on the bottom surface of the tool holder, underneath the cutting tip, whereas the MICRO 80S was mounted at the rear of the tool holder.

The two sensor signals were then amplified and band-pass filtered with two 1220A preamplifiers from Physical Acoustics Corporation. The amplifier gain can be selected to be either 40 or 60 dB, and the band-pass filter operates in the 100–1200 kHz range. Furthermore, two electronic circuits, using integrated circuit AD536AJQ from Analog Devices (Figure D.1), were used to perform the on-line RMS computation of the AE signals, allowing the choice of two RMS time

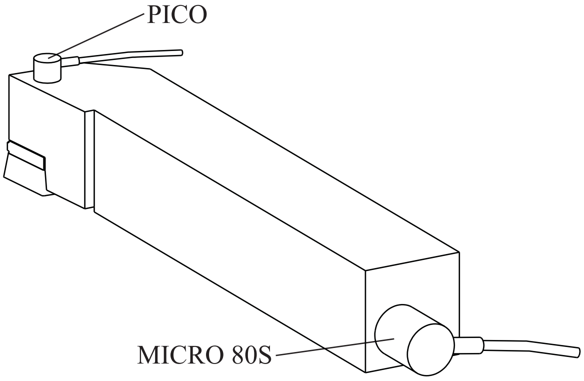

Figure 3.5: Position of AE sensors on tool holder (back-bottom view).

constants: 0.25 and 2.5 ms.

Cutting Force Measurement

For the measurement of the tangential force (F_X) and feed force (F_Y), two sets of four strain gauges were attached to the tool holder (Figure 3.6) and were arranged to form two full Wheatstone bridges[2] (Figure D.4). The strain gauges, model PP/350/PC11/A, were supplied by TSM and were bound to the tool holder with an heat curing adhesive (TSM300 adhesive kit).

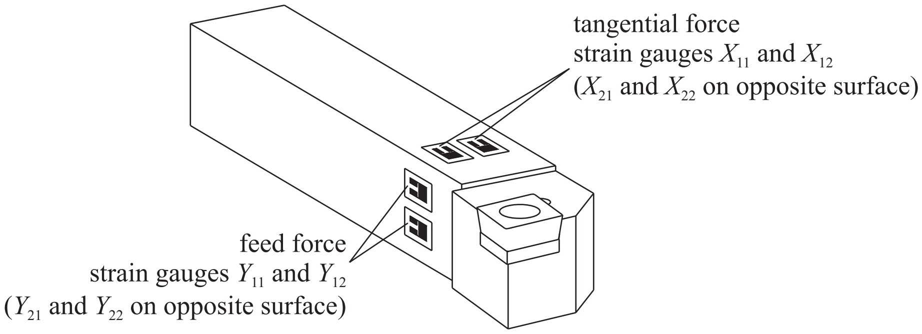

Figure 3.6: Position of strain gauges on tool holder (front-top view).

Two strain gauge amplifiers, using integrated circuit 846-171 and printed circuit board 435-692 from RS Components, were used to amplify the signals from both strain gauge bridges. Furthermore, two low-pass filters with a 10 kHz cut-off frequency (Figure D.3) were used to avoid aliasing.[3]

Static calibration of the output signals from both strain gauges was conducted by applying the gravitational forces of dead weights in the F_X and F_Y directions (Figure 3.7).

---

[2] Reference [1] can be consulted for more information on strain gauge dynamometry.

[3] All signals must be band-limited to less than half the sampling rate of the sampling system.

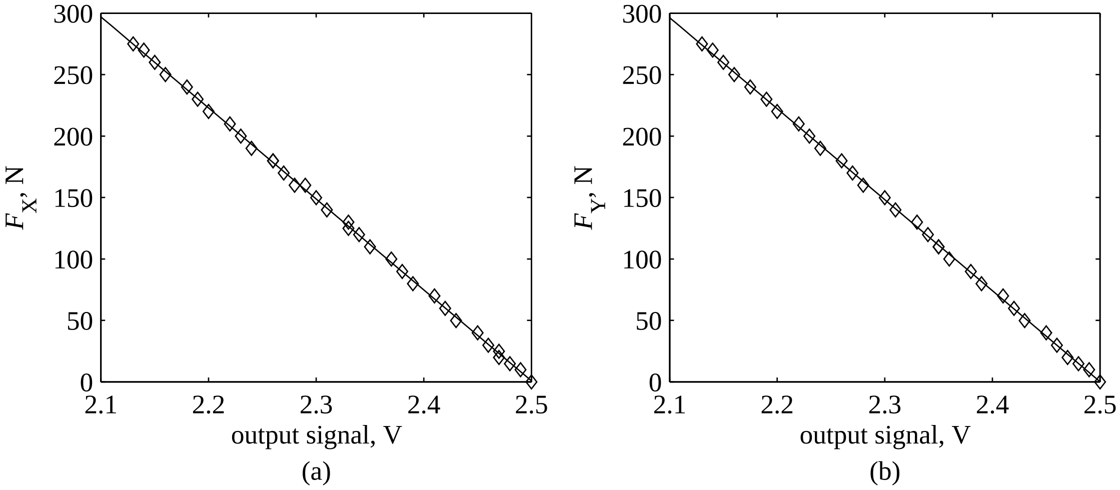

Figure 3.7: Calibration of cutting force signals. (a) Tangential force. (b) Feed force.

Vibration Measurement

An accelerometer from Kistler Instruments was used to monitor the vibrations from the cutting process. The accelerometor was an industrial model, type 8752A50, operating in the 0.6–5 kHz frequency range. Figure 3.8 shows the frequency response of the accelerometer as obtained from its calibration certificate.

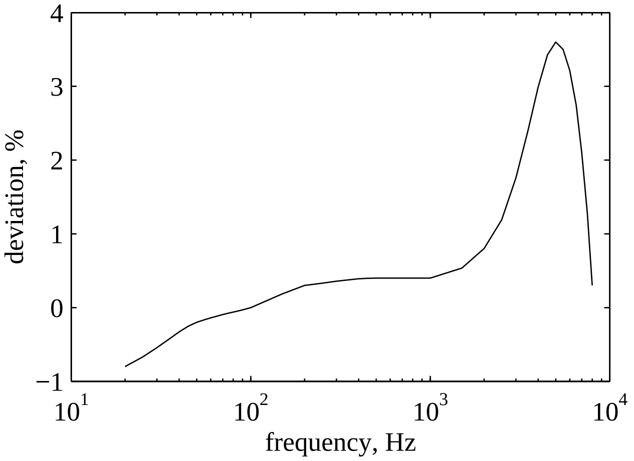

Figure 3.8: Frequency response of accelerometer.

A coupler, model 5108 from Kistler Instruments, was used to provide power to the accelerometer and read the signal from the sensor. The output from the coupler was then fed into a low-pass anti-aliasing filter with 8 kHz cut-off frequency (Figure D.3).

Temperature Measurement

In order to assess the temperatures near the cutting zone, two grooves were machined onto the opposite surfaces of the shim,[4] so that two thermocouples (thermocouples 1 and 2, 5 and 7 mm below the top of the cutting tool, respectively) could be installed under the nose of the cutting insert (Figure 3.9). The thermocouples, model 5TC-TT-K-36-36, type K, were firmly attached in the grooves with a CC high temperature cement (both products provided by OMEGA Engineering).

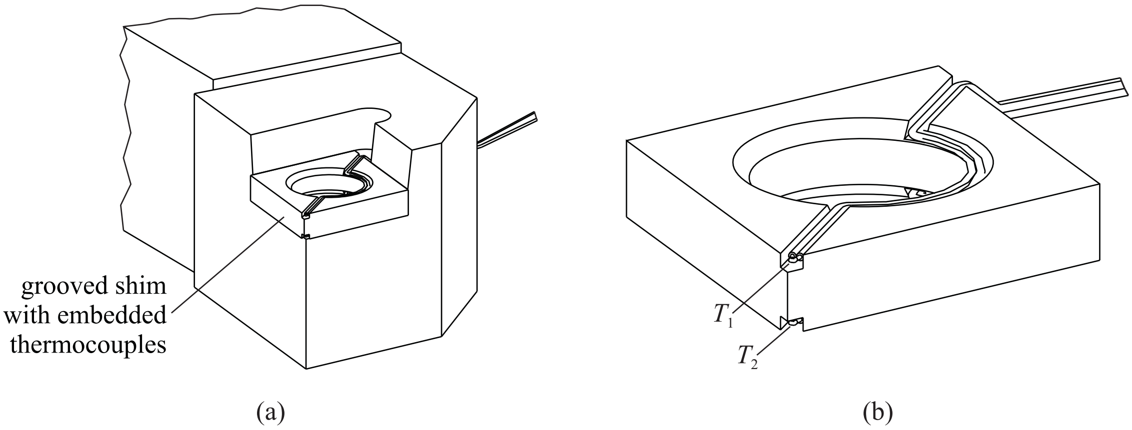

(a) (b)

Figure 3.9: Location of thermocouples. (a) View of tool holder and grooved shim without the cutting insert. (b) Shim and embedded thermocouples.

The thermocouple signals were amplified with the integrated circuit AD595AQ from Analog Devices (Figure D.2). The amplifier produced an output of 10 mV/°C. The temperatures measured with thermocouples 1 and 2 were named T_1 and T_2, respectively.

Data Acquisition System

For the acquisition and storage of data collected from the sensors described above, three acquisition boards were mounted into a personal computer:

AT-MIO-16H This 12-bit National Instruments board has a maximum of eight sampling channels available in differential mode and a maximum sampling rate of 100 kS/s.[5] This board was used to acquire the output signals from the two strain gauges, accelerometer, and AE from the RMS converter.

Lab-PC+ This 12-bit National Instruments board has a maximum of four channels in differential mode and a maximum sampling rate of 83 kS/s. This board was used to acquire the output signals from the two thermocouples.

---

[4] The shim is a plate placed between the tool and the insert.

[5] Unit S stands for number of samples.

CS1250 This 12-bit, two-channel board, supplied by Gage Applied Sciences, was used to acquire the raw AE signals. Although the sampling frequency can go as high as 50 MS/s, only rates of 5 and 10 MS/s were utilized.

3.2 Experimental Procedure

This section describes the experiments that were carried out in order to study the generation of AE from metal cutting. Two different types of experiments were accomplished: in the first type (Test A), the cutting conditions were varied over a wide range, and, in the second type (Test B), the workpieces were preheated before cutting.

3.2.1 Test A—Variation of Cutting Conditions and Materials

In this first set of tests, the variation of AE, cutting forces, vibration, and temperature were assessed for a wide range of cutting conditions and for the four work materials listed above (080A15, 080M40, 304S15, and 6082-T6). Table 3.1 shows the conditions used in the tests with varying cutting speed (V) and feed rate (t_1), and Table 3.2 shows the conditions used in the tests with varying width of cut (w).

From the output signals shown in Figure 3.3, only the following signals were used:

- Raw AE from MICRO 80S
- Tangential force
- Feed Force
- Accelerometer
- Thermocouple 1

A computer programme was produced in LabVIEW (computer package from National Instruments) to manage the acquisition of the various sensor signals into the computer (Figure 3.10). The AT-MIO-16H board was used to acquire sets of 16384 samples of the signals from the tangential force, feed force, and accelerometer at a sampling rate of 25 kS/s. The Lab-PC+ was used to acquire sets of 200 samples from the upper temperature sensor (T_1) at a sampling rate of 50 kS/s. The CS1250 board was used to acquire sets of 8388608 samples from the AE sensor at a sampling rate of 10 MS/s. The acquisition of both AT-MIO-16H and CS1250 boards was initiated at exactly the same instant, since the commencement of the acquisitions was triggered by means of a common electrical impulse. For each of the four work materials, each cutting condition was run at least twice, during which three sequential sets of readings were acquired. The results from Test A are presented in Section 4.1.

Table 3.1: Variation of cutting speed and feed rate for constant width of cut.

test	V, m/min	t_1, mm/rev	w, mm
1	75	0.01	1.2
2	75	0.02	1.2
3	75	0.04	1.2
4	75	0.06	1.2
5	75	0.1	1.2
6	75	0.2	1.2
7	200	0.01	1.2
8	200	0.02	1.2
9	200	0.04	1.2
10	200	0.06	1.2
11	200	0.1	1.2
12	200	0.2	1.2
13	50	0.02	1.2
14	100	0.02	1.2
15	150	0.02	1.2
16	300	0.02	1.2
17	50	0.1	1.2
18	100	0.1	1.2
19	150	0.1	1.2
20	300	0.1	1.2

Table 3.2: Variation of width of cut for constant cutting speed and feed rate.

test	V, m/min	t_1, mm/rev	w, mm
1	75	0.02	0.1
2	75	0.02	0.3
3	75	0.02	0.6
4	75	0.02	2.4
5	75	0.1	0.1
6	75	0.1	0.3
7	75	0.1	0.6
8	75	0.1	2.4
9	200	0.02	0.1
10	200	0.02	0.3
11	200	0.02	0.6
12	200	0.02	2.4
13	200	0.1	0.1
14	200	0.1	0.3
15	200	0.1	0.6
16	200	0.1	2.4

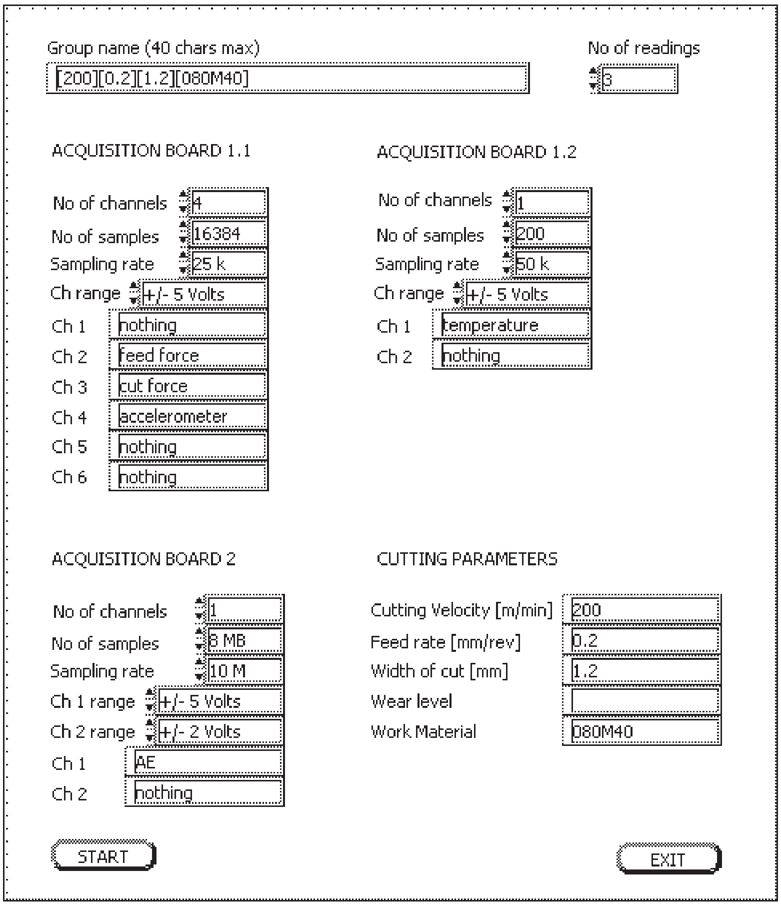
Group name (40 chars max)
[200][0.2][1.2][080M40]
No of readings
3

ACQUISITION BOARD 1.1
No of channels 4
No of samples 16384
Sampling rate 25 k
Ch range +/- 5 Volts
Ch 1 nothing
Ch 2 feed force
Ch 3 cut force
Ch 4 accelerometer
Ch 5 nothing
Ch 6 nothing

ACQUISITION BOARD 1.2
No of channels 1
No of samples 200
Sampling rate 50 k
Ch range +/- 5 Volts
Ch 1 temperature
Ch 2 nothing

ACQUISITION BOARD 2
No of channels 1
No of samples 8 MB
Sampling rate 10 M
Ch 1 range +/- 5 Volts
Ch 2 range +/- 2 Volts
Ch 1 AE
Ch 2 nothing

CUTTING PARAMETERS
Cutting Velocity [m/min] 200
Feed rate [mm/rev] 0.2
Width of cut [mm] 1.2
Wear level
Work Material 080M40

Figure 3.10: Screen shot of acquisition programme used in Test A.

3.2.2 Test B—Preset Workpiece Temperature

The aim of these tests was to observe the variation of AE with cutting temperature. The work material was firstly preheated in an oven up to a temperature of approximately 500°C. Thereafter, the material was rapidly removed from the furnace, placed in the turning machine, the temperature of the workpiece surface (T_{WS}) was measured with a handheld thermocouple, and the machining test was immediately initiated. This procedure was repeated for different values of T_{WS}, as the workpiece was allowed to cool down between tests. Two 080A15 workpieces were prepared for testing with cutting speeds of 200 and 75 m/min, whereas the remaining work materials (080M40, 304S15, and 6082-T6) were tested only for speeds of 200 m/min. For all tests, the feed rate and width of cut were set to 0.1 mm/rev and 1.2 mm, respectively. Tables 3.3–3.6 show the different initial temperatures from the handheld thermocouple measured before each test.

From the output signals shown in Figure 3.3, the following signals were used:

- Raw AE from MICRO 80S
- Raw AE from PICO

Table 3.3: Preset workpiece temperature tests for the 080A15.

75 m/min		200 m/min	
test	T_{WS}, °C	test	T_{WS}, °C
1	212	1	284
2	148	2	194
3	162	3	141
4	146	4	120
5	127	5	95
6	122	6	83
7	107	7	82
8	94	8	72

Table 3.4: Preset workpiece temperature tests for the 080M40.

test	T_{WS}, °C
1	256
2	235
3	218
4	185
5	163
6	156
7	142
8	125
9	122
10	115
11	96
12	99
13	88
14	85
15	80
16	75
17	31

- RMS of AE from PICO
- Tangential force
- Feed Force
- Accelerometer
- Thermocouple 1
- Thermocouple 2

As the raw AE signals were detected with two sensors (MICRO 80S and PICO) positioned at

Table 3.5: Preset workpiece temperature tests for the 304S15.

test	T_{WS}, °C
1	303
2	283
3	230
4	238
5	222
6	160
7	160
8	117
9	91
10	93
11	83
12	83
13	75
14	31

Table 3.6: Preset workpiece temperature tests for the 6082-T6.

test	T_{WS}, °C
1	213
2	163
3	130
4	99
5	83
6	88
7	78
8	75
9	71
10	57
11	53
12	31

different locations (Figure 3.5), it was also possible to analyse the difference in the AE emissions arriving at different locations and detected with two different AE sensors.

Another computer programme was written in LabVIEW to manage the acquisition of the various sensors into the computer (Figure 3.11). The AT-MIO-16H board was used to acquire the RMS of AE, the two cutting forces, and the accelerometer signals in a continuous process at a sampling rate of 25 kS/s. During this process, at every 500 ms, the CS1250 board was used to acquire sets of 65536 samples from the two raw AE signals at a sampling rate of 5 MS/s. Also, at every 500 ms, the Lab-PC+ was used to acquire 100 samples from the thermocouple signals at a sampling rate of 20 kS/s. The results from Test B are shown in Section 4.2.

Other two types of experiments, using the same acquisition program and the same sensor

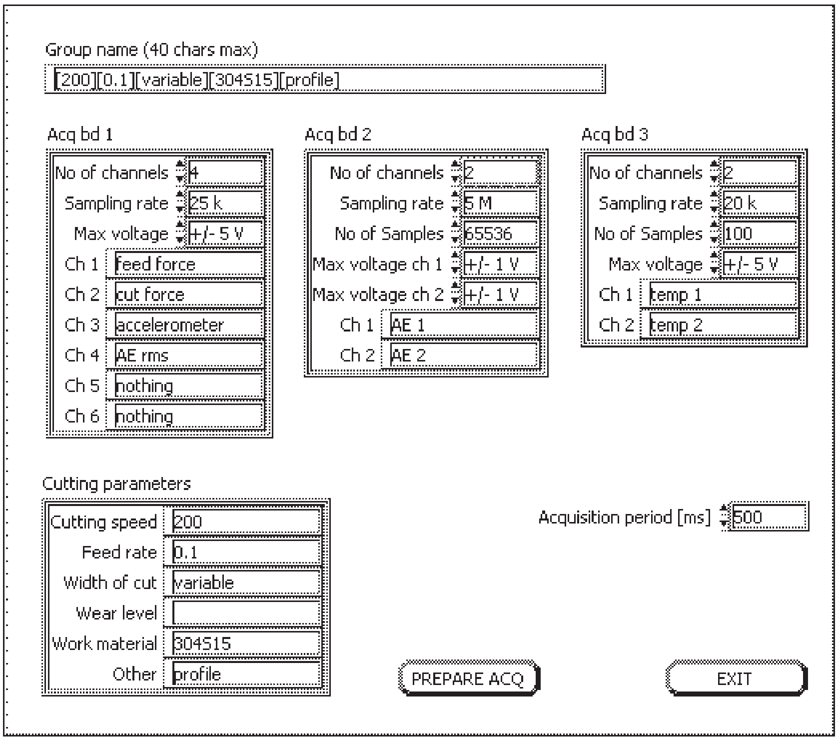

Group name (40 chars max)

[200][0.1][variable][304S15][profile]

Acq bd 1

No of channels	4
Sampling rate	25 k
Max voltage	+/- 5 V
Ch 1	feed force
Ch 2	cut force
Ch 3	accelerometer
Ch 4	AE rms
Ch 5	nothing
Ch 6	nothing

Acq bd 2

No of channels	2
Sampling rate	5 M
No of Samples	65536
Max voltage ch 1	+/- 1 V
Max voltage ch 2	+/- 1 V
Ch 1	AE 1
Ch 2	AE 2

Acq bd 3

No of channels	2
Sampling rate	20 k
No of Samples	100
Max voltage	+/- 5 V
Ch 1	temp 1
Ch 2	temp 2

Cutting parameters

Cutting speed	200
Feed rate	0.1
Width of cut	variable
Wear level	
Work material	304S15
Other	profile

Acquisition period [ms] 500

Figure 3.11: Screen shot of acquisition programme used in Test B.

signals as Test B, were performed: feed rate variation and width of cut variation tests. In the first case, the feed rate was varied quasi-continuously from 0.24 mm/rev down to a very low value of 0.005 mm/rev and then increased again to the initial value. For the width of cut variation tests, the width of cut was varied linearly from 3 to 0 mm and also reversely from 0 to 3 mm. The aim of these tests was to study the generation of AE when both feed rate and width of cut vary continuously and assume very low values. However, as the results from these two types of tests were observed to be quite affected by random noise signals, these results are not shown in Chapter 4, but a small discussion on these results is presented in Section 5.1.3.

Chapter 4

Experimental Results

In this chapter, the results obtained from the two sets of experiments (Tests A and B) described in Section 3.2 are presented. The raw data from the various sensors, acquired with the three acquisition boards and stored in the personal computer, were processed with computer programs produced with MATLAB (software from The MathWorks).

4.1 Test A—Variation of Cutting Conditions and Materials

This section presents the resultant cutting forces, measured temperatures, and acoustic emission (AE) signals generated during the cutting tests described in Section 3.2.1 for the cutting conditions shown in Tables 3.1 and 3.2 and for the four work materials 080A15, 080M40, 304S15, and 6082-T6. The first part is dedicated to the cutting force results; the second part shows the temperature results from the upper embedded thermocouple; whereas the third part is dedicated to both energy and frequency characteristics of the AE emissions.

4.1.1 Cutting Forces

The plots shown in Figures 4.1–4.6 present the variation of the tangential force (F_X) and feed force (F_Y) for different cutting conditions and work materials. Since, for a given work material and cutting condition, each test was repeated at least twice, where three readings of 16384 samples where acquired, resulting in a minimum of six readings, the following data processing technique was conducted: for each of the six readings, the mean of each 16384 samples was firstly computed; afterwards, the mean of the means of the six readings was calculated, representing each point shown on the plots (the length of the error bars represents two standard deviations).

Figure 4.1 shows the variation of F_X and F_Y with cutting speed (V) for feed rates (t_1) of 0.02 and 0.1 mm/rev and constant width of cut ($w = 1.2$ mm). It can be observe that, in most cases, both cutting forces F_X and F_Y decrease slightly with increasing V. It can also be observed that the tangential force F_X is always higher than the feed force F_Y. However, since these trends were not consistent for all tested conditions, each plot is described separately. The description of the variation of the cutting forces with V for $t_1 = 0.02$ mm/rev and for the four work materials is described next:

080A15 (Figure 4.1a) F_X and F_Y appear to remain roughly constant for speeds higher than 100 m/min. However, between 75 and 100 m/min, both F_X and F_Y exhibit an abrupt increase in amplitude.

080M40 (Figure 4.1c) Although, F_X remains approximately constant, F_Y shows an increase with increasing V, contradicting the general trend observed in the other cases. However, the data is reasonably scattered.

304S15 (Figure 4.1e) Both cutting forces appear to decrease slightly with increasing V, although the data is very scattered.

6082-T6 (Figure 4.1g) Both F_X and F_Y appear to decrease with increasing V. However, between 75 and 100 m/min, a small increase in both cutting forces is observed. Above 200 m/min an increase in F_Y is also observed.

Next, the variation of the cutting forces with V for $t_1 = 0.1$ mm/rev is described:

080A15 (Figure 4.1b) F_X and F_Y appear to increase in the 50–75 m/min speed range, to decrease between 75 and 150 m/min, and to remain more or less constant above 150 m/min.

080M40 (Figure 4.1d) F_X and F_Y are observed to rapidly increase in the 50–75 m/min speed range and then to decrease smoothly above 75 m/min.

304S15 (Figure 4.1f) Both cutting forces are observed to decrease with increasing V.

6082-T6 (Figure 4.1h) Both cutting forces are observed to decrease with increasing V, although, between 75 and 100 m/min, a small increase is observed.

Figure 4.2 shows the variation of the cutting forces with t_1 for $V = 75$ and 200 m/min, and $w = 1.2$ mm. Both cutting forces are observed to increase strongly with increasing t_1. The relationship between F_X and t_1 can be represented by a straight line with positive slope and a quasi-zero intercept. However, it can be observed that, in same cases, at high feed rates, the slope of the relationship between F_X and t_1 lowers with increasing t_1, which is most visible in Figures 4.2a and 4.2b. In all cases, F_Y is observed to increase with t_1, although its rate of increase decreases for higher t_1 values. Moreover, it can also be observed that F_X is 1.25–2 times higher than F_Y.

Figures 4.3–4.6 show the variation of the cutting forces with w for four different combinations of V (75 and 200 m/min) and t_1 (0.02 and 0.1 mm/rev). For all combinations of V and t_1, it can be concluded that the relationship between both cutting forces and w falls very closely on a straight line with positive slope, i.e. F_X and F_Y are almost directly proportional to w.

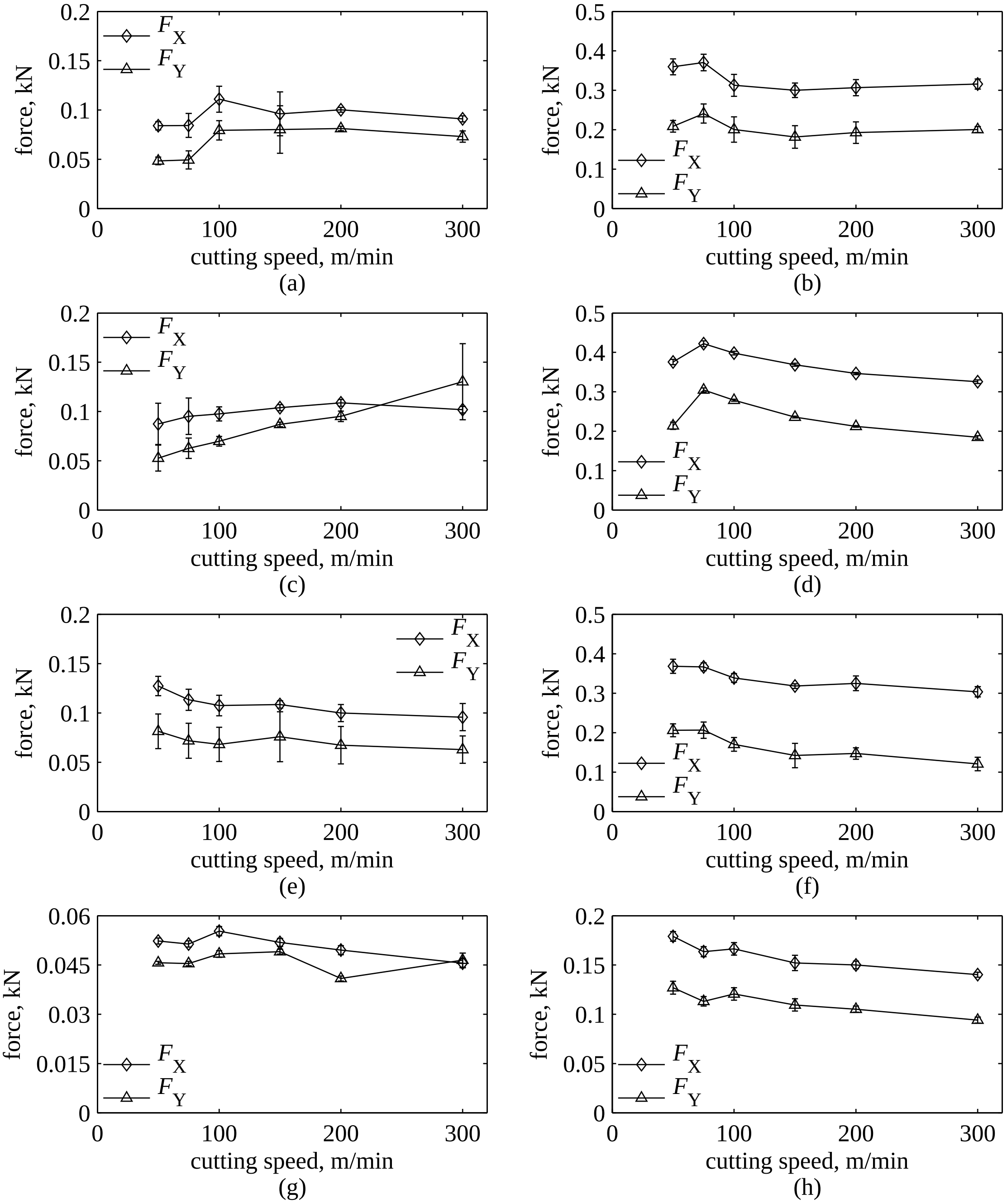

Figure 4.1: Variation of cutting forces with cutting speed. (a) 080A15, $t_1 = 0.02$ mm/rev. (b) 080A15, $t_1 = 0.1$ mm/rev. (c) 080M40, $t_1 = 0.02$ mm/rev. (d) 080M40, $t_1 = 0.1$ mm/rev. (e) 304S15, $t_1 = 0.02$ mm/rev. (f) 304S15, $t_1 = 0.1$ mm/rev. (g) 6082-T6, $t_1 = 0.02$ mm/rev. (h) 6082-T6, $t_1 = 0.1$ mm/rev.

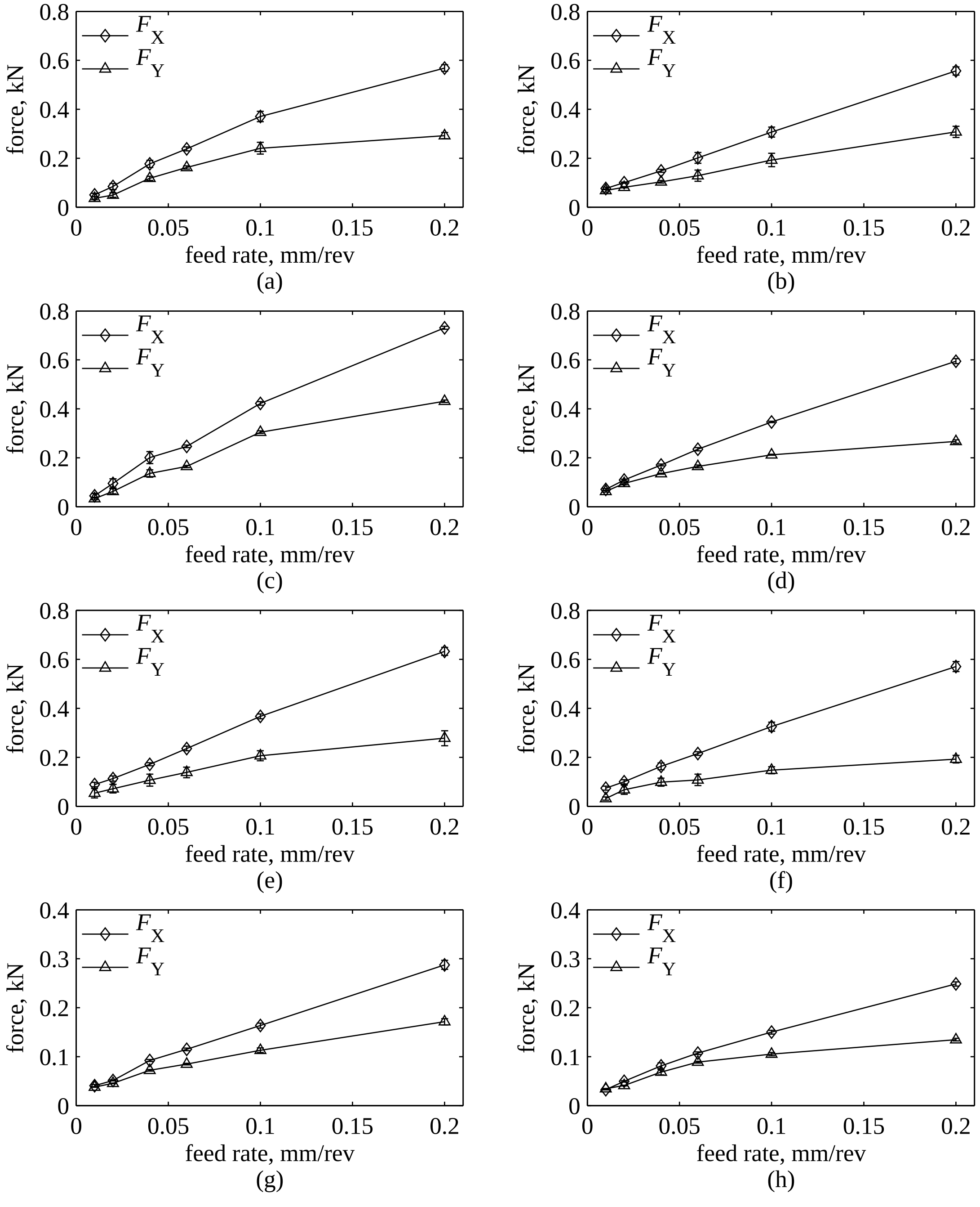

Figure 4.2: Variation of cutting forces with feed rate. (a) 080A15, $V = 75$ m/min. (b) 080A15, $V = 200$ m/min. (c) 080M40, $V = 75$ m/min. (d) 080M40, $V = 200$ m/min. (e) 304S15, $V = 75$ m/min. (f) 304S15, $V = 200$ m/min. (g) 6082-T6, $V = 75$ m/min. (h) 6082-T6, $V = 200$ m/min.

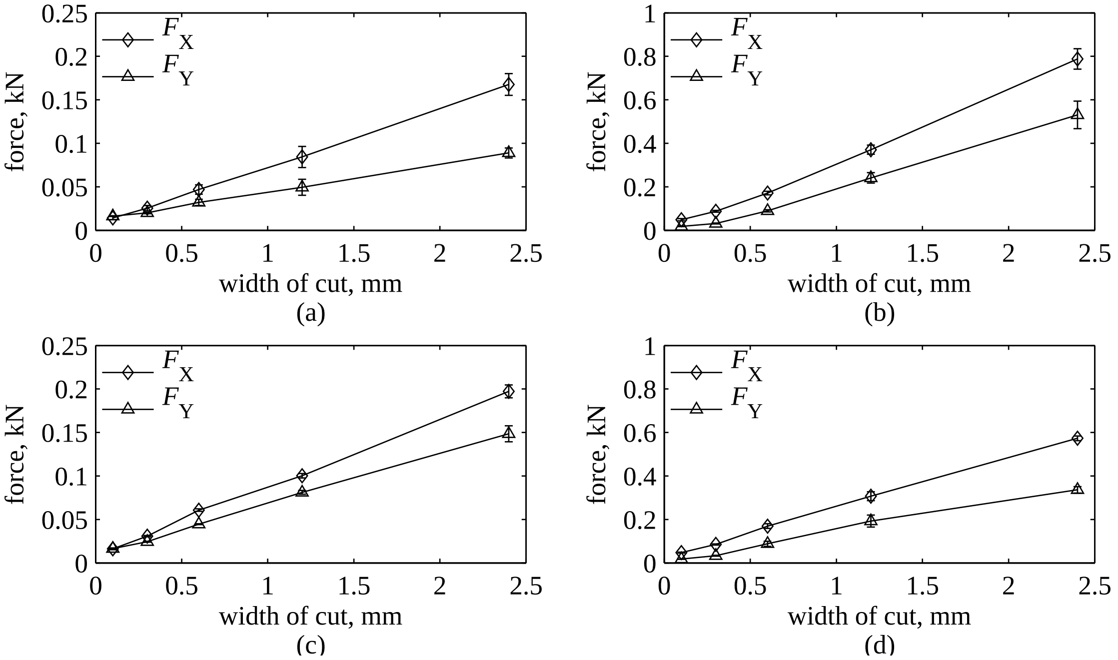

Figure 4.3: Variation of cutting forces with width of cut; work material 080A15. (a) $V = 75$ m/min, $t_1 = 0.02$ mm/rev. (b) $V = 75$ m/min, $t_1 = 0.1$ mm/rev. (c) $V = 200$ m/min, $t_1 = 0.02$ mm/rev. (d) $V = 200$ m/min, $t_1 = 0.1$ mm/rev.

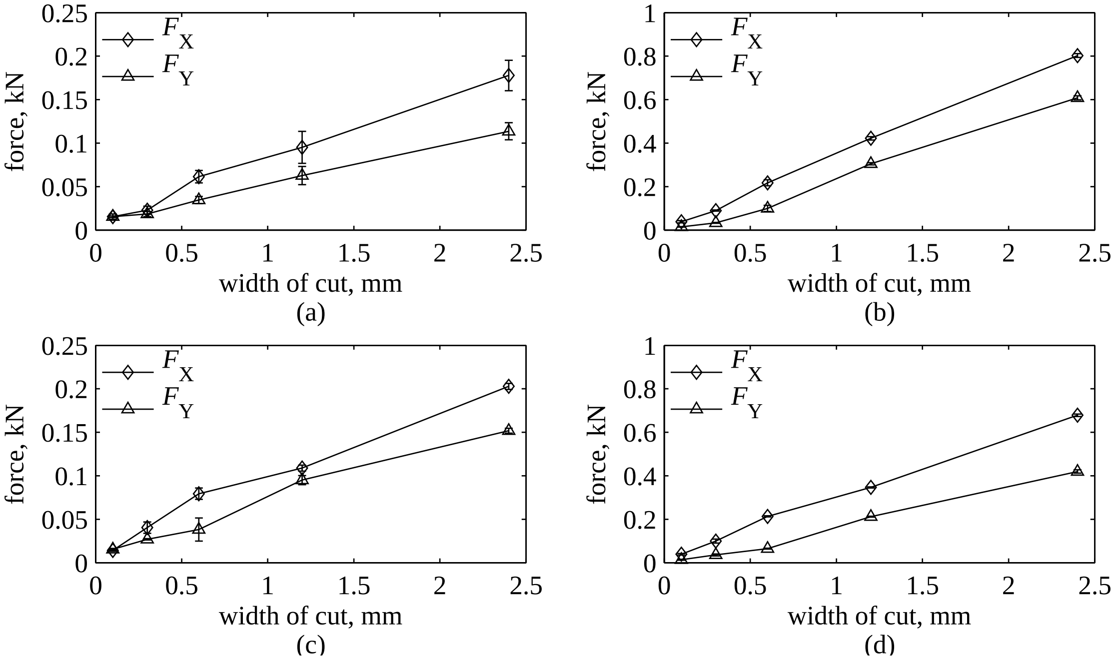

Figure 4.4: Variation of cutting forces with width of cut; work material 080M40. (a) $V = 75$ m/min, $t_1 = 0.02$ mm/rev. (b) $V = 75$ m/min, $t_1 = 0.1$ mm/rev. (c) $V = 200$ m/min, $t_1 = 0.02$ mm/rev. (d) $V = 200$ m/min, $t_1 = 0.1$ mm/rev.

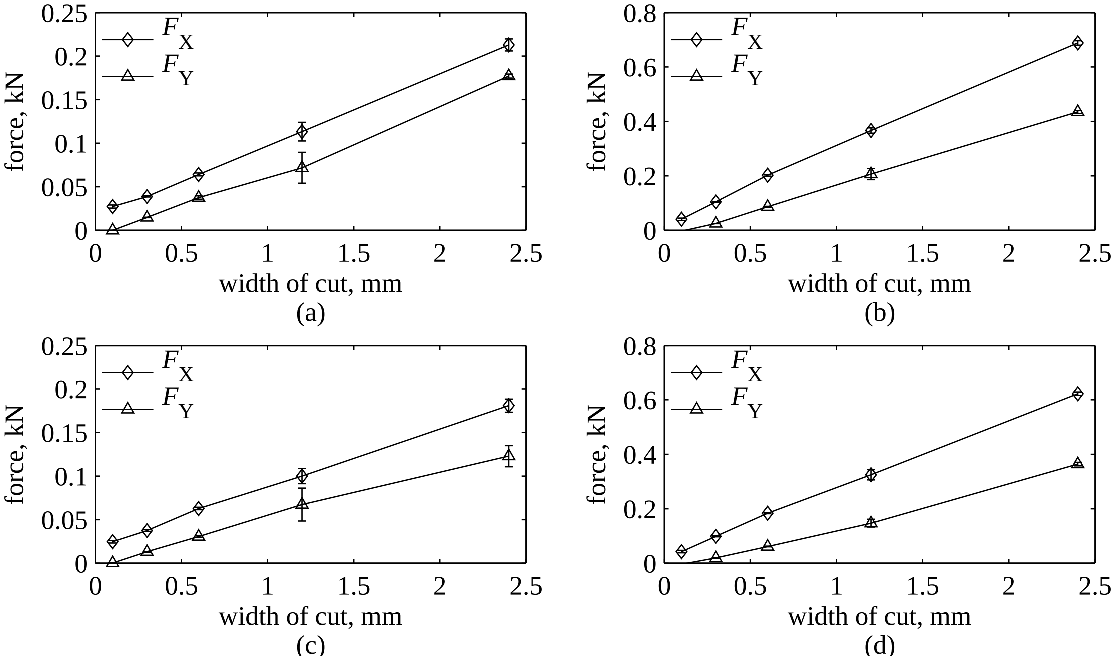

Figure 4.5: Variation of cutting forces with width of cut; work material 304S15. (a) $V = 75$ m/min, $t_1 = 0.02$ mm/rev. (b) $V = 75$ m/min, $t_1 = 0.1$ mm/rev. (c) $V = 200$ m/min, $t_1 = 0.02$ mm/rev. (d) $V = 200$ m/min, $t_1 = 0.1$ mm/rev.

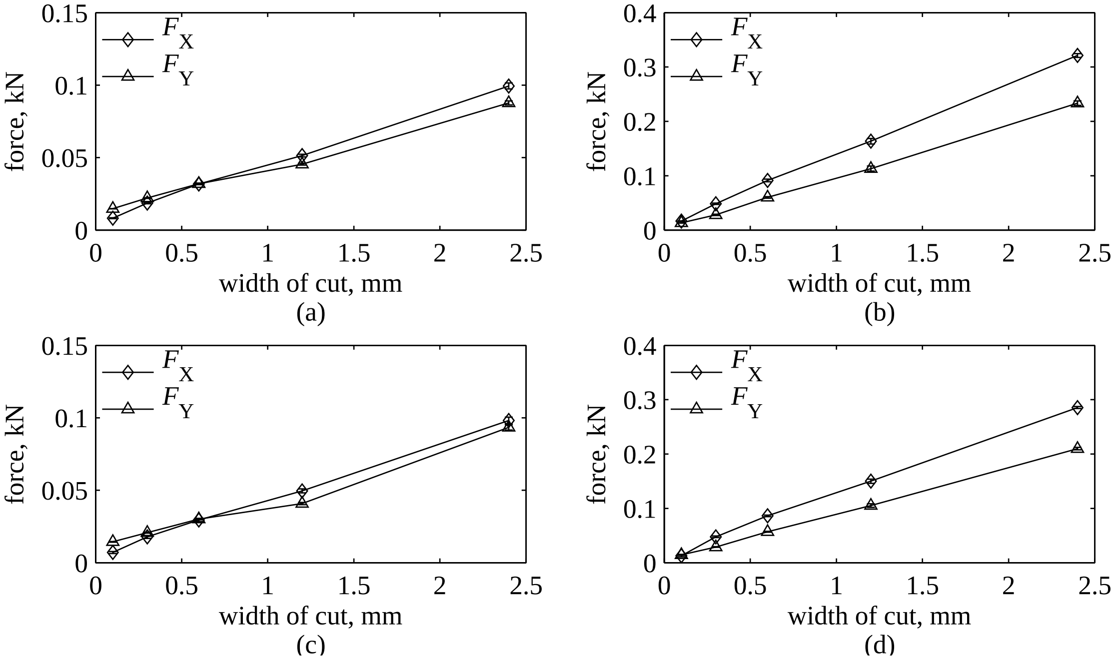

Figure 4.6: Variation of cutting forces with width of cut; work material 6082-T6. (a) $V = 75$ m/min, $t_1 = 0.02$ mm/rev. (b) $V = 75$ m/min, $t_1 = 0.1$ mm/rev. (c) $V = 200$ m/min, $t_1 = 0.02$ mm/rev. (d) $V = 200$ m/min, $t_1 = 0.1$ mm/rev.

4.1.2 Temperature

The plots shown in Figures 4.7–4.12 show the temperature variation measured by thermocouple T_1 for different cutting conditions and work materials, as described in Section 3.2.1. For each cutting condition and work material, each test was conducted at least twice, during which three reading of 200 samples were acquired, resulting in a minimum of six readings. Subsequently, each set of 200 samples was divided into 20 sets of 10 samples, and the mean of each set of 10 samples was computed, resulting in a minimum of 60 mean values. The temperature was taken as the maximum value found among these 60 mean values.

Figure 4.7 shows the variation of T_1 with V for $t_1 = 0.02$ and 0.1 mm/rev, and $w = 1.2$ mm. It can be observed that, generally, T_1 increases slightly with V; however, since this trend is not observed for all conditions, each case is described individually. When $t_1 = 0.02$ mm/rev:

080A15 (Figure 4.7a) Temperature T_1 increases with V up to 150 m/min, above which T_1 becomes constant with further increase of V.

080M40 (Figure 4.1c) Temperature T_1 increases more or less linearly with V.

304S15 (Figure 4.1e) Temperature T_1 remains more or less constant with varying V.

6082-T6 (Figure 4.1g) Temperature T_1 remains more or less constant with varying V.

When $t_1 = 0.1$ mm/rev:

080A15 (Figure 4.7b) Temperature T_1 increases with V up to 75 m/min, above which T_1 becomes constant with further increase of V.

080M40 (Figure 4.1d) Temperature T_1 increases with V up to 100 m/min, above which T_1 becomes constant with further increase of V.

304S15 (Figure 4.1f) Temperature T_1 remains more or less constant with varying V.

6082-T6 (Figure 4.1h) Temperature T_1 increases with V up to 100 m/min, above which T_1 becomes constant with further increase of V.

Figure 4.8 shows the variation of T_1 with t_1 for $V = 75$ and 200 m/min, and $w = 1.2$ mm. Generally, T_1 is observed to increase more or less linearly with increasing t_1.

Figures 4.9–4.12 show, for four different combinations of V (75 and 200 m/min) and t_1 (0.02 and 0.1 mm/rev), the variation of T_1 with w. In most cases, T_1 can be observed to increase linearly with w. However, exceptions can be observed for work material 080M40: when $V = 75$ m/min and $t_1 = 0.02$ mm/rev (Figure 4.10a), $V = 200$ m/min and $t_1 = 0.02$ mm/rev (Figure 4.10c), and $V = 200$ m/min and $t_1 = 0.1$ mm/rev (Figure 4.10d), T_1 increases quite considerably with w bellow $w = 0.6$ mm, above which T_1 increases with w with a lower rate of increase.

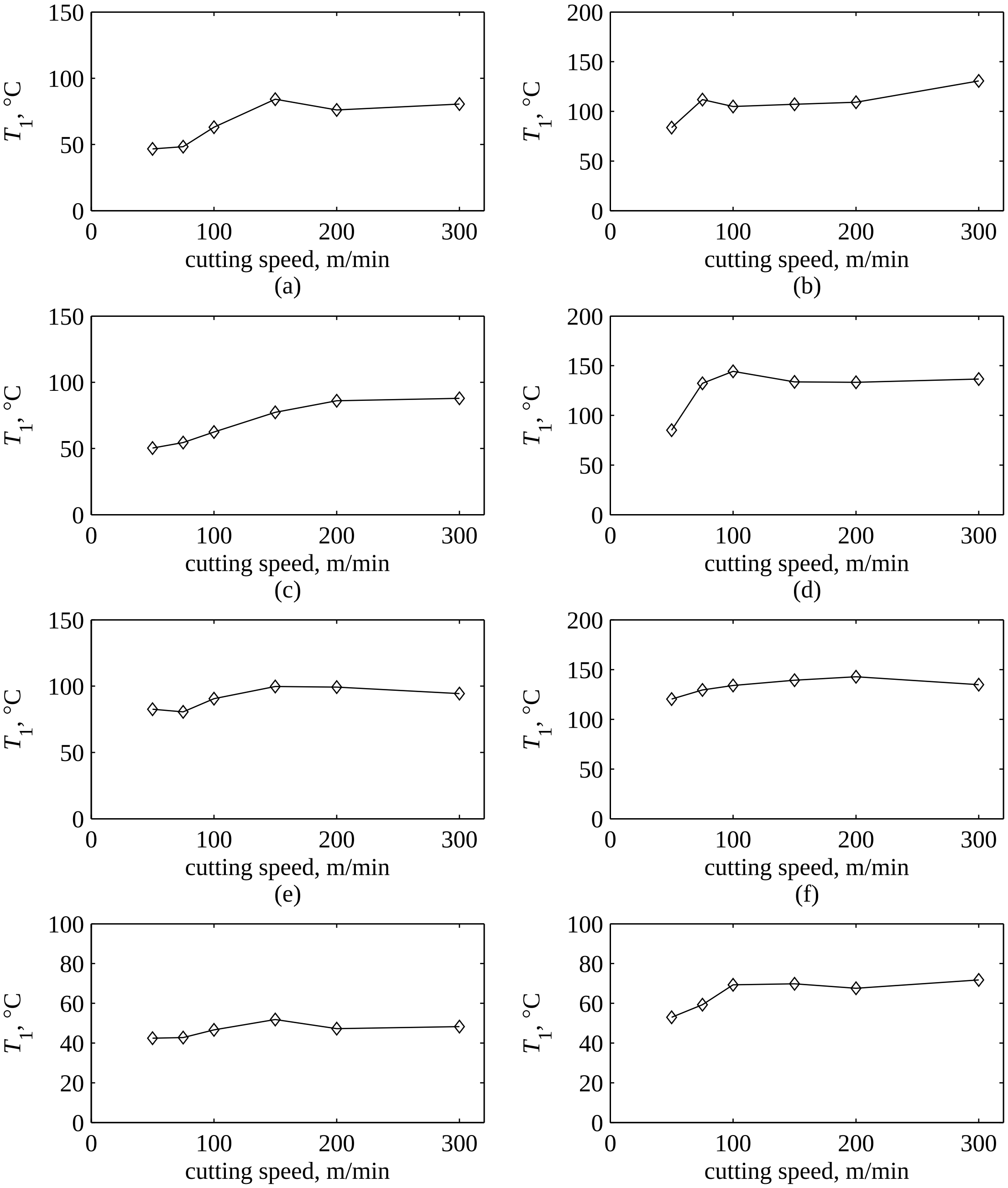

(a) (b) (c) (d) (e) (f) (g) (h)

Figure 4.7: Variation of temperature T_1 with cutting speed. (a) 080A15, $t_1 = 0.02$ mm/rev. (b) 080A15, $t_1 = 0.1$ mm/rev. (c) 080M40, $t_1 = 0.02$ mm/rev. (d) 080M40, $t_1 = 0.1$ mm/rev. (e) 304S15, $t_1 = 0.02$ mm/rev. (f) 304S15, $t_1 = 0.1$ mm/rev. (g) 6082-T6, $t_1 = 0.02$ mm/rev. (h) 6082-T6, $t_1 = 0.1$ mm/rev.

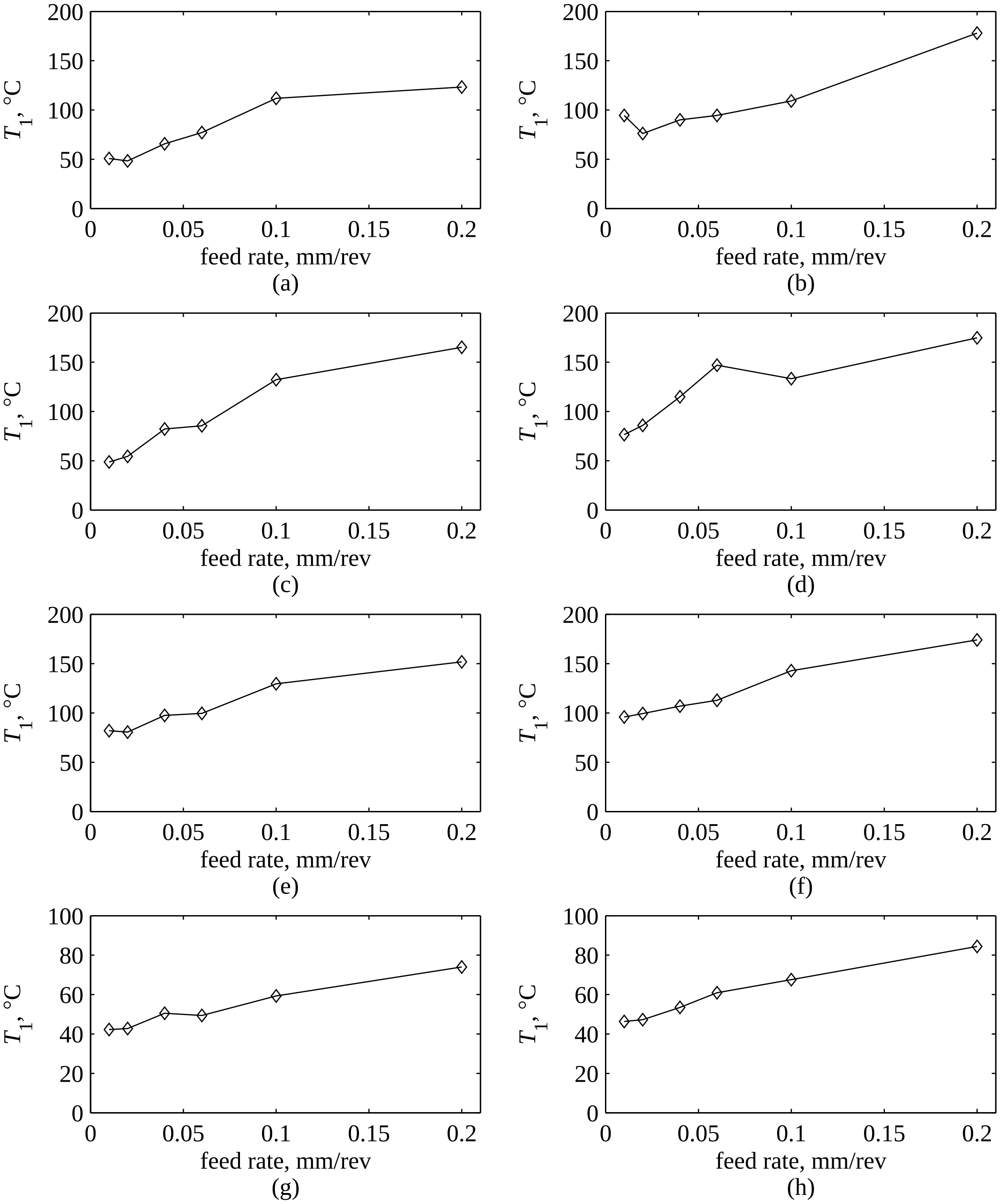

Figure 4.8: Variation of temperature T_1 with feed rate. (a) 080A15, $V = 75$ m/min. (b) 080A15, $V = 200$ m/min. (c) 080M40, $V = 75$ m/min. (d) 080M40, $V = 200$ m/min. (e) 304S15, $V = 75$ m/min. (f) 304S15, $V = 200$ m/min. (g) 6082-T6, $V = 75$ m/min. (h) 6082-T6, $V = 200$ m/min.

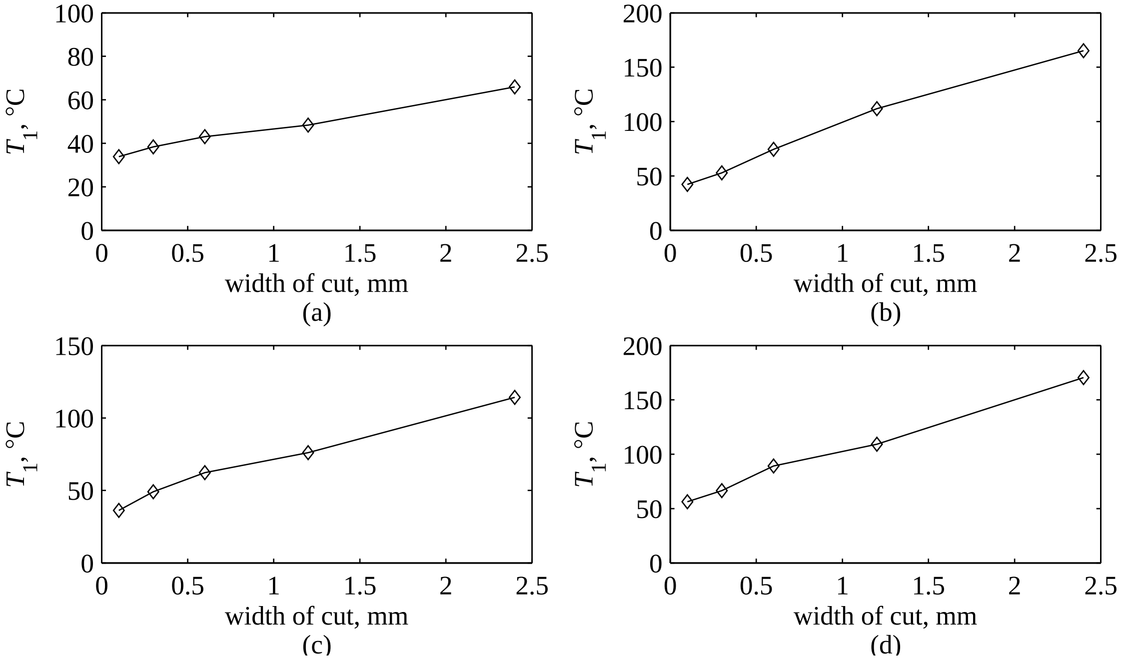

Figure 4.9: Variation of temperature T_1 with width of cut; work material 080A15. (a) $V = 75$ m/min, $t_1 = 0.02$ mm/rev. (b) $V = 75$ m/min, $t_1 = 0.1$ mm/rev. (c) $V = 200$ m/min, $t_1 = 0.02$ mm/rev. (d) $V = 200$ m/min, $t_1 = 0.1$ mm/rev.

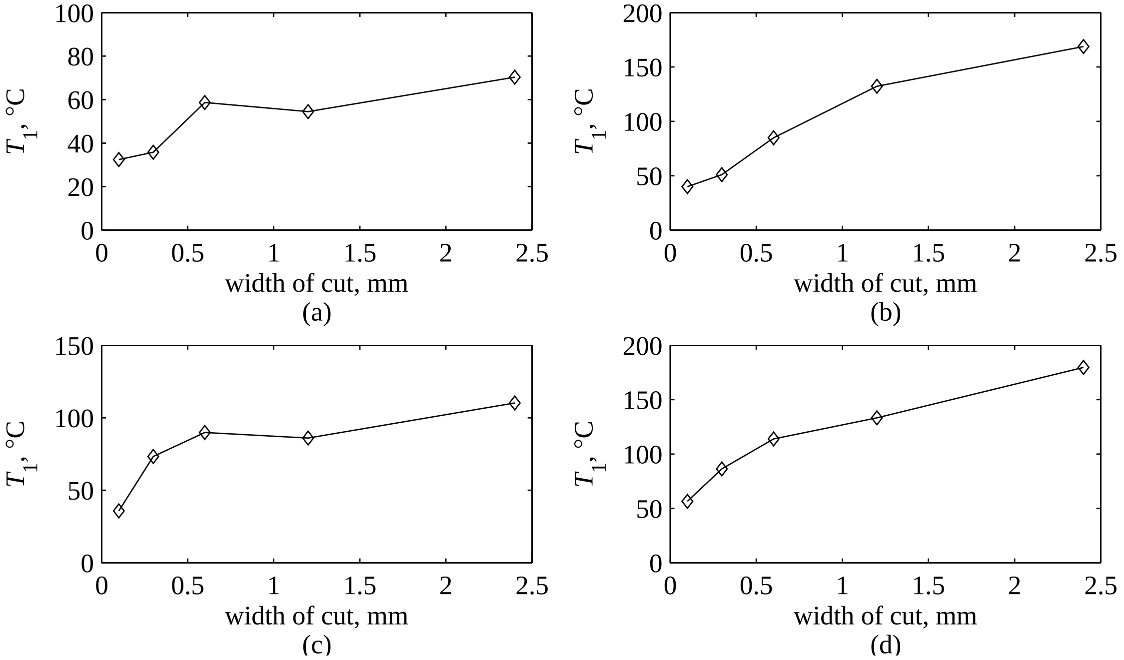

Figure 4.10: Variation of temperature T_1 with width of cut; work material 080M40. (a) $V = 75$ m/min, $t_1 = 0.02$ mm/rev. (b) $V = 75$ m/min, $t_1 = 0.1$ mm/rev. (c) $V = 200$ m/min, $t_1 = 0.02$ mm/rev. (d) $V = 200$ m/min, $t_1 = 0.1$ mm/rev.

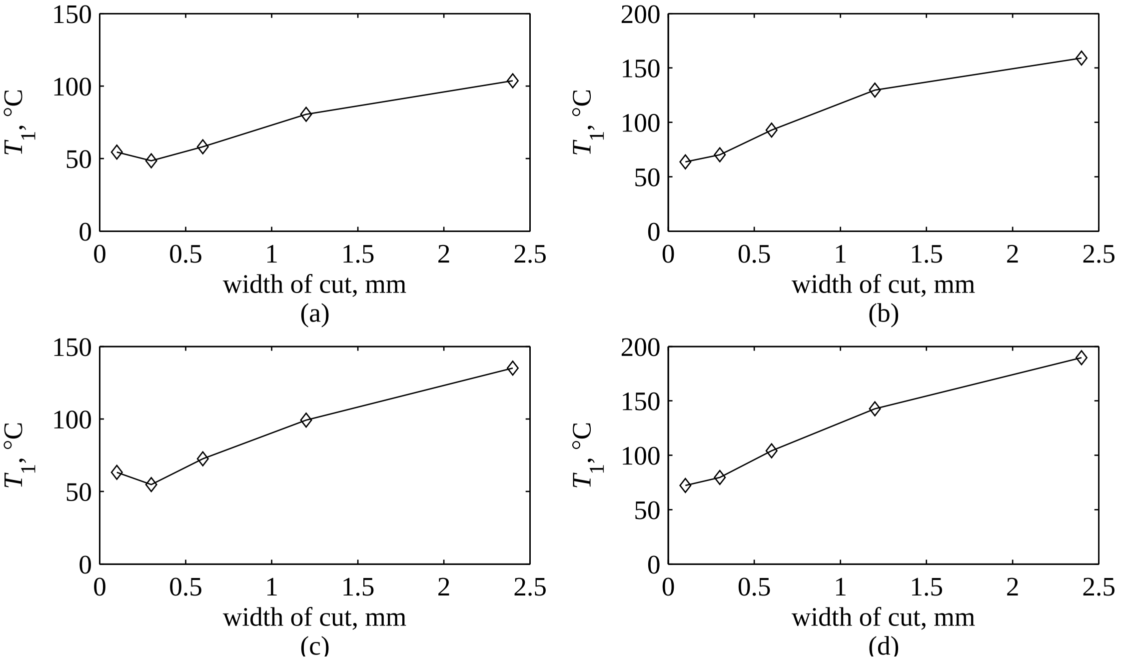

Figure 4.11: Variation of temperature T_1 with width of cut; work material 304S15. (a) $V = 75$ m/min, $t_1 = 0.02$ mm/rev. (b) $V = 75$ m/min, $t_1 = 0.1$ mm/rev. (c) $V = 200$ m/min, $t_1 = 0.02$ mm/rev. (d) $V = 200$ m/min, $t_1 = 0.1$ mm/rev.

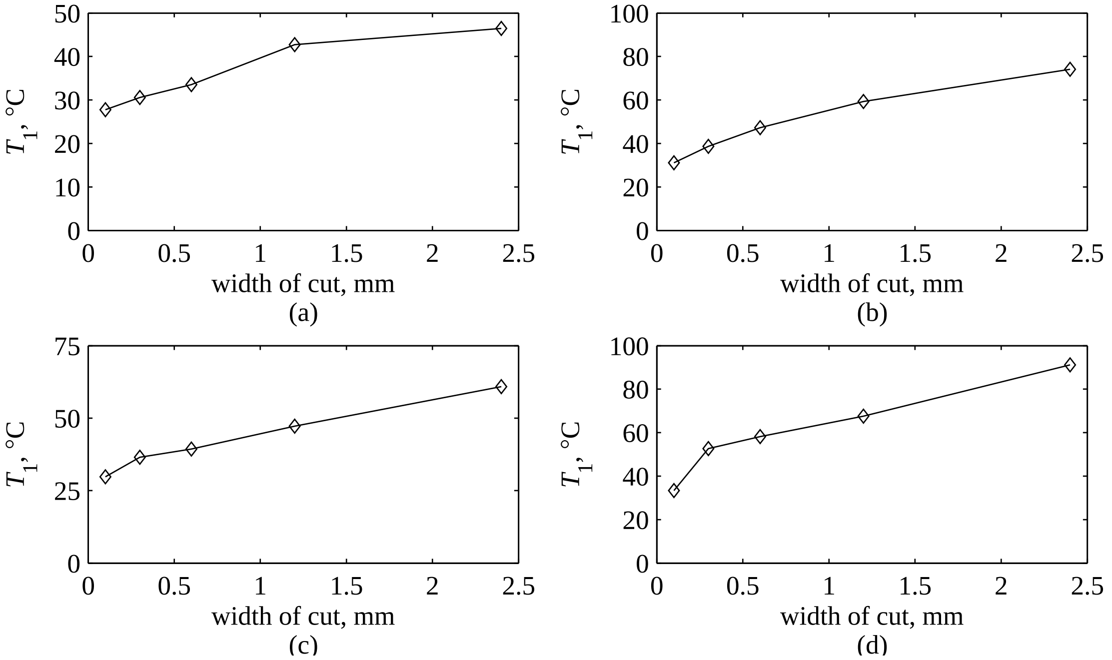

Figure 4.12: Variation of temperature T_1 with width of cut; work material 6082-T6. (a) $V = 75$ m/min, $t_1 = 0.02$ mm/rev. (b) $V = 75$ m/min, $t_1 = 0.1$ mm/rev. (c) $V = 200$ m/min, $t_1 = 0.02$ mm/rev. (d) $V = 200$ m/min, $t_1 = 0.1$ mm/rev.

4.1.3 Acoustic Emission

The plots shown in Figures 4.16–4.21 show the variation of the energy and frequency content of the AE emissions for different cutting conditions and work materials. As described in Section 3.2.1, for each cutting condition and material, each cutting test was conducted at least twice, during which three readings of 8388608 samples were acquired. Subsequently, each set of 8388608 was divided into 8 subsets of 1048576 samples, resulting, effectively, in 48 sets of 1048576 samples, which were further analysed in the following ways:

Energy analysis Primarily, each set of 1048576 samples was full-wave rectified, followed by its low-pass filtering (1000 Hz cut-off frequency). Afterwards, the probability density function of the data set was computed in order to obtain the value where the distribution reaches its maximum, the mode (I_{mode}). Since the mode is also defined as the most common value of a data set, as already referred in Section 2.2.1, the mode is less sensitive to outlying values that the mean. The example of a raw AE signal presented in Figure 4.13 shows a typical Test A continuous-type AE signal superimposed by two large bursts; a higher value of the root mean square of the AE signals (I_{RMS}) was obtained comparatively to the value of I_{mode}, indicating that the effect of the unwanted outlying bursts were disregarded in the calculation of I_{mode}. In order to obtain the points represented in the plots shown in Figures 4.16–4.21, the mean of each 48 I_{mode} values were calculated (the length of the error bars represents two standard deviations).

Frequency analysis First of all, the FFT (Section 2.2.1) of each 1048576 data set was computed. Afterwards, the spectrum was divided into 256 bands between 100 and 500 kHz, and then the values falling within each band were added together, resulting in a spectral data set of 256 elements, as shown in Figure 4.14. By observation of the AE spectra, it was concluded that changes at the higher frequency range would not be significantly detected when compared to changes at the lower frequency range, since most energy of the spectra was around the 100–200 kHz frequency range (Figure 4.14 and 4.15a). Therefore, it was decided to compute each frequency power spectrum in relation to a predetermined reference spectrum, i.e. the reference spectrum shown in Figure 4.14; this was achieved by dividing the 256 points of all the frequency spectra by the reference spectrum. As demonstrated by the example shown in Figure 4.15b, similar significance is observed for all frequencies when the spectrum is relative to the reference. Subsequently, the frequency value that divides the spectrum into two parts of equal energy, the mean frequency (f_{mean}, as defined in Section 2.2.1), was calculated for all 48 spectra of each cutting condition and work material. In order to obtain the points represented in the plots shown in Figures 4.22–4.27, the mean of each 48 f_{mean} values was computed (the length of the error bars represents two standard deviations).

Figure 4.16 shows the variation of I_{mode} with V for $t_1 = 0.02$ and 0.1 mm/rev, and $w = 1.2$ mm. It can be observed that I_{mode} is strongly dependent on V because I_{mode} increases

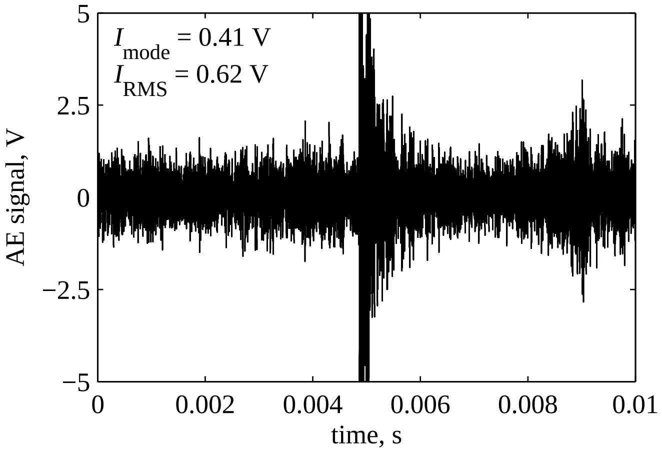

Figure 4.13: Example of a 0.01 s AE time series. (work material 080M40, $V = 200$ m/min, $t_1 = 0.1$ mm/rev, $w = 1.2$ mm).

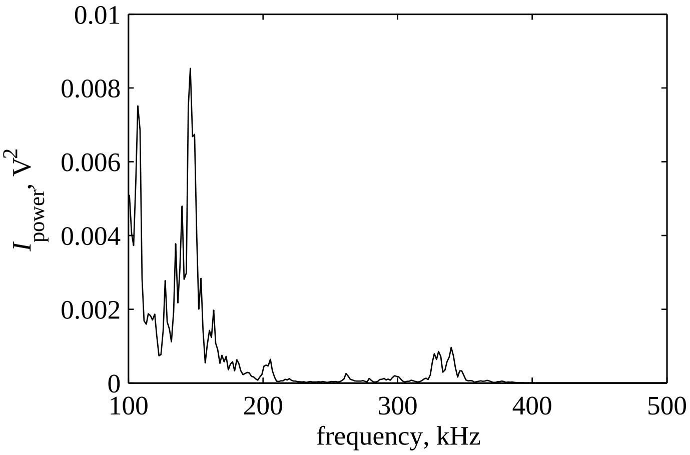

Figure 4.14: Example of AE power spectrum (work material 080M40, $V = 200$ m/min, $t_1 = 0.1$ mm/rev, $w = 1.2$ mm). This power spectrum will be used as a reference for frequency domain calculations.

almost exponentially with increasing V. However, for the lower t_1 values (0.02 mm/rev), I_{mode} increases more quickly than when $t_1 = 0.1$ mm/rev.

Figure 4.17 shows the variation of I_{mode} with t_1 for $V = 75$ and 200 m/min, and $w = 1.2$ mm. In most cases it can be stated that I_{mode} decreases slightly or remains constant with increasing t_1. However, since these trends are not observed in all cases, each plot is described separately; for $V = 75$ m/min:

080A15 (Figure 4.17a) The value of I_{mode} remains more or less constant in the 0.01–0.06 mm/rev range, and it increases slightly with t_1 above 0.06 mm/rev.

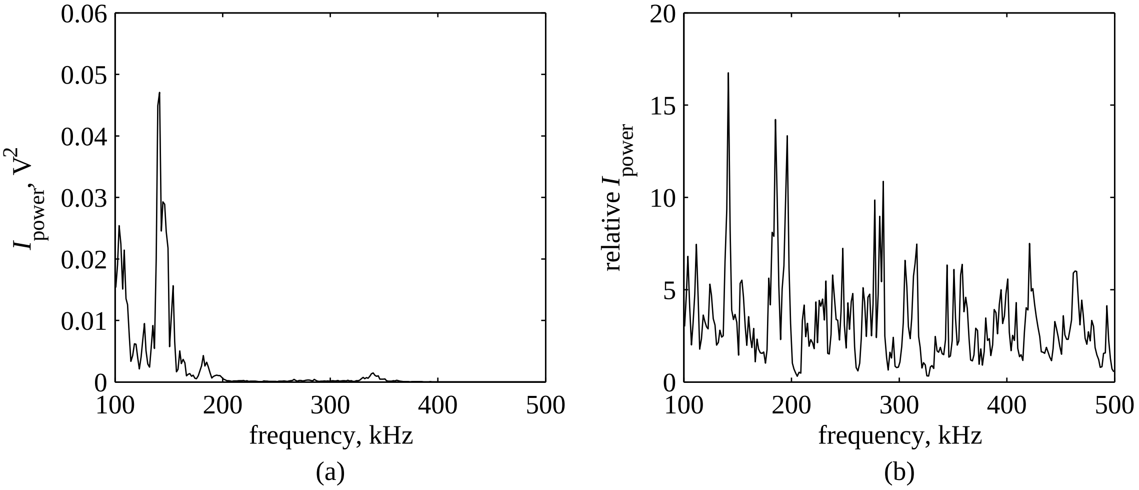

(a)

(b)

Figure 4.15: Example of AE power spectrum (work material 304S15, $V = 200$ m/min, $t_1 = 0.1$ mm/rev, $w = 1.2$ mm). (a) Original spectrum. (b) Original Spectrum divided by the reference spectrum shown in Figure 4.14.

080M40 (Figure 4.17c) Between 0.01 and 0.02 mm/rev, I_{mode} increases with t_1, between 0.02 and 0.1 mm/rev, it decreases with t_1, and above 0.1 mm/rev, I_{mode} remains more or less constant with increasing t_1.

304S15 (Figure 4.17e) The value of I_{mode} remains approximately constant with increasing t_1.

6082-T6 (Figure 4.17g) Below 0.04 mm/rev, I_{mode} decreases abruptly with t_1, and above 0.04 mm/rev, I_{mode} remains approximately constant but with a tendency to increase.

When $V = 200$ m/min:

080A15 (Figure 4.17b) The value of I_{mode} decreases with t_1. However, the rate of decrease is higher for lower values of t_1.

080M40 (Figure 4.17d) The value of I_{mode} is observed to decrease with t_1. However, the rate of decrease is higher for lower t_1 values, and above 0.1 mm/rev, I_{mode} does not change.

304S15 (Figure 4.17f) The value of I_{mode} is observed to decrease with increasing t_1.

6082-T6 (Figure 4.17h) Between 0.01 and 0.06 mm/rev, I_{mode} is observed to decrease with t_1. Above 0.06 mm/rev, I_{mode} is observed to remain constant but with a rising tendency.

Finally, it must be added that, in all cases, the data is reasonably scattered.

Figures 4.18–4.21 show the variation of I_{mode} with w for four different combinations of V (75 and 200 m/min) and t_1 (0.02 and 0.1 mm/rev). From the analysis of the plots, it can be concluded that, generally, I_{mode} increases very quickly with increasing w at low w values, and since the rate of increase of I_{mode} decreases as w rises, I_{mode} increases very slowly at higher w values, tending to settle to a constant I_{mode} value. However, this exact trend was not observed in all cases, such as: for $V = 200$ m/min, $t_1 = 0.1$ mm/rev, and 080M40 (Figure 4.19d), below widths of 0.6 mm, I_{mode} is observed to rise with increasing w, between 0.6 and 1.2 mm, I_{mode} is observed to fall, and above 1.2 mm, I_{mode} seems to settle to a constant value; for $V = 200$ m/min, $t_1 = 0.1$ mm/rev, and 304S15 (Figure 4.20d), I_{mode} remains more or less constant with varying w, and it decreases slightly above widths of 1.2 mm; for $V = 75$ m/min, $t_1 = 0.02$ mm/rev, and 6082-T6 (Figure 4.21a), I_{mode} rises in the 0.1–0.3 mm range, it falls in the 0.3–0.6 mm range, and it rises again above widths of cut of 1.2 mm; for $V = 75$ m/min, $t_1 = 0.1$ mm/rev, and 6082-T6 (Figure 4.21b), I_{mode} rises abruptly in the 0.1–0.3 mm range, it remains constant in the 0.3–0.6 mm range, and it rises again above 1.2 mm; for $V = 200$ m/min, $t_1 = 0.02$ mm/rev, and 6082-T6 (Figure 4.21c), I_{mode} rises abruptly in the 0.1–0.3 mm range, it decreases between 0.3 and 0.6 mm, and it remains constant above widths of 0.6 mm.

Figure 4.22 shows the variation of f_{mean} with V for $t_1 = 0.02$ and 0.1 mm/rev, and $w = 1.2$ mm. By observing the plots, it can be stated that, as a general trend, the value of f_{mean} decreases with increasing V in an almost linear relationship. However, some deviations from this general trend can be perceived: for $t_1 = 0.02$ mm/rev and 080A15 (Figure 4.22a), f_{mean} increases with V between 50 and 75 m/min, but it decreases above 75 m/min; for $t_1 = 0.1$ mm/rev and 080A15 (Figure 4.22b), f_{mean} remains relatively constant below speeds of 150 m/min, although very high scatter is observed; for $t_1 = 0.02$ mm/rev and 304S15 (Figure 4.22e), the relationship between f_{mean} and V can be represented by a straight line, excepting at 150 m/min, where f_{mean} falls below the straight line relationship; for $t_1 = 0.02$ mm/rev, and 6082-T6 (Figure 4.22g), f_{mean} remains constant in the 50–100 m/min speed range, it decreases in the 100–200 m/min range, and it becomes constant again above 200 m/min.

Figure 4.23 shows the variation of f_{mean} with t_1 for $V = 75$ and 200 m/min, and $w = 1.2$ mm. A common feature in all plots is that, above t_1 values of 0.06 mm/rev, f_{mean} increases with increasing t_1. Although, for $V = 200$ m/min and 6082-T6 (Figure 4.23g), f_{mean} remains relatively constant above 0.04 mm/rev. Under 0.06 mm/rev, no clear common trend can be established.

Figures 4.24–4.27 show the variation of f_{mean} with w for four different combinations of V (75 and 200 m/min) and t_1 (0.02 and 0.1 mm/rev). From the analysis of the plots, it can be affirmed that generally f_{mean} is not significantly affected by w, although very high scatter is also present in the data.

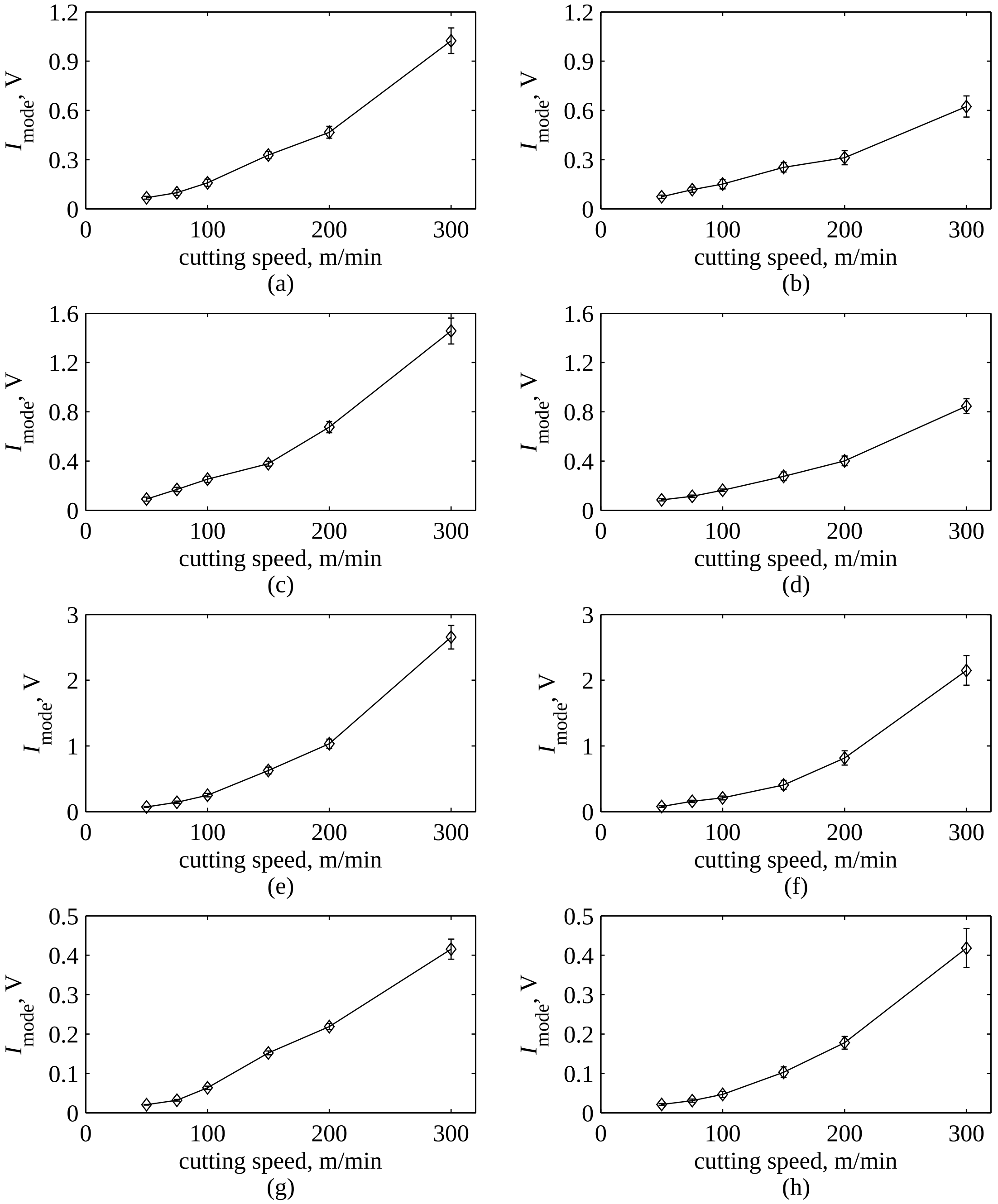

Figure 4.16: Variation of AE level with cutting speed. (a) 080A15, $V = 75$ m/min. (b) 080A15, $V = 200$ m/min. (c) 080M40, $V = 75$ m/min. (d) 080M40, $V = 200$ m/min. (e) 304S15, $V = 75$ m/min. (f) 304S15, $V = 200$ m/min. (g) 6082-T6, $V = 75$ m/min. (h) 6082-T6, $V = 200$ m/min.

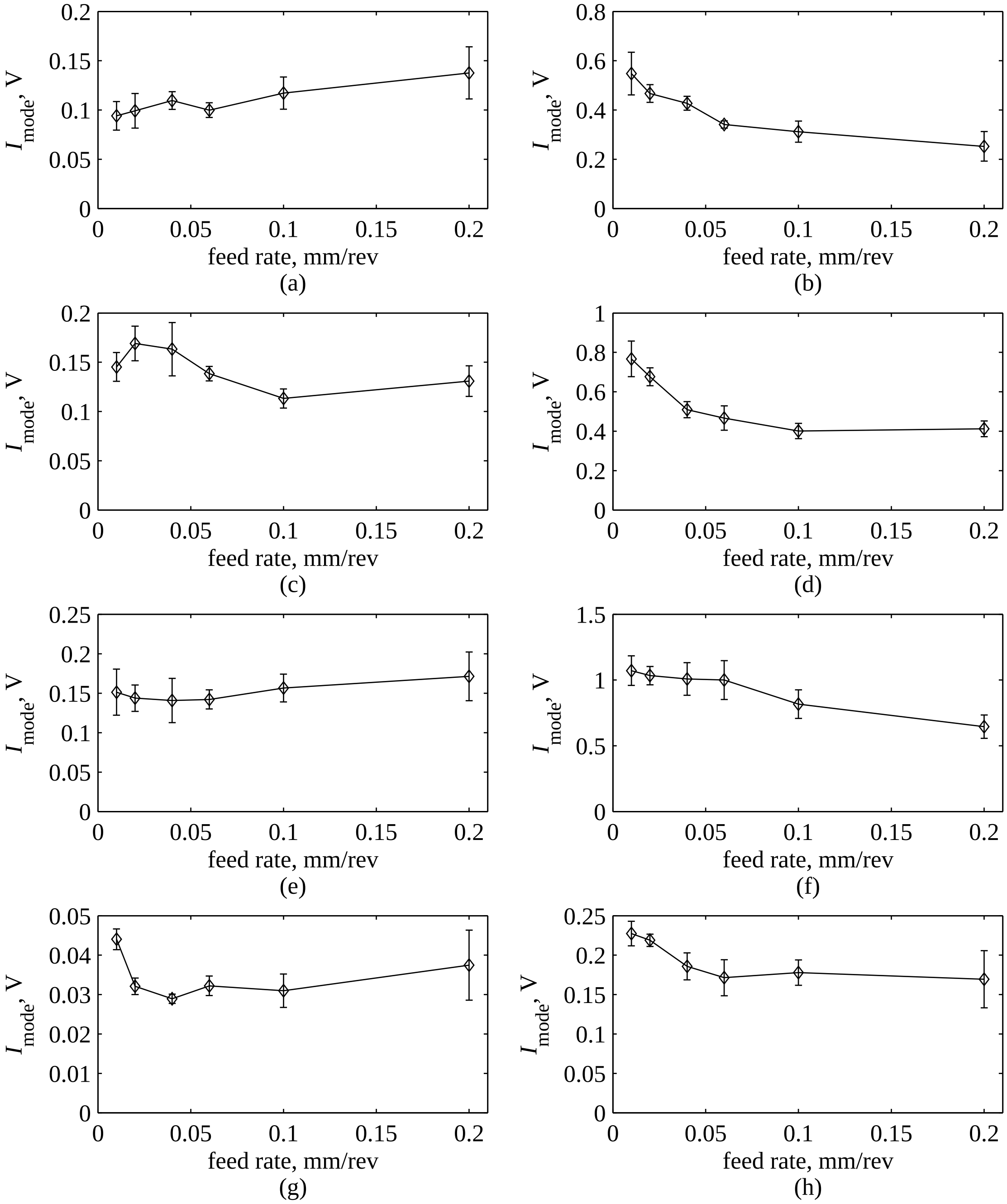

Figure 4.17: Variation of AE level with feed rate. (a) 080A15, $V = 75$ m/min. (b) 080A15, $V = 200$ m/min. (c) 080M40, $V = 75$ m/min. (d) 080M40, $V = 200$ m/min. (e) 304S15, $V = 75$ m/min. (f) 304S15, $V = 200$ m/min. (g) 6082-T6, $V = 75$ m/min. (h) 6082-T6, $V = 200$ m/min.

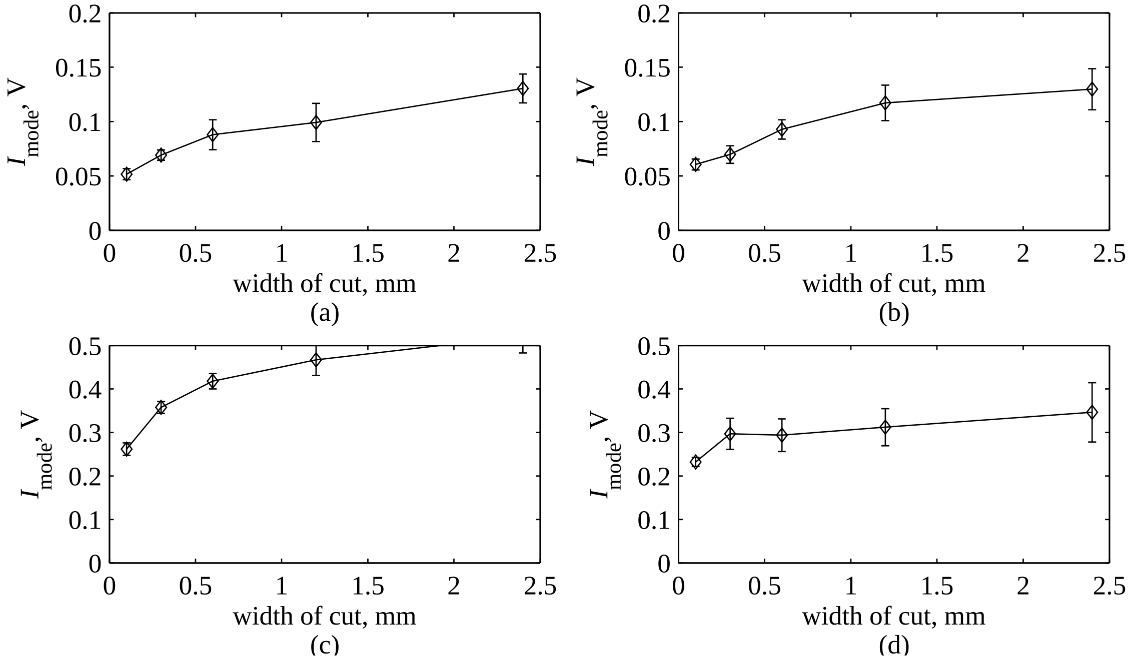

Figure 4.18: Variation of AE level with width of cut; work material 080A15. (a) $V = 75$ m/min, $t_1 = 0.02$ mm/rev. (b) $V = 75$ m/min, $t_1 = 0.1$ mm/rev. (c) $V = 200$ m/min, $t_1 = 0.02$ mm/rev. (d) $V = 200$ m/min, $t_1 = 0.1$ mm/rev.

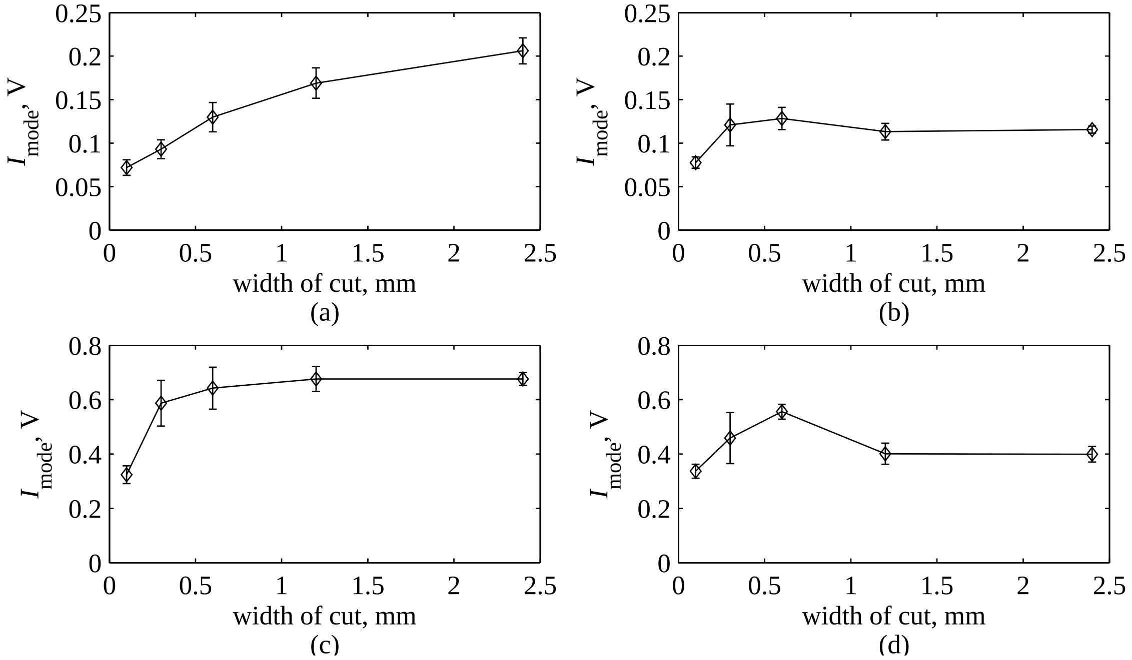

Figure 4.19: Variation of AE level with width of cut; work material 080M40. (a) $V = 75$ m/min, $t_1 = 0.02$ mm/rev. (b) $V = 75$ m/min, $t_1 = 0.1$ mm/rev. (c) $V = 200$ m/min, $t_1 = 0.02$ mm/rev. (d) $V = 200$ m/min, $t_1 = 0.1$ mm/rev.

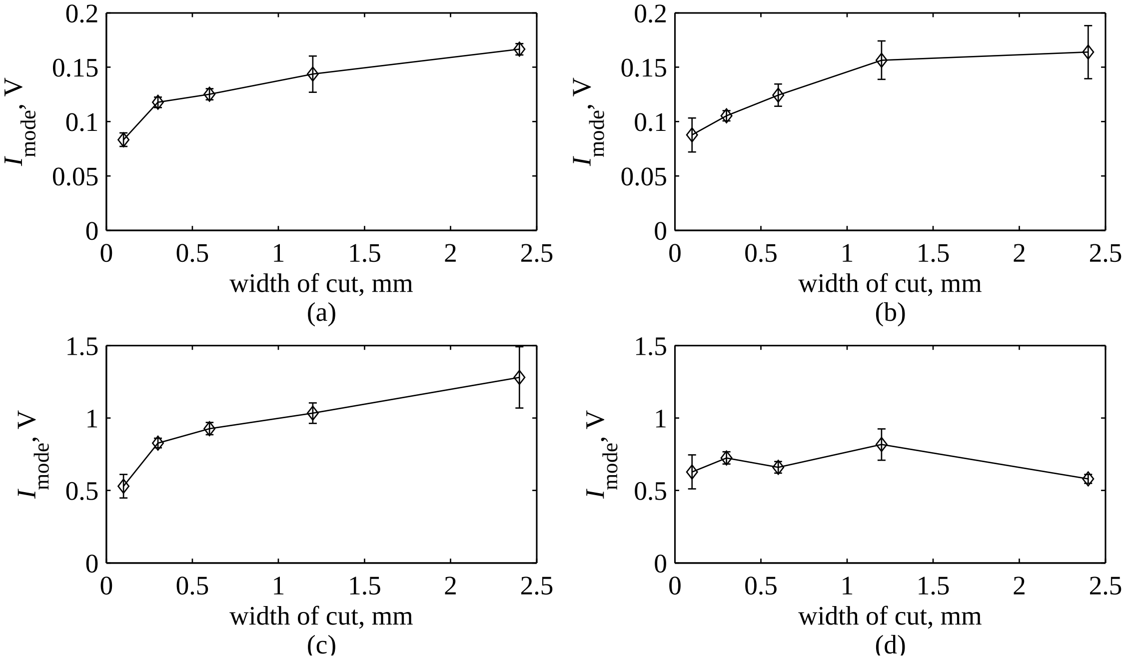

Figure 4.20: Variation of AE level with width of cut; work material 304S15. (a) $V = 75$ m/min, $t_1 = 0.02$ mm/rev. (b) $V = 75$ m/min, $t_1 = 0.1$ mm/rev. (c) $V = 200$ m/min, $t_1 = 0.02$ mm/rev. (d) $V = 200$ m/min, $t_1 = 0.1$ mm/rev.

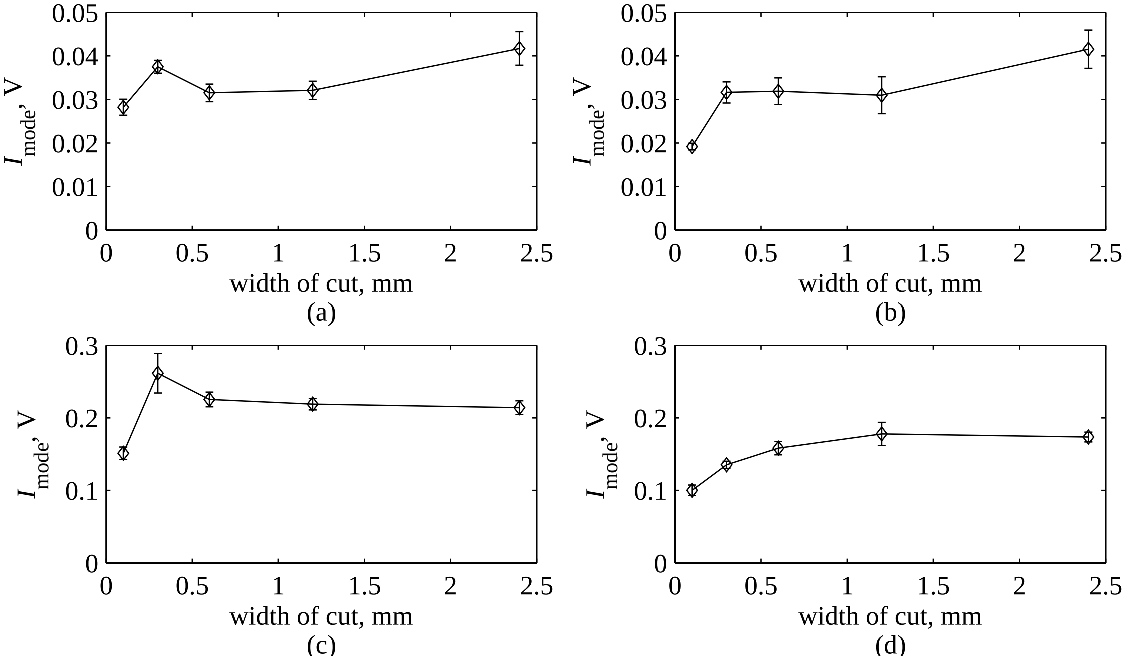

Figure 4.21: Variation of AE level with width of cut; work material 6082-T6. (a) $V = 75$ m/min, $t_1 = 0.02$ mm/rev. (b) $V = 75$ m/min, $t_1 = 0.1$ mm/rev. (c) $V = 200$ m/min, $t_1 = 0.02$ mm/rev. (d) $V = 200$ m/min, $t_1 = 0.1$ mm/rev.

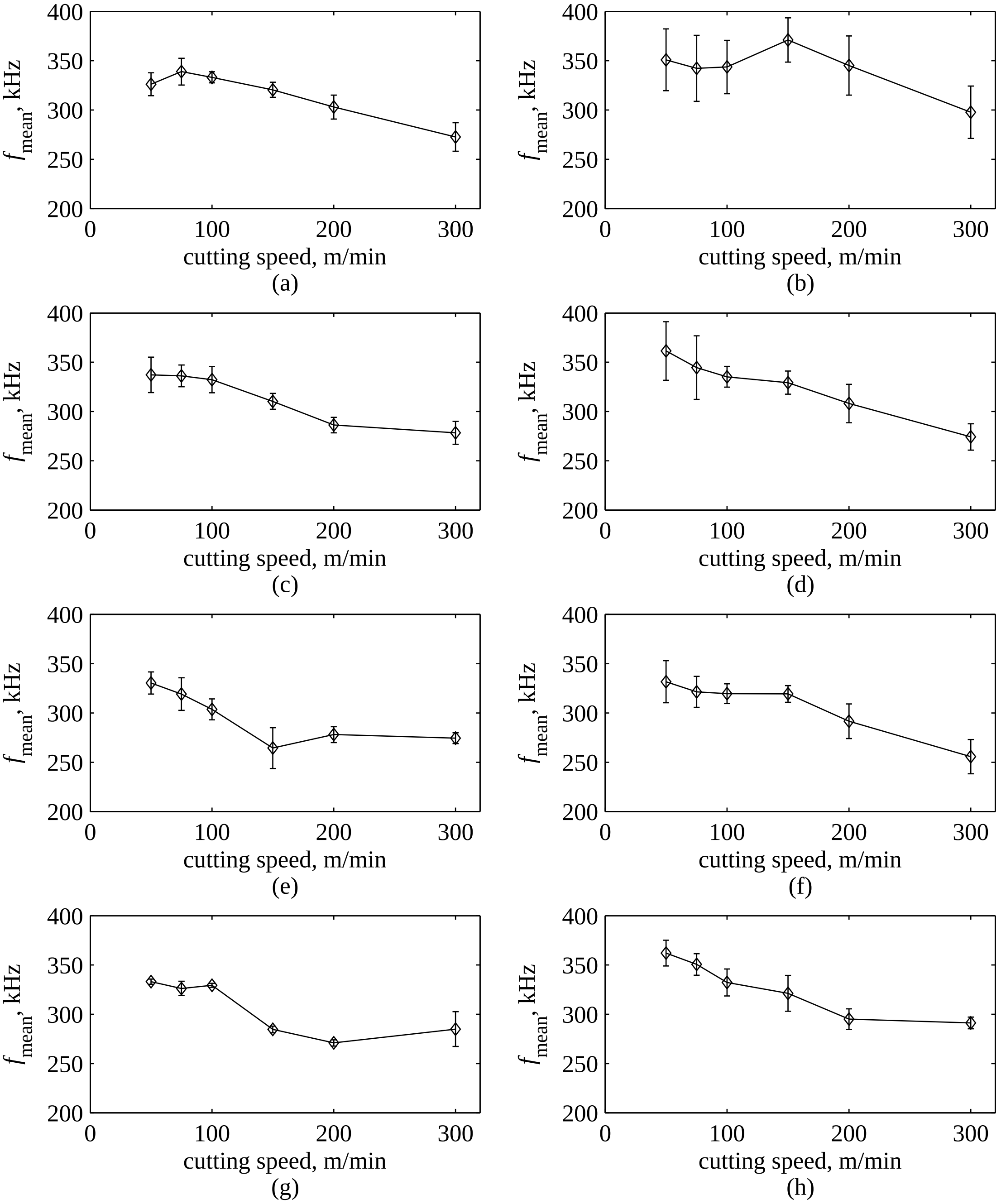

(a) (b) (c) (d) (e) (f) (g) (h)

Figure 4.22: Variation of AE mean frequency with cutting speed. (a) 080A15, $V = 75$ m/min. (b) 080A15, $V = 200$ m/min. (c) 080M40, $V = 75$ m/min. (d) 080M40, $V = 200$ m/min. (e) 304S15, $V = 75$ m/min. (f) 304S15, $V = 200$ m/min. (g) 6082-T6, $V = 75$ m/min. (h) 6082-T6, $V = 200$ m/min.

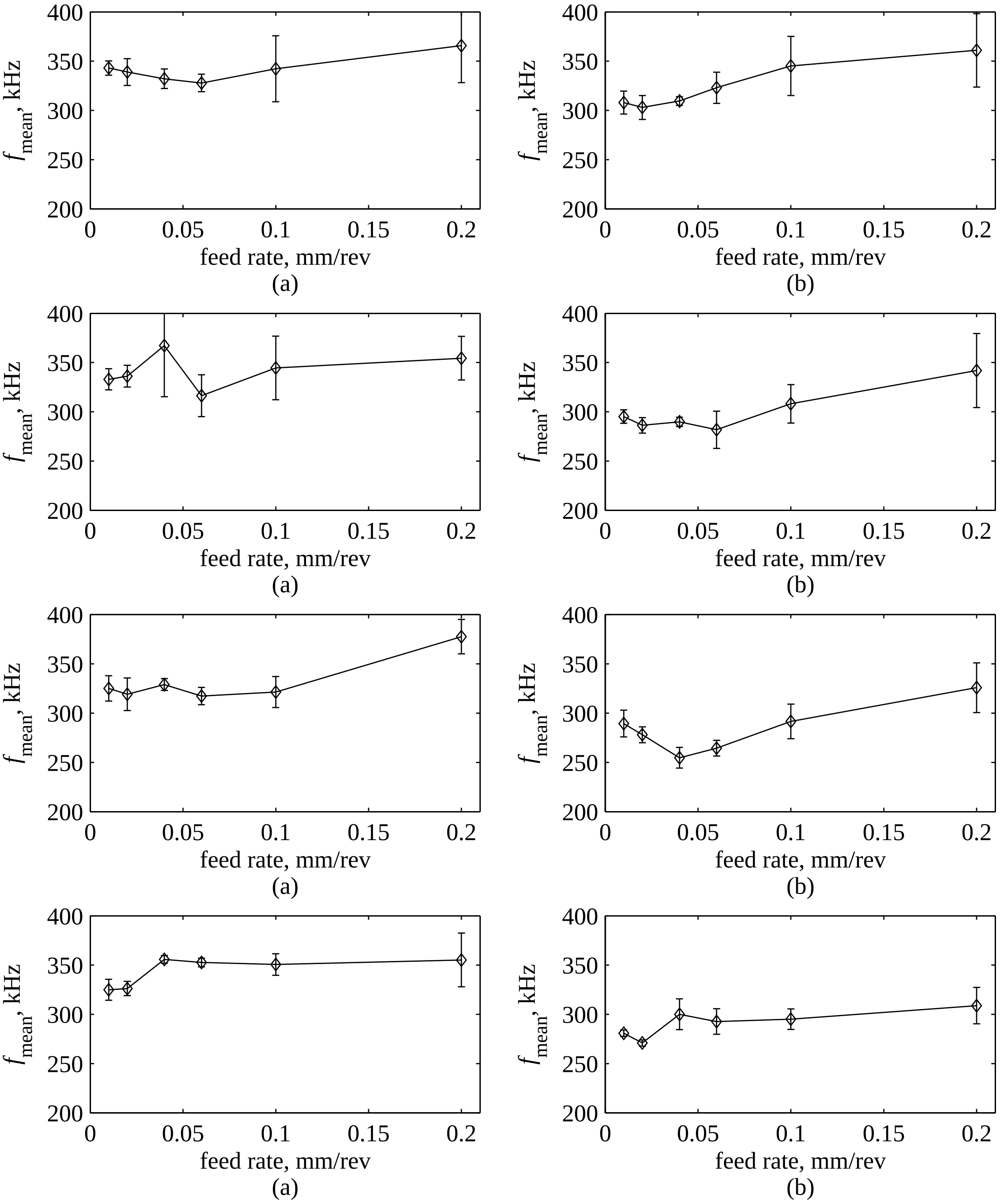

(a) (b)

(a) (b)

(a) (b)

(a) (b)

Figure 4.23: Variation of AE mean frequency with feed rate. (a) 080A15, $V = 75$ m/min. (b) 080A15, $V = 200$ m/min. (c) 080M40, $V = 75$ m/min. (d) 080M40, $V = 200$ m/min. (e) 304S15, $V = 75$ m/min. (f) 304S15, $V = 200$ m/min. (g) 6082-T6, $V = 75$ m/min. (h) 6082-T6, $V = 200$ m/min.

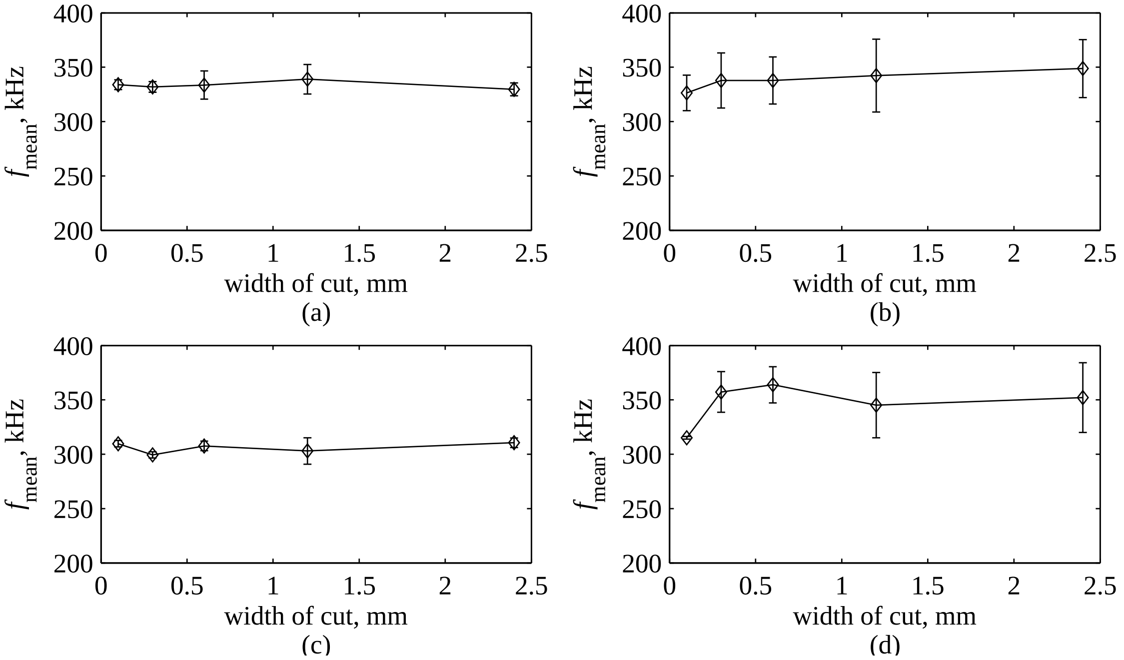

Figure 4.24: Variation of AE mean frequency with width of cut; work material 080A15. (a) $V = 75$ m/min, $t_1 = 0.02$ mm/rev. (b) $V = 75$ m/min, $t_1 = 0.1$ mm/rev. (c) $V = 200$ m/min, $t_1 = 0.02$ mm/rev. (d) $V = 200$ m/min, $t_1 = 0.1$ mm/rev.

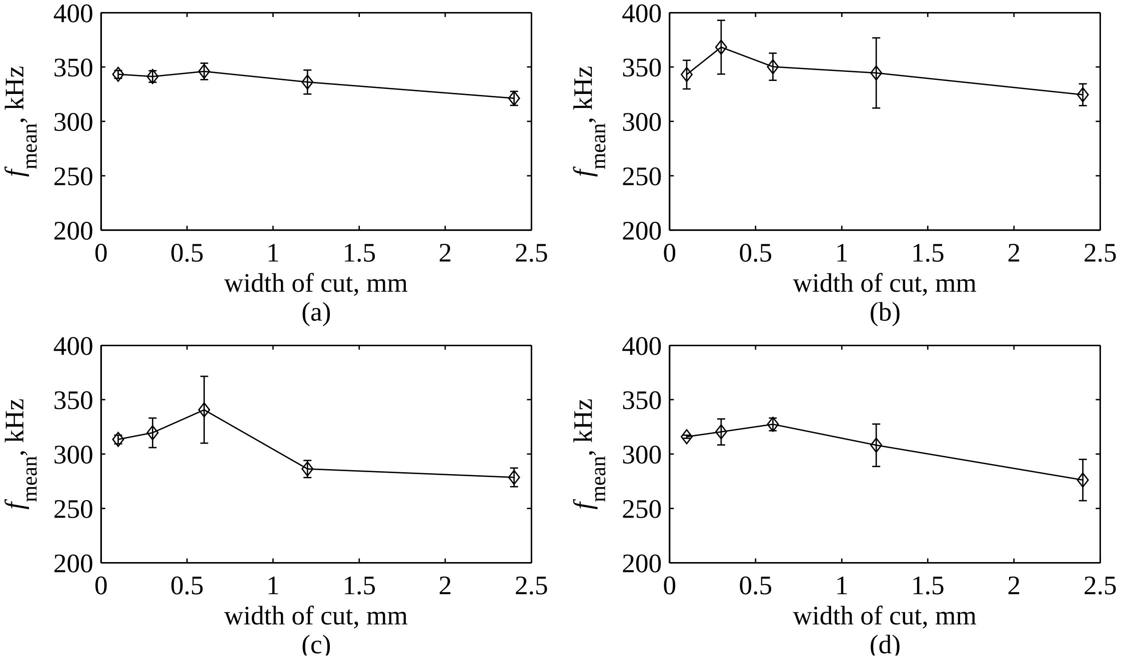

Figure 4.25: Variation of AE mean frequency with width of cut; work material 080M40. (a) $V = 75$ m/min, $t_1 = 0.02$ mm/rev. (b) $V = 75$ m/min, $t_1 = 0.1$ mm/rev. (c) $V = 200$ m/min, $t_1 = 0.02$ mm/rev. (d) $V = 200$ m/min, $t_1 = 0.1$ mm/rev.

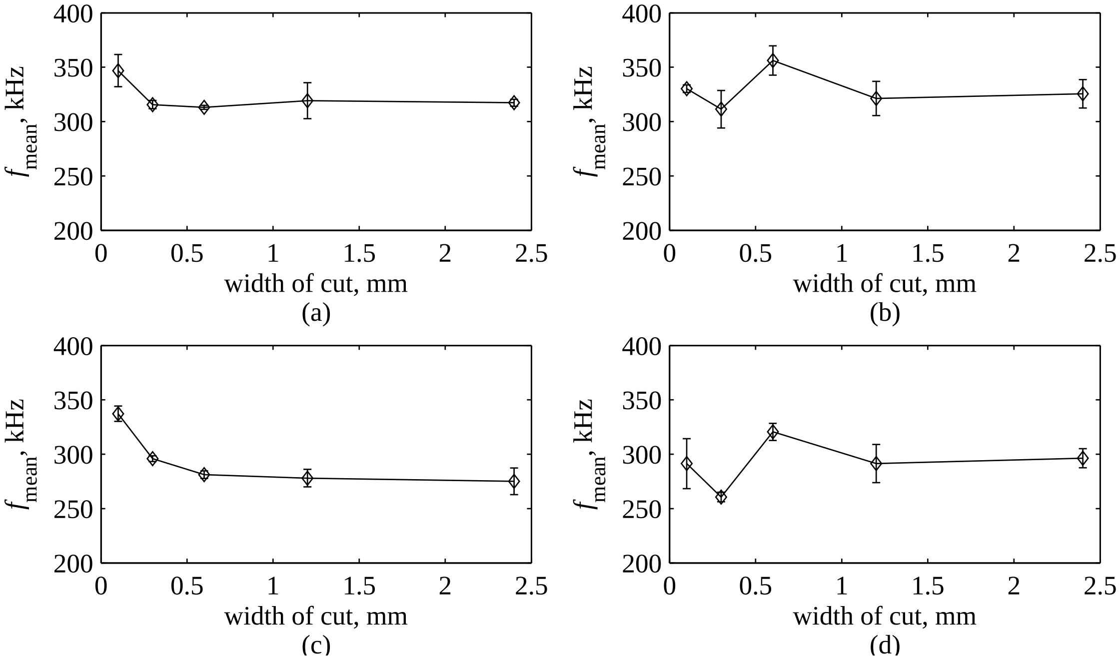

Figure 4.26: Variation of AE mean frequency with width of cut; work material 304S15. (a) $V = 75$ m/min, $t_1 = 0.02$ mm/rev. (b) $V = 75$ m/min, $t_1 = 0.1$ mm/rev. (c) $V = 200$ m/min, $t_1 = 0.02$ mm/rev. (d) $V = 200$ m/min, $t_1 = 0.1$ mm/rev.

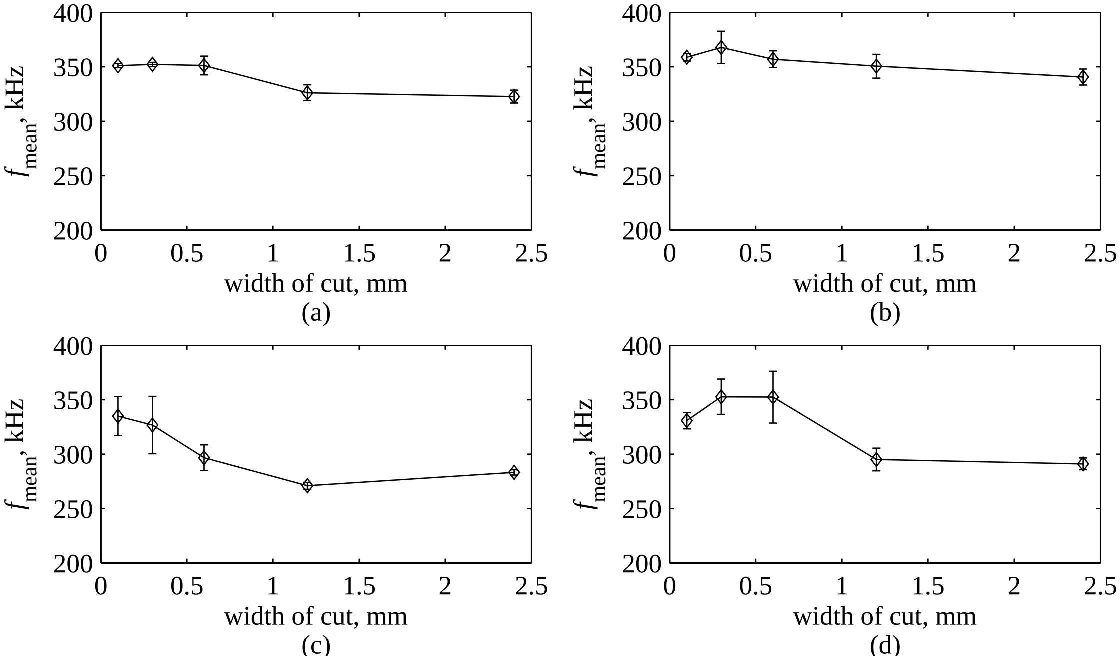

Figure 4.27: Variation of AE mean frequency with width of cut; work material 6082-T6. (a) $V = 75$ m/min, $t_1 = 0.02$ mm/rev. (b) $V = 75$ m/min, $t_1 = 0.1$ mm/rev. (c) $V = 200$ m/min, $t_1 = 0.02$ mm/rev. (d) $V = 200$ m/min, $t_1 = 0.1$ mm/rev.

4.2 Test B—Preset Workpiece Temperature

This section presents the resulting cutting forces and AE signals generated during the preset work temperature tests described in Section 3.2.2. The first part shows the variation of the cutting forces with preset temperature, while the second part shows the variation of AE with preset temperature.

4.2.1 Cutting Forces

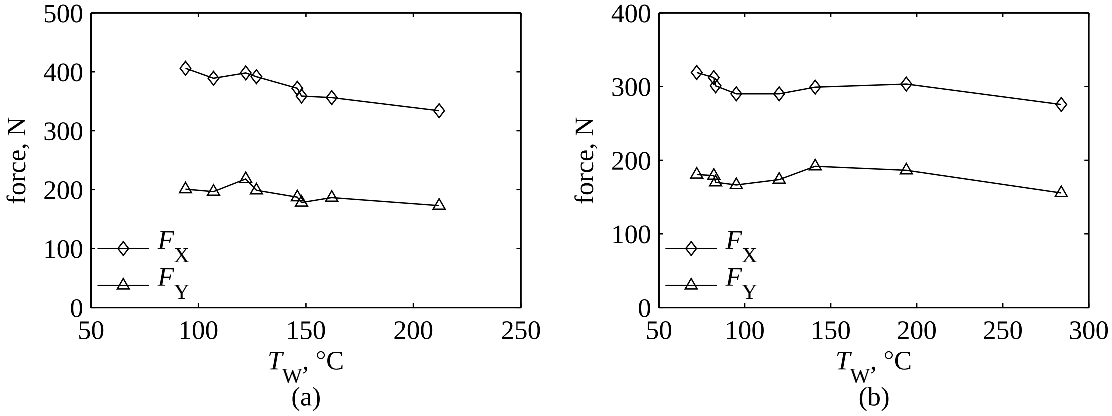

Figure 4.28: Variation of cutting forces with workpiece surface temperature; work material 080A15, $t_1 = 0.1$ mm/rev. (a) $V = 75$ m/min. (b) $V = 200$ m/min.

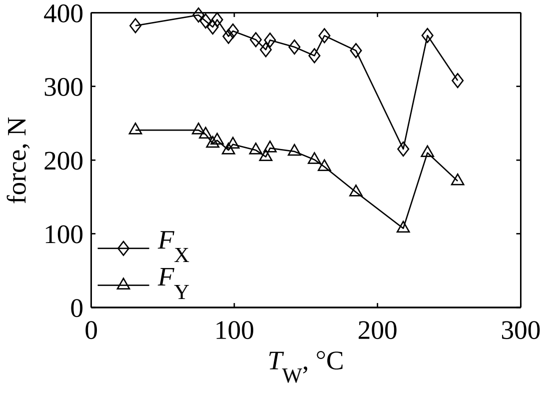

Figure 4.29: Variation of cutting forces with workpiece surface temperature; work material 080M40, $V = 200$ m/min, $t_1 = 0.1$ mm/rev.

The plots shown in Figures 4.28–4.31 present the variation of F_X and F_Y with workpiece surface temperature (T_{WS}) measured before each run (Tables 3.3–3.6). Firstly, for each T_{WS} value, the mean of the values of F_X and F_Y acquired during each 500 ms interval was computed. Thereafter, the mean of all the 500 ms means obtained along the whole cutting length was computed,

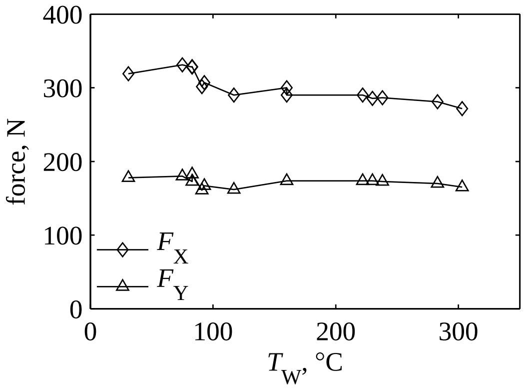

Figure 4.30: Variation of cutting forces with workpiece surface temperature; work material 304S15, $V = 200$ m/min, $t_1 = 0.1$ mm/rev.

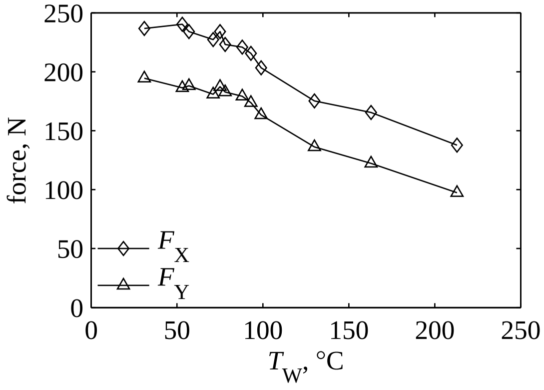

Figure 4.31: Variation of cutting forces with workpiece surface temperature; work material 6082-T6, $V = 200$ m/min, $t_1 = 0.1$ mm/rev.

resulting in the points shown on the plots (the length of the error bars correspond to two standard deviations).

In the majority of the cases, it can be observed that the cutting forces vary slightly with T_{WS}. However, as this trend was not exactly observed in all cases, it was decided to describe each one individually:

080A15 (Figure 4.28a) Both cutting forces remain more or less constant with increasing T_{WS}.

080A15 (Figure 4.28b) The cutting forces remain more or less invariant with T_{WS}.

080M40 (Figure 4.28) Bellow approximately 170°C, F_X and F_Y decrease slightly with increasing T_{WS}. However, above this temperature, the cutting forces fall abruptly down until T_{WS} approaches 220°C. From this point, F_X and F_Y rise abruptly until T_{WS} reaches approximately 240°C. Above 240°C the cutting forces start to fall again with increasing T_{WS}.

304S15 (Figure 4.30) Both cutting forces remain more or less constant with T_{WS}.

6082-T6 (Figure 4.31) Both F_{X} and F_{Y} fall almost linearly with increasing T_{WS}.

4.2.2 Acoustic Emission

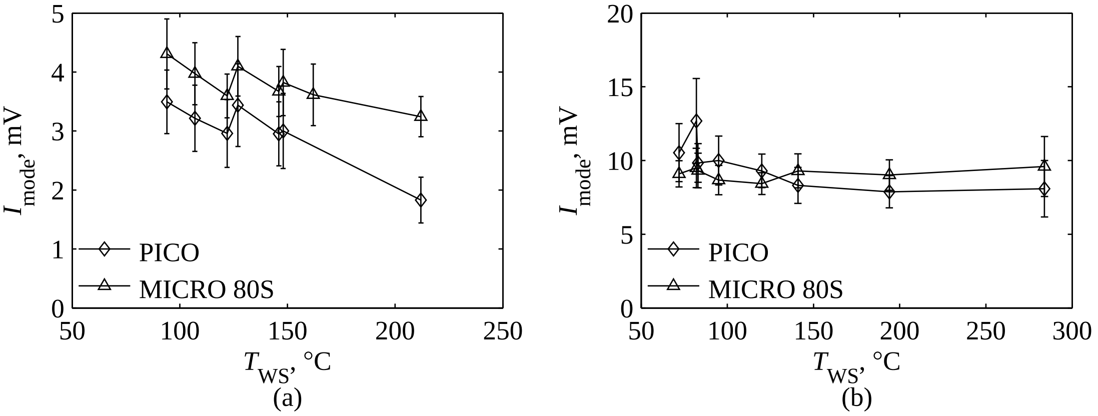

(a) (b)

Figure 4.32: Variation of AE level with workpiece surface temperature; work material 080A15 and $t_1 = 0.1$ mm/rev. (a) $V = 75$ m/min. (b) $V = 200$ m/min.

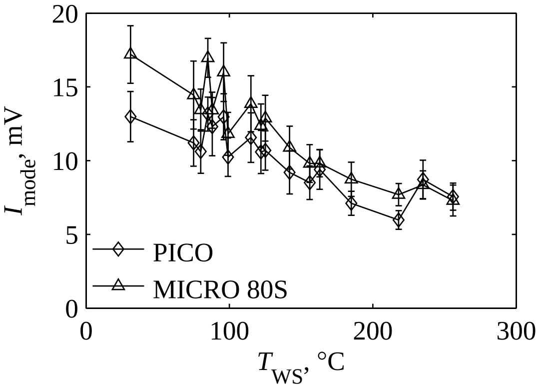

Figure 4.33: Variation of AE level with workpiece surface temperature; work material 080M40, $V = 200$ m/min, and $t_1 = 0.1$ mm/rev.

The plots shown in Figures 4.32–4.35 present the variation of AE with T_{WS} for both AE sensors (MICRO 80S and PICO). In order to process the AE data, for each T_{WS} value, the value of the I_{mode} was calculated for each set of 65536 AE data points that were acquired at every 500 ms (the low-pass cut-off frequency applied to the full-wave rectified data was 1000 Hz). Afterwards, the mean of all the I_{mode} values was computed, resulting in the points shown on the plots (the length of the error bars correspond to two standard deviations).

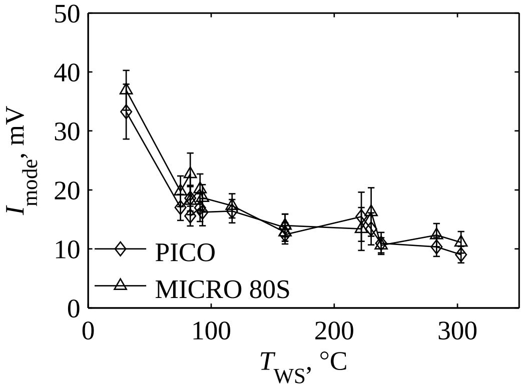

Figure 4.34: Variation of AE level with workpiece surface temperature; work material 304S15, $V = 200$ m/min, and $t_1 = 0.1$ mm/rev.

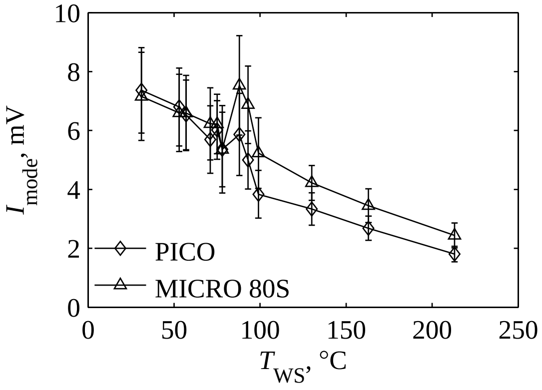

Figure 4.35: Variation of AE level with workpiece surface temperature; work material 6082-T6, $V = 200$ m/min, and $t_1 = 0.1$ mm/rev.

From the observation of the plots, it can be affirmed that the value of I_{mode} decreases as T_{WS} increases. This trend is more or less visible in all plots, being less visible in Figure 4.32b, where, especially for the MICRO 80S data, I_{mode} seems to change very little with varying T_{WS}.

Chapter 5

Analysis and Discussion

In this chapter, the experimental results presented in Chapter 4 are analysed, and from the theory expounded in Chapter 2 (and Appendices A–C), the generation mechanism of acoustic emission (AE) detected during the course of metal cutting are discussed. To begin with, a preliminary discussion regarding the experimental results, including a comparison with published material, is undertaken; a basic empirical AE model is derived, and some published AE models are discussed against the experimental data. Additionally, a theory needed for the analysis of the metal cutting process (a semi-empirical theory for metal cutting modelling), as well as the finite-difference theory (for the analysis of the measured temperatures) are discussed. Afterwards, the relationship between AE and the basic cutting parameters governing plastic deformation during metal cutting are evaluated. Finally, a model that relates AE to the motion of dislocations at the typically high strain rates and temperatures involved in metal cutting is proposed; the experimental results are revealed to be in fairly good agreement with model predictions, indicating the appropriateness of the model.

5.1 Preliminary Discussion of Results

5.1.1 Orthogonality

The analysis of the experimental data from Tests A and B (Section 3.2), which is presented throughout this chapter, was done by considering that cutting was orthogonal and, therefore, could be reduced into a two-dimensional system (Section 1.1). However, in reality, cutting was not fully orthogonal, but, as it is demonstrated in this section, the effects of this departure from orthogonality can be neglected for the present tooling system.

Cutting was semi-orthogonal since the workpieces were solid cylinders and not tubular, as required to ensure orthogonality in turning (Section 1.1). One condition to avoid great discrepancies from orthogonality is that the tool nose is small in relation to the width of cut. The radius of the nose of the cutting tool used in Tests A and B (0.4 mm) was relatively large (33%) in relation to the width of cut mostly used during the tests (1.2 mm). However, Messaritis and Borthwick [5] presented, for similar conditions (tool nose radius of 0.4 mm and widths of cut between 0.1 and 3 mm), results of AE level and cutting forces for both orthogonal and semi-orthogonal conditions, and they concluded that although the level of AE and cutting forces were slightly higher for semi-orthogonal cutting, semi-orthogonal cutting could still be used in place of orthogonal cutting with minor differences of results.

Another important departure from orthogonality is that the side cutting angle (C_S) of the cutting tool used in Tests A and B was -5°, which, in order to guarantee orthogonality, should be 0°. As stated by Lin *et al.* [69], an orthogonal model can be used if the feed rate (t_1) and width of cut (w) are changed into the new values t_1' and w', respectively, according to the following equations:

$$t_1' = t_1 \cos C_\mathrm{S} \tag{5.1}$$

$$w' = \frac{w}{\cos C_\mathrm{S}} \tag{5.2}$$

Moreover, new values of the cutting forces in the cutting speed, feed rate, and radial directions (F_X', F_Y', and F_Z', respectively) must be defined:

$$F_\mathrm{X}' = F_\mathrm{X} \tag{5.3}$$

$$F_\mathrm{Y}' = F_\mathrm{Y} \cos C_\mathrm{S} \tag{5.4}$$

$$F_\mathrm{Z}' = -F_\mathrm{Y} \sin C_\mathrm{S} \tag{5.5}$$

where F_X and F_Y are the tangential and feed forces obtained from the orthogonal model (Figure 2.5). Nevertheless, since $\cos C_\mathrm{S} \approx 1$ $(\cos(-5^\circ) = 0.996)$, and $\sin C_\mathrm{S} \approx 0$ $(\cos(-5^\circ) = -0.087)$, the following simplifications were made: $t_1' = t_1$, $w' = w$, $F_\mathrm{Y}' = F_\mathrm{Y}$, and $F_\mathrm{Z}' = 0$; or, in other words, the side cutting angle of the tool was assumed to be 0°.

5.1.2 Comparison of Test A Results with Published Data

As shown in Section 3.2.1, the importance of Test A is that it provides a general overview of the variation of AE, cutting forces, vibration, and temperature signals generated during the turning process of four different work materials and for a wide range of cutting conditions. The cutting force results are shown in Section 4.1.1, temperature results in Section 4.1.2, and AE results in Section 4.1.3. The vibration signals were not presented because they are not relevant for the present study. In this section, the results from Test A are compared with data from published material.

Cutting Forces

Figure 4.1 shows that, as a general trend, F_X and F_Y decrease with increasing cutting speed (V). Trent [35] confirms these results by stating that it is common experience that the cutting forces decrease as V is raised when cutting most metal and alloys. Wright and Robinson [31] showed similar trends for cutting force results of a copper workpiece. Stevenson and Oxley [32] presented the variation of F_X and F_Y with V for a 0.13% carbon steel, and it was shown that both F_X and F_Y decreased slightly with increasing V for high values of V, but F_X and F_Y decreased abruptly with decreasing V below a certain value of V. These results are also observed in the present results for both carbon steel materials (Figures 4.1a–4.1d). For carbon steels, these types of trends are also confirmed by other publications [33, 51].

By using the approximated relationship stated by Equation 2.30, representing the phenomenon called the size effect [1], the following relationship can be deduced:

$$F_X \propto t_1^{0.8} \tag{5.6}$$

Although the exponent 0.8 is a rough estimation, one can conclude that F_X increases with t_1, but with a rate of increase that decreases as t_1 is raised. This trend is visible in all experimental results shown in Figure 4.2, where both F_X and F_Y are observed to increase with t_1, but presenting a less significant rate of increase as t_1 increases. Experimental results showing the relationship between cutting forces and t_1 are not normally explicitly presented due to its well-known and regular relationship. In Section 5.5.1, results from Oxley's model [18] for varying t_1 are compared with the experimental cutting force results from Test A.

Experimental results showing the relationship between cutting forces and w are also not normally explicitly presented, since this relationship is also well-known and regular. It is normally assumed that changing w does only affect the scale of the cutting process [1], meaning, therefore, that both F_X and F_Y are directly proportional to w. This trend is also confirmed by the computation method used by Oxley's model [18] to predict cutting forces (Section 5.5.1). The experimental results shown in Figures 4.3–4.6 are consistent with this relationship, where F_X and F_Y are observed to increase linearly with increasing w.

Cutting Temperatures

Figures 4.7–4.12 shows the variation of temperature T_1 measured by thermocouple 1[1] (Section 3.1.2), placed 5 mm bellow the tool-chip interface. Although T_1 is the result of the heat conducted between the higher temperature at the tool-chip interface (T_{int}) and the location of thermocouple 1, there are some difficulties when one needs to calculate T_{int} based on T_1 measurements. First of all, as evidenced by published material [42, 44], once T_{int} is established at the tool-chip interface, there will be a delay until T_1 settles to is final value. However, as stated in Section 4.1.2, this problem was partially overcome, since, for each test, the maximum value of T_1 was chosen, and by the end of each test, the value of T_1 was expected to be nearly settled down to its maximum final value. Another problem is that though the value of T_1 is dependent on T_{int}, the

---

[1] Although there is a reference to two thermocouples in Section 3.1.2, as stated in Section 3.2.1, only one thermocouple was used during the course of Test A.

relationship between the two is dependent on many variables. Techniques to predict T_{int} based on temperature measurements from a remote location have been addressed by some authors [42, 44]. Moreover, in Section 5.4, it is shown how the finite-difference technique can be used to compute T_1 from known T_{int} values; in Section 5.5.2, Oxley's model [18] is used to predict T_{int}, and then these values are used to compute T_1 by using the finite-difference method, so that predictive T_1 values can be compared with the experimental T_1 values from Test A.

Acoustic Emission

Figure 4.16 shows the relationship between the level of AE (I_{mode}, as defined in Section 2.2.1) and V. Both I_{mode} and its rate of increase are observed to increase with increasing V. This relationship is repeatedly observed with small divergences in many published papers [3, 5, 7, 57, 60, 62, 65]. However, though the AE level is normally presented as the root mean square of AE (I_{RMS}), instead of I_{mode}, the two hold equivalent energetic units (Section 2.2). Some authors [3, 60, 65] sugested that the level of AE is directly proportional to V; however, when the data is analysed closely, the rate of increase of the level of AE tends to increase with increasing V. Moreover, Blum and Inasaki [7] explicitly stated that I_{mode} and its rate of increase both increase with increasing V, and, although not explicitly stated, the data presented by Messaritis and Borthwick [5] exhibit the same relationship.

Generally, the level of AE from Test A experiments is observed to decrease with increasing feed rate, especially when $V = 200$ m/min (Figures 4.17b, 4.17d, 4.17f, and 4.17h). When $V = 75$ m/min, the results are quite scattered and no clear relationship can be determined (Figures 4.17a, 4.17c, 4.17e, and 4.17g), and, as shown in Section 5.5.1, this can perhaps be attributed to the phenomenon of built-up edge (BUE). These results are supported by published material, which shows that for low cutting speeds (below around 100 m/min), the level of AE is more or less insensitive to t_1 [3, 62, 64, 66], and, for higher cutting speeds, the AE level decreases with t_1, tending to a constant value as t_1 increases [5, 7].

As shown in Figures 4.18–4.21, as a general trend, the level of AE increases with w for low values of w, but its rate of increase decreases as w increases, tending to a constant value for high w values. Many publications show that the level of AE remains constant as w is varied [3, 7, 64]; however it can be observed that this trend is observed for quite high values of w. When results are present for lower w values [5, 66], the level of AE is observed to decrease with decreasing w, in the same fashion as the experimental data shown in Figures 4.18–4.21.

Figures 4.22–4.27 show the variation of the mean frequency (f_{mean}) of the AE power spectrum of Test A data with V, t_1, and w. This parameter, which gives an indication of the frequency content of the AE signals, was introduced by Rangwala and Dornfeld [19] and is defined in Section 2.2.1. According to Rangwala and Dornfeld's results, f_{mean} increases with V up to a certain value of V (60 m/min), from which f_{mean} starts to decrease with further increase in V. Test A results of f_{mean} are observed to decrease with V for the whole range of V values (Figure 4.22). However, it must be noted that the range of V values utilized by Rangwala and Dornfeld that exhibit an increase of f_{mean} with V are mostly below the minimum V value utilized in Test A (50 m/min), and, therefore, an agreement between Rangwala and Dornfeld and Test A results must be concluded when considering the variation of f_{mean} with V. Moreover, an agreement is also obtained between Rangwala and Dornfeld and Test A (Figure 4.23) results, for the variation of f_{mean} with t_1, where f_{mean} seems to be more or less insensitive with t_1. Finally, Rangwala and Dornfeld supply no results for the variation of f_{mean} with w, but f_{mean} is presumed to be insensitive to the changes of w, since w is expected to affect solely the volume of material participating into deformation, and this should have no effect on the frequency content of the AE signals; this trend is also observed for Test A results, where f_{mean} remains more or less insensitive with w (Figures 4.24–4.27).

5.1.3 Feed Rate Variation and Width of Cut Variation Tests

As mentioned in Section 3.2.2, two other types of tests, namely feed rate variation and width of cut variation tests, were carried out, whose AE results were, unfortunately, highly affected by random noise signals. The same method as of Test B, and thus a different method from Test A, was used to acquire data during the feed rate and width of cut variation tests, and, in this section, the relative failure of the AE results from these tests is examined.

As described in Section 4.1.3, during Test A acquisition, although sets of 8388608 samples were acquired, each set was subsequently divided in smaller sets of 1048576 data points (105 ms, since the sampling rate was 10 MS/s). During the feed rate and width of cut variation tests, sets of only 65536 samples (13 ms, since the sampling rate was 5 MS/s) were acquired. Therefore, the effective length of Test A data sets was 16 times larger than that of the data sets from the feed rate and width of cut variation tests. Moreover, as stated in Sections 4.1.3 and 4.2, the main method to process the AE raw data was by computing I_{mode}, and if the data sets are too small, the peak of the probability density function of the previously full-wave rectified and low-pass filtered data will not represent the level of continuous AE if the influence of a random bust-type signal is colouring the data set. On the other hand, if the data set is large enough, a single bust-type signal will not be sufficient to move the peak of the probability density function, and, therefore, I_{mode} will represent the continuous-type AE data, which is normally associated with the plastic deformation of the cutting process. Consequently, one may conclude that the small size of the the data sets from the feed rate and width of cut variations tests is the main reason why the AE results from these tests did not provide much additional knowledge on the generation of AE from metal cutting. Therefore, it can be concluded that large samples of AE data (more than 100 ms of duration) must be acquired in order to obtain meaningful results.

One interesting observation with the width of cut variation results was the generation of AE when high chatter vibrations[2] are present. As some results showed that, within a range of width of

---

[2] Chatter is the relative motion between the cutting tool and workpiece that arrives when not enough energy is dissipated by either the damping of the structure or the friction of the cutting process. As a result, relative motion between the tool and the workpiece, at one of the natural frequencies of the system, grows beyond acceptable limits.

cut values, the value of I_{mode} abruptly rose to very high values, it was decided to investigate if this was due to the phenomenon of chatter, and, therefore, as shown in Figure 5.1, both vibrational and AE curves were plotted together. Approximately between widths of cut of 1 and 1.7 mm, the amplitude of the vibration signals is very high, indicating the onset of chattering, which is also accompanied by an abrupt rise of I_{mode}. The maximum I_{mode} value without chatter is 19 mV, whereas the maximum I_{mode} value when chatter is present is 382 mV, resulting in an increase of 20 times of I_{mode} (which is actually higher than the increase of the vibration signals). Therefore, it has to be concluded that chatter has an important impact on the generation of AE.

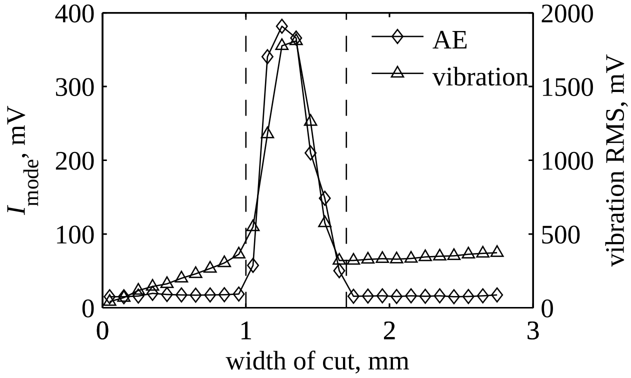

Figure 5.1: AE generation during chatter for varying width of cut.

5.2 Empirical Modelling of Acoustic Emission Energy

In this section, an empirical model of AE energy, based on Test A experimental data (Section 4.1, Figures 4.16 and 4.17) is developed. Figures 4.16 and 4.17 show, for constant width of cut ($w = 1.2$ mm), the variation of I_{mode} for different cutting conditions and work materials. In this section, a more meaningful physical representation of the level of AE was utilized, the AE power (I_{power}), which is equivalent to the energy rate of the generated AE signals: $I_{\text{power}} = I_{\text{mode}}^2$.

Figures 5.2a and 5.2b show logarithmic scale plots representing the variation of I_{power} with cutting speed for feed rates of 0.02 and 0.1 mm/rev, respectively. It can be observed in both plots that, in the logarithmic scale, the relationship between I_{power} and V can be represented, for each material, as a straight line of positive slope, suggesting the existence of a power function relationship between I_{power} and V.

Figures 5.3a and 5.3b show logarithmic scale plots of I_{power} against t_1 for cutting speeds of 75 and 200 m/min, respectively. When $V = 200$ m/min, it can be observed that, in the logarithmic scale, the relationship between I_{power} and t_1 can be approximated to straight lines of negative slope for the different materials, suggesting a power function relationship between I_{power} and t_1.

This leads to poor surface finish, reduced dimensional accuracy, increased tool wear, tool fracture, and even damage to the machine tool itself.

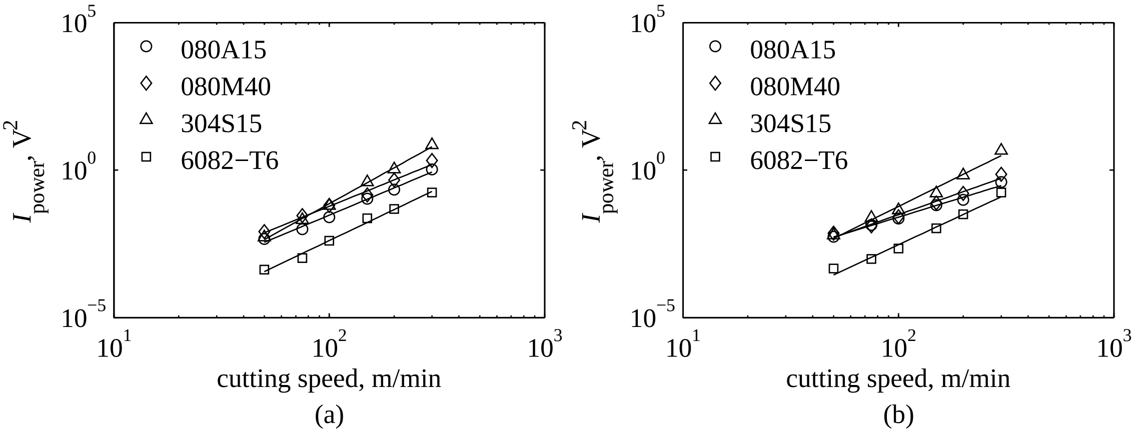

Figure 5.2: Relationship between I_{power} and cutting speed in logarithmic scale. (a) $t_1 = 0.02$ mm/rev. (b) $t_1 = 0.1$ mm/rev.

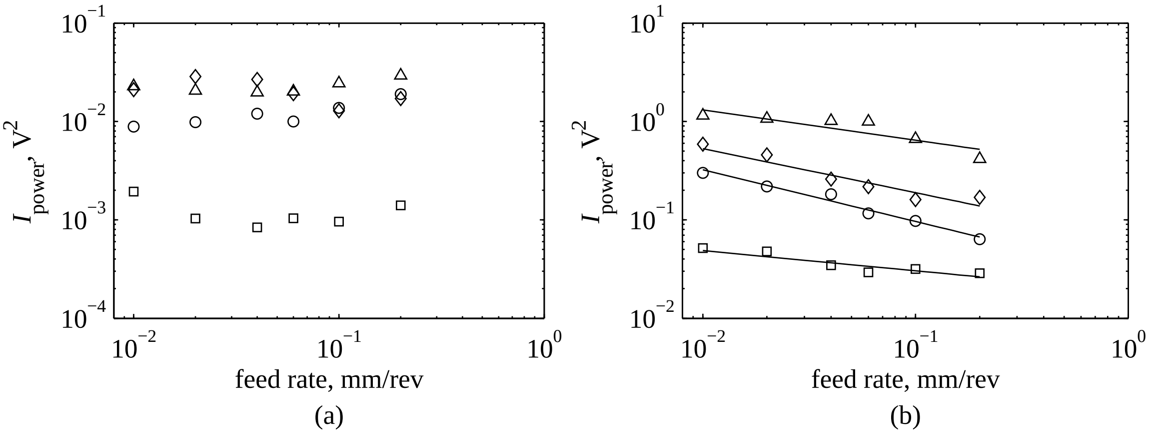

Figure 5.3: Relationship between I_{power} and feed rate in logarithmic scale. (a) $V = 75$ m/min. (b) $V = 200$ m/min.

However, when $V = 75$ m/min, I_{power} seems to be more or less insensitive to t_1, and a clear relationship is not exhibited.

Due to the power function nature of the relationship between I_{power}, V, and t_1, the following empirical relationship was investigated:

$$I_{\text{power}} = KV^{n_1}t_1^{n_2} \tag{5.7}$$

where K, n_1, and n_2 are material dependent constants. Furthermore, the data shown in Figures 4.16 and 4.17 was utilized to compute constants K, n_1, and n_2 by non-linear regression analysis with the aid of the computer software DataFit from Oakdate Engineering. The resultant constants are displayed in Table 5.1. For all materials, the coefficient of multiple determination[3]

Table 5.1: Equation 5.7 constants found by non-linear regression analysis.

material	K	n_1	n_2	r^2
080A15	9.489×10^{-11}	3.676	-0.5502	0.937
080M40	3.076×10^{-11}	3.942	-0.6311	0.964
304S15	8.201×10^{-12}	4.643	-0.2555	0.965
6082-T6	7.641×10^{-11}	3.773	-0.0103	0.946

(r^2) presents values fairly close to one, meaning that Equation 5.7 is a good empirical model to represent the relationship between I_{power}, V, and t_1. Figure 5.4 shows plots of the relationship stated by Equation 5.7 for the four work materials.

5.3 Cutting Power and Acoustic Emission Power

Most AE energy models presented in Section 2.2.2 regard I_{power} to be proportional to the plastic work rate of deformation [7, 57, 60, 62, 63, 65]. In Section 2.1.2, Equation 2.25 suggests that the total cutting power is proportional to the tangential force and cutting speed, i.e. $\dot{U} = F_X V$, and that $\dot{U}$ is essentially the summation of the work rate produced in the primary and secondary deformation zones. Consequently, the following equation can be derived:

$$I_{\text{power}} = K\dot{U} = KF_X V \tag{5.8}$$

where K is a constant of proportionality. In order to investigate this relationship, the experimental data presented in Section 4.1 (Test A results) were used to calculate values of I_{power} and $\dot{U}$. Due to the power function nature of the AE data, as described in Section 5.2, it was decided to plot the relationship between I_{power} and $\dot{U}$ on a logarithmic scale as well (Figures 5.5–5.7), in order to improve its visualization. On the logarithmic scale, the relationship between I_{power} and $\dot{U}$, as defined in Equation 5.8, is represented by a straight line with 45° inclination (slope $= 1$) and an intercept that depends on constant K. This straight line is plotted in Figures 5.5–5.7, but since K is unknown, a convenient vertical location of the line was chosen, so that it could be visualized together with the experimental data for comparison.

Figure 5.5 presents the relationship between I_{power} and $\dot{U}$ for varying V ($t_1 = 0.02$ and 0.1 mm/rev, and $w = 1.2$ mm). If the experimental data was in accordance with Equation 5.8, there would be a value for K that made all the experimental data points fall on the 45° inclination straight line. Although the experimental data seem to fall on a straight line, it shows a slope larger than 45°. However, it seems that the experimental values form a relationship between I_{power} and $\dot{U}$ that is, within a certain margin of error, independent of the work material.

---

[3] The coefficient of multiple determination $r^2 = \sum_{i=1}^{n}(\hat{y}_i - \bar{y})^2 / \sum_{i=1}^{n}(y_i - \bar{y})^2$, where $\hat{y}_i$ and y_i are the predicted and experimental response values for the i^{th} data point; and $\bar{y}$ is the mean of the experimental responses for all n data points. A good fit will result in r^2 values close to one, whereas a poor fit will result in r^2 values close to zero.

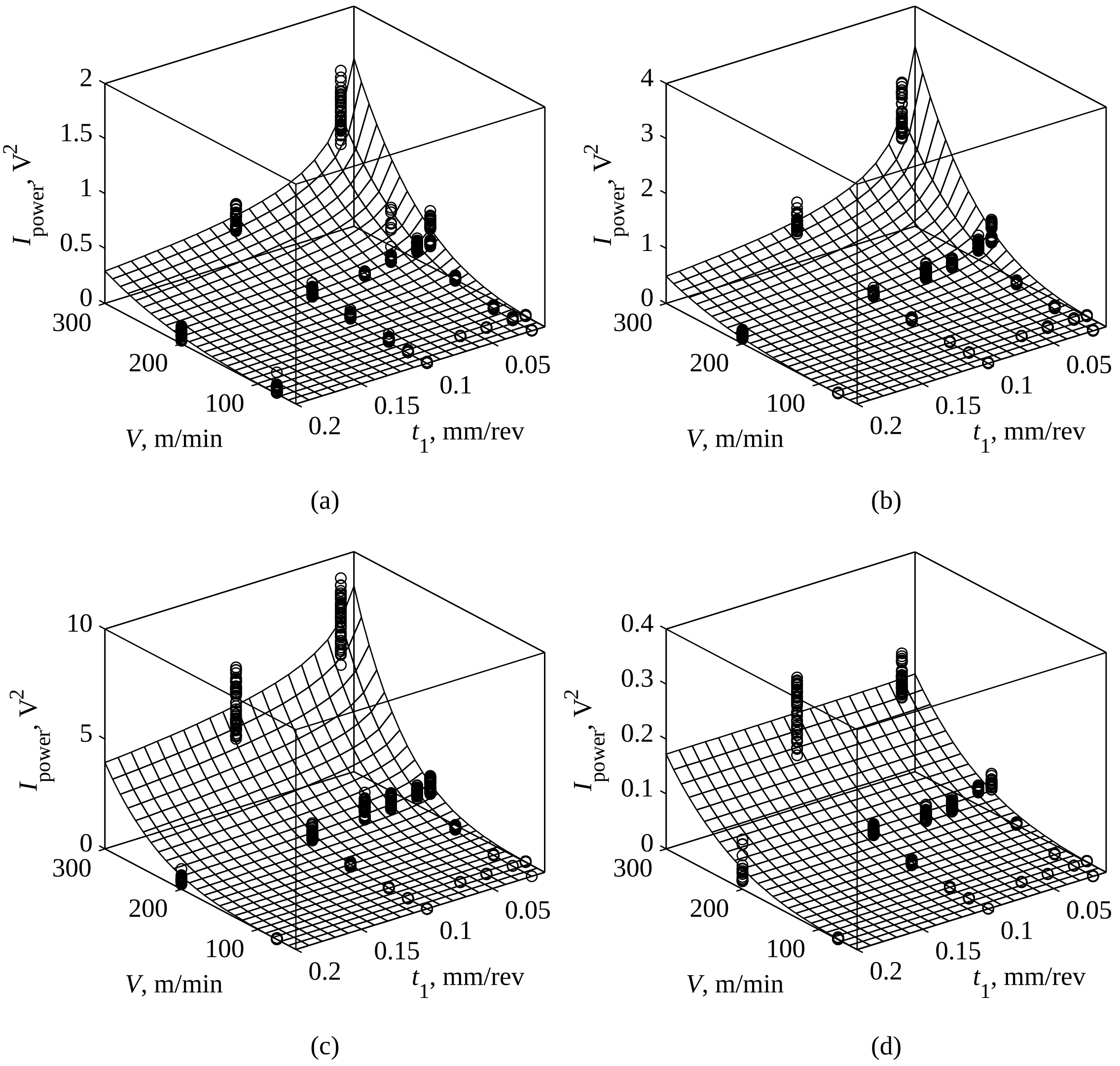

(a)

(b)

(c)

(d)

Figure 5.4: Three-dimensional representation of I_{power} as a function of cutting speed and feed rate. (a) 080A15. (b) 080M40. (c) 304S15. (d) 6082-T6.

Figure 5.6 presents the relationship between I_{power} and $\dot{U}$ for varying t_1 ($V = 75$ m/min and 200 m/min, and $w = 1.2$ mm). For $V = 75$ m/min (Figure 5.6a), I_{power} seems to be more or less insensitive to $\dot{U}$ for varying t_1, contradicting the relationship defined by Equation 5.8. Moreover, the relationship held by Equation 5.8 is also not verified when $V = 200$ m/min, since I_{power} experimental values approximate to straight lines of negative slope and different K values for different work materials. As a result, Equation 5.8 is not confirmed by the experimental data when t_1 is varied.

Figure 5.7 show the relationship between I_{power} and $\dot{U}$ for varying w. It can be observed that, in certain cases, the relationship approximates to a straight line with 45° inclination, e.g. when $V = 75$ m/min and $t_1 = 0.02$ for work materials 080A15, 080M40, and 304S15 (Figure 5.7a).

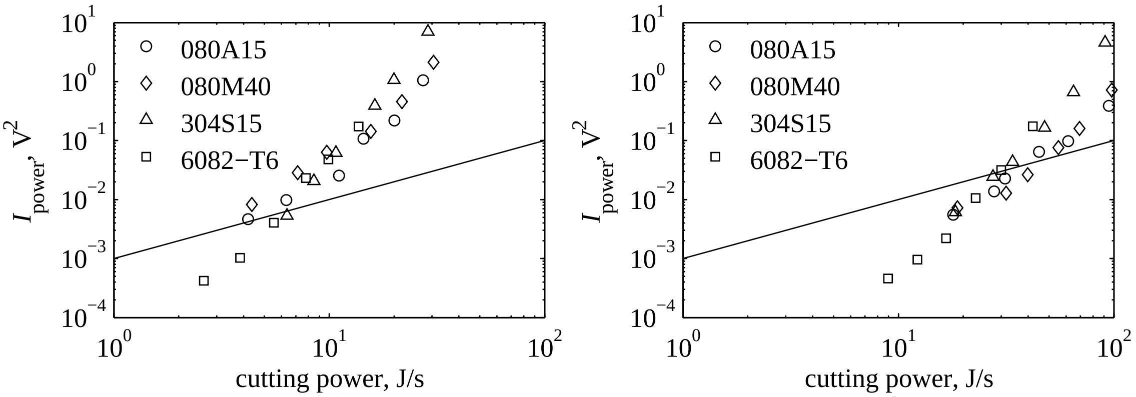

(a) (b)

Figure 5.5: Relationship between I_{power} and cutting power for varying cutting speed; $w = 1.2$ mm. (a) $t_1 = 0.02$ mm/rev. (b) $t_1 = 0.1$ mm/rev.

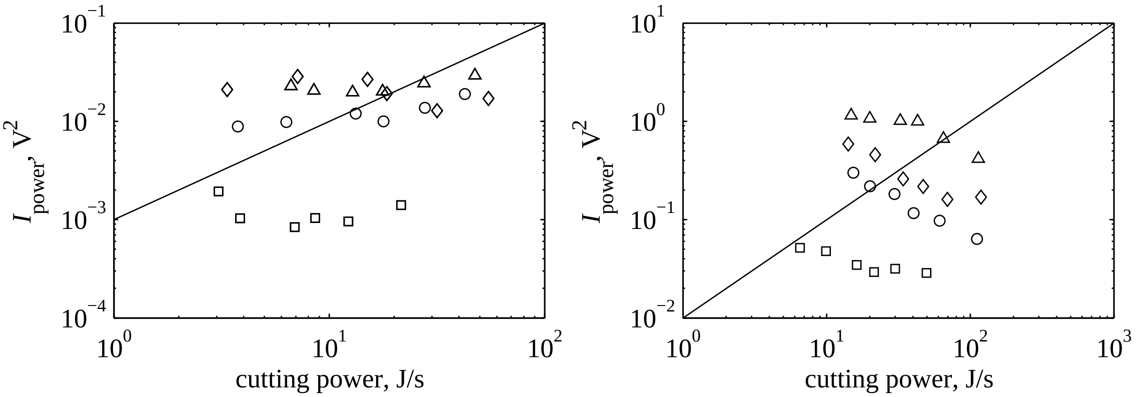

(a) (b)

Figure 5.6: Relationship between I_{power} and cutting power for varying feed rate; $w = 1.2$ mm. (a) $V = 75$ m/min. (b) $V = 200$ m/min.

However, in most cases, the relationship between I_{power} and $\dot{U}$ fall on a line with an inclination less that 45°. Moreover, it can also be observed that the experimental data of I_{power} against $\dot{U}$, when approximated to straight lines, present different values of K for different work materials, opposing the relationship held by Equation 5.8.

The relative agreement found in the published energy models [7, 57, 60, 62, 63, 65] is mainly due to the fact that the AE data was given from cutting tests where normally only V was changed, i.e. t_1 and w were kept constant. Figure 5.5 also shows that when only V is varied, the relationship between I_{power} and $\dot{U}$, when plotted on a logarithmic scale, seems to fall on a single straight line for different work materials. However, this line exhibits a slope higher than one, so that in order to fit the experimental data, Equation 5.8 may be changed as follows: $I_{\text{power}} = K\dot{U}^n$, where n is the slope of the line in the logarithmic scale ($n > 1$), and K and n depend on t_1 and w but are

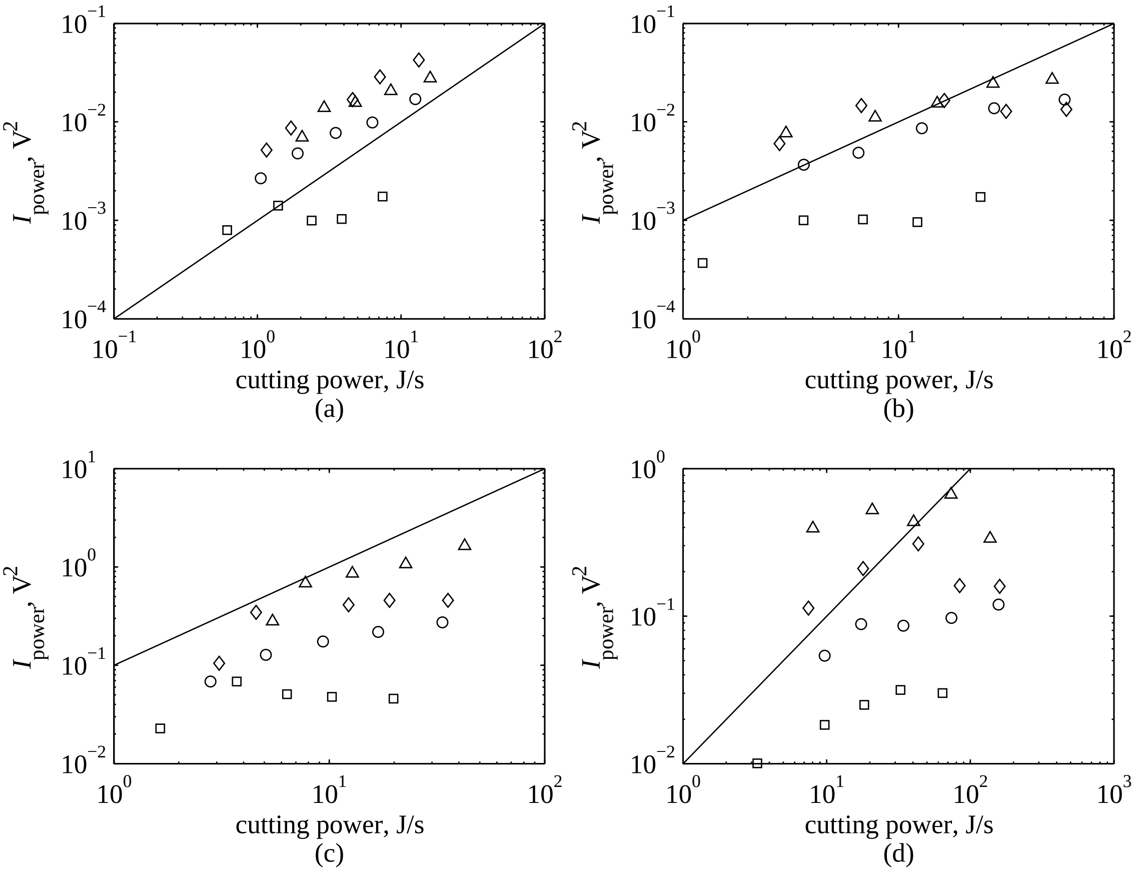

Figure 5.7: Relationship between I_{power} and cutting power for varying width of cut. $V = 75$ m/min, $t_1 = 0.02$ mm/rev. (a) $V = 75$ m/min, $t_1 = 0.02$ mm/rev. (b) $V = 75$ m/min, $t_1 = 0.1$ mm/rev. (c) $V = 200$ m/min, $t_1 = 0.02$ mm/rev. (d) $V = 200$ m/min, $t_1 = 0.1$ mm/rev.

work material independent. Dornfeld and Kannatey-Asibu [62] presented AE data for varying V and t_1, but although their energy model equated I_{power} proportional to V and t_1, I_{power} seemed to be proportional to V^n, where $n > 1$, and no clear relationship was observed between I_{power} and t_1. Lan and Dornfeld [64] pointed out that although the relationship presented by Dornfeld and Kannatey-Asibu [62] provided some indication of the cutting parameters upon which AE depends, the effects of t_1 and w have not clearly been evaluated experimentally. Kannatey-Asibu and Dornfeld [60] presented experimental AE data for varying V and tool rake angle (α), and although, in their model, I_{power} was proportional to V, straight lines were plotted for the relationship between $\sqrt{I_{\mathrm{power}}}$ and V, suggesting that I_{power} was proportional to V^2. Moreover, different relationships were observed between $\sqrt{\dot{U}}$ (theoretical $\sqrt{I_{\mathrm{power}}}$) and I_{RMS} (experimental $\sqrt{I_{\mathrm{power}}}$) for different α values, suggesting that constant K of Equation 5.8 was dependent on α. Saini and Park [65] presented a more complex model, and although it showed good agreement with experimental data, t_1 and w were, again, kept constant. The results presented by Blum and Inasaki [7] exhibited some agreement between theoretical and experimental I_{power} when V was varied, but opposite trends were observed between experimental and theoretical I_{power} when t_1, α, and w were varied. Nevertheless, the model presented by Rangwala and Dornfeld [57] presented an excellent agreement between I_{power} and the power of dislocation damping ($\dot{U}_{\text{D}}$) for experimental data where both V and t_1 were varied. However, the range of t_1 values (0.1–0.2 mm/rev) was much narrower than the range of Test A experimental values (0.01–0.2 mm/rev), and, therefore, as can be seen in Figures 4.17, the level of AE tends normally to increase with decreasing t_1 when t_1 is low, whereas the experimental data provided by Rangwala and Dornfeld exhibited more or less a constant level of AE for varying t_1.

5.4 Temperature Measurement Analysis

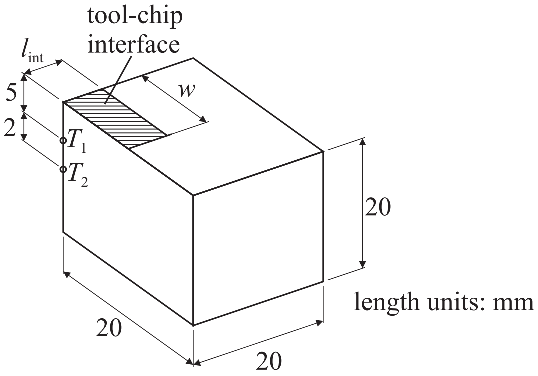

Figure 5.8: Geometry of finite-difference temperature model.

As described in Section 3.1.2 (Figure 3.9), two thermocouples were installed some distance below the top of the cutting tool (5 and 7 mm, respectively), so that the temperatures at points 1 and 2 (T_1 and T_2) were a result of the heat transfer caused by the high temperature at the tool-chip interface. Hence, the finite-difference numerical technique was employed, so that the relationship between the actual mean temperature at the tool-chip interface T_{int} and temperatures T_1 and T_2 could be determined. The finite-difference model was defined as follows (Figure 5.8): the tool was simplified to a rectangular block (20 mm in all three dimensions), where the tool-chip contact area is a rectangular zone with dimensions w (width of cut) and l_{int} (tool-chip interface length), placed at a corner of the block; temperature T_{int} was assumed constant over the whole tool-chip contact area; heat was assumed to flow from the tool-chip area to the rest of the tool due to conduction; finally, convective heat was assumed to flow between the tool and the outside surrounding air (temperature T_∞). Since the thermal conductivity of the tool material (κ) and the coefficient of heat convection (h) were unknown, these values were based on published values ($\kappa = 50$ W/m-°C and $h = 100$ W/m^2-°C) [20]. It must be added that very accurate values of κ and h are not so important, since the objective of this model is an evaluation of the relative effect of T_{int}, w, and l_{int} on the measurement of T_1 and T_2. Appendix C shows the finite-difference

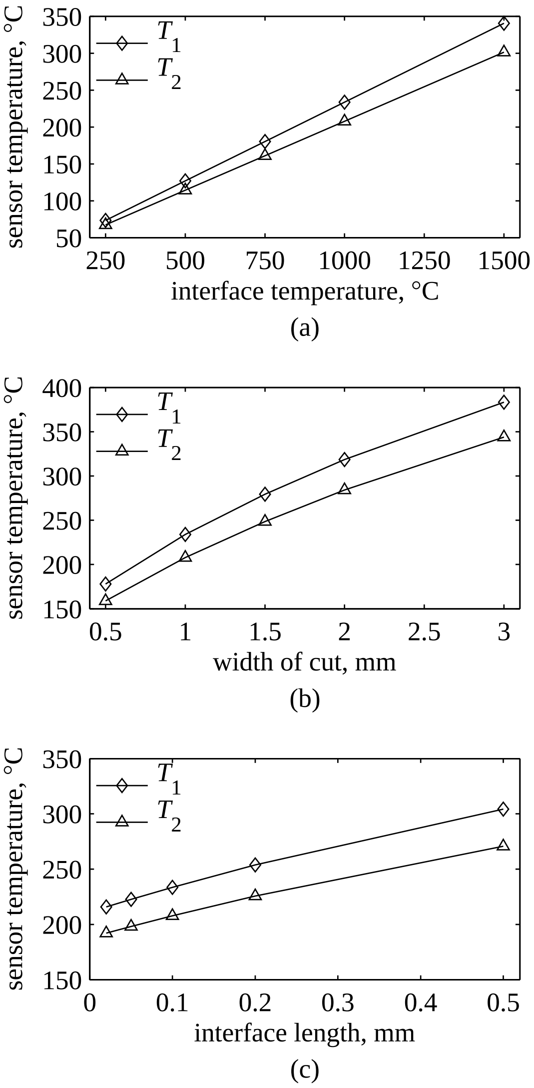

Figure 5.9: Prediction of sensor temperatures T_1 and T_2 for known T_{int} and tool-chip interface dimensions. (a) Variation of T_1 with T_{int}; $w = 1$ mm and $l_{\text{int}} = 0.1$ mm. (b) Variation of T_1 with w; $T_{\text{int}} = 1000$°C and $l_{\text{int}} = 0.1$ mm. (c) Variation of T_1 with l_{int}; $T_{\text{int}} = 1000$°C and $w = 1$ mm.

technique in more detail.

Figure 5.9 exhibits the variation of T_1 and T_2 with T_{int}, w, and l_{int} (Figures 5.9a, 5.9b, and 5.9c, respectively). It can be observed that T_1 is predicted to be higher than T_2, as expected from practical experience, since thermocouple 1 is further than thermocouple 2 from the tool-chip interface. Moreover, T_1 and T_2 increase linearly with increasing T_{int}, which is a sound relationship, since in order to calculate T_{int}, one simply needs to multiply the measured values of T_1 or T_2 by some constant value. However, it is also observed that T_{int} also varies with both w and l_{int}; this makes the prediction of T_{int} from measured values difficult because, although w is known, l_{int} is dependent on the cutting process and, therefore, unknown in advance.

5.5 Oxley's Model Results and Analysis

Section 2.1.4 and Appendix A describe a machining theory, formulated by Oxley and co-workers, that predicts, for example, the geometry, cutting forces, stresses, and temperatures of metal cutting [18]. The model requires as inputs the cutting conditions V, t_1, w, α, T_W (initial workpiece temperature), the thermal material properties c (specific heat) and κ (thermal conductivity), the density of the material (ρ), and, finally, the flow stress properties of the work material. In this section, the predictive results from the model are analysed and compared with the experimental results from Test A (Section 4.1). However, only results for the carbon steel work materials (080A15 and 080M40) were obtained, since no reliable flow stress data could be found for the other two work materials. It must be added that since the model did not converge for some of the lowest values of V and t_1, the model was run for the higher values of V and t_1, and then the results for the lower values of V and t_1 were estimated by extrapolation. Besides, experimental results from Test B (Section 4.2) for the variable workpiece surface temperature (T_WS) are compared with predictions from Oxley's model, where, in this case, T_W was assumed to be equal to T_WS.

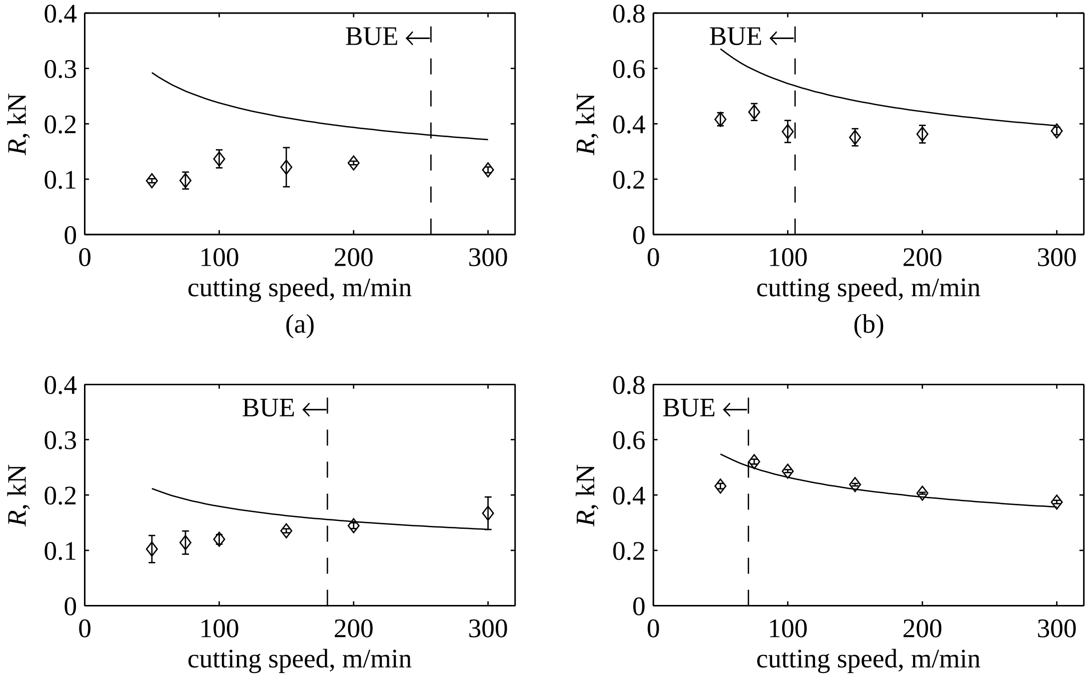

(a) (b)

(c) (d)

Figure 5.10: Variation of R with cutting speed; $w = 1.2$ mm. (a) 080A15; $t_1 = 0.02$ mm/rev. (b) 080A15; $t_1 = 0.1$ mm/rev. (c) 080M40; $t_1 = 0.02$ mm/rev. (d) 080M40; $t_1 = 0.1$ mm/rev.

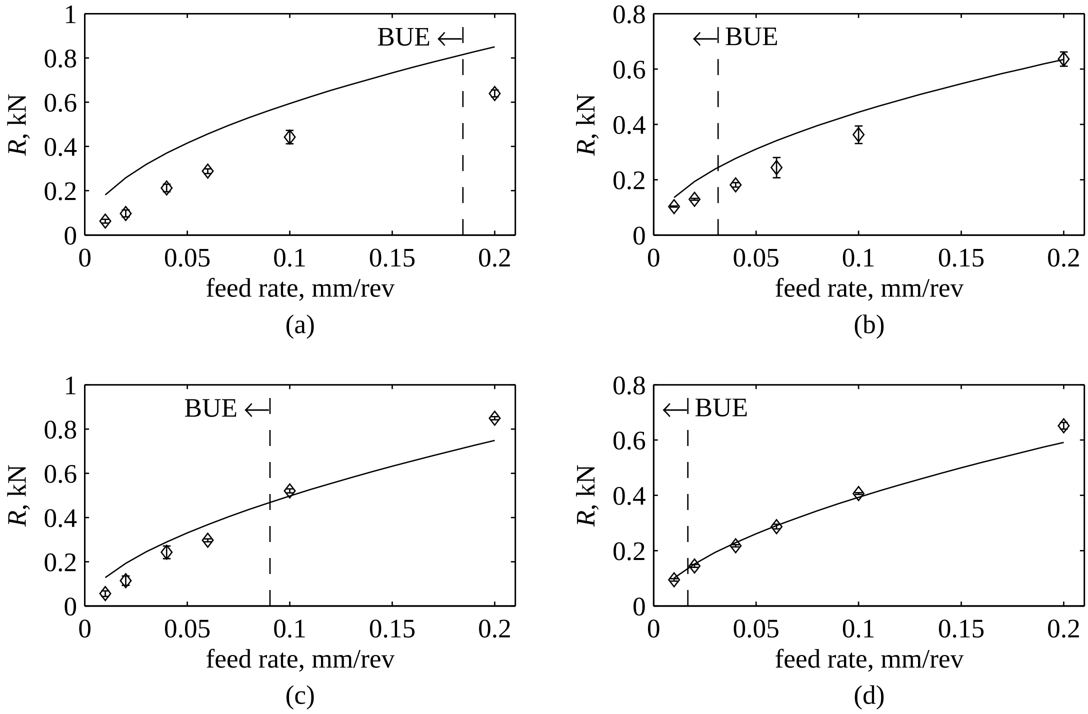

Figure 5.11: Variation of R with feed rate; $w = 1.2$ mm. (a) 080A15; $V = 75$ m/min. (b) 080A15; $V = 200$ m/min. (a) 080M40; $V = 75$ m/min. (b) 080M40; $V = 200$ m/min.

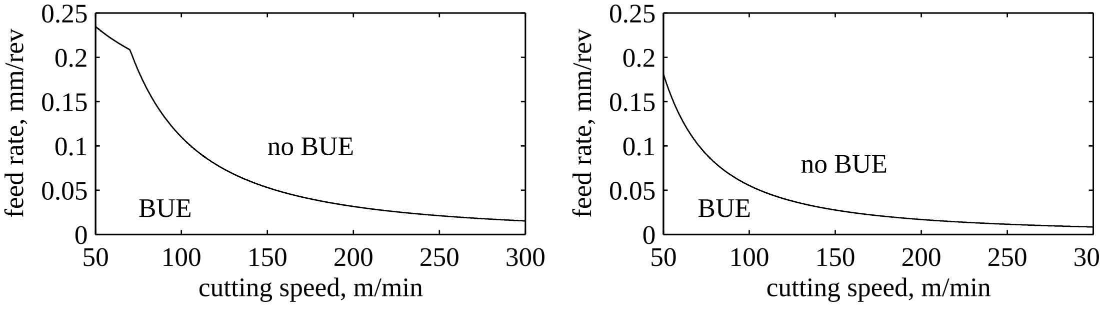

Figure 5.12: Prediction of BUE for varying cutting speed and feed rate. (a) 080A15. (b) 080M40.

5.5.1 Cutting Forces

Figure 5.10 shows the variation of the resultant cutting force (R) with V; and Figure 5.11 shows the variation of R with t_1. The predictions of R are plotted along with the experimental results from Test A. It can be observed that there is a fairly good agreement between predictive and experimental values, especially when V and t_1 are high. However, for low values of V, especially when $t_1 = 0.02$ (Figures 5.10a and 5.10c), predictions of R seem to be substantially lower than

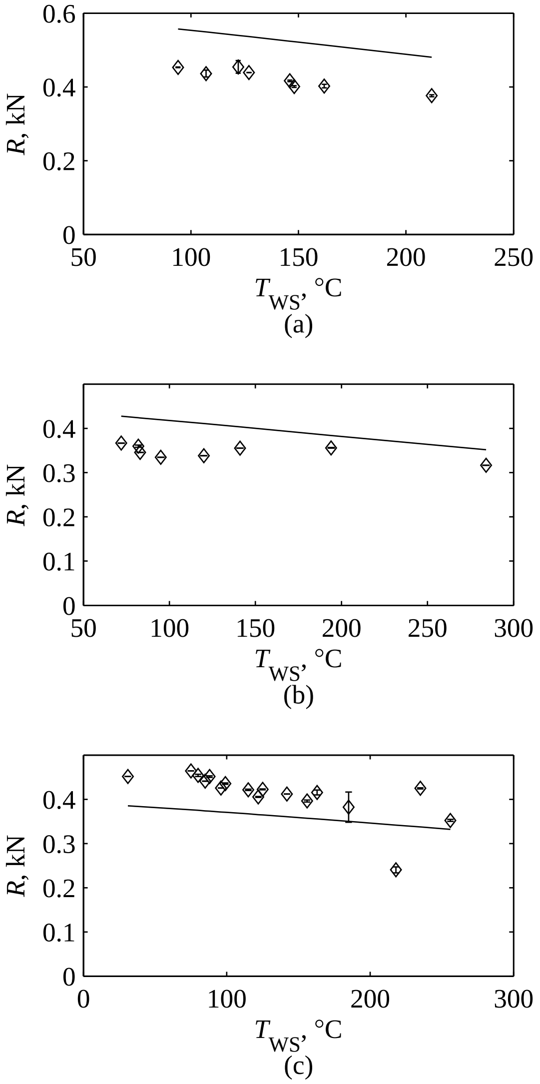

Figure 5.13: Variation of R with work surface temperature. (a) 080A15; $V = 75$ m/min; $t_1 = 0.1$ mm/rev. (b) 080A15; $V = 200$ m/min; $t_1 = 0.1$ mm/rev. (c) 080M40; $V = 200$ m/min; $t_1 = 0.1$ mm/rev.

the experimental values of R. Moreover, during the experimental procedure, the occurrence of BUE was noticed, since traces of material attached to the tool were observed after cutting for the lowest values of V and t_1. As discussed previously in Section 2.1, BUE tends to increase the effective rake angle, resulting in a reduction of the cutting forces [35]. In addition, Hastings *et al.* [18, 51] introduced the following criterion to predict BUE: BUE will be formed if $T_{\text{int}} < 1000$ K and $T_{\text{mod}} < 700$ K, where T_{int} and T_{mod} are the mean and velocity-modified temperatures at the tool-chip interface, respectively. With values of T_{int} and T_{mod} obtained from Oxley's model, the criterion of BUE predictions were calculated for different values of V and t_1; these results are shown in Figure 5.12, where the line that represents the onset of BUE is plotted against

V and T_1. This criterion was also used to mark (as a vertical dashed line) the onset of BUE in the plots shown in Figures 5.10 and 5.11. As a result, it can be observed that the experimental values of R that fall below predictions occur mainly in the range of V and t_1 that lead to the prediction of BUE according to the above criterion.

Figure 5.13 shows the variation of R with T_{WS}. Experimental data from Test B are plotted along with the prediction from Oxley's model. It can be observed that experimental and predictive values present similar trends and are in the same order of magnitude; however, experimental result from the 080A15 work material (Figures 5.13a and 5.13b) fall slightly bellow predictions, whereas experimental result for the 080M40 work material fall slightly above predictions.

5.5.2 Cutting Temperatures

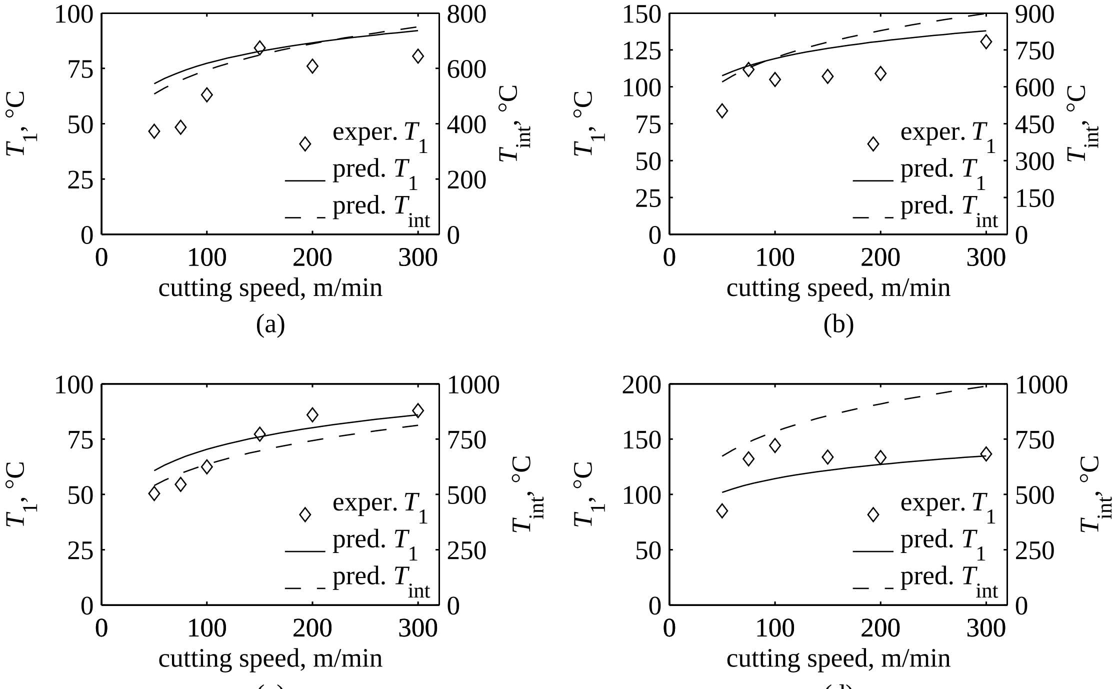

(a) (b) (c) (d)

Figure 5.14: Variation of T_{int} and T_1 with cutting speed; $w = 1.2$ mm. (a) 080A15; $t_1 = 0.02$ mm/rev. (b) 080A15; $t_1 = 0.1$ mm/rev. (c) 080M40; $t_1 = 0.02$ mm/rev. (d) 080M40; $t_1 = 0.1$ mm/rev.

Another quantity of interest is the interface temperature T_{int}. However, as indicated in Sections 3.1.2 and 5.4, although this temperature was measured during the experiments, it was measured indirectly by means of a thermocouple installed some distance below the interface (5 mm). The experimental results from thermocouple 1 (temperature T_1) are shown in Figures 5.14–5.17 along with Oxley's model predictions of T_{int}. Predictions of T_{int} are much higher than experimental values of T_1, and they also seem to exhibit fairly different trends. This difference in trends is

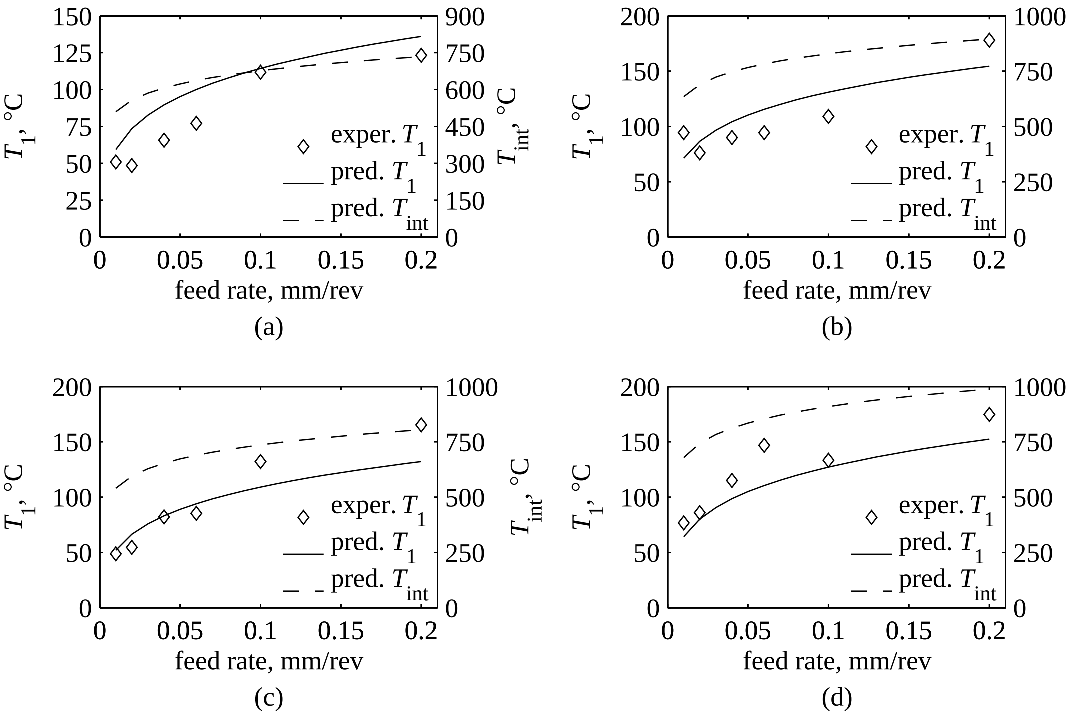

Figure 5.15: Variation of T_{int} and T_1 with feed rate; $w = 1.2$ mm. (a) 080A15; $V = 75$ m/min. (b) 080A15; $V = 200$ m/min. (a) 080M40; $V = 75$ m/min. (b) 080M40; $V = 200$ m/min.

more obvious in Figures 5.16 and 5.17, where T_{int} remains constant with w, but T_1 experimental increases with increasing w. In Section 5.4, predictions of T_1 using the finite-difference method showed that T_1 depends not only on T_{int}, but also on w and l_{int}. Subsequently, the same method was used here to determine T_1 as a function of T_{int}, l_{int}, and w (l_{int} was predicted with Oxley's model). Figure 5.18 shows the experimental values of T_1 plotted against the finite-difference predictions of T_1. Although with some scatter, a linear relationship was observed between predicted and experimental values of T_1, and, hence, a best-fitting straight line was plotted through the data points, giving the following relationship:

$$\text{experimental } T_1 = 0.586 \times \text{predicted } T_1 - 31.4°\text{C} \tag{5.9}$$

The slope of the resulting line is not equal to one, meaning that the predictive T_1 values are different but proportional to the experimental T_1 values. This is due to the inaccuracy of the thermal constants κ and h (50 W/m-°C and 100 W/m^2-°C, respectively) used during the finite-difference computations. Subsequently, it was decided to correct T_1 predictions by applying Equation 5.9. These corrected T_1 predictions are plotted in Figures 5.14–5.17 along with T_1 experimental values and T_{int} predictions. A fairly good agreement is observed between predictive and experimental values of T_1. Figure 5.14 show that although T_{int} increases with V, T_1 increases much slower with

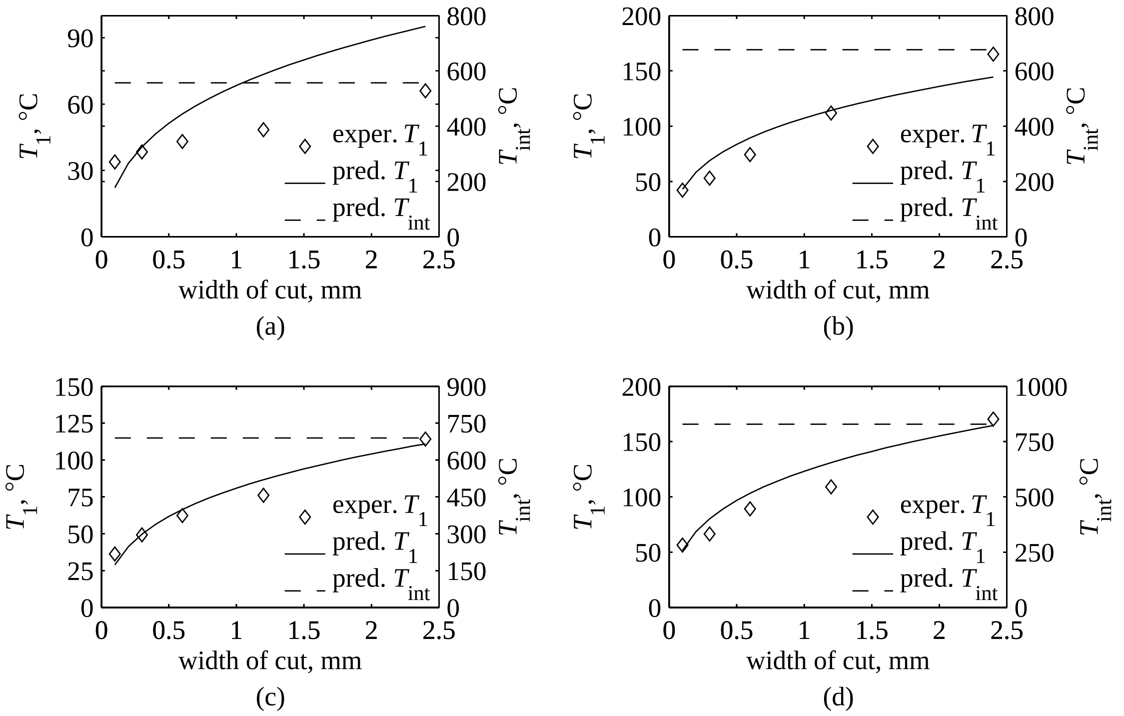

(a) (b) (c) (d)

Figure 5.16: Variation of T_{int} and T_1 with width of cut; work material 080A15. (a) $V = 75$ m/min, $t_1 = 0.02$ mm/rev. (b) $V = 75$ m/min, $t_1 = 0.1$ mm/rev. (c) $V = 200$ m/min, $t_1 = 0.02$ mm/rev. (d) $V = 200$ m/min, $t_1 = 0.1$ mm/rev.

V. This is due to the fact that l_{int} decreases with increasing V, and, as shown in Section 5.4, this tends to decrease T_1. Moreover, Figure 5.15 show that T_1 seems to increases more rapidly with t_1 than T_{int} does. This is due to the fact that l_{int} increases with t_1, and as shown in Section 5.4, this contributes to the increase in T_1. Finally, Figures 5.16 and 5.17 show that although T_{int} remains constant with w, T_1 increases considerably with w, since, as shown in Section 5.4, increasing w tends to increase T_1.

In conclusion, the previous analysis shows that the predictions of R and T_1 by means of Oxley's model (and finite-difference in the case of T_1) are in fairly good agreement with their respective experimental counterparts. This gives a good indication of the suitability of Oxley's model to simulating the mechanics of machining operations.

5.6 Influence of Width of Cut on Acoustic Emission

In orthogonal and semi-orthogonal cutting, the dimension of w is totally independent of the simplified two-dimensional geometry of the cutting process presented in Figure 1.5, and, therefore, a cutting process with width of cut Kw should act as if K independent and equivalent cutting processes with width of cut w were occurring alongside. Consequently, variables that are not directly

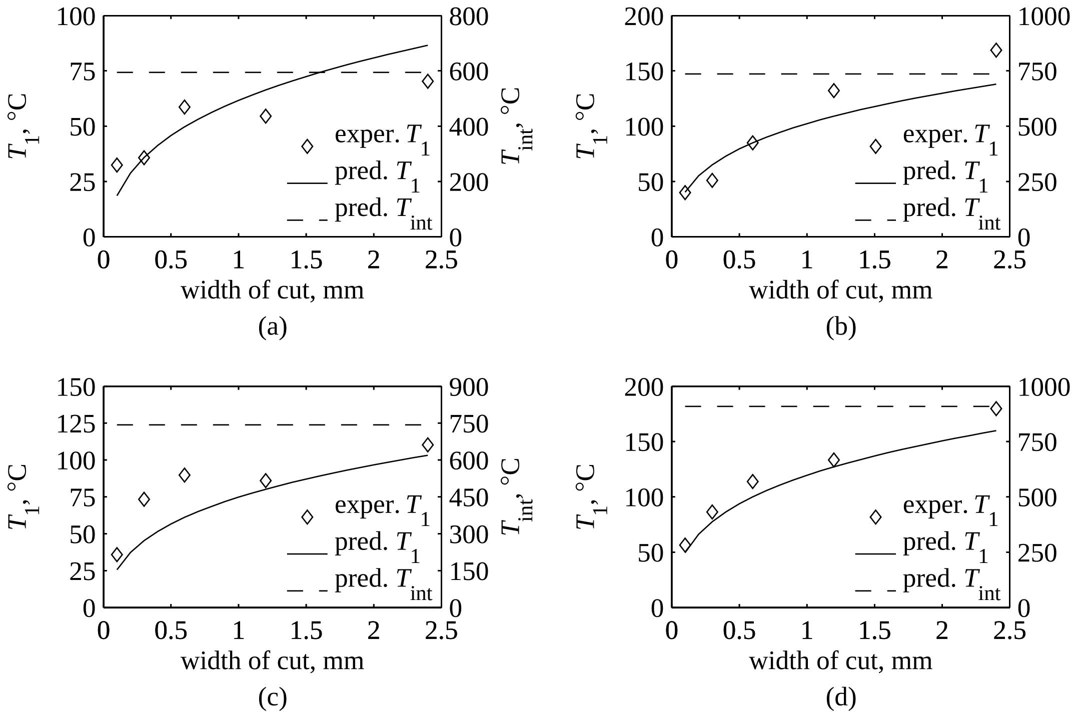

(a) (b) (c) (d)

Figure 5.17: Variation of T_{int} and T_1 with width of cut; work material 080M40. (a) $V = 75$ m/min, $t_1 = 0.02$ mm/rev. (b) $V = 75$ m/min, $t_1 = 0.1$ mm/rev. (c) $V = 200$ m/min, $t_1 = 0.02$ mm/rev. (d) $V = 200$ m/min, $t_1 = 0.1$ mm/rev.

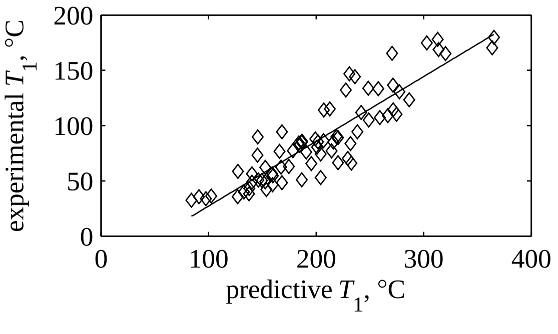

Figure 5.18: Relationship between experimental T_1 values and predictive T_1 values from finite-difference computations.

dependent on *w*, such as velocities, stresses, strains, strain rates, and temperatures, should not be affect by *w*; on the other hand, parameters that are directly dependent of *w*, such as forces and cutting power, should be a direct proportion of *w*. Following the same reasoning, if an energetic level equivalent to I_{power} were detected by a remote AE sensor for a process of width of cut *w*, and if the width of cut were increased to Kw, intuitively, an energetic level KI_{power} should be detected by the sensor. However, as discussed in Section 5.1, this is clearly not in agreement with Test A results (Figures 4.18–4.21) and also and with published results [3, 5, 7, 64, 66], since, generally, although it is true that, for low values of w, the value of I_{power} increases with increasing w, its rate of increase decreases as w increases, and for high values of w, the value of I_{power} becomes more or less constant with further increase in w. Moreover, Lan and Naerheim [66] proposed a pulsing test which employed one transmitting and one receiving AE transducer at each end of a tool holder, and they concluded that due to the phase interference between AE events at high rates, the amplitude of continuous-type AE may increase (constructive interference) or decrease (destructive interference), depending on the duration of the AE event, event rate, frequency, and characteristic of the wave propagation path. Messaritis and Borthwick [5] also suggested that an increase in volume of deforming material, due to an increase in w, should result in a proportional increase in the number of AE sources, and, consequently, in a proportional increase of AE activity; however, Messaritis and Borthwick reasoned that a remotely mounted transducer would not receive a signal proportional to the volume increase of AE activity due to the effects of attenuation, scattering, and mode conversions[4] and combinations. Consequently, it seems reasonable to conjecture that an increase in w will lead to an equivalent increase of AE activity at the generation source, but, at a remote location, this increase in AE activity may not be sensed proportionally. It is not the aim of the model that is going to be developed next to provide a truthful representation of the process of AE generation and transmission that occurs in metal cutting, but only to show how it may be possible that an increase in w may not correspond to a proportional increase of AE at a remote location in the cutting tool.

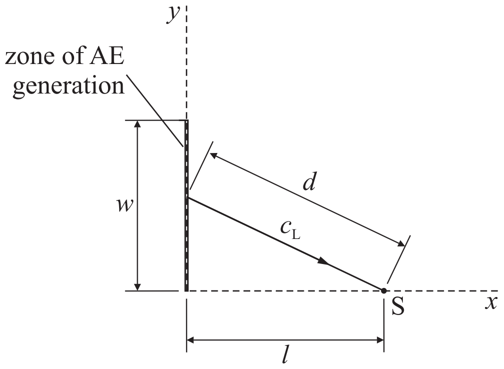

Figure 5.19: Diagram of simulation of AE generation and propagation.

The two-dimensional model presented in Figure 5.19 assumes that the generation source of AE is a line with length w (corresponding to the width of cut), and a transducer is at a point S, located perpendicular to one end of the generation line at distance l. Since this model is just an oversimplification of the real situation encountered in metal cutting, the following assumptions were made:

---

[4] Mode conversion occurs when a wave encounters an interface between materials of different acoustic impedances and the incident angle is not normal to the interface, as described in Section 2.2.1.

- All AE events occur in phase along the generation line. This is agreement with Gillis [55] (Section 2.2.1), who conjectured that if dislocation motion is the main generation mechanism of AE, each dislocation tends to move according to the stress field imposed by its moving neighbours, and, consequently, all dislocation lines should move cooperatively, so that all vibration waves produced by all moving dislocations are in phase.

- It is considered that the transmission medium (cutting tool) is infinite in size. As discussed in Section 2.2.1, when the AE waves meet the boundary of the cutting tool, the waves are reflected back into the tool, according to the law defined by Equation 2.40. Therefore, since the AE waves are reflected every time they reach a boundary, not only the direct waves represented in Figure 5.19 will arrive at point S, but also all reflected waves that get to point S. As a result, any attempt to realistically model AE propagation becomes extremely complex.

- Geometrical losses and attenuation are neglected. Since, as assumed previously, only direct waves are considered, propagation distances becomes less relevant, and, hence, geometrical losses and attenuation can be ignored because they are functions of propagation distance (Equations 2.37 and 2.38).

Moreover, at every point of the generation zone, an AE wave (per unit length) is generated according to the following equation:

$$I(t) = I_{\text{max}} \sin(2\pi f t) \tag{5.10}$$

where I_{max} is the maximum amplitude of the wave (per unit length), t is the time, and f is the frequency of the wave. Every wave generated at a location y in the generation zone will travel a distance d before reaching point S, where the integrated effects of $I(t)$ between 0 and w can be computed as follows:

$$I_{\text{S}}(t) = I_{\text{max}} \int_{y=0}^{y=w} \sin\left[2\pi f\left(t - \frac{d}{c_{\text{L}}}\right)\right] dy \tag{5.11}$$

where

$$d = \sqrt{l^2 + y^2} \tag{5.12}$$

and c_{L} is the speed of longitudinal waves travelling in the medium. A computer routine produced in MATLAB (software from The MathWorks) was used to solve the integral defined by Equation 5.11 numerically. Furthermore, numerical values had to be assigned to the constants defined in Equations 5.11 and 5.12, and this was done with quantities in the same order of magnitude of those encountered in the real situation: $c_{\text{L}} = 6000$ m/s, which is the speed of longitudinal waves travelling in steel [58] (material of cutting tool); $l = 10$ mm, which is of the same order of magnitude of the distance between the cutting zone and the two AE sensors utilized in Tests A and B

(Section 3.1.2).

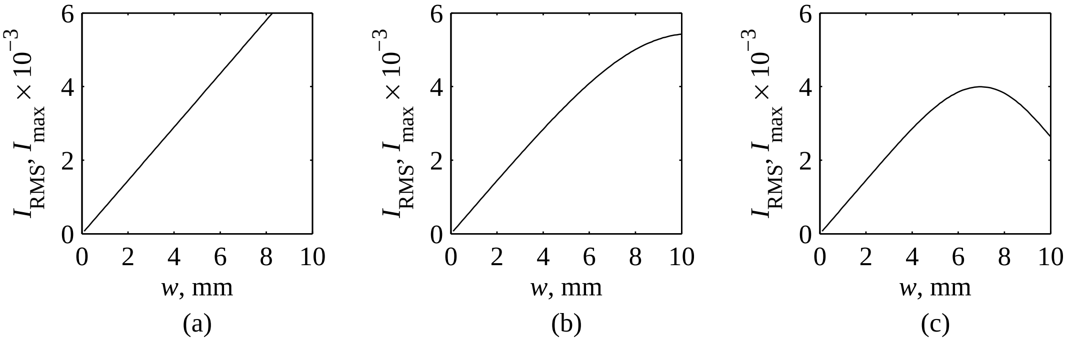

(a) (b) (c)

Figure 5.20: Simulation of detected AE at a point with varying w. (a) $f = 100$ kHz. (b) $f = 500$ kHz. (c) $f = 1000$ kHz.

Figure 5.20 shows the root mean square value of the resultant wave at point S (I_{RMS}) for different values of w and three different frequencies (100, 500, and 1000 kHz). It can be observed that when $f = 500$ kHz (Figure 5.20b), although the value of I_{RMS} increases with w, its rate of increase decreases with w, in a very similar fashion to the experimental AE trends due to varying w. Basically, as the wave generation location y increases from 0 to w, the resultant wave arriving at point S will be delayed by d/c_{L} (Equation 5.11), since distance d increases with y (Equation 5.12). At a high enough y value, the term d/c_{L} becomes significant, for, at point S, the phase difference of waves originating next to $y = 0$ and next to $y = w$ starts to be high enough, so that their interaction will not result in I_{RMS} values that are proportional to any further increase in w, resulting, ultimately, in a decrease of I_{RMS} with increasing w, as shown for $f = 1000$ kHz in Figure 5.20c.

In conclusion, the oversimplified model developed previously shows that when the sources of different AE events are located some distance away from each other, as when the generation volume is increased by increasing w in metal cutting, since the distance between the generation source and transducer may be different for different AE events, the resultant waves may arrive at the sensor out of phase, and, hence, the integration of all AE waves arriving at the transducer may be lower than what intuitively expected. The values of I_{RMS} shown in Figure 5.20 were produced for simulated waves with a single frequency, whereas the experimental results of I_{RMS} were computed from real waves with multiple frequencies within a specific frequency range; however, as it can be seen from Figure 5.20, the higher the frequency, the less linear becomes the relationship between I_{RMS} and w, and consequently, if a multiple-frequency wave were simulated, similar conclusions would be arrived at. Moreover, if the boundaries of the cutting tool were considered, the reflected waves reaching the sensor would also travel different distances if they were generated at different locations, contributing, in the same manner, to a difference in phase of the arriving waves. This model would be very complex, and geometrical losses and attenuation would have to be taken into account.

5.7 Influence of Basic Cutting Parameters on Acoustic Emission

In Section 5.3, it was shown that, in metal cutting, the energy models that relate I_{power} proportional to the work rate of deformation, though indicating some of the factors that may affect the generation of AE, generally fail to give an universal relationship that corroborates well with experimental data. Essentially, all the work of deformation ends up as thermal energy, but if considering plastic deformation as a source of AE, a minor part of this work must be released in the form of AE. Therefore, there must be some sort of relationship between AE and $\dot{U}$. By examining Equation 2.44, one may conclude that the basic parameters that influence $\dot{U}$ are: applied stress (σ), strain rate ($\dot{\varepsilon}$), and volume of material participating into deformation (v). In this section, a relationship between AE and these basic parameters is investigated, and the parameters that contribute the most to the generation of AE are evaluated. First, in Section 5.7.1, AE is analysed in terms of its energetic representation (I_{power}), and followed, in Section 5.7.2, by an analysis of the frequency content of AE (f_{mean}).

In Section 2.2.2, it was concluded that if cutting is performed with continuous chip formation, without BUE, and with a perfectly sharp tool, AE is assumed to be mainly generated due to plastic deformation from the primary and secondary zones of deformation (Figure 2.14a). However, Uehara and Kanda [15] measured AE signals simultaneously from both tool and workpiece sides and concluded that AE measured at the tool side is mainly affected by the secondary zone of deformation. Since all current experimental results of AE (Tests A and B) presented in Chapter 4 were performed with AE sensors located at the tool side (Figure 3.5), one can expect that the major contribution for the current measured AE signals is also due to the effect of secondary zone deformation. Besides, according to Oxley's theory [18], the tool-chip interface is represented by a rectangular plastic zone with uniform shear stress distribution, as represented in Figure 5.21 for a tool with a 0° rake angle. Therefore, in such a simplified case, the basic cutting parameters can be reduced to three constants: shear flow stress (k_{int}), shear strain rate ($\dot{\gamma}_{\mathrm{int}}$), and deformation volume ($v_{\mathrm{int}} = l_{\mathrm{int}}\delta t_2 w$, where δt_2 is the thickness of the secondary deformation zone).[5] Moreover, as dis-

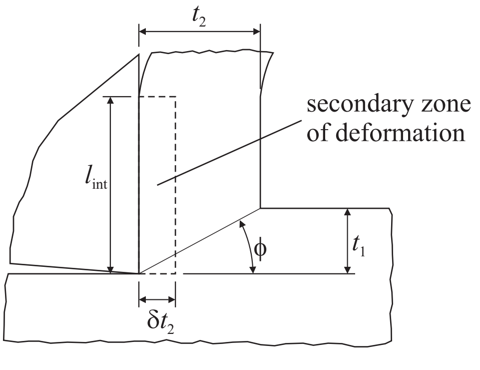

Figure 5.21: Simplified secondary shear zone geometry [18].

---

[5] In this case, the secondary work rate produced by plastic deformation at the tool-chip interface can be derived

cussed in Section 5.5, Oxley's model seems to give predictions of cutting forces and temperatures that are reasonably accurate, i.e. similar trends are obtained between predictive and experimental results, and the predictive values lie within the same order of magnitude of the experimental ones. As a result, one can reasonably expect that the values of k_{int}, $\dot{\gamma}_{\mathrm{int}}$, and v_{int} (and the other cutting parameters as well) can also be predicted by means of Oxley's model.

5.7.1 Energy Analysis

Figure 5.22 shows the variation of I_{power} with k_{int}, $\dot{\gamma}_{\mathrm{int}}$, and v_{int} for Test A data, but only for work materials 080A15 (Figures 5.22a, 5.22c, and 5.22e) and 080M40 (Figures 5.22b, 5.22d, and 5.22f), since, as discussed in Section 5.5, Oxley's model predictions are solely possible for carbon steels. No data for variable width of cut was employed ($w = 1.2$ mm), and account for the influence of w on the level of AE was discussed in Section 5.6. By observing Figure 5.22 and as discussed next, it can be concluded that none of the individual parameters can be used alone to model I_{power}:

AE and strain rate (Figures 5.22a and 5.22b) The level of AE increases with increasing $\dot{\gamma}_{\mathrm{int}}$, however, the data is very scattered, and it seems that there is another factor affecting the generation of AE.

AE and flow stress (Figures 5.22c and 5.22d) The data is very scattered and no clear trend is observed between I_{power} and k_{int}.

AE and volume (Figures 5.22e and 5.22f) Surprisingly, a quite defined relationship seems to exist between I_{power} and v_{int}: I_{power} decreases with increasing v_{int}, like the relationship $I_{\mathrm{power}} \propto v_{\mathrm{int}}^{n}$, where $n < -1$, or, in other words, I_{power} increases very rapidly as v_{int} tends to zero. This is a very disconcerting relationship, since if the only parameter affecting AE generation was v_{int}, when $v = 0$, no material was involved in cutting, and, therefore, no AE should be generated. For example, Figures 4.18–4.21, show that when w decreases ($\dot{\gamma}_{\mathrm{int}}$ and k_{int} are kept constant, and only v_{int} is affected), v_{int} decreases, and I_{power} is also observed to decrease, especially when w tends to zero, opposing the trend observed in Figures 5.22e and 5.22f. However, since v_{int} is also dependent on l_{int}, t_2 (chip thickness), and δ (ratio between thickness of secondary deformation zone and t_2), each of these three variables must be investigated in relation to its contribution to AE generation.

A strong relationship between AE energy and strain rate has been evidenced by many publications [5, 7, 57, 62], i.e. I_{power} increases with increasing strain rate. This relationship can also be acknowledged by the fact that I_{power} increases with increasing speed, which has been reported by numerous authors [5,7,57,60,62,65] and also confirmed by Test A data results (Figure 4.16), since strain rate is strongly dependent on speed. Messaritis and Borthwick [5] utilized Oxley's model

---

from Equation 2.44: $\dot{U}_{\mathrm{int}} = k_{\mathrm{int}}\dot{\gamma}_{\mathrm{int}}v_{\mathrm{int}}$.

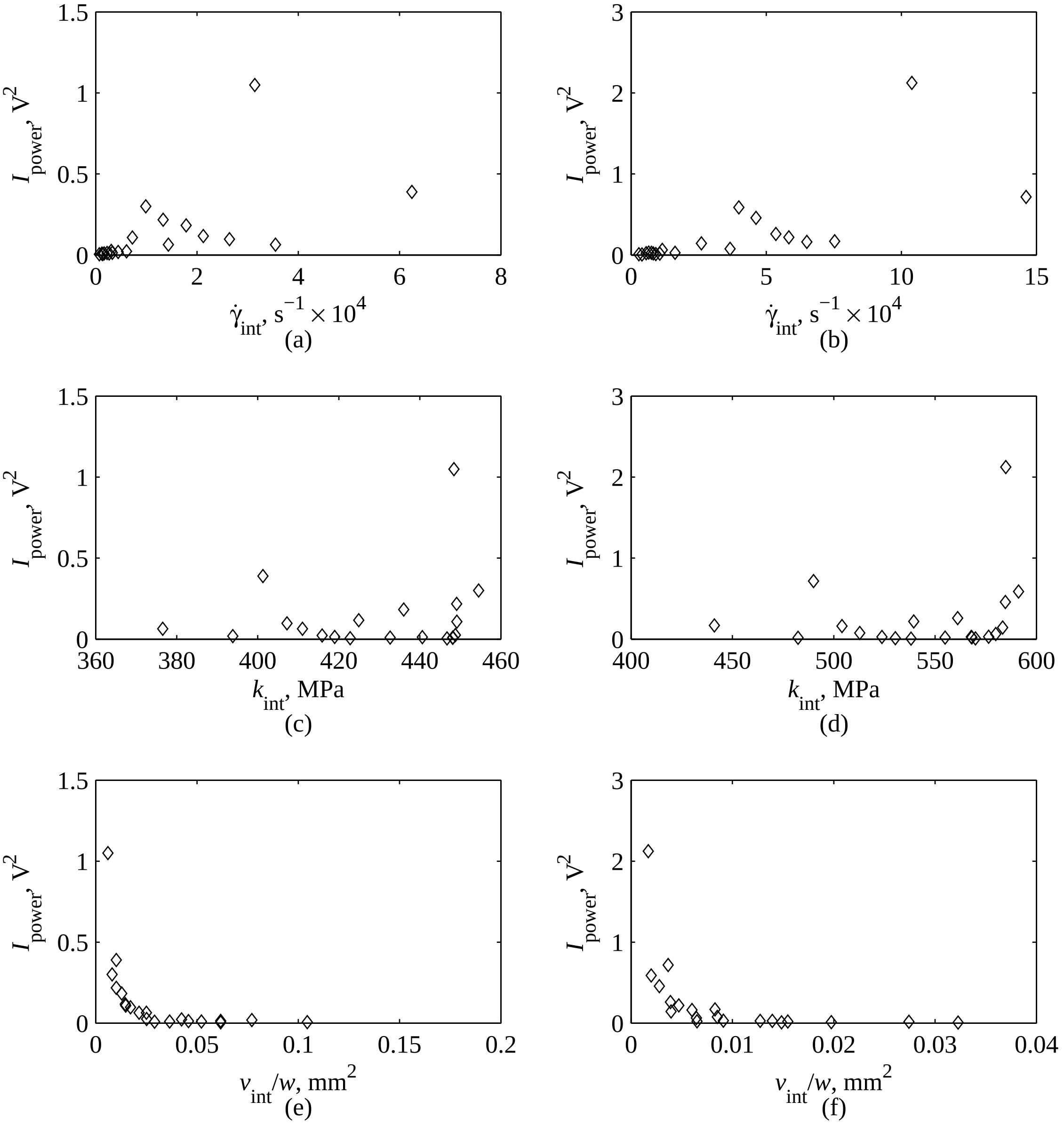

Figure 5.22: Variation of I_{power} with basic cutting parameters k_{int}, $\dot{\gamma}_{int}$, and v_{int}. (a) I_{power} against k_{int}; 080A15. (b) I_{power} against k_{int}; 080M40. (c) I_{power} against $\dot{\gamma}_{int}$; 080A15. (d) I_{power} against $\dot{\gamma}_{int}$; 080M40. (e) I_{power} against v_{int}; 080A15. (f) I_{power} against v_{int}; 080M40.

to predict shear strain rate ($\dot{\gamma}$) and concluded that since both $\dot{\gamma}$ and I_{power} present similar trends for varying values of V, t_1, and w, I_{power} might be mainly dependent on $\dot{\gamma}$, and the relationship held by Equation 2.49 was derived. However, Messaritis and Borthwick did not specify whether the value of $\dot{\gamma}$ represents the shear strain rate from the primary ($\dot{\gamma}_{AB}$) or from the secondary ($\dot{\gamma}_{int}$) zone of deformation. Therefore, it was decided to run Oxley's model, and it was found that both $\dot{\gamma}_{AB}$ and $\dot{\gamma}_{int}$ increase with V, and $\dot{\gamma}_{AB}$ decreases with t_1, which is in agreement with Messaritis and

Borthwick, whereas $\dot{\gamma}_{\mathrm{int}}$ increases with t_1, which is in disagreement with Messaritis and Borthwick. As a result, it was concluded that the value of $\dot{\gamma}$ presented by Messaritis and Borthwick must represent primary deformation strain rate $\dot{\gamma}_{\mathrm{AB}}$. Consequently, it was decided to plot I_{power} results from Test A against $\dot{\gamma}_{\mathrm{AB}}$, and, as shown in Figure 5.23, though I_{power} increases with $\dot{\gamma}_{\mathrm{AB}}$, the results are very scattered. The reason for the apparently well-behaved relationship between I_{power} and $\dot{\gamma}_{\mathrm{AB}}$ presented by Messaritis and Borthwick is due to the fact that their experiments were performed for a more reduced range of cutting conditions (V varied for an unique t_1 value, and t_1 varied for an unique V value) than the wider range of cutting conditions utilized in Test A experiments (Table 3.1).

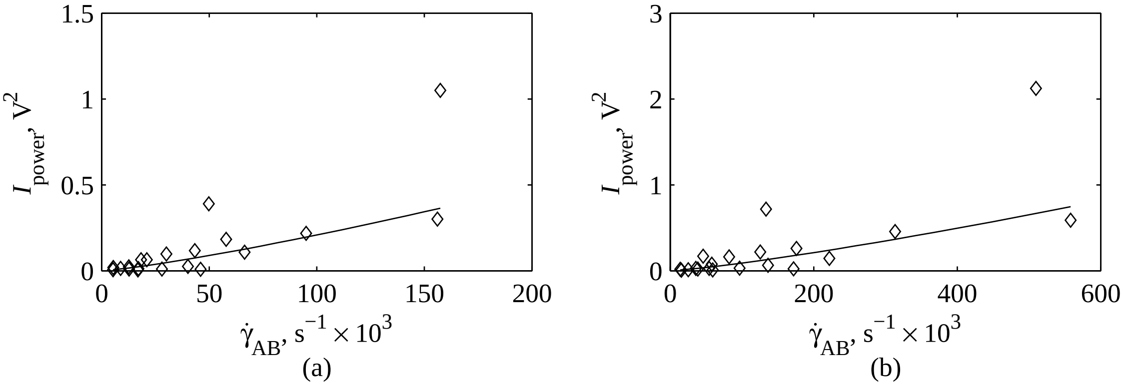

Figure 5.23: Relationship between $\dot{\gamma}_{\mathrm{AB}}$ and I_{power}. (a) 080A15. (b) 080M40.

In any case, as indicated before, the detected AE signals are thought to be mainly due to secondary zone deformation, and, therefore, a relationship between I_{power} and $\dot{\gamma}_{\mathrm{int}}$ (and also other secondary parameters) is of interest. Consequently, any apparent relationship between AE and primary parameters, as proposed by Messaritis and Borthwick [5], is observed because there must be some sort of relationship between primary and secondary parameters, which is evidenced by the two relationships shown in Figure 5.24. Consequently, as an approximately linear and material independent relationship seems to exist between the primary parameter $\dot{\gamma}_{\mathrm{AB}}$ and the product of the secondary parameters $\dot{\gamma}_{\mathrm{int}}\delta$ (Figure 5.24a), and as δ appears to form a material dependent relationship with the strain occurring at AB (γ_{AB}) (δ and its rate of increase increase with γ_{AB}, as shown in Figure 5.24b), it was decide to investigate an empirical relationship of the type

$$I_{\mathrm{power}} = K\gamma_{\mathrm{AB}}^{n_1}\dot{\gamma}_{\mathrm{int}}^{n_2} \tag{5.13}$$

The values of constants K, n_1, and n_2 were calculated by non-linear regression with the aid of computer software DataFit from Oakdale Engineering and are presented in Table 5.2.

The resultant coefficient of multiple determination r^2 is very close to one, meaning that Equation 5.13 is a good empirical model, especially because this relationship is material independent and, therefore, valid for both carbon steel work materials, as shown in Figure 5.25. From the

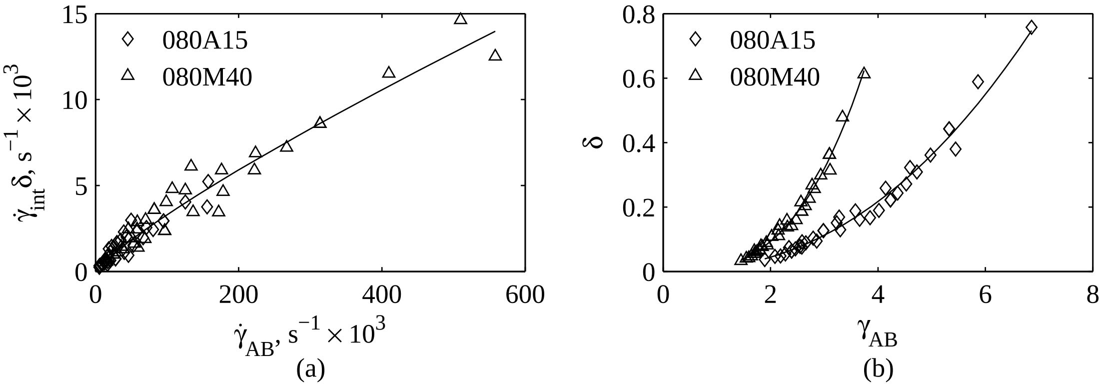

Figure 5.24: Relationship between primary and secondary parameters. (a) $\dot{\gamma}_{int}\delta$ against $\dot{\gamma}_{AB}$. (b) δ against γ_{AB}.

Table 5.2: Equation 5.13 constants found by non-linear regression analysis.

K	n_1	n_2	r^2
4.421×10^{-14}	4.511	2.385	0.994

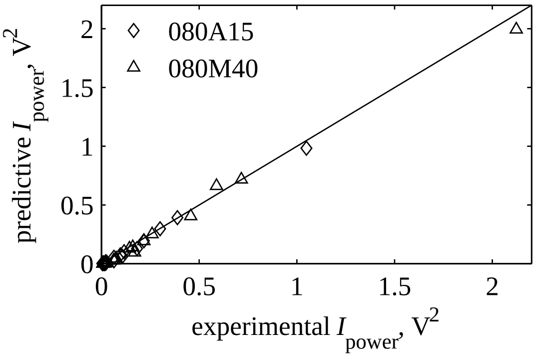

Figure 5.25: Relationship between experimental AE values and predictive empirical AE values.

preceding relationship, the following conclusions can be attained:

- As discussed before and presented by several authors, AE is strongly dependent on strain rate; I_{power} and its rate of increase increase with $\dot{\gamma}_{int}$.
- The amount of deformation work previously done to the material plays an important role on the generation of AE. Equation 5.13 shows that I_{power} and its rate of increase increase with the amount of strain that has been done to the material due to primary deformation (represented by γ_{AB}).[6]

---

[6] Actually, according to the parallel shear zone theory [30], only half of the total primary shear strain occurs at AB (Figure 2.3), so that the total shear strain occurring in the primary shear zone of deformation equals $2\gamma_{AB}$, but this does not alter the conclusions derived from Equation 5.13.

- Equation 5.13 indicates that the amount of AE generated is not dependent on work material properties. Therefore, although the flow stress properties in the primary (k_{AB}) and secondary (k_{int}) deformation zones play an important role in the macroscopic physics of cutting (such as geometry, stresses, and cutting power), it seems not to have a direct impact on the generation of AE. However, the two materials utilized are two carbon steels and, therefore, similar in structure. Therefore, it is very likely that Equation 5.13 will not be valid when AE data from a wider range of dissimilar materials is utilized.

5.7.2 Frequency Analysis

The plots shown is Figures 4.22–4.27 show that although f_{mean} remains more or less unchanged with t_1 and w, it decreases with V. At a first glance, this decrease of f_{mean} with V was quite surprising, since, as V increases the speed by which deformation takes place (strain rate), it was expected to move the spectra of the AE signals towards higher frequency levels. However, as pointed out by Rangwala and Dornfeld [19] and briefly mentioned in Section 5.1.2, increasing V results in more heat generation and, thus, in a rise of tool-chip interface temperature; as this rise in temperature tends to decrease f_{mean}, at a high enough value of V, the effect of the temperature rise offsets the effect of strain rate. As a result, it was decided to investigate the effect of both $\dot{\gamma}_{int}$ and T_{int} (values obtained by means of Oxley's theory [18]) on the value of f_{mean}.

Figure 5.26a shows the variation of f_{mean} with $\dot{\gamma}_{int}$ for work materials 080A15 and 080M40. The plot shows that, though the data is very scattered, generally, there is a slight decrease of f_{mean} with $\dot{\gamma}_{int}$. According to the previous reasoning, the increase of $\dot{\gamma}_{int}$ must also be accompanied by an increase of T_{int}, whose trend is confirmed by the plot shown in Figure 5.26b. Therefore, as confirmed by the relationship shown in Figure 5.26c, an increase of T_{int} will lead to a decrease of f_{mean}, independently on the variation of $\dot{\gamma}_{int}$. However, according to Rangwala and Dornfeld [19], for low values of V (below 60 m/min), where the cutting temperatures are low, the effects of strain rate dominate, and thus, at this range of V values, f_{mean} is expected to increase with $\dot{\gamma}_{int}$. Moreover, the relationship between f_{mean} and the other basic secondary parameters previously analysed for AE power (k_{int} and v_{int}) were also analysed, but no clear trends could be distinguished: f_{mean} remains more or less unchangeable with k_{int} and v_{int}, and the data is very scattered.

Figure 5.27 shows that f_{mean} is almost unaffected by different values of primary strain γ_{AB}; however, the data is very scattered. In fact, any relationship between f_{mean} and any cutting cutting parameter leads always to very high scatter. This is due to the fact that as AE sensors work in their range of resonance, the frequency content of the detected AE signals are dominated by this resonance frequency. The sensor used during the course of Test A (MICRO 80S) works with a peak frequency frequency of 324 kHz (from calibration certificate). The examples shown in Figures 4.14 and 4.15a show that there is a small peak at about this frequency. However, most AE energy is detected on the low frequency range of the spectrum (approximately below 200 kHz), and one likely explanation for this occurrence may be to the fact that between the generation source of AE (tool-chip interface) and the sensor, there are three interfaces of dissimilar materials

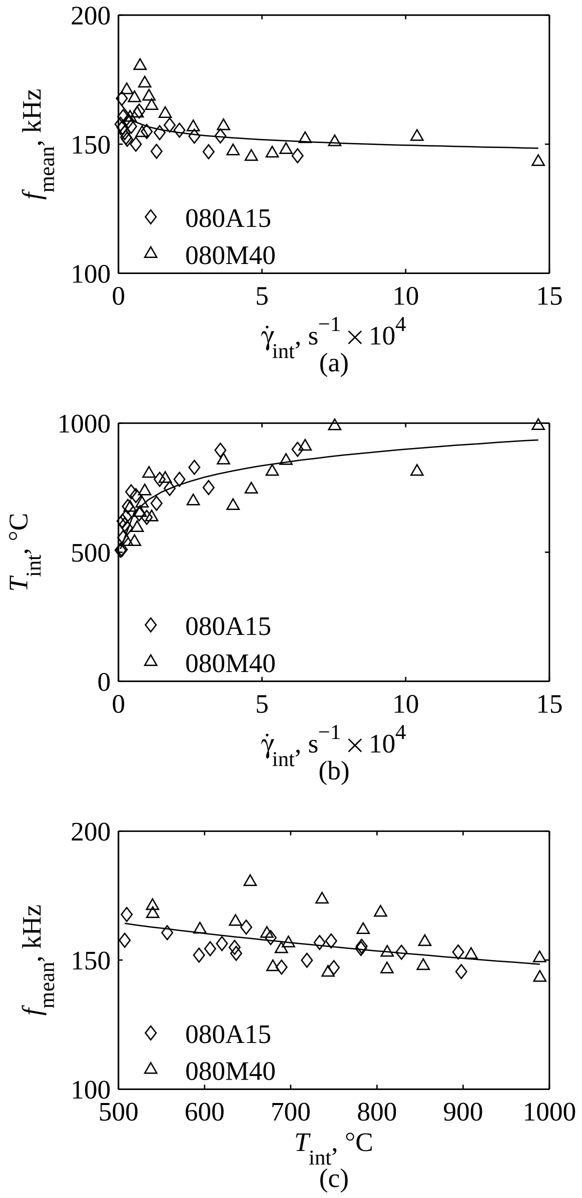

Figure 5.26: Variation of f_{mean} with $\dot{\gamma}_{int}$ and T_{int}. (a) f_{mean} against $\dot{\gamma}_{int}$. (b) T_{int} against $\dot{\gamma}_{int}$. (c) f_{mean} against T_{int}

.

(interface between cutting insert and shim, between cutting insert and tool holder, and between tool holder and AE sensor), and when AE waves cross these interfaces, the higher frequencies are the most attenuated (according to Equation 2.39, the attenuation coefficient *a* increases sharply with increasing frequency).

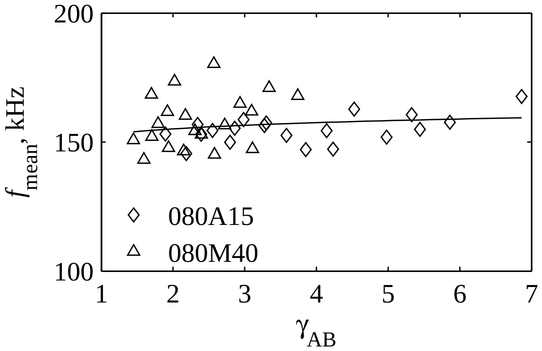

Figure 5.27: Variation of f_{mean} with γ_{AB}.

5.8 Temperature Effect on Acoustic Emission

Figure 5.28 shows that when I_{power} from Test A experiments is plotted against predictions of T_{int} from Oxley's theory [18], no clear trend can be distinguished, and the results are very scattered. However, Figures 4.32 and 4.33 in Section 4.2 show that, by using Test B experimental data from both material 080A15 and 080M40, the level of AE is observed to decrease with workpiece surface temperature (T_{WS}), and since as shown in Figure 5.29, a linear relationship is obtained between T_{WS} and predictions of T_{int} from Oxley's model (as discussed in Section 5.5, $T_{\mathrm{W}} = T_{\mathrm{WS}}$), I_{power} in Figure 5.28 should also decrease with T_{int}. Consequently, in this section, it was decided to study the influence of cutting temperature on AE using both Test A and Test B results and also to find out the apparent disagreement between Test A and Test B results.

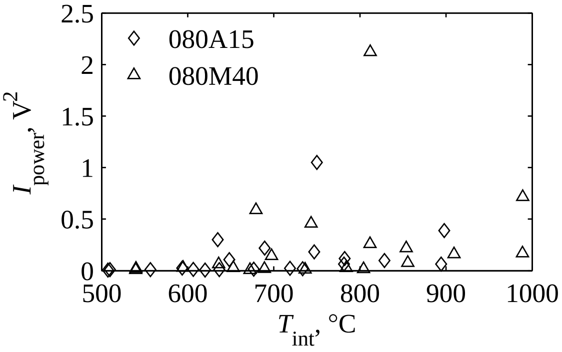

Figure 5.28: Variation of I_{power} with T_{int}.

Since the empirical relationship for I_{power} derived in Section 5.7.1 (Equation 5.13) is only dependent on γ_{AB} and $\dot{\gamma}_{\mathrm{int}}$, and not directly dependent on cutting temperature T_{int}, it was decided to find out how Test A values of γ_{AB} and $\dot{\gamma}_{\mathrm{int}}$ vary with T_{int}; this is shown in Figure 5.30 for both carbon steel work materials. Although the data is very scattered, it can be observed that γ_{AB} and

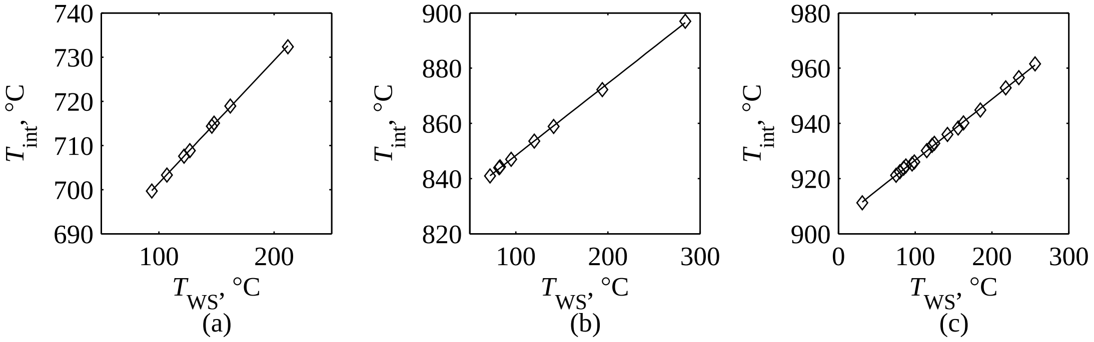

(a) (b) (c)

Figure 5.29: Variation of T_{int} with T_{WS}. (a) 080A15; $V = 75$ m/min; $t_1 = 0.1$ mm/rev. (b) 080A15; $V = 200$ m/min; $t_1 = 0.1$ mm/rev. (c) 080M40; $V = 200$ m/min; $t_1 = 0.1$ mm/rev.

its rate of decrease reduce with increasing T_{int}, and $\dot{\gamma}_{int}$ and its rate of increase rise with increasing T_{int}. Therefore, according to Equation 5.13, although increasing T_{int} should result in a decrease of I_{power} due to the reduction of γ_{AB}, in reality, the effect of increasing $\dot{\gamma}_{int}$ with T_{int} should dominate, and I_{power} should, therefore, increase, since the rate by which $\dot{\gamma}_{int}$ is increased rises with T_{int}, whereas the rate by which γ_{AB} is decreased falls with T_{int}.

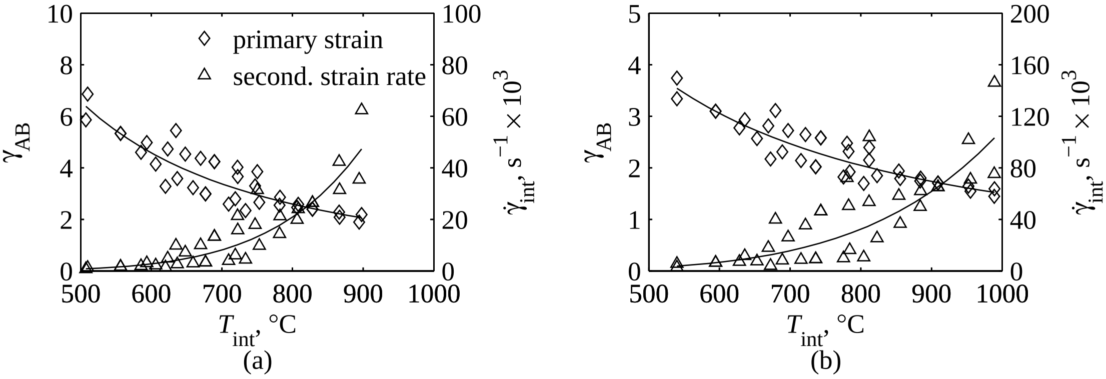

(a) (b)

Figure 5.30: Variation of γ_{AB} and $\dot{\gamma}_{int}$ with T_{int}. (a) 080A15. (b) 080M40.

It must be noted that the value of T_{int} is a result of the heat produced due to plastic deformation during metal cutting, and, therefore, T_{int} is dependent on the parameters which control plastic deformation, which clearly include γ_{AB} and $\dot{\gamma}_{int}$; however, T_{int} itself is also an important parameter governing the physics of plastic deformation. This is a consequence of the fact that in metal cutting, all variables are interrelated. Hence, if T_W is kept constant, it is believed that although increasing T_{int} contributes to a lowering of I_{power}, this effect is masked by the other two variables that are also observed to vary with increasing T_{int}, i.e. γ_{AB} and $\dot{\gamma}_{int}$. However, with Test B results, when the value of T_W is varied, an extra amount of heat is added to the cutting process, and T_{int} is not exclusively dependent on plastic deformation, and, therefore, as it can be seen in Figures 4.32

and 4.33, the level of AE is observed to decrease with increasing T_W, and with T_{int} as well, since T_{int} is proportional to T_W. Moreover, as shown in Figure 5.31, it should be noted that when T_W increases, γ_{AB} decreases and $\dot{\gamma}_{int}$ remains constant (Figure 5.31a), $\dot{\gamma}_{int}$ increases and γ_{AB} remains constant (Figure 5.31c), or both γ_{AB} and $\dot{\gamma}_{int}$ decrease (Figure 5.31b). In all these three cases, the variations of γ_{AB} and $\dot{\gamma}_{int}$ also contribute to the lowering of I_{power} together with that due to the increase of T_{int}.

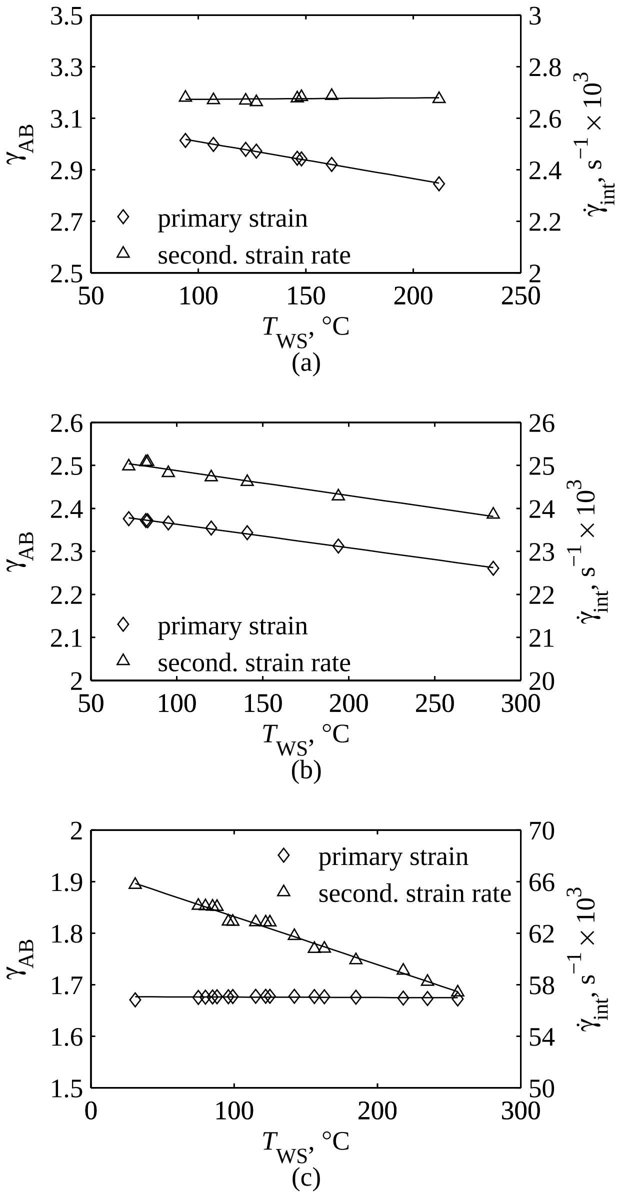

Figure 5.31: Variation of γ_{AB} and $\dot{\gamma}_{int}$ with T_{WS}. (a) 080A15; $V = 75$ m/min; $t_1 = 0.1$ mm/rev. (b) 080A15; $V = 200$ m/min; $t_1 = 0.1$ mm/rev. (c) 080M40; $V = 200$ m/min; $t_1 = 0.1$ mm/rev.

In conclusion, three variables seem to be the most significant factors affecting the generation of AE: γ_{AB} and $\dot{\gamma}_{\mathrm{int}}$, which are expected to increase the level of AE, resulting in Equation 5.13 derived in Section 5.7.1; and cutting temperature T_{int}, which is expected to lower the level of AE. However, since T_{int} is due to heat generated during the process of plastic deformation, T_{int} is related to the other process parameters like γ_{AB} and $\dot{\gamma}_{\mathrm{int}}$, and, therefore, its effect on the generation of AE is masked by the influence of γ_{AB} and $\dot{\gamma}_{\mathrm{int}}$, resulting in the indistinguishable relationship shown in Figure 5.28. However, if T_{int} is externally modified by cutting with different values of T_{W}, since γ_{AB} and $\dot{\gamma}_{\mathrm{int}}$ are not the only parameters affecting the value of T_{int}, the level of AE is very visibly seen to decrease with T_{int}, as, in this case, when T_{W} is varied, Equation 5.13 should not be valid any longer, since the effects of T_{int} due to varying T_{W} must also be taken into account.

5.9 Dislocation Motion as the Origin of Acoustic Emission

In Section 2.2.1, it is postulated that the two major sources of AE in metals are the motion of dislocations and also the development of cracks; continuous-type AE is associated with dislocation motion, whereas higher amplitude burst-type AE with cracking processes. Moreover, as discussed in Section 2.2.2, since metal cutting does not only involve plastic deformation, but also cracking due to chip and cutting tool fracture, as well as other burst-type AE emission processes, such as collision and entangling of chips, the resulting AE signal should be a combination of continuous-type emissions with randomly appearing high amplitude bursts. In principle, continuous AE should be generated if the cutting process produces continuous chips without BUE, and if the cutting tool is perfectly sharp. However, during the course of Test A cutting experiments, though continuous chips were always formed, BUE was observed for low values of V and t_1 (as illustrated in Section 5.5.1, BUE was also predicted by means of Oxley's model); besides, other burst-type generating processes, like accidental collision, entangling, and fracture of chips, as well as minor tool fracture, could not be fully prevented from happening. The example presented in Figure 4.13 shows a typical Test A AE signal that was formed by a continuous-type wave superimposed by two large bursts. Consequently, since the technique described in Section 2.2.1 to calculate the mode of the full-wave rectified and low-pass filtered AE signal is insensitive to outlying values, like randomly appearing bursts, the outcome (I_{mode}) should only reflect the energy due to the mechanisms that generate continuous emissions. Therefore, if dislocation motion is the mechanism responsible for plastic deformation in metals (Appendix B), and if continuous-type AE is due to plastic deformation, there must be a relationship between I_{mode} and dislocation motion. In this section, the process by which dislocation movement occurs during plastic deformation in metal cutting are firstly investigated; afterwards, the process by which dislocation movement may cause AE is analysed; finally, experimental AE data from Test A is used to evaluate and discuss the relationship between AE and dislocation motion during metal cutting.

5.9.1 Mechanics of Dislocation Motion in Metal Cutting

During metal cutting, plastic deformation occurs at very high strain rates and temperatures. By applying Test A cutting conditions (Table 3.1) to Oxley's model [18], predictions of strain rates and temperatures were observed to be in the ranges presented in Table 5.3.

Table 5.3: Minimum and maximum values of $\dot{\gamma}_{\text{int}}$ and T_{int} for Test A cutting conditions (Table 3.1); work materials 080A15 and 080M40.

material	$\dot{\gamma}_{\text{int}}$, s^{-1}	T_{int}, K
080A15	700–62400	780–1170
080M40	2900–146200	810–1260

According to Section B.5 in Appendix B, at temperatures approximately above $0.5T_{\text{M}}$, where T_{M} is the melting temperature in degrees K, diffusion controlled mechanisms become significant, movement of dislocations by climb becomes possible, and certain dislocations previously hindered at obstacles start to move, resulting in a higher density of mobile dislocations (ρ_{MD}). In this regime, named diffusion controlled, flow stress decreases with increasing temperature and decreasing strain rate [25, 26]. Since for carbon steels $T_{\text{M}} \approx 1730$ K, and by observing that only for the lowest values of V and t_1 (T_{int} values in Figures 5.14 and 5.15 must be converted into degrees K), T_{int} does not reach $0.5T_{\text{M}}$, it can be concluded that, for practically all Test A cutting conditions with work materials 080A15 and 080M40, secondary zone plastic deformation results from dislocation movement where diffusion mechanisms are present.

Moreover, in Section B.5, it is also stated that at high strain rates (above 1000 s^{-1} [26]), opposing viscous damping forces become the dominant mechanism governing dislocation movement. In this regime, named viscous damping, the flow stress is a combination of the stress needed to overcome dislocation obstacles like forest dislocations plus the stress needed to overcome the damping forces, where, according to Equation B.5, the latter is a linear function of strain rate [25, 26]. By analysing the very high $\dot{\gamma}_{\text{int}}$ values presented in Table 5.3, one can conclude that cutting operations with the 080A15 and 080M40 work materials and Test A conditions involve secondary zone deformation that is governed by dislocations moving in the viscous damping regime.

5.9.2 Model of Acoustic Emission due to Dislocation Motion

According to Section B.5, in the viscous damping regime, the flow stress can be expressed as:

$$k = \tau_{\text{B}} + \tau_{\text{D}} \tag{5.14}$$

where τ_{B} is the stress required to overcome the forces posed by dislocation obstacles, and τ_{D} is the stress required to overcome the damping forces. Therefore, on a microscopic level, two forces oppose the movement of a dislocation: the damping force F_{D} and the force due to dislocation obstacles like forest dislocations F_B. Force F_D is proportional to dislocation speed (V_D) and, per unit length of dislocation line, is given by

$$F_D = BV_D \tag{5.15}$$

where B is the dislocation damping coefficient. As shown in Figure 5.32, F_B increases when the dislocation position (x) gets near an obstacle: F_B starts to rise at some position x^1 in the vicinity of the obstacle, reaching a maximum F_B^{max} at an intermediate point x^{max} between x^1 and x^2; after x^{max} has been reached, F_B decreases until position x^2 is arrived at. As a result, the total force acting on the dislocation is given by

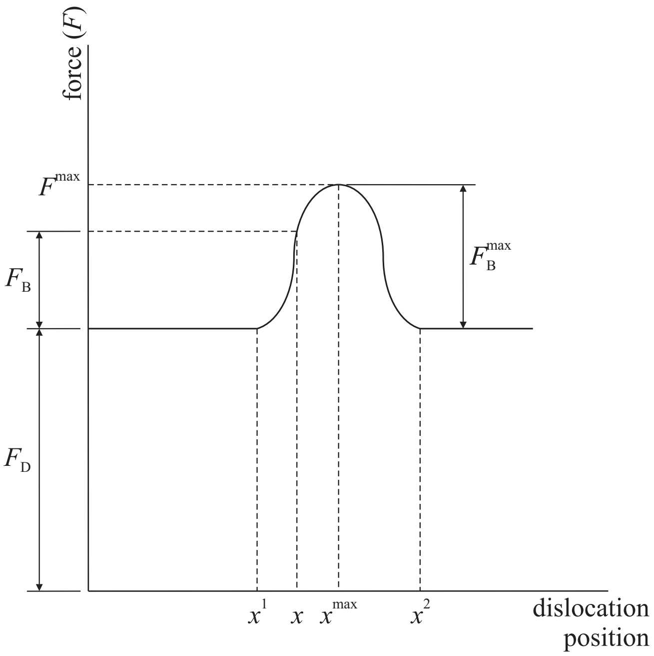

Figure 5.32: Forces opposing dislocation movement [21].

$$F = F_B + F_D \tag{5.16}$$

If there were no barriers to dislocation motion, the only force opposing the movement of a dislocation would be F_D, which is proportional to V_D. Since, according to Kumar [26], at very high strain rates, V_D is governed by constant B in Equation 5.15, and if the conditions of deformation (e.g. applied stress and temperature) are kept constant, V_D will remain steady, and so will F_D. However, in real crystals, dislocation obstacles are always present (Section B.4) and do oppose dislocations as they interact with them. However, according to Kumar, in the viscous damping region, the time a dislocation is hindered by an obstacle is negligible when compared to the time spent to travel between obstacles (the applied stress is high enough to overcome the obstacles instantaneously), and, therefore, V_D can still be assumed as constant. Moreover, since an obstacle imposes a force F_B against a moving dislocation, a reaction force, with the same amplitude but opposite direction, will be imposed by the dislocation on the obstacle, and, consequently, at every instant, the energy transmitted by the dislocation to the obstacle per unit length of dislocation line is given by:

$$\dot{U}_B = F_B V_D \tag{5.17}$$

As V_D remains constant, $\dot{U}_B$ will be proportional to F_B. Therefore, every time a dislocation surmounts an obstacle, potential strain energy $\dot{U}_B$ will be stored until position x^{max} is reached, and, between x^{max} and x^2, $\dot{U}_B$ will be released; this process is very rapid, since V_D is high and dislocation obstacles are narrow [21].

As stated in Section 2.2.1, the generation of an AE event is attributed to the rapid release of strain energy when some part of the material is stressed up to its maximum strength, so that the resulting AE wave will be formed due to the combination of a series of such events. The theory proposed by Gillis [55], presented in Section 2.2.1, states that an AE wave is generated when a dislocation that is moving between two minimum energy position in the lattice reaches its middle position of maximum energy, since strain energy is then rapidly released; however, this can only be valid for perfect crystals, without dislocation obstacles, and when dislocations do not intercept other dislocations. For real crystals, like the materials utilized in Test A, other mechanism has to be suggested. Consequently, it is proposed here that the release of strain energy when a dislocation surmounts an obstacle is the main mechanism by which the detected AE is generated during plastic deformation of metal cutting operations, since as a dislocation surpasses the obstacle, as $\dot{U}_B$ decreases, strain energy is released, the lattice vibrates, and an AE pulse is emitted. The amplitude and frequency content of the emitted pulse will be dependent on the force profile between x^1 and x^2 shown in Figure 5.32. Intuitively, the faster F_B changes, the higher the frequency content of the emitted AE wave, and the higher F_B^{max}, the higher the amplitude of AE. Moreover, since, as proposed by Ivanov [54] (Section 2.2.1), AE is formed due to a series of discrete pulses, the characteristic and shape of which is dependent on the physical mechanisms of each individual event, the detected AE in metal cutting will, consequently, be a function of the average effect of a large number of AE pulses generated due to the release of localized strain energy as dislocations surpass obstacles. However, the AE signal detected at the sensor will be a function of several factors, such as the density of obstacles (ρ_B), relationship of F_B against x between x^1 and x^2, velocity V_D, transmission wave path between AE source and sensor, and instrumentation. A qualitative description of the most relevant factors that affect the resulting acquired AE is carried out next:

Relationship between dislocation and obstacle As stated before, the shape of the F_B-curve versus dislocation position x will dictate the frequency content and energy for each AE event, i.e. the steeper the curve, the higher the frequencies, and the larger F_B^{max}, the larger the energy content of the emitted AE pulse. It is out of the scope of the current work to investigate the exact relationship between F_{B} and x; however, as discussed in Section 5.9.1, since the temperatures involved in metal cutting are high, diffusion mechanisms are present, and, according to Appendix B, in this regime, increasing temperature will facilitate dislocations to surmount obstacles, resulting in a lowering of $F_{\mathrm{B}}^{\mathrm{max}}$. A direct consequence will be the reduction of the energy level of the AE pulses, and, since the F_{B}-curve becomes less steep, the frequency content of the AE events will be reduced as well.

Density of obstacles Since all AE pulses contribute to the total detected AE wave, if more obstacles are present (higher ρ_{B}), more AE pulses are generated, and, hence, more AE is generated. Moreover, according to Appendix B, as plastic work contributes to the generation of new dislocations, the density of dislocations (ρ_{D}) is increased and thus the number of forest dislocations. As forest dislocations are the main source of dislocation obstacles, increasing plastic strain (γ) will lead to an increase in the energy level of AE. However, as the shape of the F_{B}-curve is not changed, γ is not expected to directly alter the frequency content of AE.

Dislocation speed As V_{D} increases, according to Equation 5.17, $\dot{U}_{\mathrm{B}}$ also increases, resulting in a direct rise in the energy content of the generated AE pulses. As strain rate ($\dot{\gamma}$) is a linear function of V_{D} (Equation B.2), increasing $\dot{\gamma}$ is expected to increase the energy of AE. Moreover, as increasing V_{D} will result in a faster release of strain energy, the frequency content of the generated AE pulses is also expected to increase.

Transmission path, sensor, and instrumentation An important factor to take into consideration is the distortion caused by the transmission medium, sensor coupling and sensitivity, and instrumentation to the propagating AE waves. As discussed in Section 2.2.1, amplitude attenuation is a function of frequency, and since a high frequency wave will be more attenuated than a lower one, if, at the source, the AE pulses shift towards higher frequencies, a lower AE level may be detected at the sensor. Sensor sensitivity is another factor that may be taken into account, since amplitudes of AE waves of different frequencies arriving at the sensor may be detected in different ways (waves whose frequency content is closer to the resonance of the sensor will be more amplified). Moreover, the instrumentation is also of major importance, since, for instance, if the energy level of the AE pulses within a certain frequency range increases, and if there is an electronic filter excluding signals within that frequency range, the frequency shift of the AE pulses will not be detected.

In summary, dislocation movement during a typical metal cutting processes is controlled by the viscous damping regime, and by assuming that the energy that is released when a dislocation surmounts an obstacle is the basic mechanism for AE generation, the energy level of the detected AE is expected to increase with γ and $\dot{\gamma}$, but it is expected to decrease with temperature. Moreover, the frequency content of AE is predicted to increase with $\dot{\gamma}$, to decrease with temperature, and to remain unchanged with γ. However, due to the complex effects of the transmission path, sensor, and instrumentation to the AE signal, at this stage, only a qualitative analysis is accomplished.

5.9.3 Evaluation of Dislocation Model

In this section, the conclusions achieved from the qualitative model proposed in Section 5.9.2 are going to be evaluated against the energy and frequency analysis carried out with the experimental data from Test A (Section 5.7). Afterwards, the influence of temperature on the generation of AE is evaluated with the aid of Test B results (Section 5.8). Finally, published material is evaluated and compared with the model derived in Section 5.9.2.

Acoustic Emission Energy

In Section 5.7.1, according to Equation 5.13, and also as shown in Figure 5.33, the energetic component of Test A AE data, I_{power}, and its rate of increase rise with both primary strain γ_{AB} and secondary strain rate $\dot{\gamma}_{\text{int}}$. Moreover, for the range of cutting conditions and work materials utilized in Test A, Equation 5.13 is sufficient to empirically model I_{power}, and I_{power} is not, therefore, dependent on other basic parameters. This strong dependence of I_{power} on γ_{AB} and $\dot{\gamma}_{\text{int}}$ can be explained in terms of the AE generation mechanisms proposed in Section 5.9.2:

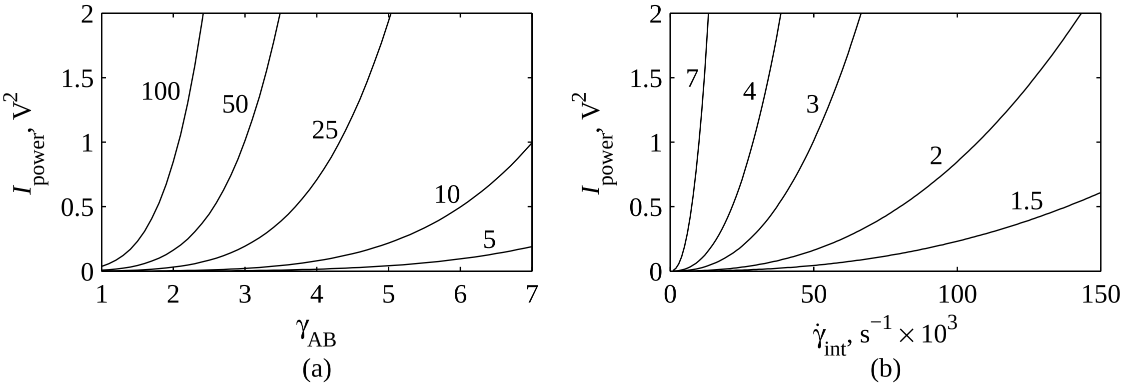

(a) (b)

Figure 5.33: Variation of I_{power} with γ_{AB} and $\dot{\gamma}_{\text{int}}$ (Equation 5.13). (a) I_{power} against γ_{AB} for $\dot{\gamma}_{\text{int}} = 5$, 10, 50, and 100×10^3 s^{-1}. (b) I_{power} against $\dot{\gamma}_{\text{int}}$ for $\gamma_{\text{AB}} = 1.5$, 2, 4, and 7.

Primary strain (Figure 5.33a) Since half of the total plastic strain occurs at the shear plane AB [30] (Figure 2.3), γ_{AB} can be used as a measure of the total plastic work done to the material before it enters the secondary zone of deformation. Furthermore, in Section 5.9.2, it was discussed that as plastic work increases the density of dislocation obstacles ρ_{B}, the resulting value of I_{power} will also increase; this conclusion is in agreement with Equation 5.13, since $I_{\text{power}} \propto \gamma_{\text{AB}}^{n_1}$, where $n_1 = 4.511$. Index n_1 is dependent on the combination of two factors: firstly, it is dependent on the relationship between γ_{AB} and ρ_{B} (the generation of dislocation obstacles due to plastic strain), and, secondary, it is also dependent on the combined effect of the transmission path, sensor, and instrumentation on the resulting acquired AE data.

Secondary strain rate (Figure 5.33b) In Section 5.9.2, it was also concluded that strain rate was directly related to increasing I_{power}. This is also in agreement with Equation 5.13, since $I_{\text{power}} \propto \dot{\gamma}_{\text{int}}^{n_2}$, where $n_2 = 2.385$. The value of n_2 is a function of the combined characteristics of the transmission path, sensor, and instrumentation.

Acoustic Emission Frequency

In Section 5.9.2, it was concluded that if the main mechanism of AE generation is the release of strain energy due to the opposition of obstacles to the displacement of dislocations, then the frequency content of AE should increase with strain rate but decrease with temperature. This is in agreement with the frequency analysis carried out in Section 5.7.2 for Test A AE data, where it was established that although f_{mean} increases with $\dot{\gamma}_{\text{int}}$, this is not observed because $\dot{\gamma}_{\text{int}}$ results in heat generation and thus higher T_{int} values, and, for the levels of strain rate encountered during Test A metal cutting, the effects of T_{int} are dominant, and, therefore, f_{mean} is seen to decrease with T_{int} even when $\dot{\gamma}_{\text{int}}$ increases. In Section 5.9.2, it was also concluded that the frequency content of AE should be independent of strain, whose predictions are clearly supported by the Test A AE result shown Figure 5.27.

Temperature and Acoustic Emission

In Section 5.9.2, it was concluded that another parameter that should have an impact on the level of AE was temperature. However, by plotting Test A I_{power} against T_{int} (Figure 5.28), high scatter was observed and no clear relationship could be established between I_{power} and T_{int}. Moreover, as concluded in Section 5.8, the apparent insensitivity of I_{power} to varying T_{int} is due to the disguising effect of the other two parameters γ_{AB} and $\dot{\gamma}_{\text{int}}$. By analysing Test B AE results, where the workpiece temperature was changed, it was concluded that the level of I_{power} is reduced with increasing T_{int} if both γ_{AB} and $\dot{\gamma}_{\text{int}}$ are kept constant, which is in agreement with the AE generation mechanism proposed in Section 5.9.2.

Published Dislocation Models

As stated in Section 2.2.2, Rangwala and Dornfeld [57] also suggested that, at the high strain rates typically encountered in metal cutting, viscous damping governs the motion of dislocations and, consequently, proposed that dislocation damping is responsible for AE generation in metal cutting. As a result, according to the relationship held by Equation 2.51, they stated that I_{power} should be proportional to the damping power ($\dot{U}_{\text{D}}$), which resulted in the following relationship:

$$I_{\text{power}} \propto \dot{\gamma}^2 \tag{5.18}$$

Rangwala and Dornfeld followed by noting that there was a linear relationship between V and experimental values of I_{RMS}, and since $\dot{\gamma}$ is basically proportional to V, Equation 5.18 was assumed to be demonstrated. However, as previously discussed in Section 5.1, by analysing the results from Test A shown in Figure 4.16 and other experimental results from published material, a relationship of the type $I_{\mathrm{mode}} \propto \dot{\gamma}^n$ (or $I_{\mathrm{RMS}} \propto \dot{\gamma}^n$), where $n > 1$ is always obtained, and since $I_{\mathrm{power}} = I_{\mathrm{mode}}^2$, a more general relationship of the type $I_{\mathrm{power}} \propto \dot{\gamma}^m$, where $m > 2$, instead of Equation 5.18, should be obtained. Moreover, at every instant, per unit length of dislocation line, $\dot{U}_{\mathrm{D}}$ is given by

$$\dot{U}_{\mathrm{D}} = F_{\mathrm{D}} V_{\mathrm{D}} = B V_{\mathrm{D}}^2 \tag{5.19}$$

Therefore, since B and V_{D} remain more or less constant for steady plastic deformation, $\dot{U}_{\mathrm{D}}$ will also remain constant during the flight of dislocations. As the high frequency AE signals are generated due to the rapid release of of strain energy, a rapid energy varying process, like the one described for $\dot{U}_{\mathrm{B}}$ in Section 5.9.2 (Equation 5.17), can justify the generation of AE. Besides, the model proposed by Rangwala and Dornfeld, does not account for the increase level of AE due to the effect of plastic strain which is, undoubtedly, a critical parameter contributing to the generation of AE, as demonstrated by the empirical model derived from Test A AE data (Equation 5.13, Figure 5.33). Consequently, although the dynamics of dislocation motion in the viscous damping regime is dependent on the two energy components $\dot{U}_{\mathrm{D}}$ and $\dot{U}_{\mathrm{B}}$, only the generation mechanisms responsible for $\dot{U}_{\mathrm{B}}$ (strain energy released due to dislocations transposing obstacles) can justify the variation of AE power with strain and strain rate.

In a subsequent paper, Rangwala and Dornfeld [19] explained the frequency content of AE according to the theory proposed by Rouby *et al.* [56], described in Section 2.2.1 (Equation 2.36), in which the frequency content of the AE waves was proportional to V_{D} but also proportional to the inverse of the distance between obstacles (d_{B}). In Section 5.9.2 it was also concluded that f_{mean} increases with V_{D}; however, f_{mean} was predicted to be unaffected by variations of ρ_{B} and, consequently, by variations of d_{B}, which is in agreement with Test A results, since, as shown in Figure 5.27, f_{mean} was observed to be more or less unaltered by γ_{AB}. Moreover, the frequency model proposed by Rangwala and Dornfeld does not explain the strong dependence of f_{mean} on temperature, shown by their own experimental data and also by Test A data (Figure 5.26c). On the other hand, the dislocation model presented in Section 5.9.2 takes into account the shift of f_{mean} towards lower values when the temperature is decreased.

In conclusion, during metal cutting, plastic deformation is governed by the motion of dislocations at high strain rates and temperatures. In this regime, named as viscous damping, two types of forces oppose the motion of dislocations: damping forces, which are proportional to strain rate, and forces due to dislocation obstacles, which are dependent on the density of the obstacles and on the strength of the obstacles against the passage of dislocations. However, although these two forces are responsible for the low frequency parameters, such as forces, stresses, and temperatures, in Section 5.9.2 it is suggested that only the forces due to the opposition of obstacles to the passage of dislocations may be responsible for the detected high frequency AE. This is contrary to the model proposed by Rangwala and Dornfeld [19, 57], who proposed that the energy due to damping was responsible for the detected AE energy. Furthermore, according to the model proposed in Section 5.9.2, the following relationships were derived: the energy content of AE should increase with increasing strain and strain rate, and decrease with increasing temperature; the frequency content of AE should increase with strain rate, decrease with temperature, and remain unchanged with strain. These relationships were confirmed by the experimental data provided by Tests A and B, indicating that, during metal cutting, although plastic deformation is mainly due to dislocation damping, AE should be generated mainly due to the opposition of obstacles to the movement of dislocations.

Chapter 6

Conclusions and Recommendations

The fundamental objective of the present thesis was the understanding of the generation mechanisms of acoustic emission (AE) during the course of metal cutting. In Chapters 1 and 2, the most relevant theories on the fields of metal cutting and AE were presented, followed by a review of the state-of-the-art models of AE generation during metal cutting. In Chapter 3, the experimental procedure was described, and the corresponding results presented in Chapter 4. In Chapter 5, a novel qualitative model relating continuous AE from metal cutting with continuous-type chip formation was developed, revealing that the opposition of obstacles against moving dislocations is the main mechanism of AE generation in the typical plastic deformation regimes occurring in metal cutting. The importance of this model arises from the fact that as an excellent agreement was found between model predictions and experimental results, a considerable contribution for the knowledge of AE generation during the course of metal cutting was undoubtedly achieved, as originally proposed, and, consequently, in the following section, the suggested mechanisms of AE generation proposed by the model are concisely described. Afterwards, all the conclusions arrived at during the analyses performed in Chapter 5 for the development of the proposed AE theory are thoroughly summarized. Finally, in the last section, some recommendations for further work are also provided.

6.1 Generation of Acoustic Emission during Metal Cutting

As continuous-type AE is thought to be generated due to plastic deformation during metal cutting with continuous chip formation, without built-up edge (BUE), and with a sharp tool (Section 2.2.2), and as dislocation motion is the main mechanism responsible for plastic deformation in metals (Section 5.9), a relationship between AE and dislocation motion was investigated for the typical plastic deformation regime encountered in metal cutting. At the high temperatures involved in metal cutting, flow stress decreases with temperature in the so-called diffusion controlled regime, and at the very high strain rates encountered in metal cutting, opposing viscous damping forces become the dominant mechanism governing dislocation movement (Section 5.9.1). Furthermore, as the flow stress is a combination of the stress needed to overcome dislocation obstacles plus the stress needed to overcome the damping forces, the total power involved in plastic deformation ($\dot{U}$) can be expressed as $\dot{U} = \dot{U}_{\mathrm{B}} + \dot{U}_{\mathrm{D}}$, where $\dot{U}_{\mathrm{B}}$ is the power necessary for the dislocations to transpose obstacles, and $\dot{U}_{\mathrm{D}}$ is the power to overcome the damping forces (Section 5.9.2).

Most published models typically relate the the power of the AE signals (I_{power}) to the total work of deformation $\dot{U}$, but, as shown in Section 5.3, this assumption is rather incorrect, since it is only valid for constant values of feed rate (t_1) and width of cut (w), although the cutting speed (V) is allowed to vary. Furthermore, Rangwala and Dornfeld [57] suggested that, as viscous damping is the main mechanism governing plastic deformation in metal cutting, I_{power} should be proportional to $\dot{U}_{\mathrm{D}}$. However, as shown in Section 2.2.1, AE is a high frequency stress wave generated due to the rapid release of strain energy, and, therefore, a process with rapid energy variation is necessary, which is not the case of $\dot{U}_{\mathrm{D}}$, since, as shown in Section 5.9.3, $\dot{U}_{\mathrm{D}}$ should remain more or less constant during dislocation movement.

The model proposed in the present thesis (Section 5.9.2) assumes that although the mechanics of plastic deformation from metal cutting is manly governed by viscous damping, AE is generated due to the rapid release of strain energy when moving dislocations surpass obstacles, since as a dislocation approaches an obstacle, strain energy is stored, and as its maximum value is reached, this strain energy is rapidly released as the dislocation overtakes the obstacle, resulting in the emission of an AE pulse (I_{power} is a function of $\dot{U}_{\mathrm{B}}$). The detected AE is a result of the combined effect of many AE pulses, generated at different locations, which are transmitted to a remote sensor. Furthermore, in Section 5.9.2, it was concluded that the energy level of the detected AE is expected to increase with strain and strain rate, but to decrease with temperature; the frequency content of AE was predicted to increase with strain rate, to decrease with temperature, and to remain unaffected by strain. Moreover, it was also concluded that the characteristics of the transmission path, sensor, and instrumentation also play an important role in the detected emissions.

In order to assess the validity of the proposed model, two sets of original metal cutting experiments (Tests A and B) were accomplished for four different work materials (two carbon steels, a stainless steel, and an aluminium alloy), during which AE and also other signals (cutting forces, vibration, and temperature) were acquired: in Test A (Section 3.2.1), the cutting conditions were varied over a wide range, and, in Test B (Section 3.2.2), the work material was preheated in order to initiate cutting with different workpiece temperatures (T_{W}). Good agreement was obtained between Test A and published results (Section 5.1.2).

Both energetic and frequency components of AE were extracted from the experimental results, according to the most appropriate data processing techniques: since phenomena that lead to unwanted AE bursts could not be completely unavoidable, a technique that disregards the influence of these random bursts in the calculation of the power of AE (I_{power}), named AE mode (I_{mode}) [7], was utilized as a representation of the energy content of continuous AE ($I_{\mathrm{power}} = I_{\mathrm{mode}}^2$);

a technique that indicates the frequency value that divides the AE power spectrum into two parts of equal energy, called mean frequency (f_{mean}) [19], was utilized as a representation of the frequency content of AE. Furthermore, in order to predict basic metal cutting parameters, such as strain, strain rate, flow stress, and temperature, a technique developed by Oxley and his co-workers [18] was employed, but only predictions for the two carbon steel work materials were possible.

In Section 5.7, it was concluded that AE is manly generated due to secondary plastic deformation, and, according to the energy analysis performed in Section 5.7.1, it was concluded that I_{power} increases with both primary strain and secondary strain rate, but, according to Section 5.8, I_{power} decreases with temperature. Moreover, in Section 5.7.2, it was concluded that f_{mean} increases with strain rate, decreases with temperature, but it remains unaffected by variations of strain. Therefore, as the results provided by the experiments together with Oxley's predictions are in agreement with the predictions of the afore-mentioned qualitative model, it substantiates the theory that the main generation mechanism of AE during metal cutting is provided by the release of strain energy when moving dislocations interact with obstacles in the material being deformed at the very high strain rates and temperatures typically encountered in metal cutting processes.

6.2 Summary of Conclusions

This section presents a summary of all the conclusions arrived at throughout the present thesis:

- Test A results showed that I_{power} increases with V and decreases with t_1, according to the approximate relationship $I_{\text{power}} \propto V^{n_1} t_1^{n_2}$, where n_1 and n_2 are work material dependent; index n_1 was found to be between 3.7 and 4.6, and n_2 between -0.63 and -0.01. Moreover, I_{power} was observed to increase with w, but with decreasing rate of increase, so that I_{power} tends to a constant value for high w values. In the frequency domain, although very scattered, f_{mean} was observed to decrease with V and to remain more or less unchanged with t_1 and w.

- Other two sets of experiments were performed in order to test AE generation when t_1 and w approach very low values: feed rate and width of cut variation tests, respectively. However, the AE data from these tests were observed to be very scattered, which was attributed to the small length of the acquired data sets (approximately 10 ms). In order to remove the unwanted effect of burst-type AE in the computation of I_{mode}, data sets longer than 100 ms must be acquired.

- Results from the width of cut variation tests showed that when high amplitude vibrations are present, named as chatter, the resulting AE signal is highly affected by these vibrations (the level of I_{power} was observed to increase up to 20 times on the onset of chatter).

- According to Test B results, I_{power} was observed to decrease with increasing workpiece temperature T_{W}.

- Since most published models [7,57,60,62,63,65] relate I_{power} to cutting power $\dot{U}$, according to the proportion $I_{\text{power}} \propto \dot{U}$, this relationship was investigated against Test A results. It was concluded that this relationship was solely observed if t_1 and w were kept constant, and only V was allowed to vary, which was the case of the experimental procedure used to derive most published models. Nevertheless, if only V was changed, Test A AE data seemed to hold a relationship of the type $I_{\text{power}} \propto \dot{U}^n$, where $n > 1$.

- The finite-difference technique was employed in order to determine the relationship between the temperature at the tool-chip interface (T_{int}) and the temperature measured by the two thermocouples (T_1 and T_2) placed below the tool-chip interface. For a given value of T_{int}, T_2 was predicted to be lower than T_1, as expected, since T_2 was measured further from the tool-chip interface, and T_1 and T_2 were predicted to increase with increasing w and l_{int}. As expected, T_1 and T_2 were found to increase with T_{int}. Moreover, since T_1 and T_2 are dependent on l_{int}, and l_{int} is dependent on the cutting process and not known in advance, this makes practical predictions of T_{int} from measurements of T_1 and T_2 rather difficult.

- In order to access the accuracy of the semi-empirical model developed by Oxley and co-workers [18] to predict basic metal cutting parameters, the experimental force and temperature results from Test A and also the temperature results from Test B were used to be compared against predictions of cutting forces and temperatures from Oxley's model. A fairly good agreement was observed between predictive and experimental results, but for the lowest values of V and t_1, the experimental cutting force results were observed to be below predictions; this was attributed to the onset of BUE, since BUE is known to contribute to the reduction of the cutting forces.

- In order to investigate the typical relationship observed between I_{power} and w (I_{power} increases with w, but its rate of increase decreases with w) shown by Test A results and also by published results [3,5,7,64,66], a very simple model for AE generation and propagation was developed. It was concluded that as w increases, and AE events are generated further apart, some AE waves travel longer distances than others to a remote AE sensor, resulting in a difference in phase delay for the different arriving waves. Consequently, due to the effect of phase attenuation, the resultant AE signal detected by the sensor does not increase proportionally to the increase of AE activity at the generation source that accompanies the increase in deformation volume due to increasing w.

- As it was demonstrated that Oxley's theory can be used to model the cutting process rather accurately, it was decided to run Oxley's model with Test A cutting conditions to predict the basic cutting parameters that govern the physics of plastic deformation in metal cutting, so that the most important parameters that influence the level of AE could be evaluated.

Besides, it was also concluded that the AE signals measured during Test A (measured at the tool side) were manly generated due to plastic deformation at the tool-chip interface [15]. Moreover, it was realized that I_{power} is mostly influence by the effect of primary strain (γ_{AB}), secondary strain rate ($\dot{\gamma}_{\mathrm{int}}$), and interface temperature T_{int}. However, it was also found out that the effect of T_{int} on I_{power}, if temperature T_{W} is kept constant, are masked by the influence of γ_{AB} and $\dot{\gamma}_{\mathrm{int}}$, and by using Test A experimental results together with Oxley's model predictions, the following empirical relationship was established: $I_{\mathrm{power}} \propto \gamma_{\mathrm{AB}}^{n_1}\dot{\gamma}_{\mathrm{int}}^{n_2}$, where $n_1 = 4.5$ and $n_2 = 2.4$. However, by analysing Test B results, where T_{W} was allowed to vary, I_{power} was clearly seen to decrease with T_{int}, and the previous empirical relationship can not, therefore, be valid any longer.

- As pointed out in the previous section, at the high strain rates and temperatures typically found in metal cutting, plastic deformation is governed by the motion of dislocations in the so-called viscous damping regime [25, 26]. In this regime, the movement of dislocations is opposed by damping forces, which are proportional to dislocation speed, and also by forces posed by dislocation obstacles. Although theses two types of forces are liable for the dynamics of the moving dislocations, and, hence, the dynamics of plastic deformation, it was suggested that only the forces posed by the obstacles could originate AE, since AE is composed by high frequency waves, and only the rapid release of strain energy due to the passage of dislocations across the obstacles could originate the high frequency of the detected emissions. According to the proposed model, the following trends were predicted: I_{power} increases with strain and strain rate, but it decreases with temperature; f_{mean} increases with strain rate, decreases with temperature, and it remains unaltered with strain. These trends agree with Test A and Test B experimental data, indicating that the release of strain energy when moving dislocations surmount obstacles may be the most relevant source of continuous AE during continuous-type chip generation processes.

6.3 Recommendations for Further Work

In this section, in order to aid any future research work to be undertaken in the areas covered by this thesis, some final recommendations and suggestions for possible alterations are provided:

- Since only predictions for the two carbon steel work materials were possible with Oxley's theory [18], an extension of the theory to use other type of work materials must be investigated. Some work has already been undertaken by Adibi-Sedeh *et al.* [70] to extend Oxley's model for other type of steels, for aluminium alloys, and for copper. Moreover, it is also proposed that, once an extended Oxley's model is accomplished, metal cutting should be simulated for the other two non-carbon steel work materials (stainless steel 304S15 and aluminium alloy 6082-T6), so that the basic cutting parameters, such as strain, strain rate, flow stress, and temperature can be predicted for these two materials as well. Subsequently, the relationship defined in Section 5.7.1 (Equation 5.13) should be verified for these other two work materials, since when tested for the two carbon steels, Equation 5.13 was observed to be material independent. All other analyses, such as the frequency analysis presented in Section 5.7.2 and the temperature analysis presented in Section 5.8, should be repeated for the two work materials 304S15 and 6082-T6. Depending on the results of the analysis of these two non-carbon steel work materials, the qualitative model presented in Section 5.9 should be revalidated or modified accordingly.

- In order to obtain valuable results from the feed rate and width of cut variation tests, these tests should be repeated with longer acquisition lengths (more than 100 ms) of the AE data sets, so that the effect of unwanted busts can be removed from the computation of I_{mode}.
- If Test A were to be repeated, the range of cutting conditions V and t_1 should be raised, since, during the experimental procedure, the occurrence of BUE was detected during the course of Test A for the lowest values of V and t_1. When BUE is present, Oxley's model predictions do not agree so well with the experimental results (Figures 5.10 and 5.11). Another reason to raise V and t_1 is due to the fact that Oxley's model did not converge for some of the lowest vales of V and t_1, and results for these conditions were found by extrapolation.

Appendix A

Oxley's Theory

This appendix is a complement to Section 2.1.4, where the calculation of parameters, such as the geometry, cutting forces, stresses, and temperatures of orthogonal cutting is described according to a predictive machining model formulated by Oxley and his co-workers [18]. The inputs for the model are the material properties, cutting speed (V), uncut chip thickness (t_1), width of cut (w), tool rake angle (α), and initial work material temperature (T_W). The following section describes the necessary material properties model inputs, and, in the subsequent section, the calculation required to attain the machining prediction.

A.1 Material Properties

An important assumption is that the plastic stress-strain properties of the work material are represented by the empirical equation

$$\sigma = \sigma_1 \varepsilon^n \tag{A.1}$$

where σ and ε are the uniaxial stress and strain respectively, and σ_1 and n are material constants that depend on strain rate and temperature. Uniaxial flow stress, strain and strain rate (σ, ε and $\dot{\varepsilon}$ respectively) are related to plane stress, strain and strain rate (k, γ, and $\dot{\gamma}$, respectively) by the following relationships:

$$\sigma = \sqrt{3}k \tag{A.2}$$

$$\varepsilon = \frac{\gamma}{\sqrt{3}} \tag{A.3}$$

$$\dot{\varepsilon} = \frac{\dot{\gamma}}{\sqrt{3}} \tag{A.4}$$

The values of σ_1 and n were obtained from stress-strain data of high speed compressions tests for a range of carbon steels [71]. Since σ_1 and n depend on strain rate and temperature, a set of functions was developed to relate σ_1 and n to a single variable that combines the effects of strain rate and temperature, called velocity-modified temperature (T_{mod}) [72]. These functions are stated in reference [18], where σ_1 and n are related to T_{mod} and carbon content. Figure A.1 shows a plot of these functions for both 080A15 and 080M40 carbon steels. Moreover, T_{mod} can be found from

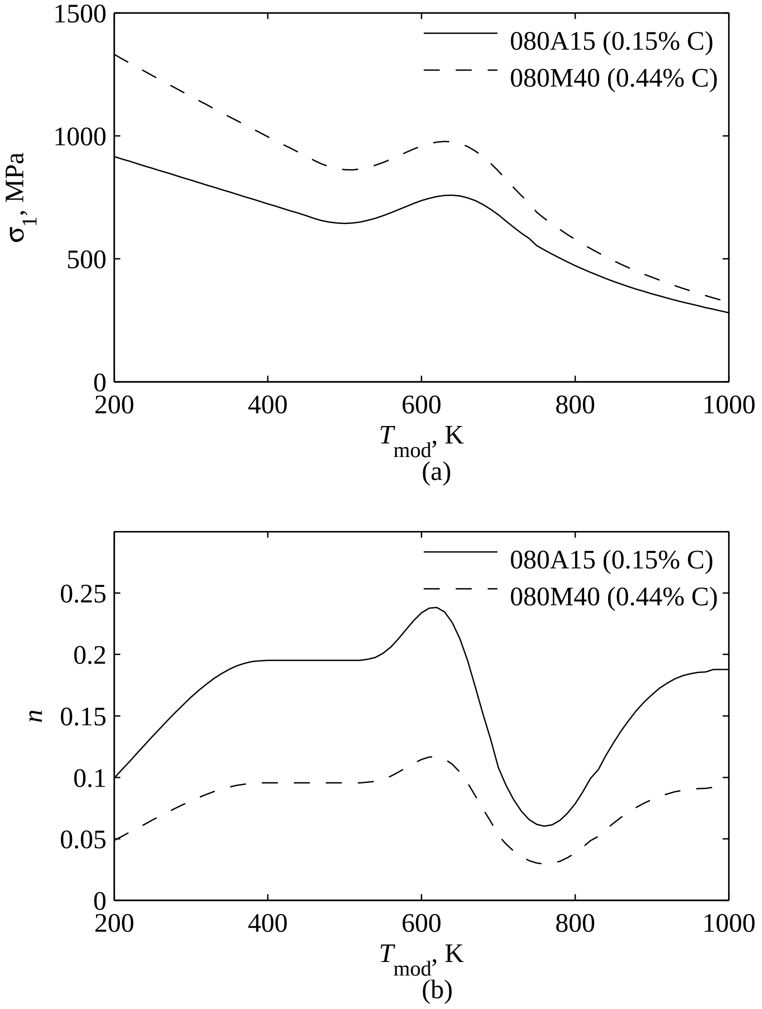

(a)
(b)

Figure A.1: Flow stress properties for work materials 080A15 and 080M40. (a) σ_1 (b) n.

the following relationship:

$$T_{\text{mod}} = T\left(1 - \nu \log_{10}\frac{\dot{\varepsilon}}{\dot{\varepsilon}_0}\right) \tag{A.5}$$

where T is the temperature in K, and ν and $\dot{\varepsilon}_0$ are constants ($\dot{\varepsilon}_0 = 1/\text{s}$ and $\nu = 0.09$).

The thermal properties of the work material are also required for the model computation: specific heat (c) and thermal conductivity (κ). Empirical temperature dependent equations for the computation of c and κ are presented in reference [18]. For carbon steels, c is given as independent from chemical composition:

$$c = 420 + 0.504T \tag{A.6}$$

where c is in J/kg-K, and the temperature T is in °C. However, chemical composition dependent functions are given for κ. For example, for the 080A15 material composition,

$$\kappa = 52.78 - 0.0283T \tag{A.7}$$

and for the 080M40,

$$\kappa = 49.35 - 0.0245T \tag{A.8}$$

where κ is in W/m-K, and the temperature T is in °C. Moreover, since the effect of temperature on work material density (ρ) is negligibly small, ρ was assumed constant and equal to 7862 kg/m^3.

A.2 Computation Procedure

As it can be observed in Figure A.2, the main computation procedure of Oxley's model is structured by three nested loops: in the outer loop, δ (ratio of secondary plastic zone thickness to chip thickness t_2) is varied until the tangential force (F_X) reaches a minimum value; in the middle loop, for each δ, C (empirical primary strain rate constant) is varied until $\sigma_N \approx \sigma'_N$, where both σ_N and σ'_N represent the normal stress at the cutting edge (B in Figure 2.3a) found by two different methods; and in the inner loop, for each C, ϕ (shear angle) is varied until $\tau_{int} \approx k_{int}$, where τ_{int} and k_{int} represent the shear flow stress of the chip at the tool-chip interface found by analysis of the stress distributions along the primary shear plane (AB in Figure 2.3a) and secondary tool-chip interface, respectively. Therefore, in order to find ϕ, the calculations are divided into two stages: analysis of primary zone and secondary zone stresses.

The first stage of the calculations begins by calculating the shear strain (γ_{AB}) and the shear strain rate ($\dot{\gamma}_{AB}$) at AB:

$$\gamma_{AB} = \frac{\cos\alpha}{2\sin\phi\cos(\phi-\alpha)} \tag{A.9}$$

$$\dot{\gamma}_{AB} = C\frac{V_S}{l_{AB}} \tag{A.10}$$

where the length of AB

$$l_{AB} = \frac{t_1}{\sin\phi} \tag{A.11}$$

and the shear velocity

$$V_S = \frac{V \cos\alpha}{\cos(\phi - \alpha)} \tag{A.12}$$

Then, the uniaxial strain (ε_{AB}) and strain rate ($\dot{\varepsilon}_{AB}$) are calculated from Equations A.3 and A.4. Afterwards, since the temperature at AB (T_{AB}) is unknown, T_{AB} is initially equated to T_W, so that T_{mod} at AB can be calculated (Equation A.5) in order to obtain σ_1 and n, as described in Section A.1. The shear force along AB is then calculated:

$$F_{AB} = \frac{k_{AB} t_1 w}{\sin\phi \cos\phi} \tag{A.13}$$

where k_{AB} can be found from Equation A.2. In order to calculate the rise in temperature at AB (ΔT_{AB}), the proportion of heat conducted into the work must be determined first:

$$\beta = \begin{cases} 0.5 - 0.35\log_{10}(R_T \tan\phi) & \text{for} \quad 0.04 \leq R_T \tan\phi \leq 10.0 \\ 0.3 - 0.15\log_{10}(R_T \tan\phi) & \text{for} \quad R_T \tan\phi \geq 10.0 \end{cases} \tag{A.14}$$

where R_T is a non-dimension thermal number given by

$$R_T = \frac{\rho c V t_1}{\kappa} \tag{A.15}$$

and c, κ and ρ are obtained with the equations stated in Section A.1. At this point, it is possible to calculate ΔT_{AB}:

$$\Delta T_{AB} = \eta \Delta T_{SZ} \tag{A.16}$$

where the rise in temperature in the primary shear zone

$$\Delta T_{SZ} = \frac{1-\beta}{\rho c t_1 w} \times \frac{F_{AB}\cos\alpha}{\cos(\phi - \alpha)} \tag{A.17}$$

and η is a correction factor because not all plastic work of chip formation occurs at AB ($\eta = 0.7$). The temperature T_{AB} can then be recalculated:

$$T_{AB} = T_W + \Delta T_{AB} \tag{A.18}$$

The previous temperature dependent calculations (Equations A.5 and A.13–A.16) are then repeated until the temperature rise ΔT_{AB} converges to a constant value. Afterwards, the resulting cutting force is calculated:

$$R = \frac{F_S}{\cos\theta} \tag{A.19}$$

where θ is the angle between R and AB:

$$\tan\theta = 1 + 2\left(\frac{\pi}{4} - \phi\right) - Cn \tag{A.20}$$

Before calculating k_{int}, the friction force at the tool-chip interface must be evaluated:

$$F_{\mathrm{int}} = R\sin\lambda \tag{A.21}$$

where the friction angle

$$\lambda = \theta - \phi + \alpha \tag{A.22}$$

Finally,

$$\tau_{\mathrm{int}} = \frac{F_{\mathrm{int}}}{lw} \tag{A.23}$$

where the tool-chip contact length

$$l_{\mathrm{int}} = \frac{t_1 \sin\theta}{\cos\lambda \sin\phi}\left[1 + \frac{Cn}{3(1 + \frac{\pi}{2} - 2\phi - Cn)}\right] \tag{A.24}$$

The second stage of the calculations starts by assuming that the initially unknown mean chip temperature (T_{C}) is equal to $T_{\mathrm{W}} + \Delta T_{\mathrm{SZ}}$, so that c can be determined (Section A.1), and thus the mean temperature rise in the chip:

$$\Delta T_{\mathrm{C}} = \frac{F_{\mathrm{int}} \sin\phi}{\rho c t_1 w \cos(\phi - \alpha)} \tag{A.25}$$

The temperature T_{C} is then recalculated:

$$T_{\mathrm{C}} = T_{\mathrm{W}} + \Delta T_{\mathrm{SZ}} + \Delta T_{\mathrm{C}} \tag{A.26}$$

and the calculations of c and ΔT_{C} are then repeated until ΔT_{C} converges to a constant value. Thereafter, κ must be calculated (Section A.1) in order to determine R_{T} (Equation A.15), so that the maximum temperature rise in the chip ($\Delta T_{\max}$) can be computed:

$$\log_{10}\frac{\Delta T_{\max}}{\Delta T_{\mathrm{C}}} = 0.06 - 0.195\delta\sqrt{\frac{R_{\mathrm{T}} t_2}{l}} + 0.5\log_{10}\frac{R_{\mathrm{T}} t_2}{l} \tag{A.27}$$

The chip thickness

$$t_2 = \frac{\cos(\phi - \alpha)}{\sin\phi} t_1 \tag{A.28}$$

The mean tool-chip interface temperature can then be determined:

$$T_{\text{int}} = T_{\text{W}} + \Delta T_{\text{SZ}} + \psi \Delta T_{\text{max}} \tag{A.29}$$

where ψ is a correction factor since T_{int} is an average value ($\psi = 0.7$). The mean shear strain rate at the interface must also be calculated:

$$\dot{\gamma}_{\text{int}} = \frac{V_{\text{C}}}{\delta t_2} \tag{A.30}$$

where the chip velocity

$$V_{\text{C}} = \frac{V \sin\phi}{\cos\phi - \alpha} \tag{A.31}$$

The uniaxial strain rate at the interface ($\dot{\varepsilon}_{\text{int}}$) is calculated from Equation A.4. Hence, having found T_{int} and $\dot{\varepsilon}_{\text{int}}$, T_{mod} can then be calculated from Equation A.5, and hence σ_1, as described in Section A.1. Finally, k_{int} can be calculated as follows:

$$k_{\text{int}} = \frac{\sigma_1}{\sqrt{3}} \tag{A.32}$$

This equation neglects the influence of strain on flow stress.

In conclusion, a unique value for ϕ is found, for each C value, when $\tau_{\text{int}} \approx k_{\text{int}}$. Next, an unique value for C and ϕ is found, for each δ value, when $\sigma_{\text{N}} \approx \sigma'_{\text{N}}$, where

$$\sigma_{\text{N}} = \frac{R \cos\lambda}{lw} \tag{A.33}$$

$$\sigma'_{\text{N}} = \left(1 + \frac{\pi}{2} - 2\alpha - 2Cn\right) k_{\text{AB}} \tag{A.34}$$

And, finally, an unique value for δ, C, and ϕ is found, when F_{X} is minimum, so that an unique solution for the cutting forces, stresses, and temperatures is determined.

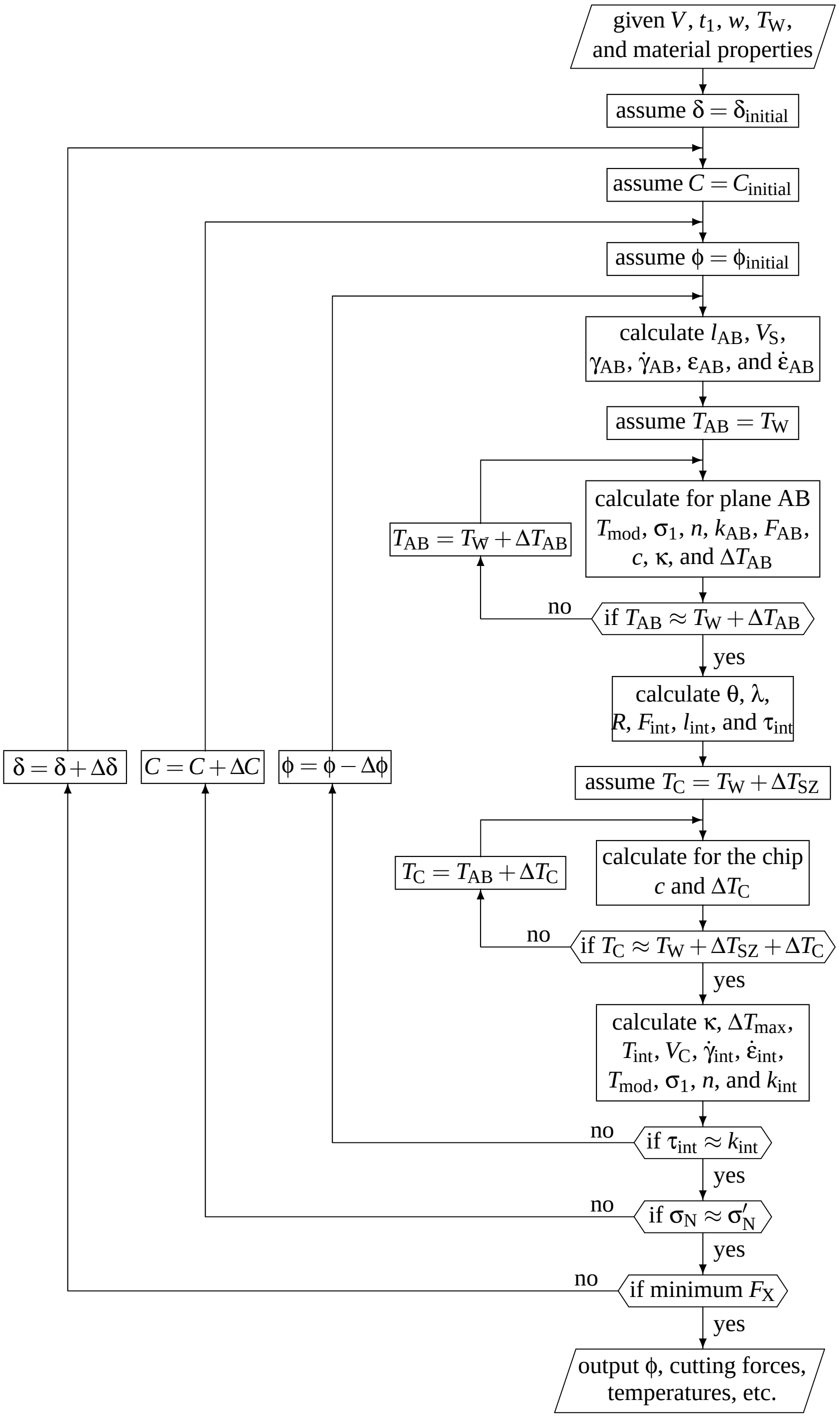

Figure A.2: Oxley’s model computation diagram.

Appendix B

Basic Dislocation Theory

This appendix gives a short introduction on dislocation theory. It is aimed to aid the understanding of the relationship between dislocation motion and AE, as presented in Section 2.2.1 and also discussed in Section 5.9. It gives some relevant information for the understanding of some of the equations that govern dislocation motion during plastic deformation. For more information on the subject, the literature from which this appendix is based must be consulted [21, 22].

B.1 Dislocation Definition

In a crystalline material, a dislocation represents a line defect or discontinuity between part of the crystal that has sheared and part which has not. A dislocation line extends over a macroscopic distance within the material and can form closed loops, branch into other dislocations, or end at the surface or grain boundary of the crystal. A dislocation is defined by two parameters (Figure B.1): the Burgers vector (b) and the dislocation line direction. A special plane, called the slip plane, is defined by these two parameters. Two simple types of dislocations can be defined:

Edge dislocations The Burgers vector is normal to the dislocation line.

Screw dislocations The Burgers vector is parallel to the dislocation line.

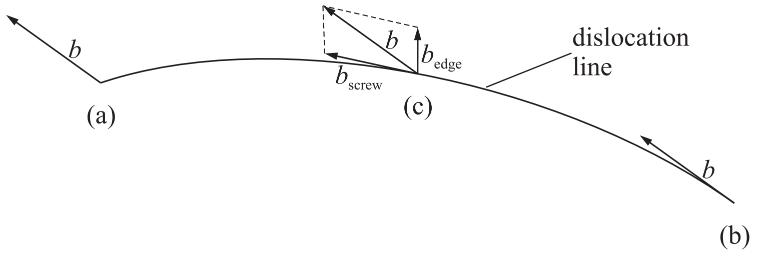

Figure B.1: Dislocation definition. (a) Pure edge type. (b) Pure screw type. (c) Mixed type.

However, as shown in Figure B.1c, dislocations normally have a mixed edge and screw character, where the Burgers vector lies at an arbitrary angle to the dislocation line direction. A mixed dislocation can be resolved into its edge and screw components: $b = \sqrt{b^2_{\mathrm{edge}} + b^2_{\mathrm{screw}}}$.

Two dislocations with opposite Burgers vectors are physical opposites of each other, and, if brought together, they annihilate and restore the perfect crystal.

B.2 Dislocation Movement

There are two basic types of dislocation movement:

Glide In this type of motion, also known as conservative, dislocations move on their slip plane. However, since the Burgers vector and line of a screw dislocation do not define an unique plane, the glide of this type of dislocation is not restricted to a specific slip plane. Glide of many dislocations results in slip, which is the the most common manifestation of plastic deformation in crystals.

Climb This type of motion is also known as non-conservative, and the dislocations move out of the slip plane. Climb requires thermal activation because it involves the diffusion of atoms either towards or away from the dislocation, and, therefore, it occurs at higher temperatures.

At a high enough shear stress acting on the slip plane, a dislocation glides on this plane, and if it reaches the surface of the crystal, it contributes to the total plastic deformation by b. More generally, if each dislocation on the crystal moves (by glide or climb) an average distance x_{D}, a relationship for the macroscopic plastic shear strain (γ) can be established:

$$\gamma = b\rho_{\mathrm{MD}}x_{\mathrm{D}} \tag{B.1}$$

where ρ_{MD} is the density of mobile dislocations. The shear strain rate ($\dot{\gamma}$) can be calculated from the following equation:

$$\dot{\gamma} = b\rho_{\mathrm{MD}}V_{\mathrm{D}} \tag{B.2}$$

where V_{D} is the average dislocation velocity.

B.3 Multiplication of Dislocations

All crystals contain dislocations, and in well-annealed crystals, dislocations are arranged in a ill-defined network (Frank net). The density of dislocations (ρ_{D}) in a crystal can be defined in two ways: as the total length of dislocation line per unit volume, or as the number of dislocations intersecting a unit area, both measured in units of mm^{-2}. In well-annealed metals, ρ_{D} is usually between 10^4 and 10^6 mm^{-2}. However, as ρ_{D} increases rapidly with plastic deformation (after large amounts of deformation, ρ_D is in the range 10^8–10^9 mm^{-2}), there must be one or more processes by which dislocations are generated due to plastic deformation. These processes are briefly described next:

Frank-Read source If a large enough stress is applied to the slip plane of a dislocation line which is locked at one or two points, a regenerative process of the dislocation line will take place. If locked at just one point, the dislocation line will spiral around the locking point, growing constantly in length; if locked at two points, the line will spiral around the two locking points, leading to the generation of closed loops that will keep generating and growing around the two locking points.

Multiple cross glide If a dislocation loop is expanding on a slip plane, it is possible that a part of the loop that is purely screw in character slips onto another plane that crosses the slip plane of the expanding loop (glide of screw dislocations is not confined to an unique plane), so that, if the conditions are favourable, a new dislocation loop can start and glide onto a plane that is parallel to the first slip plane. Thus, it is possible for a single dislocation loop to expand and multiply onto many parallel slip planes.

Multiplication by climb A regenerative process, known as the Barden-Herring source, can occur by climb in a similar way to the Frank-Read mechanism.

Grain boundary sources An important source of dislocations in poly-crystalline materials is the emission of dislocations from the boundary region between grains, which may be produced by several mechanisms.

B.4 Dislocation Obstacles

As stated previously in Section B.2 and according to the relationship hold by Equation B.1, plastic deformation of metals is a result of the displacement of dislocations within the crystal. Therefore, the ability of a metal to deform depends on the ability of dislocations to move, and, hence, the flow stress is the stress required to overcome the opposition to the movement of dislocations.

In an otherwise perfect crystal, the only resistance to the motion of a dislocation is the overcoming of the Peierls stress, which arises from the periodic variation of energy in the lattice; when a dislocation moves out of a lattice equilibrium position (where its energy is a minimum), the energy of the dislocation increases, and its maximum value (Peierls energy) is reached half way between two equilibrium positions. However, in real crystals, other obstacles oppose the motion of dislocations, such as other dislocations, grain boundary, and impurity atoms. Since work hardening results mainly from the hindering effect of other dislocations as they are generated as a result of plastic deformation (Section B.3), they are thought to be the most relevant type of obstacle opposing dislocation motion.

As referred in Section B.3, since all metals contain a network of dislocations, it follows that every slip plane is crossed by other dislocations, and, as a dislocation moves on its slip plane, it will have to intercept the dislocations crossing the slip plane. The latter are called forest dislocations. As plastic deformation proceeds, ρ_D is increased and, therefore, also the number of forest dislocations. Moreover, the intersection of one dislocation with another dislocation produces steps, called jogs, on each dislocation line, whose length is equal to the Burgers vector of the dislocation that has intercepted it. Jogs in a pure edge dislocation possess screw character, and thus do not affect the subsequent glide of the dislocation. However, since jogs on pure screw dislocations have edge character, the dislocation can only glide if the slip plane of the dislocation is the same of that of the jog; otherwise, the dislocation can only move forward and take the jog with it by climb, whose process requires thermal activation, and, consequently, the movement of the screw dislocation will be temperature dependent.

Generally, the dynamics of a dislocation attempting to overcome an obstacle can be described as follows: when a dislocation approaches an obstacle, the obstacle will impinge a force opposing the motion of the dislocation (F_B), which will increase in strength as the dislocation gets nearer to the obstacle, up to a point where the opposing force reaches a maximum value (F_B^{max}), and, as the dislocation surpasses the obstacle, this force rapidly decreases. If the length of the obstacle is l_B, the applied force of the dislocation on the obstacle will be $\tau b l_B$, where τ is the applied stress on the slip plane (thermal and damping effects are neglected, so that F_B is the only force acting on the dislocation). As a result,

$$\tau \geq \frac{F_B^{max}}{b l_B} \tag{B.3}$$

so that the dislocation can surmount the obstacle.

B.5 Flow Stress

As mentioned in Section B.4, the flow stress is the stress required to overcome the force exerted by obstacles to the motion of dislocations. In this section, the effects of temperature and strain rate on the flow stress of metals are analysed. As shown in Figure B.2, depending on the value of strain rate and temperature, four different regions can be distinguished [25, 26]:

Thermally activated (region I) In this region, both strain rate and temperature are relatively low, and if a dislocation gliding on its slip plane encounters an obstacle, it will be momentarily arrested until the combined action of thermal fluctuations and the applied stress assist the dislocation surmount the obstacle. Since, by increasing the strain rate, the time a dislocation is arrested by an obstacle is reduced, the effects of thermal fluctuations will also be reduced, and, consequently, a higher stress is required to continue motion. Therefore, the flow stress decreases with increasing temperature, and it increases with increasing strain rate.

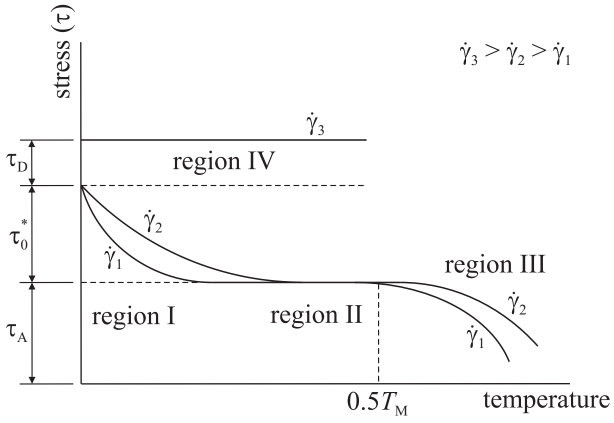

Figure B.2: Variation of flow stress with temperature and strain rate [25, 26].

Athermal (region II) In region I, the applied stress required for the material to flow is divided into an thermally activated (τ^*) and an athermal (τ_A) stress component:

$$\tau = \tau^* + \tau_A \tag{B.4}$$

When the temperature increases, only τ^* is reduced (and consequently τ), down to the point that $\tau^* = 0$, and thus $\tau = \tau_A$, so that any further increase in temperature will not aid dislocations to surmount obstacles. Also, since the time arrested by a dislocation at an obstacle becomes irrelevant, the flow stress becomes also independent of strain rate.

Diffusion controlled (region III) When the temperature becomes higher than $0.5T_M$, where T_M is the melting temperature in degrees K, diffusion controlled mechanisms become significant. Edge dislocation and previously immobile jogs on screw dislocations can now climb. Since these mechanisms are thermally activated, the flow stress decreases rapidly with increasing temperature, and since, at higher strain rates, there is less time for diffusion to aid the process, flow stress increases with increasing strain rate.

Viscous damping (region IV) At high dislocation speeds, a damping force opposing the movement of dislocations becomes relevant. This force is proportional to the dislocation speed V_D. Furthermore, at very high strain rates, the applied stress is high enough to overcome instantaneously the dislocation obstacles without the aid of thermal fluctuations. In this region, a linear relationship between the applied stress and strain rate is observed:

$$\tau = \tau_B + m\dot{\gamma} \tag{B.5}$$

where τ_B is the stress needed to overcome obstacles like forest dislocations, and m is the slope of the relationship between τ and $\dot{\gamma}$ above τ_B. Moreover, stress $\tau_B = \tau_0^* + \tau_A$, where τ_0^* is the value of τ^* at 0 K, and the stress attributed to damping $\tau_D = m\dot{\gamma}$.

Appendix C

Finite-Difference Temperature Prediction

This appendix shows, in more detail, the numerical technic used in Section 5.4 to predict the temperatures at different points of the tool for known tool-chip interface mean temperature and dimensions; it uses the finite-difference method applied for heat conduction. Information on finite-difference theory applied to heat transfer problems can be found in published material [20].

The cutting tool geometry was simplified into a rectangular block with dimensions X, Y, and Z, and this block was further divided into smaller rectangles, forming a grid of $m+1$, $n+1$, and $o+1$ elements in the x, y, and z direction, respectively (Figure C.1). To start formulating the finite difference equations, one must take into account the heat that flows into each element (i,j,k) ($i=1\ldots m+1$, $j=1\ldots n+1$, and $k=1\ldots o+1$): $\dot{Q}_1$ and $\dot{Q}_2$, with positive and negative directions along the x-axis, respectively; $\dot{Q}_3$ and $\dot{Q}_4$, with positive and negative directions along the y-axis, respectively; $\dot{Q}_5$ and $\dot{Q}_6$, with positive and negative directions along the z-axis, respectively; i.e. the heat flowing into element (i,j,k) from the 6 adjacent elements $(i-1,j,k)$, $(i+1,j,k)$, $(i,j-1,k)$, $(i,j+1,k)$, $(i,j,k-1)$, and $(i,j,k+1)$. If no heat is generated inside the element, the following energy balance applies:

$$\dot{Q}_1+\dot{Q}_2+\dot{Q}_3+\dot{Q}_4+\dot{Q}_5+\dot{Q}_6=0 \tag{C.1}$$

Depending on the location of the element, two mechanisms oh heat transfer can be considered: heat conduction between neighbouring elements ($\dot{Q}_{\text{cond}}$) and heat convection between the peripheral elements and the air surrounding the block ($\dot{Q}_{\text{conv}}$). The equation for $\dot{Q}_{\text{cond}}$ is as follows:

$$\dot{Q}_{\text{cond}}=\frac{A}{d}\kappa(T-T') \tag{C.2}$$

where A is the common heat transfer area between elements, d is the distance between elements, κ is the thermal conductivity of the material, T is the temperature of the element of interest, and

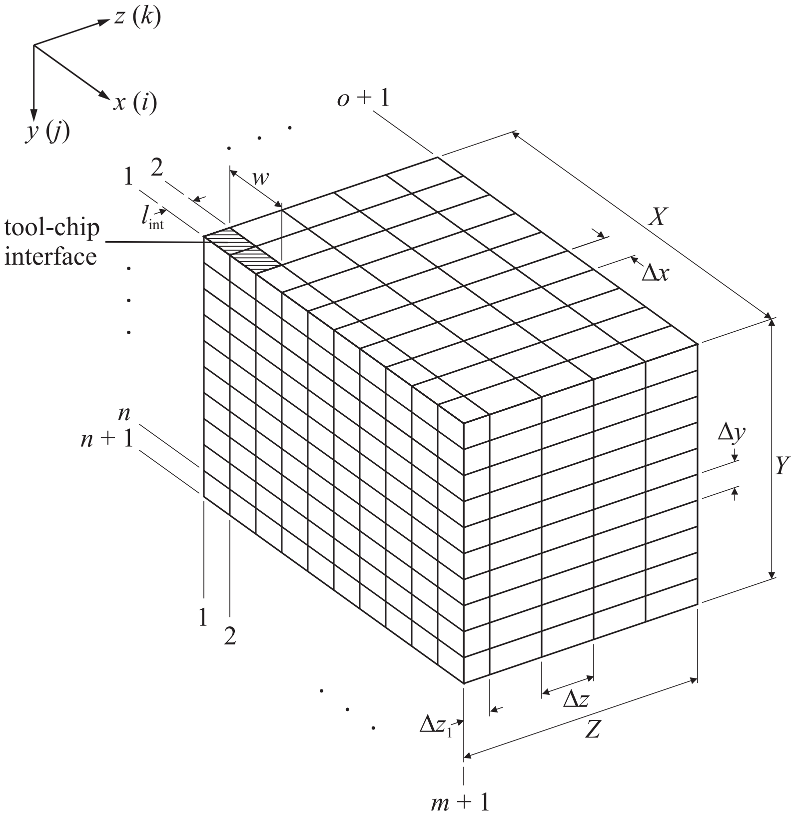

Figure C.1: Three dimension geometry of cutting tool for the finite-difference prediction of the temperature distribution.

T' is the temperature of the neighbouring element. The equation for $\dot{Q}_{\text{conv}}$ is defined as follows:

$$\dot{Q}_{\text{conv}} = Ah(T - T_{\infty}) \tag{C.3}$$

where A is the area of contact between the element and the surrounding air, h is the convective heat transfer coefficient, T is the temperature of the element, and T_{∞} is the air temperature far away from the element. Moreover, by using Equation C.1, a general relationship that relates the temperature of any element (i, j, k) with the temperatures from the six neighbouring elements can be established:

$$T^{N+1,i,j,k} = \frac{C_1^{i,j,k} T^{N,i-1,j,k} + C_2^{i,j,k} T^{N,i+1,j,k} + C_3^{i,j,k} T^{N,i,j-1,k} + C_4^{i,j,k} T^{N,i,j+1,k} + C_5^{i,j,k} T^{N,i,j,k-1} + C_6^{i,j,k} T^{N,i,j,k+1}}{C_1^{i,j,k} + C_2^{i,j,k} + C_3^{i,j,k} + C_4^{i,j,k} + C_5^{i,j,k} + C_6^{i,j,k}} \tag{C.4}$$

Before starting the numerical process, and since the temperatures of the elements are still unknown, some initial value must be assigned to the temperatures of each element (i, j, k). Subsequently, Equation C.4 can be used to predict the values of $T^{N+1,i,j,k}$ one iteration ahead $(N+1)$ from the temperature of its neighbouring elements. This procedure may be repeated until the temperatures start to converge to its final values, i.e. when the convergence criterion that follows is met:

$$\left| \frac{T^{N+1,i,j,k} - T^{N,i,j,k}}{T^{N,i,j,k}} \right| \leq e \tag{C.5}$$

where e is the convergence error criterion. Moreover, since the values of $C_1^{i,j,k}$, $C_2^{i,j,k}$, $C_3^{i,j,k}$, $C_4^{i,j,k}$, $C_5^{i,j,k}$, and $C_6^{i,j,k}$ are associated with the heat flows $\dot{Q}_1$, $\dot{Q}_2$, $\dot{Q}_3$, $\dot{Q}_4$, $\dot{Q}_5$, and $\dot{Q}_6$, their values are dependent on the location of the element (i,j,k) in the block. Next, the values of C_1 and C_2 that involve convection are stated:

$$\begin{array}{lcl}
C_1^{1,n+1,1} = C_2^{m+1,1,1} = C_2^{m+1,n+1,1} & = & \frac{\Delta y \Delta z_1}{4} h \\
C_1^{1,1,o+1} = C_1^{1,n+1,o+1} = C_2^{m+1,1,o+1} = C_2^{m+1,n+1,o+1} & = & \frac{\Delta y \Delta z}{4} h \\
C_1^{1,2\ldots n,1} = C_2^{m+1,2\ldots n,1} & = & \frac{\Delta y \Delta z_1}{2} h \\
C_1^{1,2\ldots n,o+1} = C_1^{1,1,3\ldots o} = C_1^{1,n+1,3\ldots o} & = & \\
C_2^{m+1,2\ldots n,o+1} = C_2^{m+1,1,3\ldots o} = C_2^{m+1,n+1,3\ldots o} & = & \frac{\Delta y \Delta z}{2} h \\
C_1^{1,n+1,2} = C_2^{m+1,1,2} = C_2^{m+1,n+1,2} & = & \frac{\Delta y (\Delta z_1 + \Delta z)}{4} h \\
C_1^{1,2\ldots n,3\ldots o} = C_2^{m+1,2\ldots n,3\ldots o} & = & \Delta y \Delta z h \\
C_1^{1,2\ldots n,2} = C_2^{m+1,2\ldots n,2} & = & \frac{\Delta y (\Delta z_1 + \Delta z)}{2} h
\end{array} \tag{C.6}$$

The values of C_1 and C_2 that involve conduction:

$$\begin{array}{lcl}
C_1^{m_1+2\ldots m+1,1,1} = C_1^{2\ldots m+1,n+1,1} = C_2^{m_1+2\ldots m,1,1} = C_2^{1\ldots m,n+1,1} & = & \frac{\Delta y \Delta z_1}{4\Delta x} \\
C_1^{2\ldots m+1,1,o+1} = C_1^{2\ldots m+1,n+1,o+1} = C_2 1 \ldots m, 1, o+1 = C_2^{1\ldots m,n+1,o+1} & = & \frac{\Delta y \Delta z}{4\Delta x} \kappa \\
C_1^{2\ldots m+1,2\ldots n,1} = C_2^{1\ldots m,2\ldots n,1} & = & \frac{\Delta y \Delta z_1}{2\Delta x} \kappa \\
C_1^{2\ldots m+1,2\ldots n,o+1} = C_1^{2\ldots m+1,1,3\ldots o} = C_1^{2\ldots m+1,n+1,3\ldots o} & = & \\
C_2^{1\ldots m,2\ldots n,o+1} = C_2^{1\ldots m,1,3\ldots o} = C_2^{1\ldots m,n+1,3\ldots o} & = & \frac{\Delta y \Delta z}{2\Delta x} \kappa \\
C_1^{m_1+2\ldots m+1,1,2} = C_1^{2\ldots m+1,n+1,2} = C_2^{m_1+2\ldots m,1,2} = C_2^{1\ldots m,n+1,2} & = & \frac{\Delta y (\Delta z_1 + \Delta z)}{4\Delta x} \kappa \\
C_1^{2\ldots m+1,2\ldots n,3\ldots o} = C_2^{1\ldots m,2\ldots n,3\ldots o} & = & \frac{\Delta y \Delta z}{\Delta x} \kappa \\
C_1^{2\ldots m+1,2\ldots n,2} = C_2^{1\ldots m,2\ldots n,2} & = & \frac{\Delta y (\Delta z_1 \Delta z)}{2\Delta x} \kappa
\end{array} \tag{C.7}$$

The values of C_3 and C_4 that involve convection:

$$\begin{array}{lcl}
C_3^{m+1,1,1} = C_4^{1,n+1,1} = C_4^{m+1,n+1} & = & \frac{\Delta x \Delta z_1}{4} h \\
C_3^{1,1,o+1} = C_3^{m+1,1,o+1} = C_4^{1,n+1,o+1} = C_4^{m+1,n+1,o+1} & = & \frac{\Delta x \Delta z}{4} h \\
C_3^{m_1+2\ldots m,1,1} = C_4^{2\ldots m,n+1,1} & = & \frac{\Delta x \Delta z_1}{2} h \\
C_3^{2\ldots m,1,o+1} = C_3^{1,1,3\ldots o} = C_3^{m+1,1,3\ldots o} & = & \\
C_4^{2\ldots m,n+1,o+1} = C_4^{1,n+1,3\ldots o} = C_4^{m+1,n+1,3\ldots o} & = & \frac{\Delta x \Delta z}{2} h \\
C_3^{m+1,1,2} = C_4^{1,n+1,2} = C_4^{m+1,n+1,2} & = & \frac{\Delta x (\Delta z_1 + \Delta z)}{4} h \\
C_3^{2\ldots m,1,3\ldots o} = C_4^{2\ldots m,n+1,3\ldots o} & = & \Delta x \Delta x h \\
C_3^{m_1+2\ldots m,1,2} = C_4^{2\ldots m,n+1,2} & = & \frac{\Delta x (\Delta z_1 + \Delta z)}{2} h
\end{array} \tag{C.8}$$

The values of C_3 and C_4 that involve conduction:

$$\begin{aligned}
C_3^{1,2\ldots n+1,1} = C_3^{m+1,2\ldots n+1,1} = C_4^{1,2\ldots n,1} = C_4^{m+1,1\ldots n,1} &= \tfrac{\Delta x \Delta z_1}{4\Delta} \\
C_3^{1,2\ldots n+1,o+1} = C_3^{m+1,2\ldots n+1,o+1} = C_4^{1,1\ldots n,o+1} = C_4^{m+1,1\ldots n,o+1} &= \tfrac{\Delta x \Delta z}{4\Delta y}\kappa \\
C_3^{2\ldots m,2\ldots n+1,1} = C_4^{2\ldots m_1+1,2\ldots n,1} = C_4^{m_1+2\ldots m,1\ldots n,1} &= \tfrac{\Delta x \Delta z_1}{\Delta y}\kappa \\
C_3^{2\ldots m,2\ldots n+1,o+1} = C_3^{1,2\ldots n+1,3\ldots o} = C_3^{m+1,2\ldots n+1,3\ldots o} &= \\
C_4^{2\ldots m,1\ldots n,o+1} = C_4^{1,1\ldots n,3\ldots o} = C_4^{m+1,1\ldots n,3\ldots o} &= \tfrac{\Delta x \Delta z}{2\Delta y}\kappa \\
C_3^{1,2\ldots n+1,2} = C_3^{m+1,2\ldots n+1,2} = C_4^{1,2\ldots n,2} = C_4^{m+1,1\ldots n,2} &= \tfrac{\Delta x(\Delta z_1+\Delta z)}{4\Delta y}\kappa \\
C_3^{2\ldots m,2\ldots n+1,3\ldots o} = C_4^{2\ldots m,1\ldots n,3\ldots o} &= \tfrac{\Delta x \Delta z}{\Delta y}\kappa \\
C_3^{2\ldots m,2\ldots n+1,2} = C_4^{2\ldots m1+1,2\ldots n,2} = C_4^{m1+2\ldots m,1\ldots n,2} &= \tfrac{\Delta x(\Delta z_1 \Delta z)}{2\Delta y}\kappa
\end{aligned} \tag{C.9}$$

The values of C_5 and C_6 that involve convection:

$$\begin{aligned}
C_5^{m+1,1,1} = C_5^{1,n+1,1} = C_5^{m+1,n+1,1} &= \\
C_6^{1,1,o+1} = C_6^{m+1,1,o+1} = C_6^{1,n+1,o+1} = C_6^{m+1,n+1,o+1} &= \tfrac{\Delta x \Delta y}{4} h \\
C_5^{m_1+2\ldots m,1,1} = C_5^{2\ldots m,n+1,1} = C_5^{1,2\ldots n,1} = C_5^{m+1,2\ldots n,1} &= \\
C_6^{2\ldots m,1,o+1} = C_6^{2\ldots m,n+1,o+1} = C_6^{1,2\ldots n,o+1} = C_6^{m+1,2\ldots n,o+1} &= \tfrac{\Delta x \Delta y}{2} h \\
C_5^{2\ldots m,2\ldots n,1} = C_6^{2\ldots m,2\ldots n,o+1} &= \Delta z \Delta y h
\end{aligned} \tag{C.10}$$

Finally, the values of C_5 and C_6 that involve conduction:

$$\begin{aligned}
C_5^{1,1,3\ldots o+1} = C_5^{m+1,1,3\ldots o+1} = C_5^{1,n+1,3\ldots o+1} = C_5^{m+1,n+1,3\ldots o+1} &= \\
C_6^{1,1,3\ldots o} = C_6^{m+1,1,2\ldots o} = C_6^{1,n+1,2\ldots o} = C_6^{m+1,n+1,2\ldots o} &= \tfrac{\Delta x \Delta y}{4\Delta z}\kappa \\
C_5^{m+1,1,2} = C_5^{1,n+1,2} = C_5^{m+1,n+1,2} &= \\
C_6^{m+1,1,1} = C_6^{1,n+1,1} = C_6^{m+1,n+1,1} &= \tfrac{\Delta x \Delta y}{4\Delta z_1}\kappa \\
C_5^{2\ldots m,1,3\ldots o+1} = C_5^{2\ldots m,n+1,3\ldots o+1} = C_5^{1,2\ldots n,3\ldots o+1} = C_5^{m+1,2\ldots n,3\ldots o+1} &= \\
C_6^{2\ldots m,1,3\ldots o} = C_6^{2\ldots m,n+1,2\ldots o} = C_6^{1,2\ldots n,2\ldots o} = C_6^{m+1,2\ldots n,2\ldots o} &= \tfrac{\Delta x \Delta y}{2\Delta z}\kappa \\
C_5^{m_1+2\ldots m,1,2} = C_5^{2\ldots m,n+1,2} = C_5^{1,2\ldots n,2} = C_5^{m+1,2\ldots n,2} &= \\
C_6^{m_1+2\ldots m,1,1\ldots 2} = C_6^{2\ldots m,n+1,1} = C_6^{1,2\ldots n,1} = C_6^{m+1,2\ldots n,1} &= \tfrac{\Delta x \Delta y}{2\Delta z_1}\kappa \\
C_5^{2\ldots m,2\ldots n,3\ldots o+1} = C_6^{2\ldots m,2\ldots n,2\ldots o} &= \tfrac{\Delta x \Delta y}{\Delta z}\kappa \\
C_5^{2\ldots m,2\ldots n,2} = C_6^{2\ldots m,2\ldots n,1} &= \tfrac{\Delta x \Delta y}{\Delta z_1}\kappa
\end{aligned} \tag{C.11}$$

where l_{int} is the tool-chip contact length, $\Delta x = \frac{X}{m}$, $\Delta y = \frac{Y}{n}$, $\Delta z_1 = l_{\text{int}}$, $\Delta z = \frac{Z - l_{\text{int}}}{o-1}$, and $m_1 = \frac{w}{\Delta x}$. In addition, since the temperature of the tool-chip contact area remains constant during the whole process, the following equation must be combined with Equation C.4:

$$T^{N+1,i,j,k} = T_{\text{int}} \quad \text{for} \quad i \leq \tfrac{w}{\Delta x} + 0.5 \text{ and } j = 1 \text{ and } k \leq 2 \tag{C.12}$$

Finally, it must be noted that Equations C.4 and C.12 solely define $T^{i,j,k}$ for the rectangular block shown in Figure C.1, i.e. $i = 1 \ldots m+1$, $j = 1 \ldots n+1$, and $k = 1 \ldots o+1$. However, in order to complete the model, the convective heat that flows between the air and the boundaries of the block must also be specified; this is done as follows:

$$\begin{aligned} T^{0,0\ldots n+2,0\ldots o+2} = T^{m+2,0\ldots n+2,0\ldots o+2} &= \\ T^{1\ldots m+1,0,0\ldots o+2} = T^{1\ldots m+1,n+2,0\ldots o+2} &= \\ T^{1\ldots m+1,1\ldots n+1,0} = T^{1\ldots m+1,1\ldots n+1,o+2} &= T_{\infty} \end{aligned} \tag{C.13}$$

Figure C.2 shows an example of the temperatures predicted by the finite-difference method described above for $T_{\text{int}} = 1000°\text{C}$, $T_{\infty} = 25°\text{C}$, $w = 1$ mm, $l_{\text{int}} = 0.1$ mm, $X = 20$ mm, $Y = 20$ mm, $Z = 20$ mm. The values of κ and h were estimated: 50 W/m-°C and 100 W/m^2-°C, respectively. Convergence was attained for $e = 10^{-7}$ (Equation C.5) for the successive calculated temperatures obtained at location $x = 0$ mm, $y = 5$ mm, and $z = 0$ mm, temperature T_1. Figure C.2a shows the variation of T_1 for each iteration during the finite-difference computation procedure. It can also be observed that T_1 rises initially quickly from the initial value given to the unknown elements of the block (150°C), converging later slowly to its final value (234°C). Figure C.2b shows the temperature distribution after convergence on the *xy*-face of the block that is under the tool-chip interface.

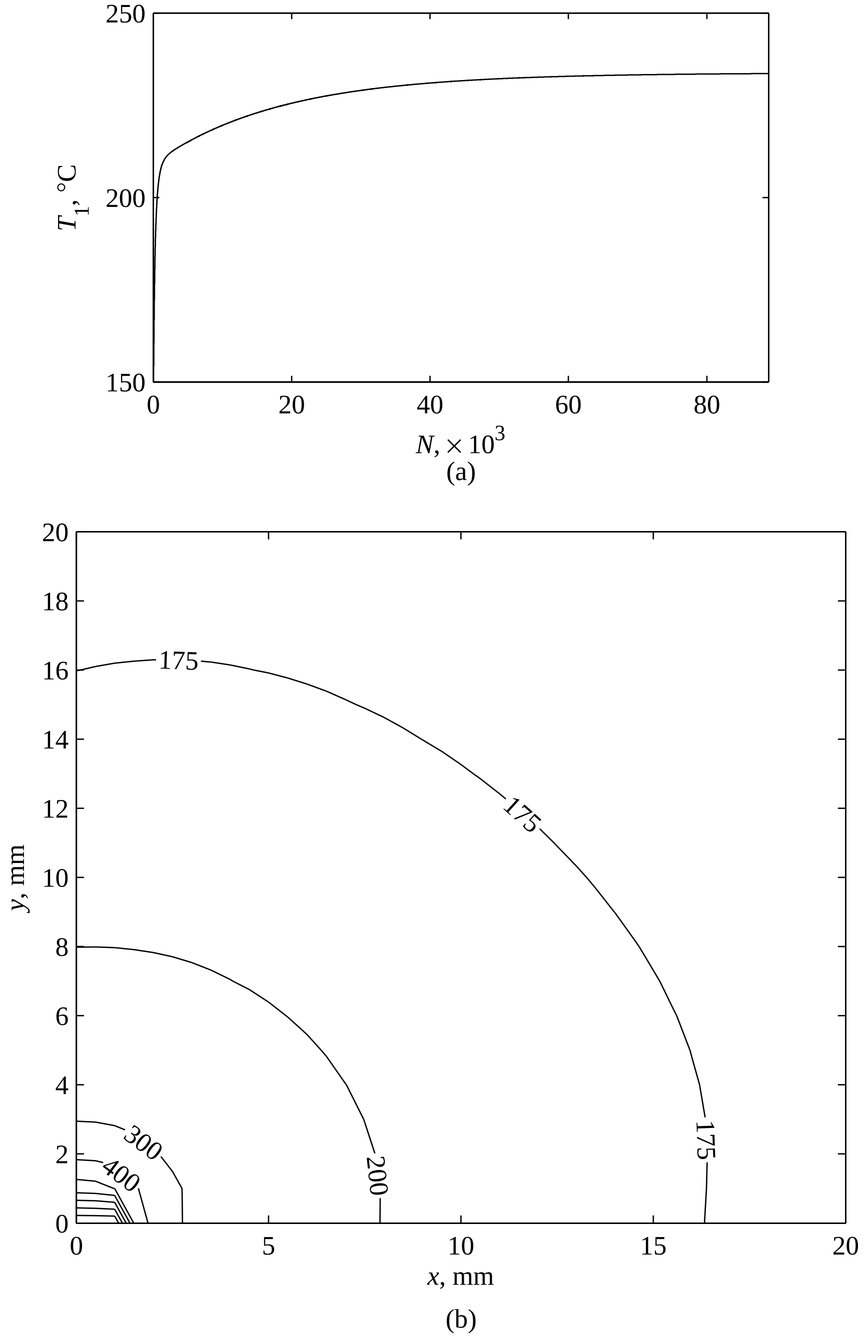

Figure C.2: Example of temperature predictions using the finite-difference method. (a) Variation of temperature T_1 with N until convergence is reached. (b) Two-dimensional temperature distribution on plane $z = 0$ mm (temperature units: °C).

Appendix D

Electronic Circuits

This appendix shows the electronic circuits built for the experimental work. All circuits are referred in Chapter 3.

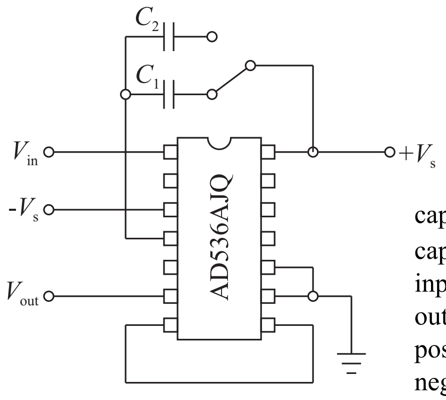

capacitor	C_1	0.01 μF
capacitor	C_2	0.1 μF
input voltage	V_{in}	
output voltage	V_{out}	
positive voltage supply	$+V_s$	+15 V
negative voltage supply	$-V_s$	-15 V

Figure D.1: Electronic circuit diagram of RMS computation using the integrated circuit AD536AJQ (Analog Devices).

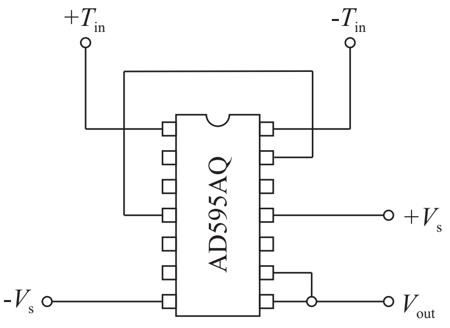

chromel thermocouple input	$+T_{in}$	
alumel thermocouple input	$-T_{in}$	
output voltage	V_{out}	
positive voltage supply	$+V_s$	+15 V
negative voltage supply	$-V_s$	-15 V

Figure D.2: Electronic circuit diagram of thermocouple amplifier using the integrated circuit AD595AQ (Analog Devices).

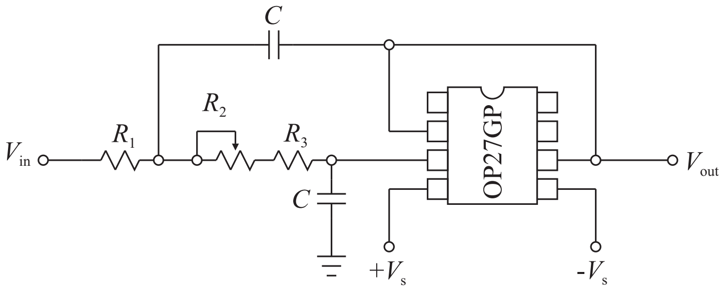

resistor	R_1	100 kΩ	input voltage	V_{in}	
variable resitor	R_2	0-20 kΩ	output voltage	V_{out}	
resistor	R_3	100 Ω	positive voltage supply	$+V_s$	+15 V
capacitor	C	1 nF	negative voltage supply	$-V_s$	-15 V

Figure D.3: Electronic circuit diagram of anti-aliasing low-pass filter with variable cut-off frequency using the integrated circuit OP37GP (Analog Devices). With this configuration, by varying R_2, it is possible to obtain Butterworth filter response with cut-off frequencies in the 3.5–50 kHz range.

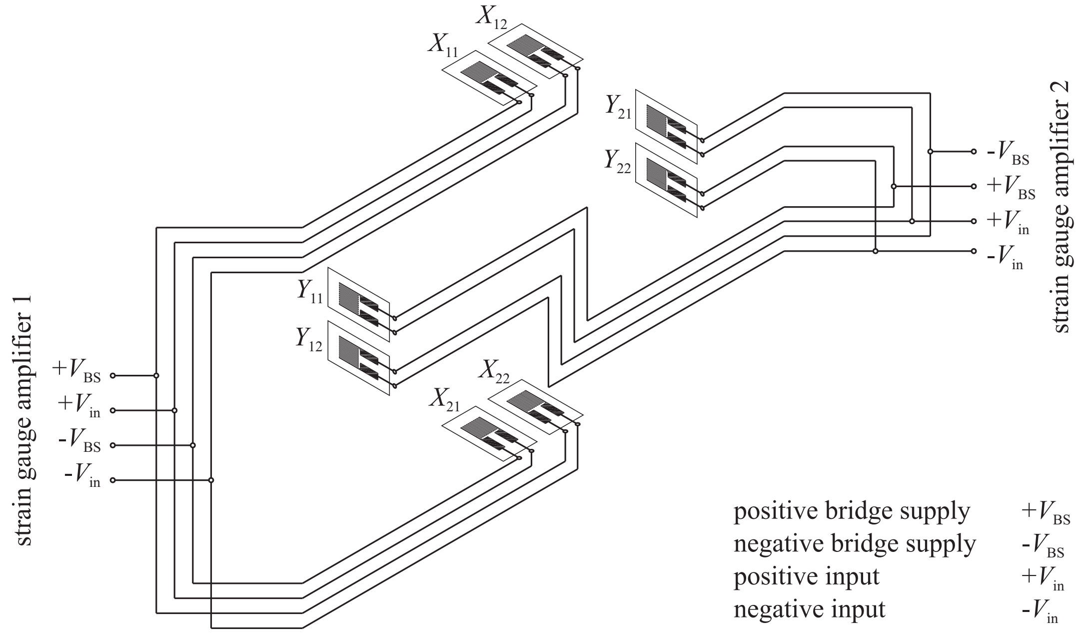

Figure D.4: Configuration of the two full Wheatstone bridges formed by the main cutting forces strain gauges (X_{11}, X_{12}, X_{21}, and X_{22}) and by the feed force strain gauges (Y_{11}, Y_{12}, Y_{21}, and Y_{22}), respectively. Each bridge arrangement is connected to a strain gauge amplifier, using integrated circuit 847-171 and circuit board 435-692 from RS Components.

References

[1] M. C. Shaw, *Metal Cutting Principles*, Oxford Series on Advanced Manufacturing, Oxford University Press, 1984.

[2] R. Reuben, The Role of Acoustic Emission in Industrial Condition Monitoring, International Journal of COMADEM **1**(4), 35–46 (October 1998).

[3] I. Inasaki and S. Yonetsu, In-Process Detection of Cutting Tool Damage by Acoustic Emission Measurement, in *Proceedings of the 22nd International Machine Tool Design and Research Conference*, pages 261–268, Manchester, 1981.

[4] M. S. Lan and D. A. Dornfeld, Experimental Studies of Tool Wear via Acoustic Emission Analysis, in *Proceedings of the 10th North American Manufacturing Research Conference*, pages 305–311, May 1982.

[5] V. Messaritis and W. K. D. Borthwick, Processing Acoustic Emission Signal Data for Characterising Cutting Tool Wear and Chip Management, in *Proceeding of the 1st International Conference on Computer-Aided Production Engineering*, pages 261–268, 1986.

[6] Y. Naerheim and M. S. Lan, Acoustic Emission Reveals Information about the Metal Cutting Process and Tool Wear, in *Proceedings of the 16th North American Manufacturing Research Conference*, pages 240–244, May 1988.

[7] T. Blum and I. Inasaki, A Study on Acoustic Emission from the Orthogonal Cutting Process, Journal of Engineering for Industry—Transactions of the ASME **112**(3), 203–211 (August 1990).

[8] D. E. Dimla, Snr., Sensor Signals for Tool-Wear Monitoring in Metal Cutting Operations—A Review of Methods, International Journal of Machine Tools and Manufacture **40**, 1073–1098 (2000).

[9] X. Li, A brief Review: Acoustic Emission Method for Tool Wear Monitoring during Turning, International Journal of Machine Tools and Manufacture **42**, 157–165 (2002).

[10] T. Moriwaki, Detection of Cutting Tool Fracture by Acoustic Emission Measurement, Annals of the CIRP **29**(1), 35–40 (1980).

[11] M. S. Lan and D. A. Dornfeld, In-Process Tool Fracture Detection, Journal of Engineering Materials and Technology—Transactions of the ASME **106**(2), 111–118 (April 1984).

[12] E. N. Diei and D. A. Dornfeld, A Model of Tool Fracture Generated Acoustic Emission during Machining, Journal of Engineering for Industry—Transactions of ASME **109**(3), 227–233 (August 1987).

[13] W. Haili, S. Hua, C. Ming, and H. Dejin, On-Line Tool Breakage Monitoring in Turning, Journal of materials Processing Technology **139**, 237–242 (2003).

[14] D. A. Dornfeld and M. S. Lan, Chip Form Detection using Acoustic Emission, in *Proceedings of the 11th North American Manufacturing Research Conference*, pages 386–389, Madison, May 1983.

[15] K. Uehara and Y. Kanda, Indentification of Chip Formation Mechanism through Acoustic Emission Measurements, Annals of the CIRP **33**(1), 71–74 (1984).

[16] D. A. Dornfeld and C. S. Pan, A Study of Continuous/Discontinuous Chip Formation using Acoustic Emission, Journal of Applied Metal Working **4**(1), 18–29 (July 1985).

[17] A. Iturrospe, D. A. Dornfeld, V. Atxa, and J. M. Abete, Bicepstrum Based Blind Identification of the Acoustic Emission (AE) Signal in Precisison Turning, Mechanical Systems and Signal Processing **19**, 447–466 (2005).

[18] P. L. B. Oxley, *Mechanics of Machining: An Analytical Approach to Assessing Machinability*, Ellis Horwood Series in Mechanical Engineering, Ellis Horwood, 1989.

[19] S. Rangwala and D. A. Dornfeld, A Study of Acoustic Emission Generated during Orthogonal Metal Cutting—2: Spectral Analysis, International Journal of Mechanical Sciences **33**(6), 489–499 (1991).

[20] J. P. Holman, *Heat Transfer*, McGraw-Hill Series in Mechanical Engineering, McGraw-Hill, 9th edition, 2002.

[21] D. Hull and D. J. Bacon, *Introduction to Dislocations*, volume 37 of *International Series on Materials Science and Technology*, Pergamon Press, 3rd edition, 1984.

[22] R. W. K. Honeycombe, *The Plastic Deformation of Metals*, Edward Arnold, 2nd edition, 1984.

[23] V. R. Skak's'kyi, O. E. Andreikiv, and O. M. Serhienko, Investigation of the Plastic Deformation of materials by the Acoustic Emission Method (Review), Materials Science **39**(1), 86–107 (January 2003).

[24] K. Onu, Current Understanding of Mechanisms of Acoustic Emission, The Journal of Strain Analysis for Engineering Design **40**(1), 1–15 (January 2005).

[25] A. Kumar, F. E. Hauser, and J. E. Dorn, Viscous Drag on Dislocations in Aluminium at High Strain rates, Acta Metallurgica **16**, 1189–1197 (1968).

[26] A. Kumar, Strain Rate Effects in Materials, Applied Polymer Symposia **12**, 67–96 (1969).

[27] ASM Committee on Machining, Machining of Steel and Cast Iron, Metal Progress, 141–151 (July 1954).

[28] D. Kececioglu, Shear-Strain Rate in Metal Cutting and its Effects on Shear-Flow Stress, Transactions of the ASME **80**, 158–168 (January 1958).

[29] H. Ernst and M. E. Merchant, Chip Formation, Friction and High Quality Machined Surfaces, Transactions of the American Society for Metals **29**, 299–378 (1941).

[30] P. L. B. Oxley and M. J. M. Welsh, Calculating the Shear Angle in Orthogonal Metal Cutting from Fundamental Stress, Strain, Strain-Rate Properties of the Work Material, in *Proceedings of the 4th International Machine Tool Design and Research Conference,* pages 73–86, 1963.

[31] P. K. Wright and J. L. Robinson, Material Behaviour in Deformation Zones of Machining Operation, Metals Technology **4**(5), 240–248 (May 1977).

[32] M. G. Stevenson and P. L. B. Oxley, An Experimental Investigation of the Influence of Strain-Rate and Temperature on the Flow Stress Properties of a Low Carbon Steel using a Machining Test, Proceedings of the Institution of Mechanical Engineers **185**, 741–754 (1970–1971).

[33] W. F. Hastings, P. L. B. Oxley, and M. G. Stevenson, Predicting a Materials's Machining Characteristics Using Flow Stress Properties Obtained from High-Speed Compression Tests, Proceedings of the Institution of Mechanical Engineers **188**, 245–252 (1974).

[34] N. N. Zorev, Interrelationship between Shear Process Ocurring along Tool Face and on Shear Plane in Metal Cutting, in *International Research in Production Engineering,* pages 42–49, 1963.

[35] E. M. Trent, *Metal Cutting,* Butterworths, 2nd edition, 1984.

[36] S. Kobayashi and E. G. Thomsen, The role of Friction in Metal Cutting, Journal of Engineering for Industry—Transactions of the ASME **82**, 324–332 (November 1960).

[37] R. G. Fenton and P. L. B. Oxley, Mechanics of Orthogonal Machining: Allowing for the Effects of Strain Rate and Temperature on Tool-Chip Friction, Procedings of the Institution of Mechanical Engineers **183**, 417–438 (1968-1969).

[38] L. I. Xiaoping, Development of a Predictive model for Stress Distributions at the Tool-Chip Interface in Machining, Journal of Materials Processing Technology **63**, 169–174 (1997).

[39] D. E. Buryta and R. Sowerby, Experimental Determination of Rake face Stress Distributions, Key Engineering Materials **138–140**, 57–125 (1998).

[40] W. F. Hosford and R. M. Caddell, *Metal Forming: Mechanics and Metallurgy,* Prentice-Hall, 1983.

[41] E. Bickel, The Temperature on a Turning Tool, in *International Research in Production Engineering,* pages 89–94, 1963.

[42] M. B. Silva and J. Wallbank, Cutting Temperature: Prediction and Measurement Methods—A Review, Journal of Materials Processing Technology **88**, 195–202 (1999).

[43] D. A. Stephenson, Tool-Work Thermocouple Temperature Measurements—Theory and Implementation Issues, Journal of Engineering for Industry—Transactions of the ASME **115**(4), 432–437 (November 1993).

[44] J. G. Chow and P. K. Wright, On-Line Estimation of Tool/Chip Interface Temperatures for a Turning Operation, Journal of Engineering for Industry—Transactions of the ASME **110**(1), 56–64 (February 1988).

[45] B. T. Chao, H. L. Li, and K. L. Trigger, An Experimental Investigation of Temperature Distribution at Tool-Flank Surface, Journal of Engineering for Industry—Transactions of the ASME **83**, 496–504 (November 1961).

[46] S. P. F. C. Jaspers, J. H. Dautzemberg, and D. A. Taminiau, Temperature Measurement in Orthogonal Metal Cutting, International Journal of Advanced Manufacturing Technology **14**, 7–12 (1998).

[47] D. A. Stephenson, Assessment of Steady-State Metal Cutting Temperature Models Based on Simultaneous Infrared and Thermocouple Data, Journal of Engineering for Industry—Transactions of the ASME **113**(2), 121–128 (May 1991).

[48] E. H. Lee and B. W. Shaffer, The Theory of Plasticity Applied to a Problem of Machining, Journal of Applied Mechanics **18**, 405–413 (December 1951).

[49] S. Kobayashi and E. G. Thomsen, Some Observations on the Shearing Process in Metal Cutting, Journal of Engineering for Industry—Transactions of the ASME **81**, 251–262 (August 1959).

[50] P. L. B. Oxley, Development and Application of a Predictive Machining Theory, Machining Science and Technology **2**, 165–189 (1998).

[51] W. F. Hastings, P. Mathew, and P. L. B. Oxley, A Machining Theory for Predicting Chip Geometry, Cutting Forces etc. from Work Material Properties and Cutting Conditions, Proceedings of the Royal Society of London **A371**(1747), 569–587 (August 1980).

[52] E. M. Trent, Tool Wear and Machinability, Institution of Production Engineers Journal **38**(105), 105–130 (1959).

[53] J. C. Spanner, *Acoustic Emission: Techniques and Applications*, Intex Publishing Company, 1974.

[54] V. Ivanov, Acoustic Emission: Some Problems, Tasks and Solutions, NDT International **17**(6), 323–328 (December 1984).

[55] P. P. Gillis, Dislocation Motions and Acoustic Emissions, Acoustic Emission, ASTM STP 505, 20–29 (1972).

[56] D. Rouby, P. Fleischmann, and P. Gobin, An Acoustic Emission Source Model Based on Dislocation Movement, in *Proceedings of the 6th International Conference on Internal Friction and Ultrasonic Attenuation in Solids*, pages 811–815, 1977.

[57] S. Rangwala and D. A. Dornfeld, A Study of Acoustic Emission Generated during Orthogonal Metal Cutting—1: Energy Analysis, International Journal of Mechanical Sciences **33**(6), 471–487 (1991).

[58] J. Blitz, *Ultrasonics: Methods and Applications*, Butterworths, 1971.

[59] A. E. Diniz, J. J. Liu, and D. A. Dornfeld, Correlation Tool Life, Tool Wear and Surface Roughness by Monitoring Acoustic Emission in Finish Turning, Wear **152**, 395–407 (1992).

[60] E. Kannatey-Asibu, Jr. and D. A. Dornfeld, Quantitative Relationships for Acoustic Emission from Orthogonal Metal Cutting, Journal of Engineering for Industry—Transactions of the ASME **103**(3), 330–340 (August 1981).

[61] T. Moriwaki, Application of Acoustic Emission Measurement to Sensing of Wear and Breakage of Cutting Tool, Bulletin of the Japan Society of Precision Engineering **17**, 154–160 (September 1983).

[62] D. A. Dornfeld and E. Kannatey-Asibu, Jr., Acoustic Emission during Orthogonal Metal Cutting, International Journal of Mechanical Science **22**(5), 285–296 (1980).

[63] M. J. Schmenk, Acoustic Emission and the Mechanics of Metalcutting, in *Acoustic Emission Monitoring and Analysis in Manufacturing—Winter Annual Meeting of the ASME*, pages 95–106, December 1984.

[64] M. S. Lan and D. A. Dornfeld, Acoustic Emission and Machining—Process Analysis and Control, Advanced Manufacturing Processes **1**(1), 1–21 (1986).

[65] D. P. Saini and Y. J. Park, A Quantitative Model of Acoustic Emission in Orthogonal Cutting Operations, Journal of Materials Processing Technology **58**, 343–350 (1996).

[66] M. S. Lan and Y. Naerheim, Application of Acoustic Emission Monitoring in Machining, in *Proceedings of the 13th North American Manufacturing Research Conference*, pages 310–313, May 1985.

[67] I. Grabec and P. Leskovar, Acoustic Emission of a Cutting Process, Ultrasonics **15**(1), 17–20 (January 1977).

[68] Z. Yaohui and X. Rongbao, A Study on the Separation of Acoustic Emission Signals in Metal Cutting Process, in *Progress in Acoustic Emission IV—The Japanese Society for NDI*, pages 462–469, 1988.

[69] G. C. I. Lin, P. Mathew, P. L. B. Oxley, and A. R. Watson, Predicting Cutting Forces for Oblique Machining Conditions, Proceedings of the Institute of Mechanical Engineers **196**, 141–148 (1982).

[70] A. H. Adibi-Sedeh, V. Madhavan, and B. Bahr, Extension of Oxley's Analysis of Machining to Use Different Material Models, Journal of Manufacturing Science and Engineering—Transactions of the ASME **125**(4), 656–666 (November 2003).

[71] M. Oyane, F. Takashima, K. Osakada, and H. Tanaka, The Behaviour some Steels under Dynamic Compression, 10th Japan Congress on Testing Materials, 72–76 (1967).

[72] C. W. MacGregor and J. C. Fisher, A Velocity-Modified Temperature for the Plastic Flow of Metals, Journal of Applied Mechanics **13**, A11–A16 (March 1946).